Physics of Atomic Nuclei, Vol. 65, No. 4, 2002, pp. 583–592. From Yadernaya Fizika, Vol. 65, No. 4, 2002, pp. 615–624.

Alpha Clustering in $4n$ Nuclei from ^{4}He to ^{40}Ca*

G. S. Anagnostatos**, **C. Politis**[1)], **C. Syros**[1)], **P. K. Kakanis**[2)], **and J. Giapitzakis**[1)]

Institute of Nuclear Physics, National Center for Scientific Research "Demokritos," Aghia Paraskevi, Attiki, Greece

Received September 6, 2001

Abstract—The α clustering in nuclei from ^{4}He to ^{40}Ca has been presented on a systematic footing which depicts the similarities from nucleus to nucleus. Here, the isomorphic shell model has been employed, which is a hybrid between the conventional shell model and liquid drop model in conjunction with the nucleon finite size and which, in addition, uses no adjustable parameters. In the framework of the model an α-like particle is defined as four close-by nucleons (two neutrons and two protons) in relative angular momentum zero. Thus, up to ^{40}Ca nine such α-like particles and two deuterons are formed whose average positions are well specified in the model. Hence, each time an α-like particle is formed (following the aforementioned definition), this could have an average position only at one of the above nine available positions for such particles. Any $4n$ nucleus arranges its n α-like particles in the same way and any such arrangement corresponds to the ground state or to an excited state of this nucleus and serves as the band head of a rotational band. For ^{20}Ne nine such bands have been found, while for ^{12}C and ^{28}Si two and five bands, respectively. The linear α-chain for ^{12}C and persisting α-planar structures for heavier nuclei appear in a natural way in the framework of the model and are supported by many observables. The real novelty of this presentation is the fact that the axis of rotation and the number of rotating nucleons inside the same rotational band may change in such a way that the relevant moment of inertia increases monotonically in steps forming for each step a new branch of the band. Thus, several such bands have the same band head, a fact which closely resembles the phenomenon of superdeformation. This phenomenon here is the result of existence of several axes of symmetry and of several axes of rotation which, by changing the axis of rotation, permit the moment of inertia to increase up to the solid body limit.

1. INTRODUCTION

The study of alpha clustering has a long history in nuclear physics and many geometries of α-cluster configurations have been examined in the literature ranging from three-dimensional to two-dimensional and even to one-dimensional configurations [1–14].

A common characteristic of many α-cluster models is that the α particles involved in the nuclear structure are considered preformed and thus the nucleus appears in the framework of these models as an aggregate of α-particle subunits. Despite the apparent successes of these models, however, the wealth of nuclear reactions does not support this α-particle composition of nuclei even for the $4n$ nuclei. One thus could compromise the situation by assuming that each such α-like particle is composed of four close-by nucleons (two neutrons and two protons) with the same n and l quantum numbers (i.e., of four nucleons in a relative s state) instead of being composed of four nucleons in a real s state as usually assumed [15–17]. Thus, effectively nucleons and not α particles could be the fundamental constituents of a nucleus.

In the present study an alternative approach, along the lines of the isomorphic shell model [18–21], has been considered, where indeed nucleons and not α-particles compose the nuclei and, thus, possible α particles and their spatial distributions in nuclei are derived. The common point between the isomorphic shell model and any α-cluster model is that both models consider the geometry of the average positions of the constituent particles as the starting point for describing the total wave function of a nucleus.

The present study starts with a brief development of the isomorphic shell model and continues with its applications on several nuclear properties of $4n$ nuclei with emphasis on rotational bands. For applications on more properties and additional nuclei one could consult the cited references [15–17].

*This article was submitted by the authors in English.

[1)]University of Patras, School of Engineering, Patras, Greece.
[2)]Greek Atomic Energy Commission, Aghia Paraskevi, Attiki, Greece.
**e-mail: anagnos@mail.demokritos.gr

1063-7788/02/6504-0583$22.00

2. THE MODEL

The model employed here is the isomorphic shell model (ISM), which is a microscopic nuclear-structure model that incorporates into a hybrid model the prominent features of single-particle and collective approaches in conjunction with the nucleon finite size.

The model consists of two complementary parts, namely, the semiclassical part [18] and the quantum mechanical part [19]. Both parts give very good results which are consistent with each other.

2.1. The Quantum Mechanical ISM

The Hamiltonian of the model is analyzed in partial state-dependent Hamiltonians which are different for neutrons (n) and for protons (Z) as follows, where crossing terms between partial Hamiltonians of different shells, H_{ij}, have been omitted:

$$H = {}_N H_{1s} + {}_N H_{1p} + {}_N H_{1d2s} + \ldots + {}_Z H_{1s} + {}_Z H_{1p} + {}_Z H_{1d2s} + \ldots, \quad (1)$$

where the harmonic oscillator is taken as the central potential.

The different ω_i are not taken as adjusted parameters, but all are determined from the harmonic oscillator relation [22]

$$\hbar\omega_i = \left(\frac{\hbar^2}{m\langle r_i^2\rangle}\right)\left(n_i + \frac{3}{2}\right), \quad (2)$$

where $\langle r_i^2\rangle^{1/2}$ is the root-mean-square radius of nucleon centers for the particular neutron or proton shell under consideration and is estimated in the semiclassical part of the model (given bellow) with respect to only two numerical parameters.

In addition to eigenvalues for the energy derived from Eq. (1), Coulomb, spin–orbit, isospin, and last odd nucleon (neutron or proton, if it exists) energies are introduced in the estimation of the binding energy of a nucleus as usual.

2.2. The Semiclassical ISM

This part of the model is based on two assumptions, namely, that of equilibrium of nucleon average positions on spherical shells and that of packing of the average forms of nuclear shells [18]. The first leads uniquely to the conclusion that the average forms of nuclear shells have the high symmetry of equilibrium (regular) polyhedra [23], while the second leads uniquely to the sizes of these polyhedra, when they are considered superimposed with a common center and nucleons are taken with finite size ($r_p = 0.860$ fm and $r_n = 0.974$ fm).

Figure 1 shows the average forms of the first three neutron shells and those of the first three proton shells in relative size and orientation, while Fig. 1 of [18] shows the average polyhedral forms of all nuclear shells up to ^{208}Pb. The sizes of these polyhedra are also given at the bottom of each block of these figures. From Fig. 1 here and Fig. 1 of [18] it is apparent that a magic number is reproduced, all the way up to ^{208}Pb, each time a polyhedron is completed.

One should further notice in Fig. 1 that the vectors labelled ${}_n\theta_l^m$ precisely represent the orbital angular momentum quantization of directions and that the value labelled ρ at the lower right corner of each block of Fig. 1 stands for the maximum possible distance of the polyhedral vertices from these vectors. These ρ values are used for the estimation of the kinetic-energy part due to nucleon orbiting as will be understood shortly [21].

In this part of the model the binding energy of a nucleus is given by

$$E_B = \sum_{ij} V_{ij} + \sum_{nlm}\langle T_{nlm}\rangle + \sum_{ij}(E_{\rm C})_{ij} + \sum(E_{\rm SO})_{ij} + E_{\rm ISO} + E_{\text{odd }n}, \quad (3)$$

where the expressions for the last four terms are taken in the usual way as mentioned in the quantum-mechanical part of the model [18, 19], while the first two terms are computed by using Eqs. (4) and (5) below [20]:

$$V_{ij} = \frac{1.7\times 10^{17}\exp(-31.8538 r_{ij}) - 187\exp(-1.3538 r_{ij})}{r_{ij}} \ \text{(in MeV)}, \quad (4)$$

$$\langle T_{nlm}\rangle = \frac{\hbar^2}{2m}\left[\frac{1}{R_{\max}^2} + \frac{l(l+1)}{\rho_{nlm}^2}\right], \quad (5)$$

where $R_{\max}$ is the outermost polyhedral radius (R) plus the relevant nucleon radius (i.e., $r_n = 0.974$ fm

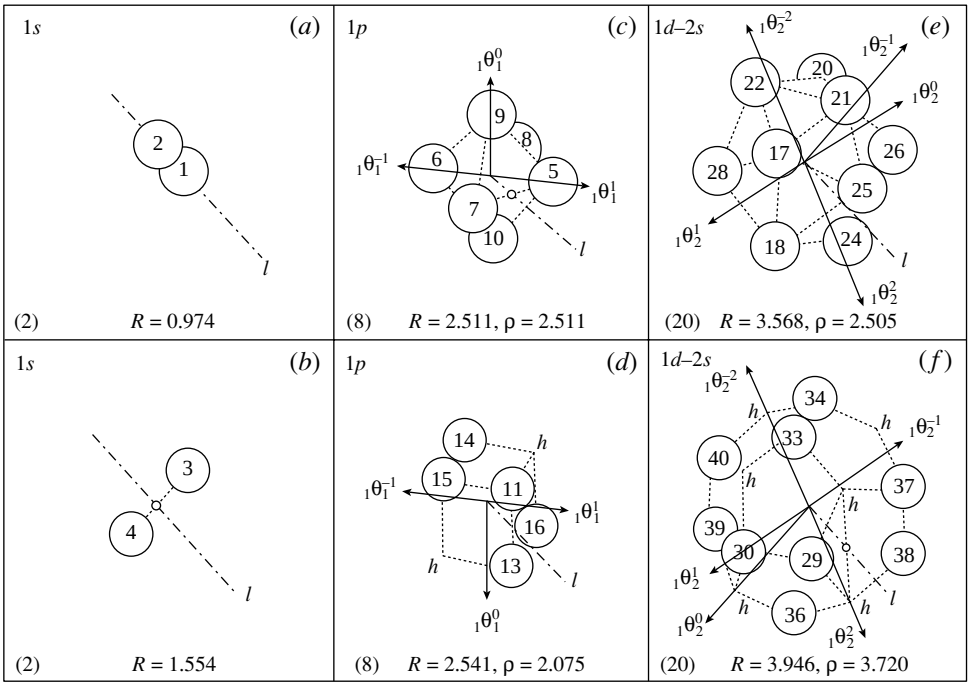

Fig. 1. Average structure of the first three neutron and the first three proton shells in the ISM. The letter h stands for empty vertices (holes), while arrows precisely present the orbital angular momentum quantization of directions as shown. Values of R give the average sizes of the relevant shells (in fm) and values of ρ give the maximum distances of polyhedral vertices from the aforementioned arrows. Finally, numbers in brackets stand for the cumulative numbers of vertices up to each polyhedral shell and coincide with the magic numbers.

and $r_p = 0.860$ fm), i.e., it is the radius of the nuclear volume in which the nucleons are confined, and ρ_{nlm} as is explained earlier [21].

The mass nuclear radius for both parts of the model is given by

$$\langle r^2\rangle_m^{1/2} \tag{6}$$
$$= \left[\frac{\sum_{i=1}^{Z} R_i^2 + \sum_{i=1}^{N} R_i^2 + Z(0.8)^2 + N(0.91)^2}{Z+N}\right]^{1/2},$$

from which one can get the expression for the neutron radius by taking $Z = 0$ or the expression for the charge radius by taking $N = 0$. In the latter case one could consider an extra small term equal to $-0.116(N)$, where -0.116 fm^2 is the mean-square charge radius of a neutron [21].

3. ALPHA-LIKE PARTICLES IN ISM

In the framework of the model an α-like particle is defined as four close-by nucleons (two neutrons and two protons) in relative angular momentum zero. In this sense the following ten α-like particles are formed up to ^{40}Ca composed by two protons and two neutrons in the states $1s1/2$ (1), $1p3/2$ (2), $1p1/2$ ("1"), $1d5/2$ (3), $1d3/2$ (2), and $2s1/2$ (1), where inside parentheses the number of identical α-like particles is given. It is noticeable that in the model the α-like particle with nucleons in $1p1/2$ states is questionable since, while each one neutron has one close-by proton, the two neutron–proton pairs are not close to each other but have relative positions diametrically apart. Thus, according to our aforementioned definition, one could say that an α-like particle with nucleons in $1p1/2$ states does not exist and instead we have two deuterons which are not close to each other but diametrically sited.

Concerning the size of the above remaining nine α-like particles in ^{40}Ca, in the framework of the model, there are three sizes, one for each of the shells $1s$, $1p$, and $1d2s$. In all these three cases the form of an α-like particle is a highly deformed tetrahedron. Finally, the interaction taken is a nucleon–nucleon interaction [20], that is, not an α–α interaction.

Further, the α-like particles in the model are not in general preformed; however, the $1s$ and $2s$ α-like particles could be considered somehow preformed. The time evolution of an α-like particle in the model leads each of the four constituent nucleons into the relevant shell model orbital. The α-like particles are both on the nuclear surface and in the nuclear interior and their average positions are well determined in the model.

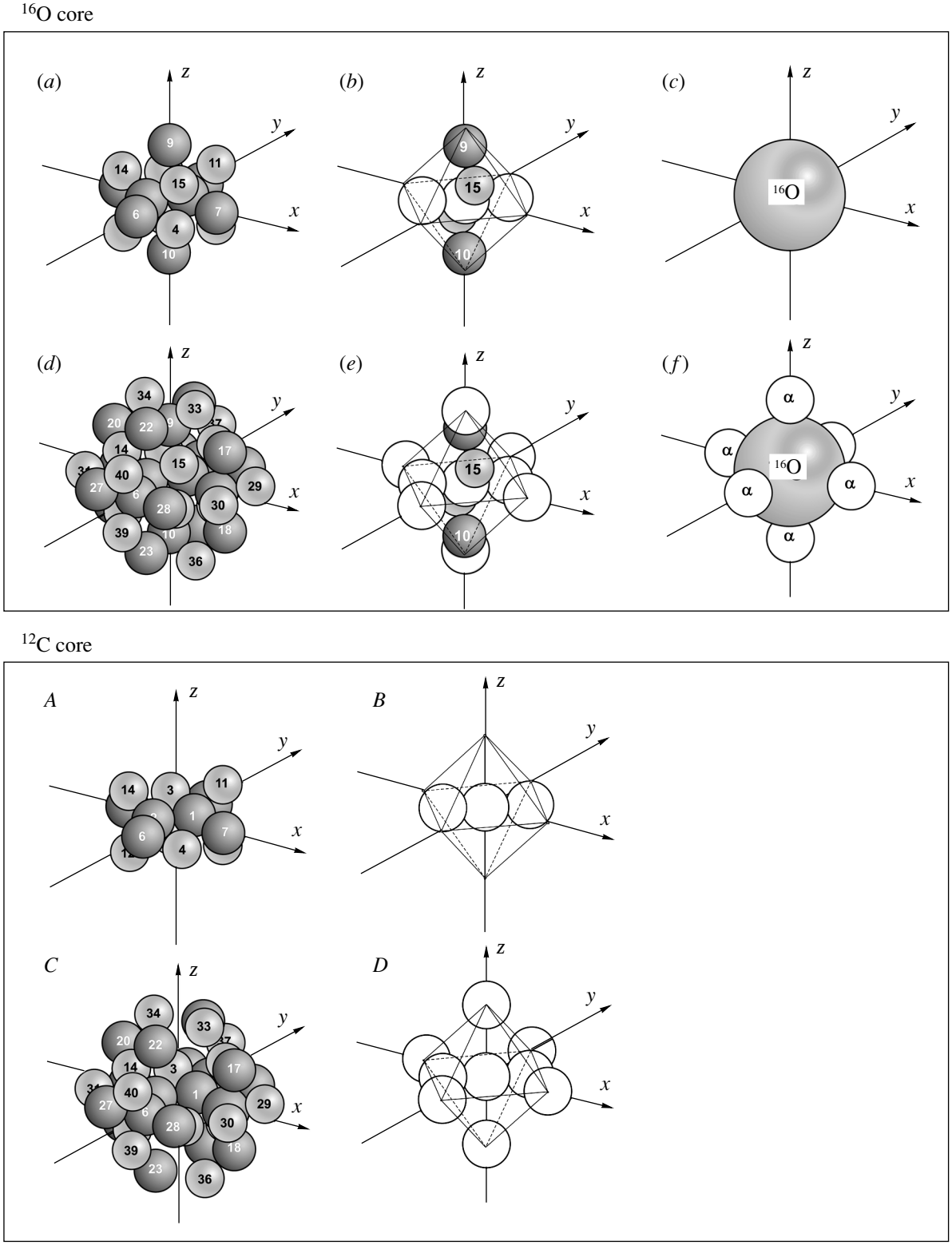

Fig. 2. Average structures of ^{12}C, ^{16}O, ^{36}Ar, and ^{40}Ca considering nucleon average positions and α-like particle average positions. Specifically, (*a*)–(*c*) present ^{16}O, (*d*)–(*f*) ^{40}Ca, (*A*), (*B*) ^{12}C and (*C*), (*D*) ^{36}Ar. Numbering is the same as in Fig.1. In (*b*) and (*e*), in addition to the α-like particle average positions, the nucleon average positions numbered 9, 10 for neutrons and 15, 16 for protons (not forming an α-like particle but two deuterons) are shown (number 16 is hidden by the other nucleon spheres). White numbered spheres designate protons; gray numbered spheres, neutrons. Large, white, unnumbered spheres designate α-like particles.

Figures $2a$–$2f$ demonstrate the geometry of the average positions for the nine α-like particles and the two deuterons that appeared in ^{40}Ca. It is noticeable that the average positions of the three α-like particles appeared in ^{12}C ($1s$ and $1p3/2$ states) are in a straight line, while the average positions of the six α-like particles appeared after ^{16}O; i.e., the three $1d5/2$, the two $1d3/2$, and the one $2s1/2$ α-like particles form a regular octahedron. The aforementioned straight line bisects two opposite edges of this octahedron as shown and thus this straight line is situated on the same plane with the three $1d5/2$ and the one $2s1/2$ α-like particles, while the remaining two $1d3/2$ α-like particles are on an axis perpendicular to this plane, the z axis (on which are also the neutron average positions of the two deuterons numbered 9 and 10). The axes x and y are diagonals of the square formed by the average positions of the ($1d5/2$ and $2s1/2$) four α-like particles as shown. When ^{12}C (see Figs. $2A$–$2D$) and not ^{16}O (see Figs. $2a$–$2f$) is the core for α-cluster nuclei heavier than ^{12}C, then the aforementioned two deuterons are moved on the outer shell and together form one of the six α-like particles of the octahedral α-cluster shell.

It is worthwhile to be more specific with Fig. 2 since starting from this figure the average α-cluster structure of the g.s. or of an excited state of any of the $4n$ nuclei up to ^{40}Ca can be created, as will be understood shortly. Specifically, Fig. $2a$ stands for the average positions of the eight neutrons and of the eight protons in ^{16}O, which are identical and possess the same numbering with the average positions for the $1s$ and $1p$ neutrons and protons presented in Figs. $1a$, $1b$ and Figs. $1d$, $1e$, respectively. Figure $2b$ comes from Fig. $2a$ when each of the three sets of four nucleons [the close-by two neutrons and two protons numbered 1, 2 and 3, 4 ($1s$ states); 5, 7 and 11, 13 ($1p3/2$ states); and 6, 8 and 13, 14 ($1p3/2$ states)] is presented by an α-like particle at its center of gravity, while the $1p1/2$ nucleon average positions numbered 9, 10 and 15, 16 are not presented as an α-like particle since they are not all close-by (and thus do not fulfill both requirements for an α-like particle). Figure $2c$ presents ^{16}O as a sphere despite the fact that its average shape is a polyhedral one.

In Fig. $2d$ the average structure of ^{40}Ca is shown made of the average positions of the 20 neutrons and of the 20 protons in the states $1s$, $1p$, and $1d2s$ presented by Figs. $1a$–$1f$ and depicted by the same numbering. In Fig. $2e$ the nine α-like particles and the two deuterons of ^{40}Ca are shown made of the sets of the close-by two neutron and two proton average positions numbered (in Figs. 1 and 2) 1, 2 and 3, 4 ($1s$ states); 5, 7 and 11,13 ($1p3/2$ states); 6, 8 and 12, 14 ($1p3/2$ states); 21, 22 and 33, 34 ($1d5/2$ states); 23, 24 and 35, 36 ($1d5/2$ states); 25, 26 and 37, 38 ($1d5/2$ states); 27, 28 and 39, 49 ($2s1/2$ states); 17, 18 and 29, 30 ($1d3/2$ states), and 19, 20 and 31, 32 ($1d3/2$ states). Figure $2f$ comes from Fig. $2e$, when ^{16}O is presented by a sphere.

In a way similar to that used for Figs. $2a$–$2e$ one can describe Figs. $2A$–$2D$. Specifically, Figs. $2A$ and $2B$ present the average structure of ^{12}C, while Figs. $2C$ and $2D$ present the average structure of an excited state of ^{36}Ar and help one to describe the average structure of any $4n$ nucleus from ^{12}C to ^{36}Ar when ^{12}C is its core.

In the cases of either ^{16}O core or ^{12}C core, all possible average positions of α-like particles are fixed in space as part of Fig. 2 and can accommodate α-like particles for the g.s. or excited states of the relevant $4n$ nuclei.

4. APPLICATIONS ON SPECIFIC $4n$ NUCLEI

Figure 3 stands for the study of ^{20}Ne [16]. Specifically, Figs. $3a$ and $3A$ show the α-like cluster structures of different states of this nucleus when nucleons are taken as the constituent particles and the core is ^{16}O or ^{12}C, respectively, while Figs. $3b$ and $3B$ show the same structures when the center of gravity of the four nucleon average positions constituting each α-like particle is considered in place of these four nucleons. Finally, Fig. $3c$ presents again the same structures when ^{16}O core is represented by a sphere. From Fig. 3 one can see the relationship of the α-like structure of ^{20}Ne states with that of Fig. 2 referred to ^{40}Ca and ^{36}Ar. Indeed, all average positions of α-like particles in Fig. 3 are average positions in Fig. 2. The x, y, z axes noted in both these figures help this visualization. The numbering of nucleon average positions shown in Fig. 3 helps one to see the relationship of this figure with Fig. 1, where the nucleon average positions are depicted with the same numbers in both figures. In each row of Figs. $3a$–$3c$ the two close-by columns present degenerate structures (i.e., structures possessing the same energy).

Each block of Table 1 corresponds to a part of Fig. 3 and is identified by the relevant core, the valence nucleon average positions, and the valence α-like particles on x, y, and z axes. This table gives the binding energies corresponding to all parts of Fig. 3 (by applying Eq. (3)) and their assignment to experimental specific 0_n^+ values as specified. For the assignment of each excited band head, the difference of its binding energy from that of the ground-state energy (as estimated in the present calculations) is considered. As seen from this table, the cases (a)–(c)

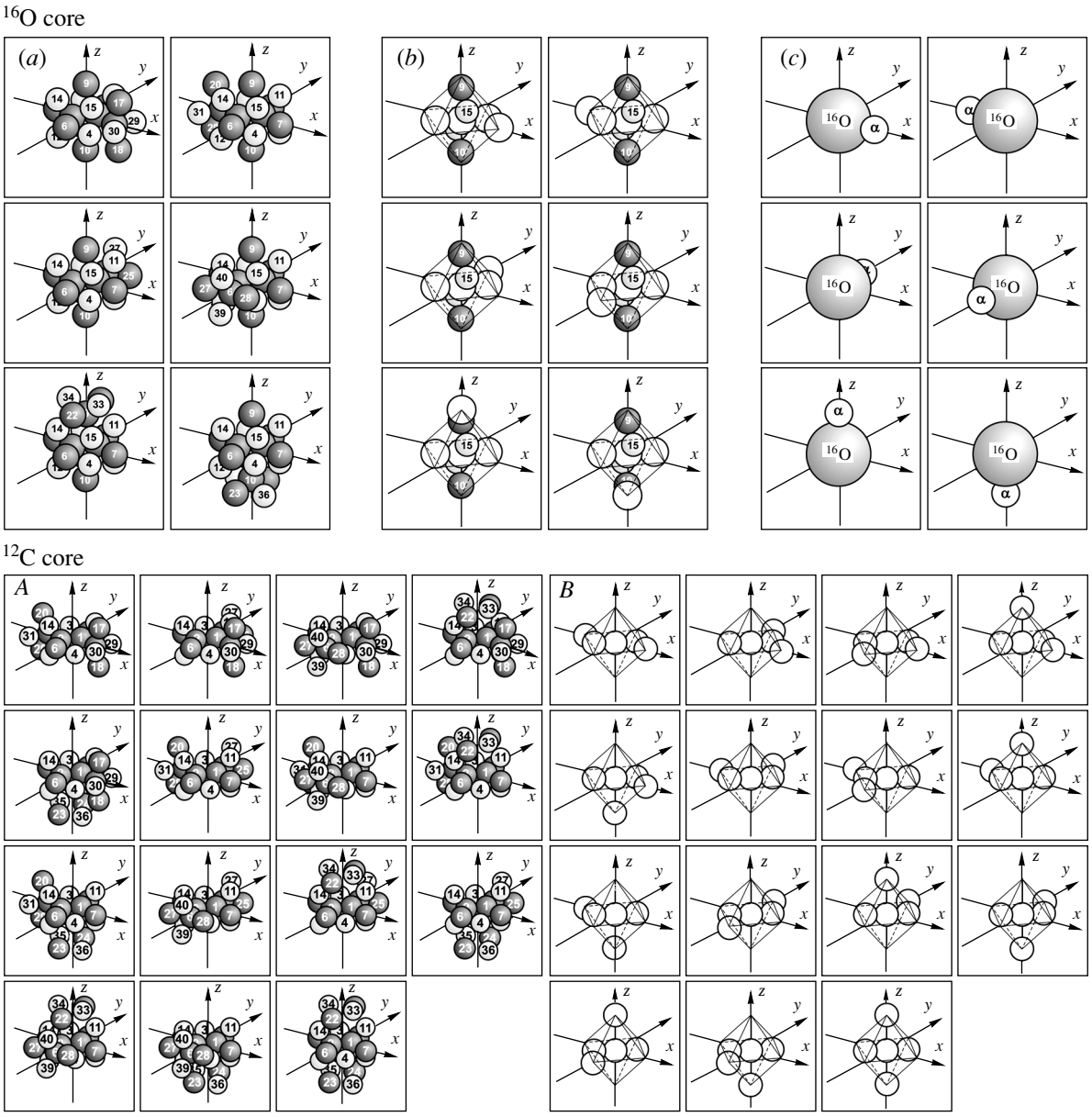

Fig. 3. Alpha-cluster structures of different states of ^{20}Ne. Specifically, (*a*) six different such structures are presented by nucleon average positions, (*b*) the same structures are presented by α-like particle average positions, and (*c*) again the same structures, where the ^{16}O core of all these structures becomes transparent. (*A*) fifteen different such structures are presented by nucleon average positions and (*B*) the same structures are presented by α-like particle average positions, where the ^{12}C core of all these structures is apparent according to Fig. 2*B*. In (*b*) and (*B*) one may locate pairs of structures with the same energy. White numbered spheres designate protons, while gray numbered spheres neutrons. Large white unnumbered spheres designate α-like particles.

are not assigned to band heads but to the shell model levels 0^+_4, 2^+_4, and 4^+_4.

In Table 2 the moments of inertia and the corresponding excitation energies from experiments and model predictions for $I = 0$–8 of the rotational bands 0^+_1, 0^+_2, 0^+_5, 0^+_8, and 0^+_9 are given.

It is noticeable that in the cases of 0^+_2, 0^+_5, and 0^+_8, more than one band correspond to the same bandhead. Both bands with bandhead 0^+_8 are complete (i.e., no in-between states are missing), while the two bands with 0^+_5 bandhead are complete and the third band starts from $I = 4^+$. Finally, in the case of the 0^+_2 bandhead, two bands start from $I = 6^+$, one band starts from $I = 4^+$, while the fourth band has only 0^+ and 2^+ states.

This multiband appearance with the same band-

Table 1. Binding energies E_B (MeV), excitation energies E_x, and band head assignment of nine α-like vertex configurations of ^{20}Ne. (Each block of the table corresponds to a specific block of Fig. 3 having the same letter labeling. The cases (f), (h), and (i) possess excitations beyond available experimental data. The terms "normal" and "relaxed" refer to two different average positions of the first two protons, namely, nos. 3 and 4 (see [16]). Experimental errors for the energies are given in [16].)

	(a)		(b)		(c)	
	Core ^{16}O (Nos 1–16)					
	valence 1α on x axis (nos. 17, 18; 29, 30)		valence 1α on y axis (nos. 25, 26; 37, 38)		valence 1α on z axis (nos. 21, 22; 33, 34)	
	normal	relaxed	normal	relaxed	normal	relaxed
E_B	167.4		167.9		166.2	
E_x(mod)	9.1		8.6		10.3	
E_x(exp)	~ 8.8		~ 8.7		10.8	
I_n^+	2_4^+		0_4^+		4_4^+	
	(d)		(e)		(f)	
	Core ^{12}C (1–8,11–14)					
	valence 2α on x axis (17, 18; 29, 30) (19, 20; 31, 32)		valence 2α on y axis (25, 26; 37, 38) (27, 28; 39, 40)		valence 2α on z axis (21, 22; 33, 34) (23, 24; 35, 36)	
	normal	relaxed	normal	relaxed	normal	relaxed
E_B	160.3	169.5	163.5	176.5	100.6	104.9
E_x(mod)	16.2	7.0	13.0	0.0	75.9	71.6
E_x(exp)	16.4	6.7	13.2	0.0		
I_n^+	0_9^+	0_2^+	0_8^+	0_1^+		
	(g)		(h)		(i)	
	Core ^{12}C (1–8,11–14)					
	1α on x axis 1α on y axis (17, 18; 29, 30) (25, 26; 37, 38)		1α on y axis 1α on z axis (25,26; 37, 38) (21, 22; 33, 34)		1α on z axis 1α on x axis (21, 22; 33, 34) (17, 18; 29, 30)	
	normal	relaxed	normal	relaxed	normal	relaxed
E_B	165.4	176.5	135.6	144.3	134.0	140.8
E_x(mod)	11.1	0.0	40.9	32.2	42.5	34.7
E_x(exp)	11.0	0.0				
I_n^+	0_5^+	0_1^+				

head recalls similar phenomena observed in the well-deformed region (and elsewhere) characterized as superdeformation, e.g., see Fig. 4a for ^{152}Dy [24]. According to the present study, an interpretation of superdeformation is suggested with the help of Fig. 4b, where two mechanical analogs are shown to support this interpretation. Figure 4b shows a rod (I) and a ring (II) rotating around their vertical symmetry axis with the help of a mechanism (see top of the figure). As long as the rotational speed is relatively small, the rod and the ring continue to rotate around this axis, which possesses the smallest moment of inertia (vertical axis). However, when the rotational speed exceeds a certain limit, which the most probable is different for the rod and the ring, the rod and the ring start to rotate firmly around their axis of largest

Table 2. Model predictions for five rotational bands (E_B in MeV) in ^{20}Ne and their experimental bands together with corresponding moments of inertia $\Im$ (fm^2). (The first line for each band stands for experimental energies, while second line for model predictions. Experimental errors for the energies are given in [16].)

I_n^+	$\Im$	$I=0^+$	2^+	4^+	6^+	8^+
0_1^+	Mixed configuration	0.0	1.63	4.25	8.78	15.87
		0.0	1.63	4.26	8.78	15.88
0_2^+	189.54	6.73	7.42			
		6.73	7.39			
	124.48			9.99	13.93	18.96
				10.06	13.72	18.72
	137.74				13.11	17.30
					13.05	17.56
	151.30				12.59	16.75
					12.48	16.59
0_5^+	93.04	10.97	12.33	15.33	20.17	28.00
		10.97	12.31	15.43	20.33	27.02
	96.14		12.22	15.33	20.03	
			12.26	15.28	20.03	26.50
	186.54			13.05	15.70	18.96
				13.19	15.64	18.97
0_8^+	131.54	13.22	14.12	16.33	19.85	24.90
		13.00	14.17	16.37	19.84	24.57
	183.34		13.91	15.33	18.29	
			13.90	15.48	17.99	
0_9^+	189.54	15.82	16.44	18.08	20.42	23.40
		15.82	16.48	18.01	20.41	23.70

moment of inertia (horizontal axis) [see dotted parts of Fig. 4*b*].

This mechanical analog, in the framework of the ISM, explains the appearance of deformed and superdeformed bands of nuclei in the well-deformed region and in other regions of nuclei like here in ^{20}Ne. This explanation implies the existence of more than one axes of rotation in nuclei, a fact which is very well justified in the framework of the ISM. According to this model there are several axes of symmetry and several axes of rotation, as one can easily conceive from Figs. 1–3 or from [15–17]. Thus, the appearance of more than one band with the same band head (as in Table 2), or the appearance of a deformed and a superdeformed band in the framework of the ISM, implies the change of the axis of rotation of the average structure of the nucleus, e.g., like in Fig. 4*b*.

In Table V of [16] one can find the model predictions for the radius, the electric quadrupole moment, the reduced electric quadruple transition, the mean lifetime, the deformation parameter, and the average moment of inertia for the g.s. (together with experimental values) of ^{20}Ne derived from the same average structure (see Fig. 3) by just applying the definition of the aforementioned observables.

Additional strength to the applicability of the ISM to $4n$ nuclei one can obtain from [15, 17], where the ^{12}C($n=3$) and ^{28}Si ($n=7$) nuclei have been treated in detail.

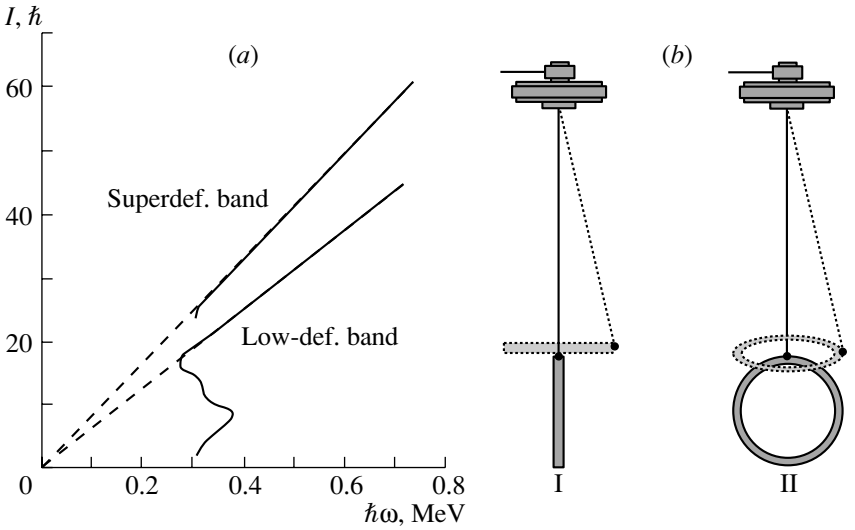

Fig. 4. (*a*) Low-deformation and superdeformation bands of ^{152}Dy. (*b*) Mechanism for a rod (I) and for a ring (II) to demonstrate that after a certain angular speed the rod and the ring become horizontal (dotted figures) rotating around their axis of maximum moment of inertia.

5. CONCLUSIONS

As proved here, the isomorphic shell model is a useful tool in studying the α-cluster structure in 4n nuclei. In the framework of this model α-like particles are not considered preformed and the close-by two neutrons and two protons composing each α-like particle evolve in time into some shell model orbitals. In addition, the average shape of an α-like particle in the model is a highly distorted tetrahedron which has a different size and deformation for an α-like particle in the $1s$, $1p$, and $1d2s$ shells.

The different $4n$ nuclei, considered in their α-like particle presentation [15–17], may have a three-dimensional or a two-dimensional or even linear average structure. Since in the framework of the isomorphic shell model each α-like particle has a well-specified composition of four nucleons with well-specified average positions, two nucleon forces are applied instead of a two α particle force for the determination of binding energies and other observables.

Up to ^{40}Ca at maximum, nine α-like particles and two deuterons compose the average structure of any $4n$ nucleus. A ^{12}C core is composed of three α-like particles in a row, while an ^{16}O core is composed of a ^{12}C plus two deuterons. Heavier $4n$ nuclei, having either ^{12}C or ^{16}O as a core, arrange their valence α-like particles at the vertices of a regular octahedron for their g.s. and excited states.

In the framework of the isomorphic shell model, the average structure of an α-like nucleus possesses several axes of symmetry and several axes of rotation. By increasing the speed of rotation around a specific axis, the rotational band may jump from this axis to another axis of rotation of a larger moment of inertia. This jump is responsible for the appearance of different rotational bands with the same band head, i.e., for the appearance of the phenomenon of superdeformation [24].

Finally, in this model entirely new rotational bands may be predicted for a nucleus, since the corresponding moment of inertia is determined from the average structure of this nucleus and knowledge of experimental rotational levels is not necessary.

REFERENCES

1. J. A. Wheeler, Phys. Rev. **52**, 1083 (1937).
2. W. Wefelmeier, Z. Phys. **107**, 332 (1937).
3. D. Dennison, Phys. Rev. **57**, 454 (1940).
4. D. Dennison, Phys. Rev. **96**, 378 (1954).
5. S. L. Kameny, Phys. Rev. **103**, 358 (1956).
6. D. M. Brink, in *The Alpha-Particle Model of Light Nuclei, Proceedings of the International School of Physics "Enrico Fermi," Course XXXVI,* Ed. by C. Bloch (Academic, New York, 1966).
7. D. M. Brink, H. Friedrich, A. Weiguny, *et al.*, Phys. Lett. B **33B**, 143 (1970).
8. D. Robson, Phys. Rev. Lett. **42**, 876 (1979).
9. D. Robson, Phys. Rev. C **25**, 1108 (1982).
10. W. Bauhoff, H. Schultheis, and R. Schultheis, Phys. Lett. B **95B**, 5 (1980); **106B**, 278 (1981); Phys. Rev. C **22**, 861 (1980); **29**, 1046 (1984).
11. S. Marsh and W. D. M. Rae, Phys. Lett. B **180**, 185 (1986).
12. W. D. M. Rae and A. C. Merchant, Mod. Phys. Lett. A **8**, 2435 (1993); J. Zhang and W. D. M. Rae, Nucl. Phys. A **564**, 252 (1993).
13. A. C. Merchant and W. D. M. Rae, Nucl. Phys. A **549**, 431 (1992).

14. W. D. M. Rae, A. C. Merchant, and J. Zhang, Phys. Lett. B **321**, 1 (1994).
15. G. S. Anagnostatos, Phys. Rev. C **51**, 152 (1995).
16. P. K. Kakanis and G. S. Anagnostatos, Phys. Rev. C **54**, 2996 (1996).
17. G. S. Anagnostatos, P. Ginis, and J. Giapitzakis, Phys. Rev. C **58**, 3305 (1998).
18. G. S. Anagnostatos, Int. J. Theor. Phys. **24**, 579 (1985).
19. G. S. Anagnostatos, Can. J. Phys. **70**, 361 (1992).
20. G. S. Anagnostatos and C. N. Panos, Phys. Rev. C **26**, 260 (1982).
21. C. N. Panos, G. S. Anagnostatos, J. Phys. G **8**, 1651 (1982).
22. W. F. Hornyak, *Nuclear Structure* (Academic, New York, 1975), p. 240.
23. J. Leech, Math. Gazelle **41**, 81 (1957).
24. P. J. Twin, B. M. Nyako, A. H. Nelson, *et al.*, Phys. Rev. Lett. **56**, 2680 (1986).

Physics of Atomic Nuclei, Vol. 65, No. 4, 2002, pp. 593–598. From Yadernaya Fizika, Vol. 65, No. 4, 2002, pp. 625–630.

A Simple Semiempirical Equation of State for Cold Nuclear Matter*

Chr. Bargholtz**

Department of Physics, Stockholm University, Sweden

Received August 31, 2001

Abstract—On the basis of gross properties of nuclei, a simple semiempirical equation of state is developed for cold hadronic matter composed of light quarks of two flavors. The source of binding energy in the model is the decreasing asymmetry between the number of up and down quarks in extended regions of overlapping nucleons. The resulting incompressibility of symmetric nuclear matter at equilibrium density is $K = 324$ MeV. The incompressibility decreases rapidly with decreasing density but increases only slowly with increasing density until homogenous quark matter is reached at a density just above three times ordinary nuclear matter density. © *2002 MAIK "Nauka/Interperiodica".*

1. INTRODUCTION

The properties of nuclear matter away from equilibrium have been at the center of attention within nuclear physics for several decades. Fits to measured properties of nuclei provide information on the equation of state of cold nuclear matter in the vicinity of equilibrium. Heavy-ion collisions in combination with complex theoretical modelling provide information on the properties under more extreme conditions. Theoretically, starting from microscopic theories of hadron interactions, expressions for the equation of state are derived which are matched to the results of experiments and then used in calculations of the properties of neutron stars.

This paper has a more restricted aim. Starting from the well-known gross properties of nuclear masses, we develop an expression for the equation of state which provides a conceptually simple connection between the binding energy, the symmetry energy, and the incompressibility of nuclear matter.

The main trend of the masses of nuclei in their ground state as a function of A and Z can be understood in terms of a simple semiempirical formula [1]

$$M(A,Z) = Zm_p + (A-Z)m_n - a_{\rm vol}A + a_{\rm surf}A^{2/3} + a_{\rm sym}\frac{(A-2Z)^2}{A}, \quad (1)$$

where we have suppressed the Coulomb term. In contemporary theory protons and neutrons are described as being made up of quarks and gluons and a transformation can be made expressing A and Z in the number of valence quarks u and d. Then

$$A = \frac{u+d}{3}, \quad Z = \frac{2u-d}{3}, \quad (2)$$

and the nuclear mass

$$M(u,d) = \frac{2u-d}{3}m_p + \frac{2d-u}{3}m_n - a_{\rm vol}\frac{u+d}{3} + a_{\rm surf}\left(\frac{u+d}{3}\right)^{2/3} + a_{\rm sym}\frac{3(u-d)^2}{u+d} = \frac{u+d}{6}(m_p+m_n-2a_{\rm vol}) + \frac{u-d}{2}(m_p-m_n) + a_{\rm surf}\left(\frac{u+d}{3}\right)^{2/3} + a_{\rm sym}\frac{3(u-d)^2}{u+d}. \quad (3)$$

Naively applying (3) to the three-quark system and interpreting the delta resonance, Δ^{++}, as the ground state of three up quarks we obtain $M_\Delta - M_N \approx 8a_{\rm sym}$. The value of the symmetry coefficient varies somewhat in the literature. A value of approximately 25 MeV/c^2 [2] is appropriate for the simple form of (1) and leads to a value within roughly 30% of the empirical nucleon–delta mass difference.

Inspired by this observation we develop, in Section 2, a phenomenological expression for the mass and volume of the ground state of homogenous, color-neutral quark-matter objects with an integer baryon number combining features of the semiempirical mass formula and bag models of the nucleon. Using this expression we proceed, in Section 3, to develop an equation of state of extended nuclear matter. Four numerical constants appearing in the equation of state are determined in Section 4, by a fit to empirical values for the nucleon mass and the equilibrium density, binding energy and symmetry energy of

*This article was submitted by the author in English.

** e-mail: bargholtz@physto.se

nuclear matter. In Section 5 results are presented for the binding energy and incompressibility as a function of density for nuclear matter with a varying neutron to proton ratio. In the final section our main results are briefly summarized and directions for future development of the model are indicated.

2. A PHENOMENOLOGICAL EXPRESSION FOR THE MASS OF THE NUCLEONIC BAG

In the static spherical MIT bag model [3, 4], the mass of the nucleon and delta is given by

$$M(R) = \frac{4\pi}{3}BR^3 + 3\frac{T_q}{R} \mp \frac{\eta}{R} + \frac{Z_0}{R}. \qquad (4)$$

The first term corresponds to the energy needed in order to create a perturbative vacuum of volume $V = (4\pi/3)R^3$ within which the quarks are confined. The second term is the total kinetic energy of three massless quarks free to move in the volume V. The color-electric and the color-magnetic hyperfine interaction gives rise to the third term, responsible for the N–Δ mass splitting. The last term, with $Z_0 < 0$, collects effects that are difficult to calculate like spurious center of mass motion and zero-point energy of the bag surface. The equilibrium radius, R_N, of the bag is determined by requiring that

$$\frac{dM}{dR}\Big|_{R=R_0} = 0, \qquad (5)$$

which is equivalent to requiring a balance of pressure. Different values are quoted in the literature for the parameters B, η, and Z_0; however, a general feature is that they give a rather large radius for the nucleon, $R_N \approx 1.1$ fm. For this radius the baryon density in the nucleon bag is approximately the same as that of ordinary nuclear matter.

We will follow a different, more phenomenological route, adopting for the mass of the ground state of a nucleonic bag the expression

$$M_b(u,d,V) = B\cdot V + \left(b_V(u+d) + b_S\frac{(u-d)^2}{u+d}\right)\left(\frac{u+d}{V}\right)^x + (u+d-3)f_{Z_0}(u,d,V), \qquad (6)$$

where with n a positive definite integer $u + d = 3n$. The first term is the same as in the MIT bag model (4), whereas the second term is identical in form to the first and last terms of the semiempirical mass formula (3) multiplied by a common density dependence. In the last term we hide effects of the spurious center-of-mass motion, zero-point motion, etc. Or to be more precise, we neglect these effects for the three-quark bag and therefore should make corrections for their dependence on the quark number and bag size for heavier bags. However, we will neglect this term for the time being and return to it later. The requirement of a balance of pressure determines the equilibrium volume of the bag to be

$$V^{\rm eq}(u,d) = \left(\frac{x(u+d)^x}{B}\left(b_V(u+d) + b_S\frac{(u-d)^2}{u+d}\right)\right)^{\frac{1}{1+x}}. \qquad (7)$$

3. NUCLEAR MATTER AS AN AGGREGATE OF NUCLEONIC BAGS

Bags with $3n$ quarks have half-integer spin and obey Fermi statistics. For a degenerate gas of A noninteracting nucleon bags within the volume V_A, the average kinetic energy is therefore

$$\frac{E_{\rm kin}}{A} = \frac{3h^2}{40M_N}\left(\frac{3A}{2\pi V_A}\right)^{2/3}, \qquad (8)$$

where M_N denotes the nucleon mass and we have assumed a degeneracy of 4. This is, thus, the appropriate kinetic energy to be used in conventional descriptions of symmetric nuclear matter, i.e., matter with equal numbers of neutrons and protons. However, we will assume a constant degeneracy of four irrespective of the neutron to proton ratio. The underlying quark structure of nucleons is the reason for this. As long as two bags do not overlap, the expectation value of the total kinetic energy of the quarks receives no contribution from quark exchange between the bags because the wave functions describing quark states in distinct bags do not overlap. The kinetic energy of a gas of nontouching bags is thus the same irrespective of the ratio of neutron to proton bags. However, in a gas, bags will inevitably touch. We shall assume that the effects of the required antisymmetry of quark wave functions in a situation where n bags are touching or overlapping one another, in our model, receive the remaining contribution from the symmetry term in the resulting merged $3n$-quark bag. The symmetry term, it should be noted, is exactly zero only in the case where an equal number of neutron and proton bags are involved. What is the probability for individual nucleon bags to merge in the gas? We will apply a naive combinatorial approach in order to answer this question. In a homogenous gas of spherical bags we select a volume V_A containing on the average $3A$ quarks. The volume V_A should be chosen large but must not be mistaken for the volume of the gas, which we assume to be infinite. Nucleon bags each have a volume $V^{\rm eq}(2,1)$.

Neutron and proton bags have the same equilibrium volume in our model. Assuming that two bags merge if their centers are closer than twice the bag

radius the probability that a certain nucleon bag does not merge with any other bag is

$$P_1^A = \left(1 - \frac{8V^{\rm eq}(2,1)}{V_A}\right)^{A-1} \tag{9}$$

and the average number of 3-quark bags within the volume V_A is $N_1^A = A \cdot P_1^A$. Similarly, the average number of $3n$-quark bags within V_A, or equivalently, the number of bags with baryon number n, is given by

$$N_n^A = \left(1 - \frac{8V^{\rm eq}(2,1)}{V_A}\right)^{A-n} \times \left(\frac{8V^{\rm eq}(2,1)}{V_A}\right)^{n-1} \binom{A}{n}. \tag{10}$$

This expression, however, must be modified. For n substantially larger than two, the n bags may all merge even if the centers of two bags are further apart than twice the radius of a 3-quark bag. We, admittedly somewhat arbitrarily, choose the following modified form:

$$N_n^A = \frac{\prod_{i=0}^{n-1}\left(\frac{V_A}{(V^{\rm eq}(\frac{A+Z}{A}i, \frac{2A-Z}{A}i)^{1/3} + V^{\rm eq}(2,1)^{1/3})^3} - 1\right)^{-1}}{\sum_{j=1}^{A}\binom{A-1}{j-1}\prod_{i=0}^{j-1}\left(\frac{V_A}{(V^{\rm eq}(\frac{A+Z}{A}i, \frac{2A-Z}{A}i)^{1/3} + V^{\rm eq}(2,1)^{1/3})^3} - 1\right)^{-1}}\binom{A}{n}. \tag{11}$$

Our choice is based on the assumption that a nucleon bag will merge with a given number i of other nucleon bags if it touches or overlaps the equivalent volume of i merged bags. Exchanging, in (11), $V^{\rm eq}(\frac{A+Z}{A}i, \frac{2A-Z}{A}i)$ for $V^{\rm eq}(2,1)$ we recover (10).

In a gas where Z out of A "nucleons" within V_A correspond to protons, the average number of bags with baryon number n and charge z is

$$N_{n,z}^{A,Z} = N_n^A \frac{\binom{Z}{z}\binom{A-Z}{n-z}}{\binom{A}{n}}. \tag{12}$$

The energy per nucleon in homogenous nuclear matter with density $\rho = A/V_A$ and a proton fraction Z/A is then given by

$$\lim_{A\to\infty}\frac{E}{A} = \lim_{A\to\infty}\left(\frac{3h^2}{40M_N}\left(\frac{3A}{2\pi V_A}\right)^{2/3} + \frac{1}{A}\sum_{n=1}^{A}\sum_{z=\max(0,n+Z-A)}^{\min(n,Z)} N_{n,z}^{A,Z} \times M_b^x(n+z, 2n-z, V^{\rm eq}(n+z, 2n-z))c^2\right), \tag{13}$$

$$M_b^x(u,d,V) = B\cdot V + \left(b_V(u+d) + b_S\frac{(u-d)^2}{u+d}\right)\left(\frac{u+d}{V}\right)^x, \tag{14}$$

where we keep the density constant when taking the limit.

We have included in (13) the kinetic energy appropriate for a nucleon gas for all densities. This reflects our ignorance concerning the kinetic energy of strongly overlapping bags. However, the correction corresponding to the hitherto neglected last term in (6) at least has the same sign as the first term in (13). For the time being we will assume that the way we have included the kinetic energy makes up for the neglected term in (6).

In the limit of very low density, the equation of state (13) corresponds to that of a dilute gas of nucleons, whereas, at the density

$$\rho = \lim_{A\to\infty}\frac{A}{V^{\rm eq}(A+Z, 2A-Z)}, \tag{15}$$

it connects to the equation of state of a single bag with $3A$ quarks, i.e., of quark matter.

4. DETERMINATION OF THE PARAMETERS IN THE EQUATION OF STATE

The equilibrium density of nuclear matter, ρ_0, is determined by the requirement of zero pressure, $P(\rho_0) = 0$,

$$P\left(\rho = \frac{A}{V_A}\right) = -\lim_{A\to\infty} A\frac{\partial(E/A)}{\partial V_A}. \tag{16}$$

The incompressibility is calculated as

$$K\left(\rho = \frac{A}{V_A}\right) = \lim_{A\to\infty} 9V_A^2\frac{\partial^2(E/A)}{\partial V_A^2}. \tag{17}$$

We now proceed to determine the four arbitrary constants, B, b_V, b_S, and x by fitting (14) (and (7)) to the average of the neutron and proton mass,

Results obtained with the semiempirical equation of state for $A = 400$

Nuclear property	Present result	Empirical value
Nucleon mass, M_N (MeV/c^2)	938.91 (fitted)	938.91
Volume of nucleon, $V^{\rm eq}(2,1)$ (fm^3)	2.3	
Delta mass, M_Δ (MeV/c^2)	1218	1232
Volume of delta, $V^{\rm eq}(3,0)$ (fm^3)	2.9	
Equil. density, ρ_0 (fm^{-3})	0.145 (fitted)	0.145 [5]
E/A at $\rho = \rho_0$ (MeV)	922.95 (fitted)	922.95 [5]
Symmetry energy, $E_{\rm sym}$ (MeV)	37.2 (fitted)	36.8 [5]
Incompr., $K(\rho = \rho_0)$ (MeV)	324	240 [5]

$M_N = 938.91$ MeV/c^2, and (13) and (16) to empirical values by Myers [5] for the equilibrium density, $\rho_0 = 0.145$ fm^{-3}, the energy per nucleon, $E/A = 922.95$ MeV, and the symmetry energy,

$$E_{\rm sym} = \lim_{A\to\infty} \frac{\left.\frac{E}{A}\right|_{Z=A\frac{1-\delta}{2}} - \left.\frac{E}{A}\right|_{Z=\frac{A}{2}}}{\delta^2} = 36.8 \text{ MeV}.$$

Such a fit returns a value of $x = 0.9997$. We therefore choose x to be exactly one and the equation of state simplifies to

$$\lim_{A\to\infty}\frac{E}{A} = \lim_{A\to\infty}\left(\frac{3h^2}{40M_N}\left(\frac{3A}{2\pi V_A}\right)^{2/3} + \frac{1}{A}\sum_{n=1}^{A}\sum_{z=\max(0,n+Z-A)}^{\min(n,Z)} N_{n,z}^{A,Z} \times M_b^1(n+z, 2n-z, V^{\rm eq}(n+z,2n-z))c^2\right), \quad (18)$$

where

$$M_b^1(u,d,V) = B\cdot V + b_V\frac{(u+d)^2}{V} + b_S\frac{(u-d)^2}{V} \quad (19)$$

and

$$V^{\rm eq}(u,d) = \sqrt{\frac{b_V}{B}(u+d)^2 + \frac{b_S}{B}(u-d)^2}. \quad (20)$$

Fitting (16), (18), and (19), for $A = 400$, to the nucleon mass and the empirical values for the energy per nucleon and the symmetry energy at equilibrium density as determined by Myers, we obtain the following values for the coefficients:

$$B = 207.169146 \text{ MeV } c^{-2} \text{ fm}^{-3},$$
$$b_V = 108.091778 \text{ MeV } c^{-2} \text{ fm}^3,$$
$$b_S = 90.963175 \text{ MeV } c^{-2} \text{ fm}^3.$$

Different sets of values for the energy per nucleon, the equilibrium density, and the symmetry energy of infinite nuclear matter occur in the literature, based on fits to nuclear masses. Choosing a different set we obtain somewhat different values for the coefficients. However, qualitatively, our results remain the same. In particular, x stays close to one.

The convergence of the limits in (16) and (18) depend on the baryon density. At ordinary nuclear matter density the result for the energy per nucleon differs by less than 30 keV choosing $A = 300$ or 400.

5. RESULTS AND DISCUSSION

With the empirically determined values for the coefficients, we obtain the results in the table. In the fit the weighting was done in such a way that the small deviation caused by our choice of $x = 1$ only affects the result for the symmetry energy. The result we obtain for the nucleon volume, $V^{\rm eq}(2,1) = 2.3$ fm^3, corresponds to a radius of 0.82 fm. The nucleon-delta mass splitting comes out within less than 5% of the empirical value even though the value was in no way included in the fitting. Remarkably, the result for the incompressibility at equilibrium, $K = 324$ MeV, is only 35% larger than the value adopted by Myers, $K = 240$ MeV, but it varies rapidly (and nonlinearly) with density. Decreasing the density by 20% the incompressibility falls to 136 MeV, whereas, for a 20% increase in density, the incompressibility increases to 379 MeV.

The radius of the nucleonic bag is only weakly dependent on the ratio of the number of up and down quarks. In this respect the delta isobar is extreme with a radius 10% larger than that of the nucleon. The bag with equal numbers of up and down quarks is only 1.5% smaller than the bag corresponding to pure neutron matter, $d/u = 2$. The approximation in

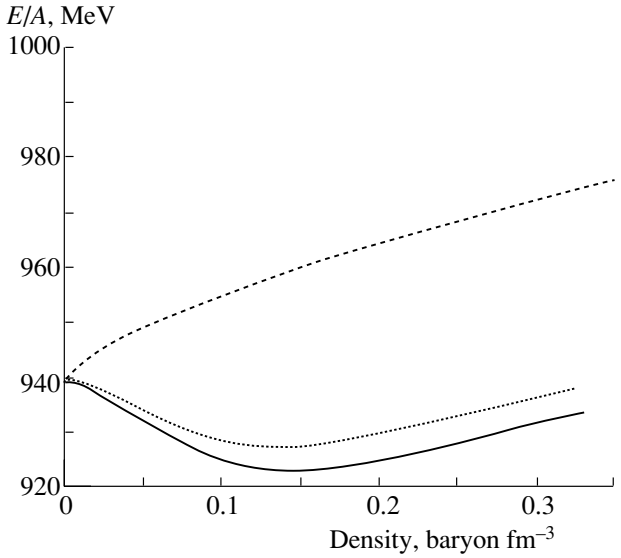

Fig. 1. Energy per baryon in nuclear matter for different proton fractions: $Z/A = 0$ (dashed curve), $Z/A = 0.33$ (dotted curve), and $Z/A = 0.5$ (solid curve).

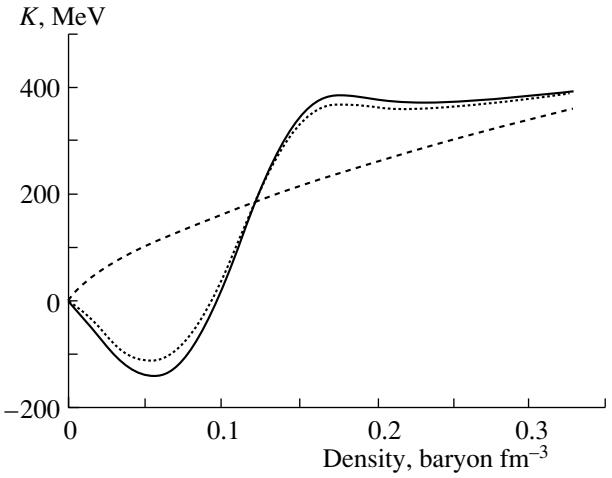

Fig. 2. Incompressibility of nuclear matter for different proton fractions: $Z/A = 0$ (dashed curve), $Z/A = 0.33$ (dotted curve), and $Z/A = 0.5$ (solid curve).

(11), where we neglected the varying composition of overlapping bags, therefore, is a rather good one.

Even though we are intrigued by these results, we feel obliged to stress that many simplifying assumptions and approximations have been made along the way. The neglect of any dynamic and quantum effects prohibits us from applying the model in its present form to finite nuclei, in particular, to light nuclear systems where quantum effects are essential to the binding. In a finite nucleus the probability for bag overlap falls off smoothly near the surface and so the model is expected to reproduce, in principle, the surface effects well known from the semiempirical mass formula.

Perhaps the detailed workings of our model are not so essential, but rather its conceptual foundations. In the present model the decreasing asymmetry between the number of up and down quarks in overlapping bags is the sole source for binding in nuclear matter and therefore the incompressibility and the symmetry energy are strongly covariant. More asymmetric nuclear matter is less bound and has a lower incompressibility at equilibrium density than symmetric matter because the probability to form joint bags with equal numbers of up and down quarks is smaller.

We now proceed to calculate the predictions regarding the properties of nuclear matter far from equilibrium. In Figs. 1 and 2 we show our results for the energy per nucleon and the incompressibility as a function of density for different proton fractions. From (15) we obtain the baryon density at which the transition to homogenous quark matter is completed,

$$\rho_{\rm qm} = \frac{1}{3}\sqrt{\frac{B(u+d)^2}{b_V(u+d)^2 + b_S(u-d)^2}}, \qquad (21)$$

to be for symmetric nuclear matter $\rho_{\rm qm}(\delta = 0) = 0.46$, and for pure neutron matter, $\rho_{\rm qm}(\delta = 1) = 0.44$. For densities greater then these the quark density inside the bag would have to increase and so our simple equation of state can no longer be expected to be relevant as it explicitly assumes the bags to remain in their ground state. However, even before that point at a density between twice and three times ordinary nuclear matter density, our neglect of strangeness is expected to significantly influence the results [6].

The semiempirical equation of state remains fairly soft until homogenous quark matter is reached. The incompressibility (Fig. 2) is larger for asymmetric nuclear matter than for symmetric for densities well below equilibrium nuclear matter density, whereas for densities between nuclear matter density and the transition to quark matter, symmetric nuclear matter has the largest incompressibility.

6. CONCLUSION

Based on analogy with the mass formula for nuclei and the MIT bag model, we have formulated a simple semiempirical equation of state for cold nuclear matter. The source of binding energy is the decreasing asymmetry between the number of up and down quarks in overlapping bags and the incompressibility and the symmetry energy are strongly covariant. The striking simplicity of the equation of state and its success in reproducing empirically known properties

of nuclear matter and the nucleon–delta mass difference suggests that it models important aspects of the properties of hadronic matter. A smooth transition from nuclear matter to quark matter is predicted, the transformation being completed at approximately three times the equilibrium density of nuclear matter. The incompressibility at equilibrium density is predicted somewhat above the most commonly quoted values; however, it increases only slowly until homogenous quark matter is reached.

Neutron star matter at a few times nuclear matter density may have finite strangeness in the ground state [6]. In order to investigate the effects of strangeness work to extend our model to include the strange quark is under way.

ACKNOWLEDGMENTS

I owe many thanks to Lennart Holmberg and Per-Erik Tegnér for their careful reading of the manuscript.

REFERENCES

1. C. F. von Weizsäcker, Z. Phys. **96**, 431 (1935); H. A. Bethe and R. F. Bacher, Rev. Mod. Phys. **8**, 82 (1936).

2. A. Bohr and B. R. Mottelson, *Nuclear Structure* (Benjamin, New York, 1969), Vol. 1, p. 141.

3. A. Chodos, R. L. Jaffe, K. Johnson, *et al.*, Phys. Rev. D **9**, 3471 (1974); **10**, 2599 (1974).

4. R. K. Bhaduri, *Models of the Nucleon* (Addison-Wesley, New York, 1988), p. 95, and references therein.

5. W. D. Myers, At. Data Nucl. Data Tables **17**, 411 (1976).

6. K. Schertler, C. Greiner, J. Schaffner-Bierlich, *et al.*, Nucl. Phys. A **677**, 463 (2000), and references therein.

Physics of Atomic Nuclei, Vol. 65, No. 4, 2002, pp. 599–602. From Yadernaya Fizika, Vol. 65, No. 4, 2002, pp. 631–634.

Nuclear Structure of ^{181}Hf Studied in (n, γ) and (d, p) Reactions*

P. Prokofjevs†, L. I. Simonova, V. A. Bondarenko, J. Berzinš, N. Kramere, T. von Egidy[1)], H.-F. Wirth[1)], A. Metz[2)], G. Graw[2)], L. Rubacek[1)], J. Honzátko[3)], I. Tomandl[3)], Y. Eisermann[2)], and R. Hertenberger[2)]**

Institute of Solid State Physics, University of Latvia, Riga, Latvia

Received July 20, 2001

Abstract—The level structure in ^{181}Hf is studied by using (n, γ) and (d, p) reactions. Gamma–gamma coincidences permit an unambiguous placement of the majority of gamma transitions in the level scheme up to 1.8 MeV, while the (d, p) angular distributions and vector analyzing powers are used to deduce spin–parity assignments. Forty-three levels are grouped into 12 rotational bands built on one-quasiparticle and quasiparticle-plus-vibrational states. The proposed level structures are in qualitative agreement with earlier quasiparticle-phonon-model calculations. © *2002 MAIK "Nauka/Interperiodica".*

1. INTRODUCTION

Up to the present time, information about the nuclear levels in ^{181}Hf has been rather scarce and ambiguous [1]. Only two rotational bands, $1/2^-[510]$ and $3/2^-[512]$, in the vicinity of the ground state have been firmly assigned. The bandhead of the $9/2^+[624]$ Nilsson orbital has been established at the excitation energy of about 600 keV. Also, the bandhead $7/2^-[503]$ orbital was assigned to a level at 670 keV. The others states reported in [1], apart from those mentioned above, could only be tentatively assigned to specific Nilsson configurations because of the experimental uncertainty in the spins of these levels. The experimental methods used in the past included (d, p) [2], (n, γ) [3, 4], and (t, p) [5] reactions, together with β decay [6]. In the present study, we focus first on clarifying the problem of the discrepancy in energy between old (d, p) and (n, γ) measurements and second on extending the level scheme and on performing a comparison with the quasiparticle-phonon-model (QPM) predictions [7].

2. EXPERIMENTS AND RESULTS

Thermal-neutron-capture studies of ^{180}Hf were performed at the light-water reactor LWR-15 at Řež near Prague. A much higher sensitivity of the present measurements was achived by using a neutron guide [8]. A 28% HPGe detector with a resolution of 2.0 keV at 1332 keV (^{60}Co line) and 4.8 keV at 6530 keV and a 12% detector with about the same resolution were applied. The sample of 300 mg of oxide powder enriched in ^{180}Hf to 96.2% was used. The appropriate placement of the γ-ray transitions in the level scheme was ensured by $\gamma\gamma$-coincidence measurements. About 4×10^8 coincidences were recorded.

The (d, p) measurements were performed with a 24-MeV vectorially polarized deuteron beam provided by the Lamb shift ion source at the Munich MP tandem accelerator. The protons were analyzed with a Q3D magnetic spectrograph and detected by a 1.8-m-long position sensitive proportional chamber. A Hf target of thickness about 105 μg/cm^2 enriched in ^{180}Hf to 96.2% was prepared by evaporating HfO_2 onto a 5.6 μg/cm^2 carbon foil backing. The proton spectra with an energy resolution of 5 to 6 keV (FWHM) were recorded up to 3 MeV at ten scattering angles between 11° and 45° and with two polarizations. The excitation energies were obtained after the calibration of the (d, p) peaks by using the present (n, γ) measurements. Spin–parity assignments and spectroscopic factors were obtained from a comparison with the cross-section and asymmetry values calculated by using the DWBA method. Also, the importance of inelastic collective processes is clearly seen in the present measurement by observing the rotational members of the ground-state band up to $15/2^-$. In the calculations based on the CHUCK3

*This article was submitted by the authors in English.

†Deceased.

[1)]Physik-Department, Technische Universität München, Germany.

[2)]Sektion Physik, Universität München, Garching, Germany.

[3)]Nuclear Physics Institute, Řež, Czech Republic.

**e-mail: jberzins@latnet.lv

code, we added some "coupled channels" (CC) with collective form factors (β_2 and β_4).

3. LEVEL SCHEME

The observed levels were grouped into 12 rotational bands (see figure). These assignments were made with allowance with our new results and available experimental data on the neighboring nuclei.

The $1/2^-[510]$ band (energies in keV): 0 ($1/2^-$), 45.8 ($3/2^-$), 98.5 ($5/2^-$), 204.0 ($7/2^-$), 303.9 ($9/2^-$), 466 ($11/2^-$), 619 ($13/2^-$), and 834 ($15/2^-$).

The $3/2^-[512]$ band: 252 ($3/2^-$), 329.4 ($5/2^-$), 440.8 ($7/2^-$), 573.9 ($9/2^-$), 751.0 ($11/2^-$), 931.0 ($13/2^-$), and 1185.0 ($15/2^-$).

The levels up to $7/2^-$ in both bands have already been known. We have added the rotational members from $9/2^-$ to $15/2^-$.

The $9/2^+[624]$ band: 595.3 ($9/2^+$), 801.5 ($11/2^+$), and 1010 ($13/2^+$).

The $11/2^+[615]$ band: 620 ($11/2^+$) and 758.6 ($13/2^+$).

The bandhead of the $9/2^+[624]$ Nilsson configuration has been firmly established in the (t, p) reaction [5] at about 600 keV. Using the prompt $\gamma\gamma$-coincidence data, we have established the level at 595.3 keV, which was deexcited by four transitions to the levels of the $1/2^-[510]$ and $3/2^-[512]$ bands. Because we did not observe populating transitions in prompt coincidences, we identify this latter state with the $9/2^+$ state of [5]. An additional analysis of the delayed $\gamma\gamma$ coincidences gives evidence for the half-life of 1.2 ± 0.4 μs. Thus, the $9/2^+[624]$ bandhead is the lowest positive-parity state in ^{181}Hf decaying through ΔK-forbidden $E1$ transitions. There are two proton peaks at 801 and 1010 keV with a high l value in the (d, p) spectra; they could be considered as rotational members of this band. In the (d, p) spectra, we have also observed a clear $l = 6$, $13/2^+$ state at 759 keV. Most likely, this is a "particle" state that belongs to the $i_{13/2}$ shell—namely, the $11/2^+[615]$ Nilsson configuration. Following [5], we consider the level at 620 keV as a reasonable candidate for the bandhead.

The $7/2^-[503]$ band: 663.8 ($7/2^-$), 800.0 ($9/2^-$), and 964.8 ($11/2^-$).

The bandhead has already been observed in previous (d, p) measurements as the strongest $l = 3$ "particle" state in this region carrying almost the entire strength of the $7/2^-[503]$ band. In thermal-neutron capture, this state is depopulated by five $M1$ and one $E2$ transitions. The $9/2^-$ rotational level has been identified at 800.0 keV in $\gamma\gamma$ coincidences and (d, p) spectra. The $11/2^-$ member of this rotational band was observed in the (d, p) spectra. The angular distributions are comparatively flat, and the asymmetry distributions are compatible with the CCBA shape for the $11/2^-$ state.

The $7/2^-[514]$ band: 904.4 ($7/2^-$) and 1031.7 ($9/2^-$).

The $I^\pi = 7/2^-$ level at 904.4 keV was established in the β decay of ^{181}Lu [6] and has been confirmed in the present (d, p) studies. The rotational $9/2^-$ member is located at 1032 keV for which the angular distributions and asymmetry are consistent with a $l = 5$ transfer to the $9/2^-$ state. Very tentatively, we suggest the $11/2^-$ state at 1173 keV. All rotational bands mentioned above constitute structures built on rather pure one-quasineutron states. These results agree with the earlier QPM calculations from [7], where the single-particle fractions amount to 95%. Above these energies, the level structure becomes progressively more complicated.

The $1/2^-[510] + Q_{20}$ band: 1044.9 ($1/2^-$), 1086.2 ($3/2^-$), and 1134.7 ($5/2^-$).

Two levels at 1045 and at 1086 keV, both populated by primary transitions in thermal-neutron capture, are depopulated by $M1$ and $E2$ transitions to the ground-state band. A very similar rotational spacing, evidence of $E2$ transitions, and the entire absence in the (d, p) spectra allow us to identify these levels with β-vibrational states based on the $1/2^-[510]$ Nilsson configuration. Also, the third state at 1134 keV demonstrates significant $E2$ branches to the $1/2^-$ and $9/2^-$ levels of the ground-state band. Very similar moments of inertia and decoupling parameters in the latter and in the parent band indicate a minor admixture of other configurations expected at these energies.

The $1/2^-[510] - Q_{22}$ band: 1117.1 ($3/2^-$) and 1178.3 ($5/2^-$).

The state at 1117 keV has already been observed in previous thermal-neutron-capture studies without a definite spin–parity assignment. Based on our observation of an additional state at 1178 keV with a similar decay mode predominantly to the ground-state band, we group these two levels into a band. The missing (d, p) strength indicates its possible vibrational character, suggesting the γ-vibrational band based on the $1/2^-[510]$ Nilsson configuration. It is instructive to note that, in the neighboring even–even Hf nucleus, the lowest vibrations are the 2^+ and 0^+ states near 1200 keV. According to QPM calculations, the lowest purely γ-vibrational state based on the ground-state configuration appears only at 1464 keV.

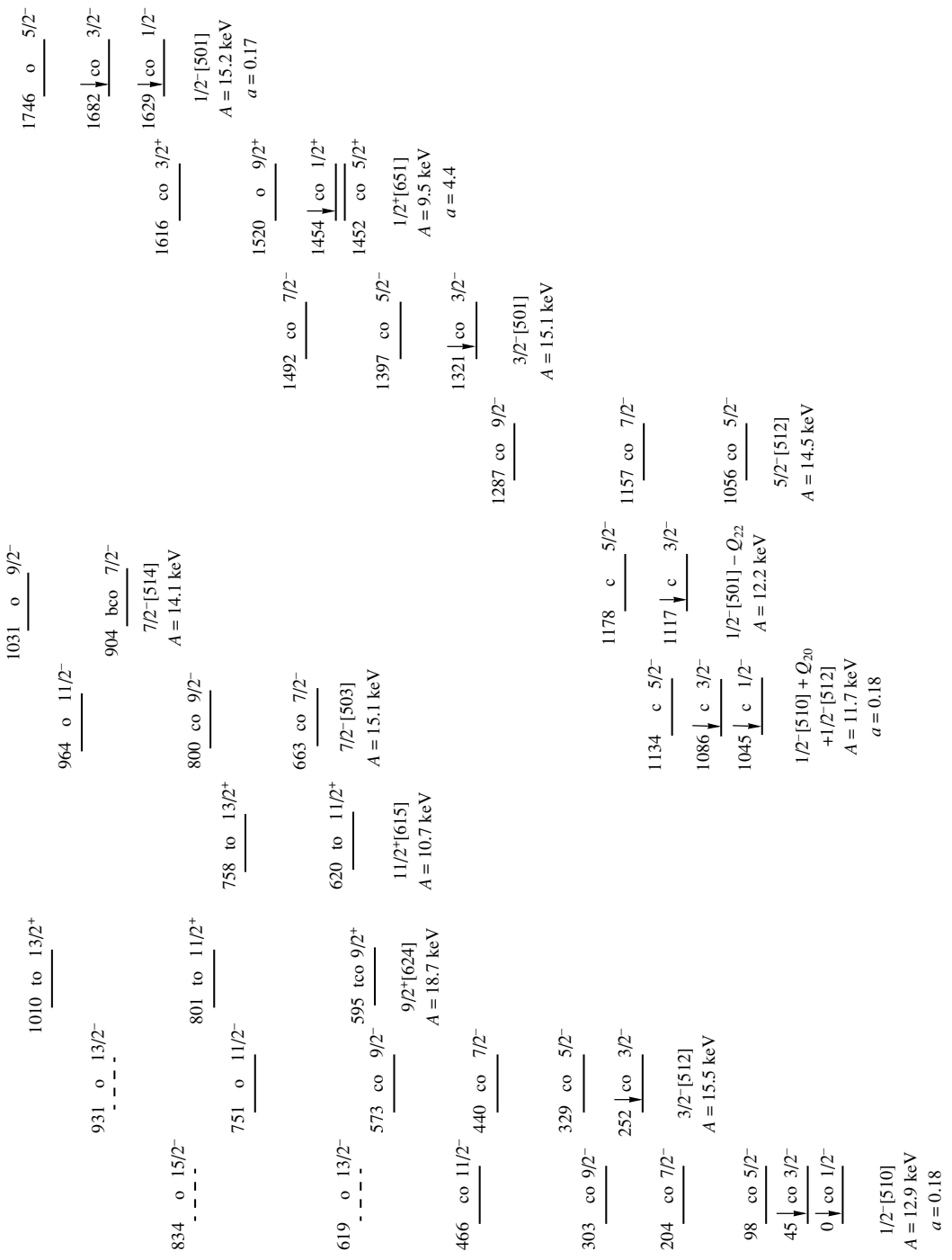

Level scheme of ^{181}Hf. Arrows indicate that the levels are populated by primary γ transitions. The symbols b, o, t, and c correspond to β decay, the (d, p) reaction, the (t, p) reaction, and $\gamma\gamma$-coincidence method, respectively.

The $5/2^-[512]$ band: 1056.0 $(5/2^-)$, 1157.5 $(7/2^-)$, and 1287.3 $(9/2^-)$.

The new level at 1056 keV was established in the present thermal-neutron-capture study by depopulation through six transitions, which imply the most likely $5/2^-$ characteristic. The corresponding (d, p) peak observed at this energy unfortunately belongs to ^{179}Hf. The neigboring (d, p) peak in this energy region at 1157 keV displays a clear $l = 3$ transfer to $7/2^-$. Taking into account a reasonable rotational spacing between the two levels and the expected "fingerprint" patterns, we associated these two levels with the $5/2^-[512]$ Nilsson configuration. The third member $9/2^-$ of this band could be tentatively located

at 1287 keV on the basis of the only coincident transition at 231 keV from this level. Again, a part of the intensity of the 1287- keV (d, p) peak belongs to ^{179}Hf. The calculated QPM structure of the $5/2^-[512]$ state is complicated: $5/2^-[512]$ 68%, $\{1/2^-[510] + Q_{22}\}$ 29%, and $\{9/2^+[624] + Q_{32}\}$ 1%.

The $3/2^-[501]$ band: 1321.8 ($3/2^-$), 1397.0 ($5/2^-$), and 1492.7 ($7/2^-$).

There are two particle states, $3/2^-[501]$ and $1/2^-[501]$, according to the Nilsson scheme which could be expected as the strongest peaks in the (d, p) spectra of Hf nuclei. The lowest one of this family of strongly populated $l = 1$ levels is the $3/2^-$ state at 1322 keV, which is also populated by a strong primary transition in thermal-neutron capture. The rotational member $5/2^-$ was established at 1397 keV; its decay mode is very similar to the bandhead level at 1322 keV. The corresponding (d, p) peak shows a clear $l = 3$ transfer with the asymmetry distribution peculiar to $5/2^-$. The $7/2^-$ rotational member was observed in coincidences at 1493 keV. The decay mode of these levels shows some similarity to the decay of the $3/2^-[501]$ state at 1459.0 keV in ^{179}Hf [9]. Noteworthy, the strong $E2$ decay from the $3/2^-$ bandhead state to the $7/2^-[503]$ state at 663 keV strongly suggests an admixture of the $\{7/2^-[503] + Q_{22}\}$ vibrational component. This observation agrees well with the QPM predictions, which give the following structure: $3/2^-[501]$ 27%, $3/2^-[512]$ 1%, $\{7/2^-[503] + Q_{22}\}$ 56%, and $\{3/2^-[512] + Q_{20}\}$ 13%.

The $1/2^-[501]$ band: 1629.4 ($1/2^-$), 1682.7 ($3/2^-$), and 1746 ($5/2^-$).

A pair of $l = 1$ states at 1629 and 1683 keV known previously only from (n, γ) studies are assigned here to the $1/2^-[501]$ band. The next member $5/2^-$ was established at 1746 keV. The relative cross sections for all three levels follow rather well the expected fingerprints for the $1/2^-[501]$ Nilsson configuration.

The $1/2^+[651]$ band: 1454.0 ($1/2^+$), 1616.2 ($3/2^+$), 1452.2 ($5/2^+$), and 1520.2 ($9/2^+$).

There are the two strongest peaks in the (d, p) spectra at 1452 and 1520 keV, which provide rather firm $l = 2$ and $l = 4$ angular-momentum transfers and unambiguous spin–parity assignments of $5/2^+$ and $9/2^+$. A much weaker state was observed at 1616 keV, which indicates a clear $l = 2$ transfer with an evident asymmetry oscillations peculiar to a $3/2^+$ state. These three levels are grouped into a rotational band with the moment of inertia and decoupling parameter given in the figure. The $1/2^+$ bandhead is placed very close to the $5/2^+$ state. Thermal-neutron-capture data provide a definite population and decay information for the level at 1454 keV, which is seen in the 4242–1454 two-step cascade. A similar positive-parity structure was observed only in ^{175}Yb [10]. No band with the proposed structure was predicted by the QPM in this energy interval. On the contrary, the two lowest $1/2^+$ states reported in [7] are formed by the octupole phonons Q_{31} coupled to the two low-lying Nilsson states of negative parity. The observation of possible octupole structures is very problematic in the present study because of their expected very weak population both in thermal-neutron capture and in the (d, p) reaction.

CONCLUSION

Our new experimental results, containing data on the $(n, \gamma\gamma)$ and (d, p) reactions have allowed us to develop the level scheme of ^{181}Hf up to about 1.8 MeV. Eight new rotational bands have been established; two of them have been observed only in the (n, γ) reaction and interpreted as relatively pure γ- and β-vibrational bands belonging to the ground-state configuration. The rotational parameters are close to the corresponding values in the neighboring Hf and W nuclei. The interpretation of levels does not contradict the earlier QPM calculations. Experimental details, a further extension of the level scheme, and a comparison with calculations will be published elsewhere.

ACKNOWLEDGMENTS

We gratefully acknowledge the support of the Beschleunigerlaboratorium der Universität und Technischen Universität München and the Deutsche Forschungsgemeinschaft, Bonn.

REFERENCES

1. R. B. Firestone, Nucl. Data Sheets **62**, 101 (1991).
2. F. A. Rickey and R. K. Sheline, Phys. Rev. **170**, 1157 (1968).
3. G. Alenius, S. E. Arnel, C. Schale, *et al.*, Phys. Scr. **3**, 105 (1971).
4. V. A. Bondarenko *et al.*, Izv. Akad. Nauk SSSR, Ser. Fiz. **55**, 2091 (1991).
5. D. G. Burke *et al.*, Can. J. Phys. **62**, 192 (1984).
6. K. Rykaczewski *et al.*, Nucl. Phys. A **499**, 529 (1989).
7. F. A. Gareev *et al.*, Sov. J. Part. Nucl. **4**, 410 (1973).
8. J. Honzátko *et al.*, Nucl. Instrum. Methods Phys. Res. A **376**, 434 (1996).
9. R. Richter *et al.*, Nucl. Phys. A **499**, 221 (1989).
10. D. Breitig, Z. Naturforsch. A **26**, 371 (1971).

Physics of Atomic Nuclei, Vol. 65, No. 4, 2002, pp. 603–606. From Yadernaya Fizika, Vol. 65, No. 4, 2002, pp. 635–638.

Structure Studies of ^{11}Be and ^{12}Be: Observation of Molecular Rotational Bands*

H. G. Bohlen**, **W. von Oertzen**, **A. Blažević**, **B. Gebauer**, **S. M. Grimes**[1)], **R. Kalpakchieva**[2)], **T. N. Massey**[1)], **and S. Thummerer**

Hahn-Meitner-Institut, Berlin, Germany

Received August 31, 2001

Abstract—Excited states of ^{11}Be have been studied with several transfer reactions. Nine states between 3.96 and 25.0 MeV excitation energy show the characteristic energy dependence of a rotational band. The deduced large moment of inertia is consistent with a 2α structure with large deformation. In ^{12}Be four high-lying states observed at 7.3, 10.7, 14.6, and 21.7 MeV in the reaction ^{9}Be(^{15}N,^{12}N)^{12}Be, also form a rotational band with almost the same moment of inertia; tentative spin assignments of 2^+–8^+ are used.

1. INTRODUCTION

Neutron-rich Be isotopes show pronounced 2α-cluster structures, and molecular structures can be found in excited states with the two α particles bound by additional neutrons [1]. It is known from earlier studies that the *ground states* of Be isotopes with $A \geq 10$ have a more compact shape. Molecular states are localized at higher excitation energy, as discussed by von Oertzen [1]. For ^{11}Be the states at 3.96 MeV ($3/2^-$), 5.25, 6.72, and 8.82 MeV, known from ^{9}Be(t,p) reactions [2, 3], form a molecular rotational band with the $3/2^-$ bandhead. Several theoretical papers have been published recently about the structure of ^{10}Be [4–6]. Kanada-En'yo *et al.* [4] obtained in AMD calculations pronounced molecular structures of excited states of ^{10}Be, whereas the ground state is less deformed. In these calculations it is characteristic that the α–α distance is large, and, e.g., in the case of ^{10}Be (0_2^+, 6.18 MeV), the density distribution of the two extra neutrons corresponds to a σ-bond, whereas the more compact form of the ground state is related to the π-bond [1, 4–6].

2. A MOLECULAR ROTATIONAL BAND IN ^{11}Be

We have investigated the structure of ^{11}Be using two-neutron transfer reactions on ^{9}Be, and also the one-neutron transfer reaction (^{14}N,^{13}N) on a radioactive ^{10}Be target. In the latter reaction we found that only the single-particle states were populated, up to the $3/2^-$ state at 3.41 MeV, above which no more states were observed. This behavior changes dramatically using ^{9}Be as target and two-neutron transfer reactions: in the ^{9}Be(^{14}N, ^{12}N)^{11}Be reaction at $E_{\rm lab} \simeq 218$ MeV (Fig. 1, upper panel), all the states known from (t,p) and a formerly unknown state at 5.98(4) MeV were observed, and in the ^{9}Be(^{13}C,^{11}C)^{11}Be reaction at 379 MeV, states even up to 25 MeV excitation energy were populated due to the more favorable excitation conditions at the higher incident energy. In the latter reaction five new states were found at 10.8, 13.8, 18.6, 21.6, and 25.0 MeV [7] (Fig. 1, center panel). When these new states are included in the $K = 3/2^-$ molecular band starting at 3.96 MeV excitation energy, a rather good linear dependence is obtained in a plot of excitation energies vs. $J(J+1)$ (Fig. 1, lower panel). The spins of the band members run up to a maximum spin of $19/2^-$ for the highest lying state. From the slope ($\hbar^2/2\Theta = 0.23$ MeV) of the line in Fig. 1 (lower panel), a large moment of inertia $2\Theta/\hbar^2 = 4.3$ MeV^{-1} is deduced, which corresponds to a large α–α distance in the core (~ 6 fm) and supports the interpretation as a molecular structure. The highest spin $19/2^-$ can only be explained in a molecular model: the two α particles are separated by a large distance and rotate

*This article was submitted by the authors in English.

[1)]Department of Physics and Astronomy, Ohio University, Athens, USA; e-mail: massey@oual3.phy.ohiou.edu

[2)]Flerov Laboratory of Nuclear Reactions, JINR, Dubna, Russia, and Bulgarian Academy of Science, Sofia, Bulgaria; e-mail: kalpak@sungraph.jinr.ru

**e-mail: bohlen@hmi.de

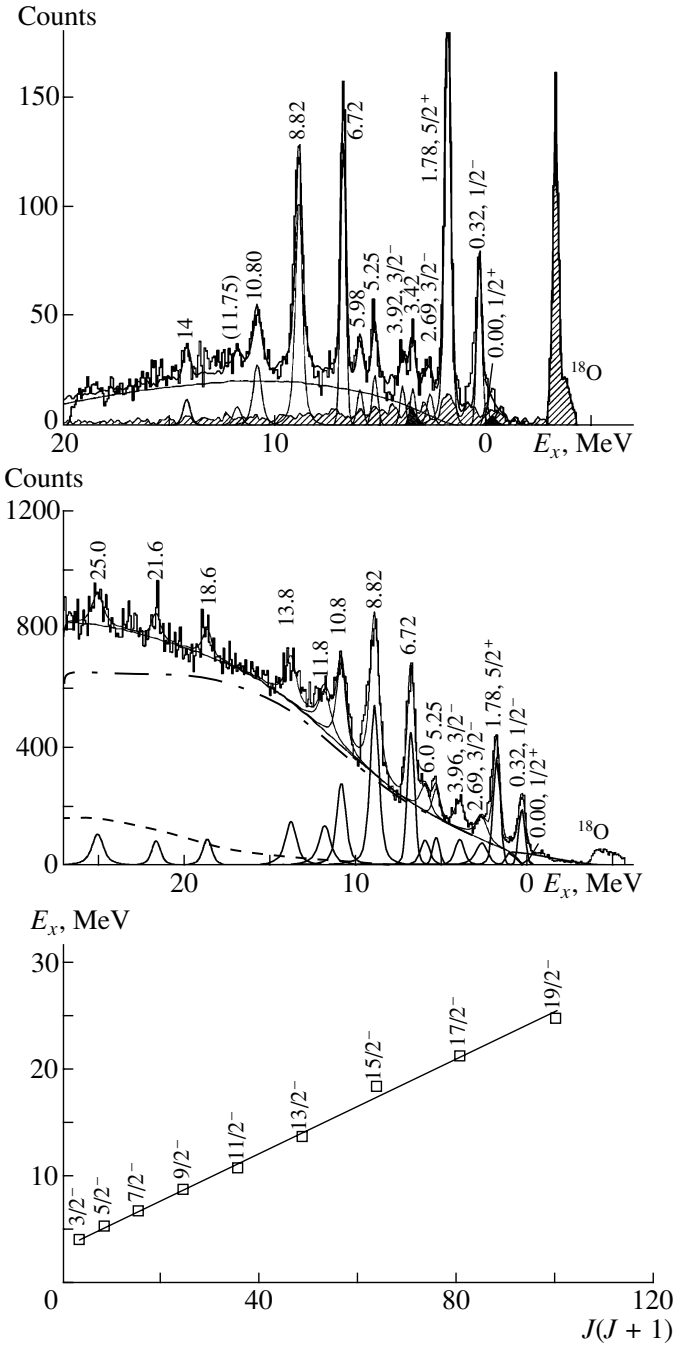

Fig. 1. Spectra of the ^{9}Be (^{14}N,^{12}N)^{11}Be (upper panel, $E_{\rm lab} = 217.9$ MeV, $\theta_{\rm lab} = 2.0^\circ - 5.9^\circ$) and ^{9}Be(^{13}C,^{11}C)^{11}Be reactions (center panel, $E_{\rm lab} = 379$ MeV, $\theta_{\rm lab} = 4^\circ - 8^\circ$). The background results from ^{16}O in the target (hatched area), ^{12}C (black area) and from three-body contributions. The lower panel shows a plot of excitation energies vs. $J(J+1)$ for the $K = 3/2^-$ molecular rotational band of ^{11}Be ($\hbar^2/2\Theta = 0.23$ MeV). The broad distributions correspond to $^{13}\mathrm{N}^* \to {}^{12}\mathrm{N} + n$ decay (upper panel); $^{12}\mathrm{C}^* \to {}^{11}\mathrm{C} + n$, ^{10}Be (g.s.), (dash-dotted curve), ^{10}Be (7.34 MeV) (center panel).

in an $l = 4$ resonance state. Higher l values are not observed as resonances in α–α scattering [8]. The first 4^+ state of ^{8}Be is found at 11.4 MeV excitation energy. Furthermore, for the $19/2^-$ state of ^{11}Be the two transferred neutrons are placed into molecular orbitals of $\sigma(d5/2)$ bonds and couple to a maximum spin of 4^+, and the single neutron of the ^{9}Be target adds with $J^\pi = 3/2^-$ to give the total spin $19/2^-$.

The observed widths of the nine band members are rather small (< 15 keV [2] for the $3/2^-$ bandhead; they increase to 0.7 MeV for the state at 25.0 MeV excitation energy). The moderate width is consistent with a

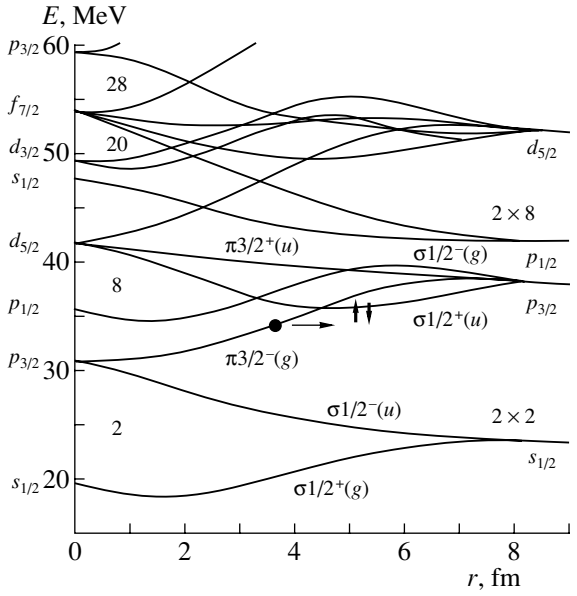

Fig. 2. Correlation diagram for molecular states of neutrons in the potential of two α particles (schematic, adopted from [1]); the α–α distance r is given on the x axis.

shape isomeric state at high spin. We want to remark that in this reaction the new state at 6.0(1) MeV is observed again.

In a third $2n$-transfer reaction we have measured the ^{9}Be(^{15}N, ^{13}N)^{11}Be reaction, $E_{\rm lab} = 240$ MeV, where the states at 10.8, 13.8, and 21.6 MeV were confirmed.

From previous studies we know that the formation of molecular structures in transfer reactions depends sensitively on the structure in the initial channel and the reaction mechanism. As we have seen, the molecular band of ^{11}Be could be well populated starting with ^{9}Be as the target, which has *in its ground state* already a strongly deformed 2α structure, whereas this was not the case using a ^{10}Be target. In Fig. 2 a schematic picture of the correlation diagram for neutrons in a two-center potential of two α particles is shown. Asymptotically the external neutrons are bound in a $p3/2$ state of one of the α particles (states on the right), while, at a small distance, there is the deformed bound state potential of the compound system. At intermediate distances, σ and π bonds are developing as indicated. For the ^{9}Be ground state the potential minimum is located at an α–α distance of about 3.2 fm (the dot in Fig. 2). When two neutrons are transferred on ^{9}Be to the molecular $\sigma1/2^+(u)$ orbits, this distance is increased to more than 5 fm. The increase of the α–α distance for this molecular configuration in ^{11}Be with two neutrons in the σ bond is indicated in Fig. 2 by the horizontal arrow.

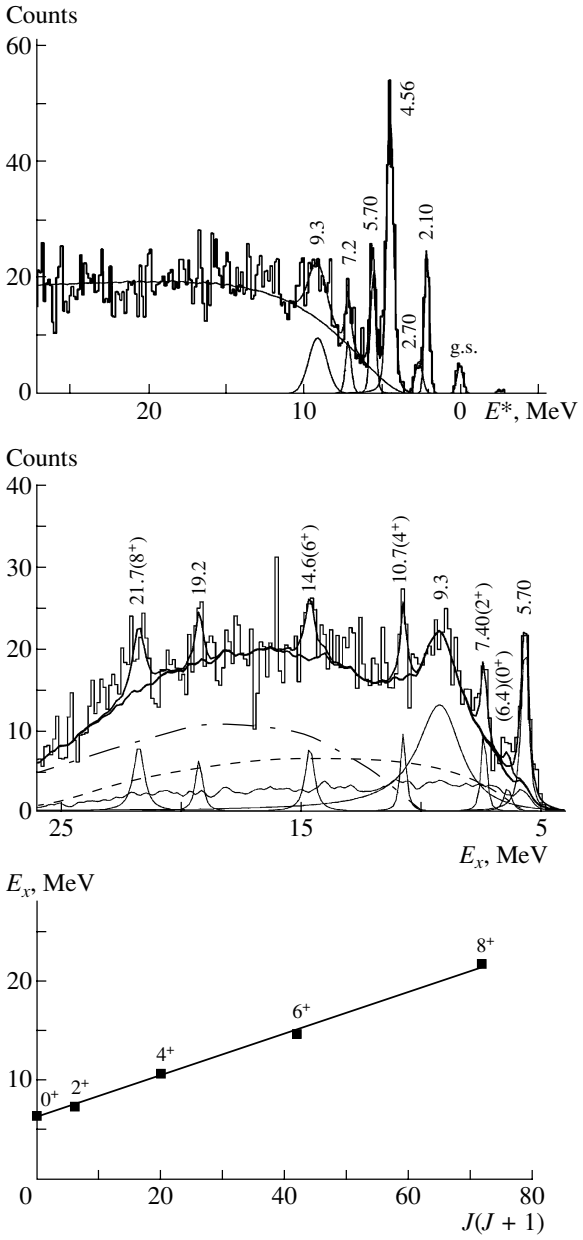

Fig. 3. Spectra of reactions, which populate final states of ^{12}Be: the double-charge-exchange reaction (^{14}C,^{14}O) on ^{12}C (upper panel), and the $3n$-transfer reaction ^{9}Be(^{15}N,^{12}N)^{12}Be (center panel). The broad distributions correspond to sequential decay contributions (e.g., ^{16}O* $\rightarrow$ ^{14}O $+n+n$ for upper panel and ^{13}N* $\rightarrow$ ^{12}N $+n$ for central panel). The lower panel shows a plot of excitation energies vs. $J(J+1)$ for the molecular rotational band of ^{12}Be found in the $3n$-transfer reaction ($\hbar^2/2\Theta = 0.21$ MeV).

3. MOLECULAR STRUCTURE STUDIES OF ^{12}Be

Low-lying states of ^{12}Be up to 5.7 MeV excitation energy have been measured by Alburger *et al.* [9] and Fortune *et al.* [10] using the (t,p) reaction on

^{10}Be. Spins have been assigned only to the two lowest excited states: 2^+ at 2.10 MeV [9] and recently 1^- for the 2.70 MeV [11]. In earlier studies of neutron-rich nuclei, we measured the double-charge-exchange reaction ^{12}C(^{14}C, ^{14}O)^{12}Be, $E_{\rm lab} = 336$ MeV (Fig. 3, upper panel) and found two higher lying states: a narrow state at 7.2(1) MeV and a broad peak at 9.3 MeV excitation energy with a width of 2.0(3) MeV [12]. The experimental resolution in this measurement is 0.4 MeV.

Exotic cluster structures of ^{12}Be have been searched for also by Korsheninnikov *et al.* [13] using the $^{12}\mathrm{Be} + p$ inelastic scattering. The authors found two peaks at 8.6 ± 0.15 and 10.0 ± 0.15 MeV. The observed structures consist of only two channels at a higher counting rate above the background, which are separated by one channel. The common center of gravity of the observed structure is located at about 9.3 MeV, making it probable that it may be the same as the one we observed in the (^{14}C, ^{14}O) reaction. Further measurements with better statistics and resolution are necessary to clarify the situation at this region of excitation energy.

An extremely deformed molecular band of ^{12}Be has been found by Freer *et al.* [14] at excitation energies between 12 and 21 MeV using the fragmentation of ^{12}Be into ^{6}He+^{6}He by coincident detection of two correlated ^{6}He fragments. From the angular correlation they propose spin assignments from 4^+ to 8^+.

In the ^{12}C(^{14}C, ^{14}O) reaction we did not observe states at higher excitation energies than 9.3 MeV. However, using a ^{9}Be target and the three-neutron transfer reaction ^{9}Be(^{15}N, ^{12}N)^{12}Be, further states at energies of 10.7, 14.6, 19.2, and 21.7 MeV were found (Fig. 3, center panel) with significances larger than 4σ. In ^{12}Be, a molecular rotational band can be formed in a similar way as for ^{11}Be using the same configurations: an α–α core with rotational states 0^+, 2^+, 4^+ and two neutrons transferred to the $1d5/2$ orbit of the molecular system, which can couple to a maximum spin of 4^+; the third transferred neutron in the $1p3/2$ orbit couples to zero with the $3/2^-$ neutron from the ^{9}Be target. A maximum spin of 8^+ can be obtained in this case. Using the tentative assignment of 8^+ for the state at 21.7 MeV, which is consistent with the results of Freer *et al.*, a molecular rotational band can be assigned with the members 14.6 MeV (6^+), 10.7 MeV (4^+), and 7.40 MeV (2^+) according to the linear dependence of the excitation energies on $J(J+1)$ in Fig. 3 (lower panel). A moment of inertia of 4.76 MeV^{-1} is obtained, very similar to the case of ^{11}Be. The 0^+ bandhead is not directly observed in the spectrum due to the small cross section expected for a 0^+ state, but its position can be predicted from the extrapolation of the straight line to $J = 0$. An excitation energy of 6.4 MeV is deduced for this 0^+ bandhead.

4. SUMMARY

High-lying states have been found in ^{11}Be and ^{12}Be up to excitation energies of 25.0 and 21.7 MeV, respectively. Molecular rotational bands have been assigned according to a linear dependence of the excitation energies of the band members on $J(J+1)$. From the slope parameters, large moments of inertia are deduced: $\Theta(^{11}\mathrm{Be}) = 91 \pm 5$ u fm^2 and $\Theta(^{12}\mathrm{Be}) = 100 \pm 8$ u fm^2, respectively. These values can be interpreted by molecular structures with two α particles at a large distance.

ACKNOWLEDGMENTS

This work is supported by NATO grant no. 960375 and DOE grant no. DE-FG02-88ER40387.

REFERENCES

1. W. von Oertzen, Z. Phys. A **357**, 355 (1997).
2. F. Ajzenberg-Selove *et al.*, Phys. Lett. B **40B**, 205 (1972).
3. G. B. Liu and H. T. Fortune, Phys. Rev. C **42**, 167 (1990).
4. Y. Kanada-En'yo, H. Horiuchi, and A. Doté, Phys. Rev. C **60**, 64304 (1999).
5. N. Itagaki and S. Okabe, Phys. Rev. C **61**, 44306 (2000).
6. Y. Ogawa *et al.*, Nucl. Phys. A **673**, 122 (2000).
7. H. G. Bohlen *et al.*, Prog. Part. Nucl. Phys. **42**, 17 (1999).
8. F. Ajzenberg-Selove *et al.*, Nucl. Phys. A **490**, 1 (1988).
9. D. E. Alburger *et al.*, Phys. Rev. C **18**, 2727 (1978).
10. H. T. Fortune, G. B. Liu, and D. E. Alburger, Phys. Rev. C **50**, 1355 (1994).
11. H. Iwasaki *et al.*, Phys. Lett. B **491**, 8 (2000).
12. W. von Oertzen, H. G. Bohlen, *et al.*, Nucl. Phys. A **588**, 129c (1995).
13. A. A. Korsheninnikov *et al.*, Nucl. Phys. A **588**, 23c (1995).
14. M. Freer *et al.*, Phys. Rev. Lett. **82**, 1383 (1999).

Physics of Atomic Nuclei, Vol. 65, No. 4, 2002, pp. 607–611. From Yadernaya Fizika, Vol. 65, No. 4, 2002, pp. 639–643.

Systematic Investigation of Light Heavy-Ion Reactions*

I. Boztosun[1)]**

Department of Nuclear Physics, University of Oxford, UK

Received July 20, 2001

Abstract—We introduce a novel coupling potential for the scattering of deformed light heavy-ion reactions. This new approach is based on replacing the usual first derivative coupling potential by a new, second derivative coupling potential in the coupled-channels formalism. This new approach has been successfully applied to the study of the $^{12}C + {}^{12}C$, $^{12}C + {}^{24}Mg$, $^{16}O + {}^{28}Si$, and $^{16}O + {}^{24}Mg$ systems and made major improvements over all the previous coupled-channels calculations for these systems. This paper also shows the limitations of the standard coupled-channels theory and presents a global solution to the problems faced in the previous theoretical accounts of these reactions. © *2002 MAIK "Nauka/Interperiodica".*

1. INTRODUCTION

We investigate the elastic and inelastic scattering of light heavy-ions, which have stimulated a great deal of interest over the last 40 years. There has been extensive experimental effort to measure the elastic and inelastic scattering data as well as their 90°- and 180°-excitation functions. A large body of experimental data for these systems is available (see [1–4] and references therein). A variety of theoretical accounts based on dynamical models or purely phenomenological treatments have been proposed to explain these data [1, 5]. The elastic scattering data have already been studied in detail using an optical model and coupled-channels method.

Although most of these models provide reasonably good fits, no unique model has been proposed that explains consistently the elastic and inelastic scattering data over a wide energy range without applying any *ad hoc* approaches. Consequently, the following problems continue to exist for light heavy-ion reactions: (1) explanation of anomalous large angle scattering data (ALAS); (2) reproduction of the oscillatory structure near the Coulomb barrier; (3) the lack of the correct oscillatory structure agreement between theoretical predictions and experimental data for the ground and excited states; (4) simultaneous fits of the individual angular distributions, resonances, and excitation functions (for the $^{12}C + {}^{12}C$ system in particular); (5) the magnitude of the mutual-2^+ excited state data in the $^{12}C + {}^{12}C$ system is unaccounted for; (6) the deformation parameters (β values): previous calculations require β values that are at variance with the empirical values and are physically unjustifiable.

Therefore, in this paper, we are concerned with the measured experimental data for $^{12}C + {}^{12}C$, $^{16}O + {}^{28}Si$, $^{12}C + {}^{24}Mg$, and $^{16}O + {}^{24}Mg$ in an attempt to find a global model, which simultaneously fits the elastic and inelastic scattering data for the ground and excited states in a consistent way over a wide energy range and which throws light on the underlying mechanism of the reactions and on the nature of the interactions involved.

2. STANDARD COUPLED-CHANNELS MODEL

Although we have considered and studied four different reactions in detail, we will show some of the results for the $^{16}O + {}^{28}Si$ and $^{12}C + {}^{12}C$ reactions. The details of the models and a complete set of the results for all four reactions can be found in [6–9].

We describe the interaction between ^{16}O and ^{28}Si nuclei with a deformed optical potential. The real potential is assumed to have the square of a Woods–Saxon shape:

$$V_N(r) = \frac{-V_0}{[1 + \exp((r - R)/a)]^2}, \qquad (1)$$

where $V_0 = 706.5$ MeV, $R = r_0(A_p^{1/3} + A_t^{1/3})$ with $r_0 = 0.7490$ fm and $a = 1.40$ fm. The parameters of the real potential were fixed as a function of energy and were not changed in the present calculations, although it was observed that small changes could improve the quality of the fits.

*This article was submitted by the author in English.

1)Permanent address: Department of Physics, Erciyes University, Kayseri, Turkey.

**e-mail: i.boztosun1@physics.ox.ac.uk

1063-7788/02/6504-0607$22.00

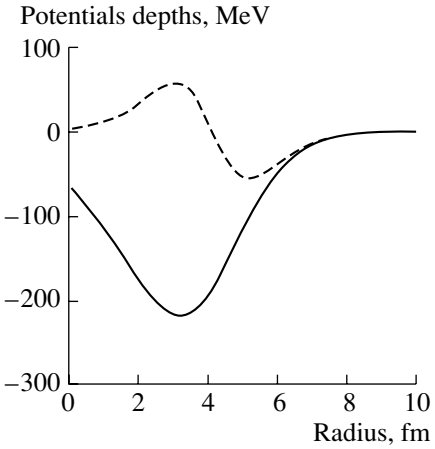

Fig. 1. For $^{16}O + ^{28}Si$: The comparison of the standard coupling potential (solid curve) which is the first derivative of the central potential and our new coupling potential (dashed curve), which is parametrized as the second derivative of Woods–Saxon shape and which has $V = 155.0$ MeV, $R = 4.160$ fm, and $a = 0.81$ fm.

The imaginary part of the potential was taken as in [4] as the sum of a Woods–Saxon volume and surface potential, i.e.,

$$W(r) = -W_V f(r, R_V, a_V) + 4W_S a_S df(r, R_S, a_S)/dr, \quad (2)$$

$$f(r, R, a) = \frac{1}{1 + \exp((r - R)/a)} \quad (3)$$

with $W_V = 59.9$ MeV, $a_V = 0.127$ fm, and $W_S = 25.0$ MeV, $a_S = 0.257$ fm. These parameters were also fixed in the calculations and only their radii increased linearly with energy according to the following formulas:

$$R_V = 0.06084E_{\text{c.m.}} - 0.442, \quad (4)$$

$$R_S = 0.2406E_{\text{c.m.}} - 2.191. \quad (5)$$

Since the target nucleus ^{28}Si is strongly deformed, it is essential to treat its collective excitation explicitly in the framework of the coupled-channels formalism. It has been assumed that the target nucleus has a static quadrupole deformation and that its rotation can be described in the framework of the collective rotational model. It is therefore taken into account by deforming the real optical potential in the following way:

$$R(\theta, \phi) = r_0 A_p^{1/3} + r_0 A_t^{1/3}[1 + \beta_2 Y_{20}(\theta, \phi)], \quad (6)$$

where $\beta_2 = -0.64$ is the deformation parameter of ^{28}Si. This value is actually larger than the value calculated from the known $BE(2)$ value. However, this larger β_2 was needed to be able to fit the magnitude for the 2^+ data.

In the present calculations, the first two excited states of the target nucleus ^{28}Si: 2^+ (1.78 MeV) and 4^+ (4.62 MeV) were included and the 0^+–2^+–4^+ coupling scheme was employed. The reorientation effects for 2^+ and 4^+ excited states were also included. The calculations were performed with an extensively modified version of the code CHUCK [10].

Using the standard coupled-channels theory, we found, as other authors had found, that it was impossible to describe consistently the elastic and inelastic scattering of this and other reactions we considered.

3. NEW COUPLING POTENTIAL

The limitations of the standard coupled-channels theory in the analyses of these reactions compelled us to look for another solution. Therefore, a second-derivative coupling potential, as shown in Fig. 1, has been used in the place of the usual first-derivative coupling potential. The interpretation of this new coupling potential is given in [11]. Here we employed the same method with small changes in the potential parameters. The empirical deformation parameter (β_2) is used in these calculations.

4. RESULTS

4.1. $^{16}O + ^{28}Si$

The first system we consider is $^{16}O + ^{28}Si$, which shows ALAS. In the present work, we consider an extensive *simultaneous* investigation of the elastic and the inelastic scattering of this system at numerous energies from $E_{\text{lab}} = 29.0$ to 142.5 MeV over the whole angular range up to 180°. In this energy range, the excitation functions for the ground and 2^+ states are also analyzed [6, 12].

Several *ad hoc* models have been proposed to explain these data, but no satisfactory microscopic models have been put forward yet. The most satisfactory explanation proposed so far is that of Kobos and Satchler [4], who attempted to fit the elastic scattering data with a microscopic double-folding potential. However, these authors had to use some small additional *ad hoc* potentials to obtain good agreement with the experimental data.

Using the standard coupled-channels method, some of the results obtained for the 180°-excitation functions for the ground and 2^+ states of the reaction $^{16}O + ^{28}Si$ are shown in Fig. 2. The magnitude of the cross sections and the phase of the oscillations for the individual angular distributions are given correctly at most angles. However, there is an out-of-phase problem between the theoretical predictions and the experimental data towards large angles at higher energies. This problem is clearly seen in the

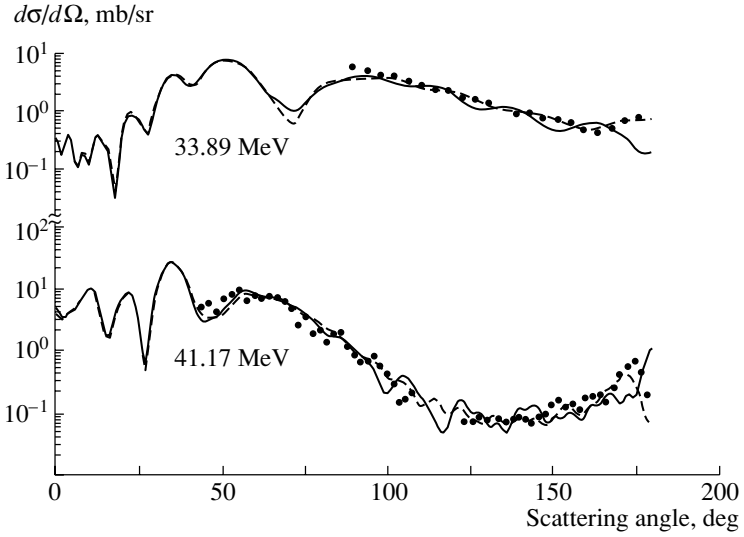

Fig. 2. The $^{16}O + ^{28}Si$ system: The angular distribution. The solid curves are the results of standard coupled-channels calculations, and the dashed curves are the results obtained using new coupling potential for the inelastic scattering data. The dots represent experimental data.

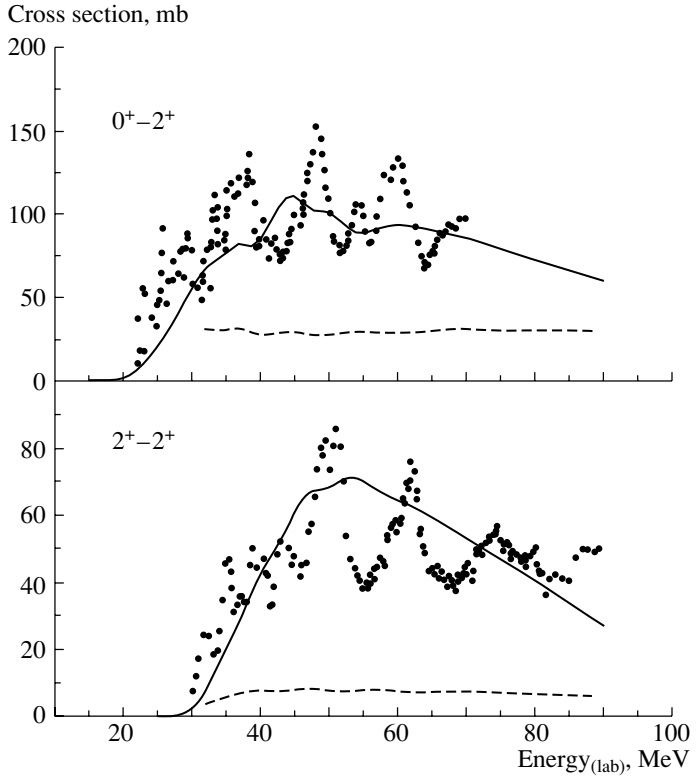

Fig. 3. The $^{12}C + ^{12}C$ system: The itegrated cross section of the single- and mutual-2^+ states. The solid curves are the results of the new coupling potential, while the dashed curves are the results of standard coupled-channels model. The dots represent experimental data.

180°-excitation functions, which are shown in the figure. A number of models have been proposed, ranging from isolated resonances to cluster exchange between the projectile and target nucleus to solve these problems (see [1] for a detailed discussion).

We have also attempted to overcome these problems by considering (i) changes in the real and

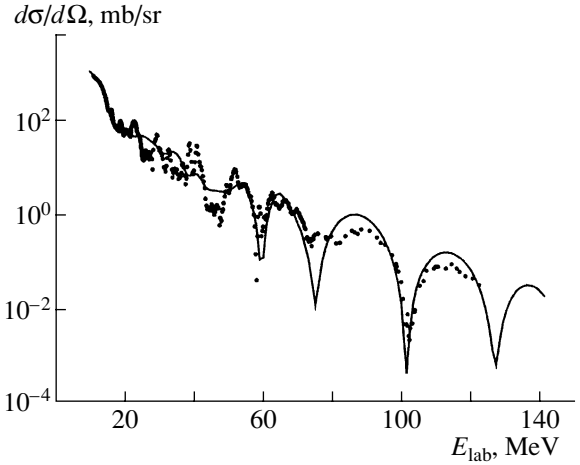

Fig. 4. The $^{12}C + ^{12}C$ system: 90°-excitation function for the elastic scattering using new coupling potential (solid curve). The dots represent experimental data.

imaginary potentials, (ii) the inclusion of the 6^+ excited state, (iii) changes in the β_2 value, and (iv) the inclusion of the hexadecapole deformation (β_4). These attempts failed to solve the problems at all [6, 12]. We were unable to get an agreement with the elastic and the 2^+ inelastic data as well as the 180°-excitation functions simultaneously within the standard coupled-channels formalism. However, as shown in Fig. 2, the new coupling potential has solved the out-of-phase problem for the 180°-excitation functions and fits the ground state and 2^+ state data simultaneously.

4.2. $^{12}C + ^{24}Mg$ and $^{16}O + ^{24}Mg$

The second and third examples we have considered are $^{12}C + ^{24}Mg$ and $^{16}O + ^{24}Mg$. Fifteen complete angular distributions of the elastic scattering of $^{12}C + ^{24}Mg$ system were measured at energies around the Coulomb barrier and were published recently [2]. We have studied these 15 complete elastic scattering angular distributions as well as some inelastic scattering data measured by Carter *et al.* [13, 14] some 20 years ago. Excellent agreement with the experimental data was obtained by using this new coupling potential. Our model has also solved some problems in $^{16}O + ^{24}Mg$ scattering [8].

4.3. $^{12}C + ^{12}C$

The final system we have considered is that of $^{12}C + ^{12}C$, which has been studied extensively over the last 40 years. There has been so far no model that fits consistently the elastic and inelastic scattering data, mutual excited state data, or the resonances and excitation functions. Another problem is the predicted magnitude of the excited state cross sections, in particular for the mutual-2^+ channel. The conventional coupled-channels model underestimates its magnitude by a factor of at least two and often much more [15–17]. We have also observed this in our conventional coupled-channels calculations as shown in Fig. 3 with dashed curves. There are also resonances observed at low energies, which have never been fitted by a potential, which also fits either the angular distributions or the excitation functions. Therefore, the experimental data at many energies between 20.0 and 126.7 MeV in the laboratory system have been studied simultaneously to attempt to find a global potential.

Using this new coupling potential, we have been able to fit the energy average of all the available ground, single-2^+, mutual-2^+ and the backgrounds in the integrated cross sections, as well as the main gross features of the 90°-excitation function, as shown in Figs. 3 and 4, simultaneously. Our preliminary calculations of resonances using no imaginary potential are promising but there are problems with the widths of the resonances.

To summarize, while these four systems show quite different properties and problems, a unique solution has come from a new coupling potential. Although the origin of this new coupling potential is still speculative and needs to be understood from a microscopic viewpoint, the approach outlined here is universal and applicable to all the systems. Studies using this new coupling potential are likely to lead to new insights into the formalism and the interpretation of these systems. Therefore, this work represents an important step towards understanding the elastic and inelastic scattering of light deformed heavy-ion systems.

ACKNOWLEDGMENTS

Special thanks to W.D.M. Rae, Y. Nedjadi, S. Aittahar, G.R. Satchler, and D.M. Brink for valuable discussions and providing some data. The author also would like to thank the Turkish Council of Higher Education (YÖK) and Oxford and Erciyes (Turkey) Universities for their financial support.

REFERENCES

1. P. Braun-Munzinger and J. Barrette, Phys. Rep. **87**, 209 (1982).
2. W. Sciani, R. M. Lepine-Szily, F. R. Lichtenthaeler, *et al.,* Nucl. Phys. A **620**, 91 (1997).
3. R. G. Stokstad, R. M. Wieland, G. R. Satchler, *et al.,* Phys. Rev. C **20**, 655 (1979).
4. A. M. Kobos and G. R. Satchler, Nucl. Phys. A **427**, 589 (1984).

5. M. E. Brandan and G. R. Satchler, Phys. Rep. **285**, 143 (1997).
6. I. Boztosun and W. D. M. Rae, in *Proceedings of the 7th International Conference on Clustering Aspects of Nuclear Structure and Dynamics,* Ed. by M. Korolija, Z. Basrak, and R. Caplar (World Sci., Singapore, 2000), p. 143.
7. I. Boztosun and W. D. M. Rae, Phys. Rev. C **63**, 054607 (2001).
8. I. Boztosun and W. D. M. Rae, Phys. Lett. B **518**, 229 (2001).
9. I. Boztosun, PhD Thesis (Univ. of Oxford, 2000).
10. P. D. Kunz, *CHUCK, A Coupled-Channel Code* (unpublished).
11. I. Boztosun and W. D. M. Rae, Phys. Rev. C **64**, 054607 (2001).
12. I. Boztosun and W. D. M. Rae, Phys. Rev. C **65**, 024603 (2002).
13. J. Carter, R. G. Clarkson, V. Hnizdo, *et al.,* Nucl. Phys. A **273**, 523 (1976).
14. J. Carter, J. P. Sellschop, R. G. Clarkson, *et al.,* Nucl. Phys. A **297**, 520 (1978).
15. R. Wolf, O. Tanimura, U. Mosel, *et al.,* Z. Phys. A **305**, 179 (1982).
16. Y. Sakuragi, M. Ito, M. Katsuma, *et al.,* in *Proceedings of the 7th International Conference on Clustering Aspects of Nuclear Structure and Dynamics,* Ed. by M. Korolija, Z. Basrak, and R. Caplar (World Sci., Singapore, 2000), p. 138.
17. P. E. Fry, PhD Thesis (Univ. of Oxford, 1997).

Physics of Atomic Nuclei, Vol. 65, No. 4, 2002, pp. 612–615. From Yadernaya Fizika, Vol. 65, No. 4, 2002, pp. 644–647.

Aspects of Alpha-Particle Scattering and Structure of the Nuclear Surface*

M. W. Brenner**, **K. A. Gridnev**[1)], **S. E. Belov**[1)], **K. W. Ershov**[1)], **and E. Indola**

Department of Physics, Åbo Akademi, Turku, Finland

Received August 31, 2001

Abstract—The interaction of α particles above 5 MeV with a $2s$–$1d$ target is dominated by resonances. It cannot be described only in terms of a mean-field one-body potential. An analysis of the elastic α-particle scattering by ^{28}Si encourages the comprehension of the resonance states to be mainly fragments of a mixed-parity band. In the present article, the angular distributions of particles scattered by ^{32}S are analyzed in terms of such bands. The analysis of new data from an experiment made at Florida State University reveals the existence of states that do not belong to the above bands. This follows from a coupled-channel analysis of the elastic and inelastic (2^+) cross sections. An α-particle structure at the nuclear surface is suggested. © *2002 MAIK "Nauka/Interperiodica"*.

1. RESONANCES OBSERVED IN THE EXCITATION FUNCTION

The large backward yield of elastically scattered particles was called anomalous large-angle scattering (ALAS). Many explanations of this phenomenon were proposed [1]. The cross section depends strongly on energy and scattering angle. In order to study α-particle scattering, experimental data should preferably be taken with small energy steps of a few MeV up to about 20 MeV or more. Moreover, the energy and the angular resolution should be 10 keV and 0.2° or better. Only a few experiments satisfy one of these requirements, but none satisfies all of them [2–12]. The energy dependence of elastic $\alpha + {}^{28}$Si scattering at 173° was measured between 3 and 28 MeV [6, 7, 13–15]. The energy resolution between 6.5 and 19.0 MeV was typically 15 keV.

The diffraction pattern of the angular distributions has mostly been analyzed in terms of scattering by a complex potential. Mostly, the real and imaginary parts of the potential were of the Woods–Saxon (WS) form or its square $(WS)^2$. These approaches give good fits to experimental angular distributions for bombarding energies above 22 MeV. Below that energy, the (WS) and $(WS)^2$ fits are generally poor. Similarly, the global potential proposed by Malik has to be modified at, e.g., 14.5 MeV [16]. The shortcomings of fits based on potential scattering exclusively is demonstrated by α scattering on ^{32}S [9]. We have improved the fits considerably by adding a complex resonance term to the amplitude of potential scattering on $(WS)^2$.

Various circumstances indicate that the peaks observed in the excitation function are single or overlapping resonances, whose spins can be assigned uniquely [6, 7]. The effect of intermediate states or resonances on α scattering was considered by several investigators before (e.g., [3, 17–19]). Nevertheless, the strong variation of the cross section was sometimes considered as the result of statistical fluctuations [20]. Recently, however, an analysis of $\alpha + {}^{28}$Si data in terms of the contribution of resonances resulted in a successful fit to the elastic and the inelastic excitation function at many backward angles [21]. It excludes a claim that the peaks observed in the excitation function would be due to statistical fluctuations.

Two interfering mechanisms, resonance scattering and nonresonance potential scattering, are thus considered. The effect of large-angle scattering is mainly due to the former. It is proportional to the squared Legendre polynomial of order L. Since the target and the projectile are spinless, the spins J of the resonances involved are equal to L. The contribution of potential scattering to the cross section can frequently be considered as a small "background." In comparison, especially high-spin resonances contribute much more. The cross section may increase by one or more orders of magnitude upon going over from 165° to the most backward experimental angles [22].

*This article was submitted by the authors in English.

[1)]St. Petersburg State University, Petrodvorets, Russia; e-mail: gridnev@nuclpc1.phys.spbu.ru

**e-mail: brenner@abo.fi

2. ASSIGNMENT OF SPINS FROM ANGULAR DISTRIBUTIONS

Scattering by silicon targets was compared in a previous study with (^{6}Li, d) stripping measurements [23]. The excitation function for elastic scattering showed peaks at the same excitation energy in ^{32}S as the excitation function for the stripping reaction ^{28}Si(^{6}Li, d)^{32}S. The spins were obtained from a comparison of the angular distributions with the squared Legendre polynomials $P_L^2(\cos\theta)$. The parities are natural: 0^+, 1^-, 2^+, 3^-, and so on.

In the scattering of 10- to 20-MeV α particles by silicon, resonance spins between 7 and 9 are observed. The energy range 14.3–15.4 MeV was investigated in more detail by using the Florida State University Pelletron. The current good energy resolution of this experiment led to an observation of about eight times more resonances than before in that energy range. From a correlation analysis, we deduced the mean resonance width of 20 keV. For a couple of resonances, all were assigned a spin of 8 [8]. A coupled-channel analysis of the same energy region reveals ten $J = 5$, one $J = 6$, 13 $J = 7$, ten $J = 8$, and three $J = 9$ resonances [21].

3. MIXED-PARITY ROTATIONAL BANDS AND SURFACE STRUCTURE

A linear dependence has been noted when the energies of the resonance in $\alpha + {}^{28}$Si are plotted versus $J(J+1)$ [5]. A similar line describes α-particle transfer to ^{24}Mg by (^{6}Li, d) stripping [24]. This has been understood to be an indication of the existence of a mixed-parity band [3, 25], whose states are represented by many fragments of equal spin. Bands of even- and odd-parity states are not expected from fundamental theories based on the interaction between fermions. In terms of the Pauli exclusion principle, there should be so-called Firsov splitting between bands of opposite parities [26]. The lack of the splitting implies that the nuclear surface has a structure of bosons, which interact with incoming α particles [25]. The low density at the nuclear surface makes the existence of α matter probable there. Nuclear-matter theories do indeed imply that, below the point of the matter being compressible, there is no thermodynamically stable uniform state of it. Below this point, the system breaks up into clusters [27, 28]. The variety of possible clusters may be illustrated by the Ikeda diagram [29]. The bosonization mentioned here is considered to occur when the Broglie wavelength corresponding to the interacting α particles is commensurate with the distance between them [30].

The moment-of-inertia parameter C of the relation $E = CJ(J+1) + E_0$ is small in relation to that expected for a single α-particle orbiting the target nucleus. If we assume that the orbit radius is equal to the sum of the target and the α-particle radius, $1.25A^{1/3} + 1.60$, we expect, for $A = 24$ and 28, the rotational constants $C = 225$ and 205 keV (energy in the c.m. frame). However, the experimental constants are $C = 131$ and 103 keV. The radius parameter of 1.25 gives, e.g., a ^{28}Si radius of 3.8 fm. The Hofstadter rms radius of the target is 3.04 fm. The latter would yield an even greater rotational constant, which would deviate more strongly from the experimental value.

We conclude that the value of C cannot be reproduced by assuming a single particle orbiting a nonrotating target. Agreement with experimental data is, however, achieved if a part of the target nucleus is assumed to rotate jointly with the captured α particle [5]. The rotating mass of ^{28}Si and ^{32}S may be considered to consist of three and four α particles orbiting the ^{16}O core [31].

Parameters of the angular-distribution fits (the real and the imaginary radius and diffuseness parameters were fixed at $r_V = 1.37$ fm, $a_V = 1.30$ fm, $r_W = 1.75$ fm, and $a_W = 0.70$ fm)

E_α, MeV	V, MeV	W, MeV	J	Γ_α/Γ	$P_{\rm res}$	J [31]
10.1	207.3	7.6	5	0.60	0.0	5
10.3	211.8	7.8	5	0.60	2.9	5
10.6	206.4	7.3	6	0.40	3.0	5
11.0	199.6	1.5	6	0.06	3.0	6
11.3				No fit		
11.8				No fit		7
12.0	198.9	3.0		No res.		6
12.2	200.6	3.2		No res.		7
12.5	212.9	4.3		No res.		7
12.9	208.6	4.2	8	0.11	0.18	7
13.4	184.1	11.1	6	0.40	0.55	6
13.6	210.5	11.0	7	0.26	0.7	7
13.9	196.4	9.1	7	0.20	0.3	7
14.3	186.8	7.2	7	0.40	1.9	7
14.8	208.3	6.8	8	0.16	0.3	8
15.2	182.3	9.9	8	0.34	0.4	8
15.5	215.4	11.2	8	0.26	3.1	8
15.9	194.5	6.6		No res.		8
16.1	209.5	7.1		No res.		8

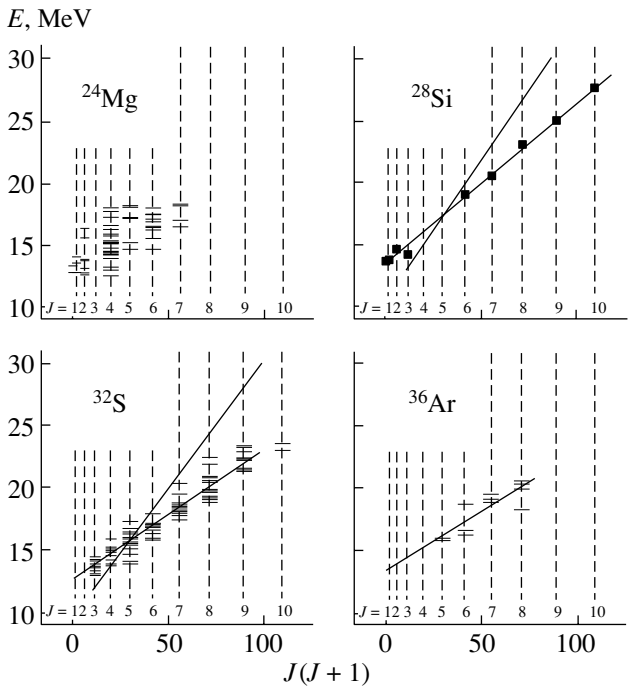

Energies of states formed in elastic scattering of α particles by some α-particle nuclei. Straight solid lines were fitted to the excitation energies of the compound system and plotted versus $J(J+1)$. For silicon and sulfur, steep lines correspond to the moment-of-inertia parameters of one orbiting particle.

The formation of α particles from valence nucleons was discussed by Lönnroth [32]. Microscopic shell-model calculations were mentioned as a means for generating α-cluster correlations. One possibility would be to start from ^{16}O and to advance toward more complicated cases of a greater number of nucleons. A sudden cutoff of the cross section at 27 MeV is indicative of an upper limit on the spin near $12\hbar$ to $14\hbar$. It may be due to the "running out of valence particle spin." If so, it indicates the limitation in the number of valence particles, i.e., to particles within the skin at the nuclear surface mentioned above.

The occurrence of even and odd spins in the same band also implies that the rotating object has not more than one symmetry axis. We may think of a rotating pear or of an asymmetric disk, which has the symmetry axis in the plane of the disk. Such shapes would occur if an α particle is captured by a spherical target. As was mentioned above, only part of the target will start to rotate jointly. We may expect various shapes of that jointly rotating part and consider its thickness to depend on the azimuthal and polar angles.

4. ALPHA-PARTICLE SCATTERING BY ^{32}S

Only a few authors reported on resonance states in the $\alpha + {}^{32}$S system at high energies [10, 33]. For this reason, the angular distributions of α particles scattered by ^{32}S deserve more investigations for a comparison with states in other $2s$–$1d$ nuclei.

The angular distributions of α particles elastically scattered by ^{32}S were previously published in the article of Aldridge *et al.* [9]. Rapid variations of the optical-model parameters were indeed assumed to occur owing to compound-system resonances, but a determination of energies and spins of such resonances was not aimed at. Since the energy was varied in large steps (100 keV), the energies of resonances could not be determined from the excitation function. The authors extracted numerical data for 76 angular distributions between 10 and 17.5 MeV from the published figures. The coordinates of the cursor at data points and scale marks were read when the scanned figures were displayed on a PC. In the 100-keV-step excitation function, 19 peaks were considered to sample the strongest resonances. At these energies, the angular distributions from 25° to 175° were fitted in the same way as was described above for $\alpha + {}^{28}$Si.

Potential scattering was assumed to be described by the real and the imaginary part (V and W, respectively) of the squared WS form. The radius and the diffuseness parameters were fixed at the values used in [34, 35]. To obtain a good fit, the potentials V and W, the ratio Γ_α/Γ of the α partial width and the total width, and the phase shift $P_{\rm res}$ were varied [35]. For the best fits, the values of the parameters are given in the table. We note that the fits to the angular distributions at 12.0, 12.2, 12.5, 15.9, and 16.1 MeV are not improved upon the addition of a resonance amplitude to the scattered wave. Strong backward scattering at 11.3 MeV and that at 11.8 MeV could not be fitted so far. For the remaining energies, the spins could be assigned. The excitation energies in ^{24}Mg [4], ^{28}Si [24], ^{32}S [6, 7], and ^{36}Ar are plotted versus $J(J+1)$ in the figure as obtained from $\alpha + {}^{20}$Ne, ^{24}Mg(^{6}Li, d)^{28}Si, $\alpha + {}^{28}$Si, and $\alpha + {}^{32}$S. Solid lines have been fitted to the silicon, sulfur, and argon points. The spin-0 crossings of the energy axis are in all cases approximately 13 MeV. This corresponds to the bombardment energy 6.5 MeV in the case of the ^{28}Si target. It is roughly where many spin-0 levels are found in $\alpha + {}^{28}$Si. The slope gives the values of 130, 103, and 93 keV for the moment-of-inertia parameter C. For $\alpha + {}^{32}$S, the value is consistent with the moment of inertia of three orbiting α particles. From the corresponding plot for $\alpha + {}^{40}$Ca, we obtain one to two α-particles in ^{44}Ti. Thus, the last two estimates

mentioned above are not in agreement with the assumption of a structure of α particles orbiting a ^{16}O core, as was suggested for ^{28}Si and ^{32}S.

5. DISCUSSIONS AND CONCLUSIONS

In the present article, the existence of resonances in the scattering of α particles by $2s$–$1d$ targets is placed without dispute by experimental evidence. Bands of resonance states at excitation energies over 13 MeV in ^{28}Si and ^{32}S are explained in terms of a model of, respectively, three and four α particles orbiting a ^{16}O core. This model is deduced from the systematics of resonances of highest spins. The dynamical properties of these particles have been discussed in the context of published theoretical models. A vibrational degree of freedom [31, 36] and soliton or boson quantum numbers [30, 37] have been mentioned as exciting issues. They hint at the occurrence of new kinds of nuclear dynamics [6]. The recently found resonances of lower spins do not fit in the systematics under discussion. These resonances have merely been deduced in fitting the excitation functions and angular distributions of α particles scattered by the aforementioned two targets; they have not been observed if resonances of highest spin occur. These circumstances should not weaken interest in the nuclear properties being discussed. New measurements for elastic and inelastic scattering that would cover wide energy ranges scanned in small energy and angular steps are required for promoting the understanding of the current experimental results.

REFERENCES

1. K. A. Gridnev and A. A. Ogloblin, Fiz. Élem. Chastits At. Yadra **6**, 393 (1975) [Sov. J. Part. Nucl. **6**, 158 (1975)].
2. A. E. Antropov, M. Brenner, V. Z. Goldberg, *et al.*, in *Proceedings of the 7th International Conference on Nuclear Reaction Mechanisms, Varenna, Italy* (Department of Physics, Milano Univ., 1994), p. 430.
3. R. Stock, G. Gaul, R. Santo, *et al.*, Phys. Rev. C **6**, 1226 (1972).
4. R. Abegg and C. A. Davies, Phys. Rev. C **43**, 2523 (1991).
5. M. Brenner, Z. Phys. A **349**, 64 (1994).
6. M. Brenner, in *Proceedings of International Workshop on Fission Dynamics, Luso, Portugal, 2000.*
7. K.-M. Källman, Doctoral Dissertation in Physics (Åbo Akademi, Turku, 1998).
8. M. Brenner, N. R. Fletcher, J. A. Liendo, *et al.* (in press).
9. J. P. Aldridge, G. E. Crawford, and R. H. Davis, Phys. Rev. **167**, 1053 (1968).
10. V. Z. Goldberg, G. V. Rogachev, M. Brenner, *et al.*, Yad. Fiz. **63**, 1603 (2000) [Phys. At. Nucl. **63**, 1518 (2000)].
11. C. P. Robinson, J. P. Aldridge, J. John, *et al.*, Phys. Rev. **171**, 1241 (1968).
12. D. Frekers, R. Santo, and K. Langanke, Nucl. Phys. A **394**, 189 (1983).
13. K.-M. Källman, Z. Phys. A **356**, 278 (1996).
14. L. Jarczyk, Preprint No. 7 (Institute of Physics, Silesian University, Katowice, 1979).
15. E. Indola, Masters Thesis in Physics (Åbo Akademi, Turku, 1999).
16. P. Manngård, M. Brenner, M. M. Alam, *et al.*, Nucl. Phys. A **504**, 130 (1989).
17. C. R. Gruhn and N. S. Wall, Nucl. Phys. **81**, 161 (1966).
18. P. P. Singh, B. A. Watson, J. J. Kroepfl, *et al.*, Phys. Rev. Lett. **17**, 968 (1966).
19. C. Bergman and R. K. Hobbie, Phys. Rev. C **3**, 1729 (1971).
20. T. Ericson, Ann. Phys. (N.Y.) **23**, 390 (1963).
21. V. V. Lazarev, private communication.
22. J. S. Eck, W. J. Thompson, K. A. Eberhard, *et al.*, Nucl. Phys. A **255**, 157 (1975).
23. K. P. Artemov, M. Brenner, M. S. Golovkov, *et al.*, Yad. Fiz. **55**, 884 (1992) [Sov. J. Nucl. Phys. **55**, 492 (1992)].
24. K. P. Artemov, M. S. Golovkov, V. Z. Goldberg, *et al.*, Yad. Fiz. **51**, 1220 (1990) [Sov. J. Nucl. Phys. **51**, 777 (1990)].
25. M. Brenner, in *Clustering Phenomena in Atoms and Nuclei* (Springer-Verlag, Heidelberg, 1991), Springer Series in Nuclear and Particle Physics, p. 327.
26. K. A. Gridnev, in *Clustering Phenomena in Atoms and Nuclei* (Springer-Verlag, Heidelberg, 1991), Springer Series in Nuclear and Particle Physics, p. 153.
27. J. W. Clark, Ann. Phys. (N.Y.) **40**, 127 (1966).
28. M. T. Johnson and J. W. Clark, Kinam **2**, 3 (1980).
29. H. Horiuchi, K. Ikeda, and Y. Suzuki, Prog. Theor. Phys. Suppl., No. 52, 89 (1972).
30. K. A. Gridnev, S. E. Belov, K. V. Ershov, *et al.*, in *Proceedings of International Conference on Achievements and Perspectives in Nuclear Physics, Crete, Greece, 1999* (Institute of Nuclear Physics N.C.S.R. Demokritos, Athens, 1999).
31. M. Brenner, E. Indola, K.-M. Källman *et al.*, Heavy Ion Phys. **7**, 355 (1998).
32. T. Lönnroth, Nuovo Cimento A **110**, 961 (1997).
33. A. Coban, M. S. Abdelmonem, F. Z. Khiari, *et al.*, Nucl. Phys. A **645**, 3 (1999).
34. Th. Delbar, Gh. Grégoire, G. Paic, *et al.*, Phys. Rev. C **18**, 1237 (1978).
35. M. Brenner, K.-M. Källman, Z. Máté, *et al.*, Heavy Ion Phys. **2**, 269 (1995).
36. U. Abbondano, N. Cindro, and P. M. Milazzo, Nuovo Cimento A **110**, 955 (1997).
37. A. Ludu, A. Sandulescu, W. Greiner, *et al.*, J. Phys. G **21**, L41 (1995).

Physics of Atomic Nuclei, Vol. 65, No. 4, 2002, pp. 616–620. From Yadernaya Fizika, Vol. 65, No. 4, 2002, pp. 648–652.

T-Odd Correlation in Ternary Fission*

V. E. Bunakov**

Institute of Physics, St. Petersburg State University, Petrodvorets, Russia

Received August 31, 2001

Abstract—A possible explanation is presented of the T-odd correlation observed in ternary fission induced by polarized cold neutrons. © *2002 MAIK "Nauka/Interperiodica".*

I. Recently, a collaboration of ILL, Tuebingen, Darmstadt, ITEP, and PNPI observed (see, e.g., [1, 2]), in ternary fission, a triple correlation $\boldsymbol{\sigma}_n \cdot [\mathbf{p}_{\rm LF} \times \mathbf{p}_{\rm TP}]$ between the vectors of the incident-neutron spin and the momenta $\mathbf{p}_{\rm LF}$ and $\mathbf{p}_{\rm TP}$ of the light fragment and the ternary particle. The scheme of the experimental setup can be found in [1, 2]. The polarization vector of incident cold neutrons is directed either along or against the neutron-beam direction. The fission-fragment and ternary-particle detectors are located in the plane perpendicular to the beam direction and allow one to choose events where the light fragment goes either to the left or to the right, while the ternary particle goes either upward or downward. The definition of the asymmetry coefficient is [1]

$$D = \frac{N(+) - N(-)}{N(+) + N(-)}, \qquad (1)$$

where $N(\pm)$ is the number of coincidences for positive and negative neutron helicities, respectively. One can also reverse the direction of the light-fragment or of the ternary-particle momentum. The corrected values of the observed asymmetry D resulting from the inversion of any of three vectors is [3]

$$D = (-2.43 \pm 0.11) \times 10^{-3} \quad \text{for a } {}^{233}\text{U target},$$

$$D = (+0.40 \pm 0.08) \times 10^{-3} \quad \text{for a } {}^{235}\text{U target}.$$

It was also observed that the magnitude of the effect is roughly proportional to the ternary-particle final energy (see, e.g., Fig. 1 for the case of a ^{233}U target).

Although this correlation is formally T-odd, it was continuously indicated (see, e.g., [4, 5]) that (in contrast to what occurs in the case of parity violation) a nonzero T-odd correlation is directly related to T invariance only in the case of elastic scattering. In all inelastic processes like β and γ decays or fission, this direct connection can be established only if the process can be described in the first-order Born approximation and, even then, is strongly camouflaged by effects of initial- or final-state interactions. The strong-interaction process of fission can hardly be treated in the Born approximation. Therefore, one should seek the possible explanations of the observed correlation in fission dynamics rather than treat it as a signature of T-invariance violation. A feasible qualitative version of such an explanation is presented here.

II. The absorption of the polarized neutron with polarization P_n by a target nucleus with spin I creates partially polarized compound resonances with the polarizations

$$P(J^+) = \frac{(2I+3)}{[3(2I+1)]} P_n \quad \text{for} \quad J^+ = I + 1/2,$$

$$P(J^-) = -1/3 \cdot P_n \quad \text{for} \quad J^- = I - 1/2$$

(recall that the direction of polarization changes sign in this case).

Let us first consider, for the sake of simplicity, the situation of one isolated resonance (say J^+). The probability of neutron-induced ternary fission can then be written as

$$W_{n,\rm tf} \sim \pi\lambda^2 \frac{2J^+ + 1}{3(2I+1)} \times \frac{\Gamma_n \Gamma_{\rm tot}}{(E - E(J^+))^2 + \Gamma_{\rm tot}^2/4} \left[w_{\rm tf} + P(J^+) w_{\rm tf}^P \right]. \qquad (2)$$

Here, the structure in front of the brackets is the probability $\sigma(J^+)$ of the compound-resonance formation.

In order to estimate the probability $w_{\rm tf}$ of the ternary fission of an unpolarized nucleus, we will use the statistical approach, whose validity in describing

*This article was submitted by the author in English.

** e-mail: vadim.bunakov@pobox.spbu.ru

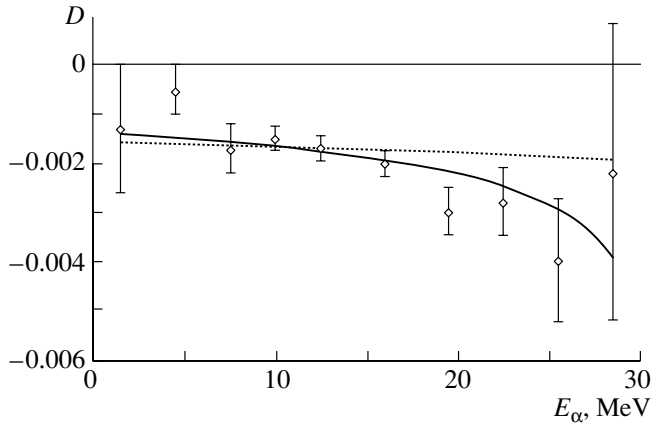

Fig. 1. T-odd correlation D as a function of the final α-particle energy E_α for the ternary fission of a ^{233}U target. The points with error bars represent the experimental data. The dotted curve is a theoretical fit corresponding to the hypothesis of $E^*_{\rm LF}/E^*_{\rm HF} \approx 1$. The solid curve represents a fit that corresponds to the hypothesis of fixed $E^*_{\rm HF} \approx 15$ MeV. Both curves are normalized to experimental data at $E_\alpha = 16$ MeV.

fission was established in many cases. In this approach, we have

$$w_{\rm tf} \sim \rho\left(A, E^*_f, J\right) \tag{3}$$
$$\sim \exp\left[2\sqrt{a\left(E^*_f - E_{\rm rot}(J)\right)}\right] \approx \exp\left[2\sqrt{aE^*_f}\right],$$

where $\rho(A, E^*_f, J)$ is the standard expression for the level density in the system upon the emission of a ternary particle. The rotational energy $E_{\rm rot} = \hbar^2 J(J+1)/2\mathcal{J}$ is usually about one MeV or even less, which allows one to neglect it in the above equation in relation to the internal excitation E^*_f of the system.

In order to write the probability $w^P_{\rm tf}$ of ternary fission for a polarized compound nucleus, one should rather use an expression for the level density $\rho(A, E^*_f, M)$ for a system with a fixed projection M of its total angular momentum J onto a given axis. According to Eq. (2.324) in [6], it is

$$\rho(A, E^*, M) \sim \exp\left[2\sqrt{a\left(E^* - \hbar^2 M^2/2\mathcal{J}\right)}\right] \tag{4}$$
$$\approx \exp\left[2\sqrt{aE^*}\left(1 - \hbar^2 M^2/4\mathcal{J}E^*\right)\right].$$

Now, the main idea of our approach is that, if the angular momentum of the outgoing ternary particle (let it be α), $\mathbf{l}_\alpha = [\mathbf{r}_\alpha \times \mathbf{p}_\alpha]$, is parallel to the spin $\mathbf{J}$ ($J_z = M = J$) of the polarized system, then the emitted α particle carries away part of the total angular momentum of the system, so that $M_f = M - l_\alpha$. If $\mathbf{l}_\alpha$ is antiparallel to $\mathbf{J}$, then the system receives, as a recoil, $M_f = M + l_\alpha$. Therefore, the emission of α increases or decreases the final level density of the system, so that

$$w^{P\uparrow}_{\rm tf} - w^{P\downarrow} \approx e^{\left(2\sqrt{aE^*_f}\right)} \frac{\hbar^2 M l_\alpha \sqrt{a}}{\mathcal{J}\sqrt{E^*_f}} \tag{5}$$
$$\equiv e^{\left(2\sqrt{aE^*_f}\right)} \Delta.$$

Now, the number of coincidences for the case of $\mathbf{l}_\alpha$ parallel to the spin $\mathbf{J}$ of the polarized system is

$$N_{\rm par} \approx N_0 \left[1 + P(J^+)\left(1 - \frac{\hbar^2 (M - l_\alpha)^2 \sqrt{a}}{\mathcal{J}\sqrt{E^*_f}}\right)\right]. \tag{6}$$

For $\mathbf{l}_\alpha$ antiparallel to $\mathbf{J}$, we have

$$N_{\rm anti} \approx N_0 \left[1 + P(J^+)\left(2 - \frac{\hbar^2 (M + l_\alpha)^2 \sqrt{a}}{\mathcal{J}\sqrt{E^*_f}}\right)\right]. \tag{7}$$

Therefore, the expression for the asymmetry coefficient (1) is

$$D = \frac{P(J^+)\Delta}{2[1 + P(J^+)]}, \tag{8}$$

where Δ is defined [see Eq. (5)] as

$$\Delta = \frac{\hbar^2 M l_\alpha \sqrt{a}}{\mathcal{J}\sqrt{E^*_f}}. \tag{9}$$

III. The sign and the magnitude of Δ depend on the dynamics of the process. Let us first consider the rather unrealistic but simple case where the ternary particle is emitted before scission. In this case (see Fig. 2), the radius vector $\mathbf{r}_\alpha$ issues from the center

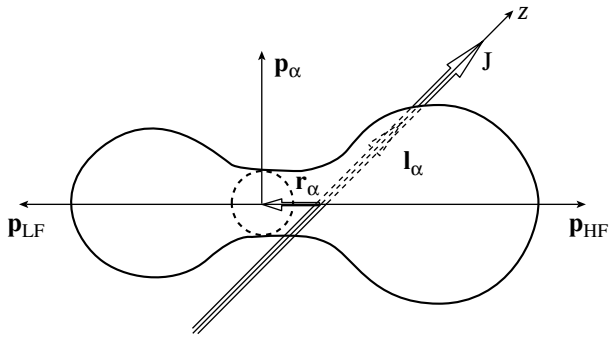

Fig. 2. Case of ternary-particle emission before scission.

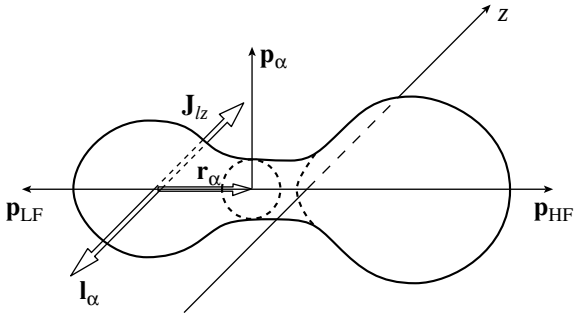

Fig. 3. Case of ternary-particle emission in the double neck rupture.

of mass of the entire system. For $\mathbf{p}_\alpha$ directed upward and the light fragment going to the left, the α-particle momentum is then parallel to $\mathbf{J}^+ \uparrow\uparrow \boldsymbol{\sigma}_n$ (see Fig. 2). If the neutron helicity is reversed, $\mathbf{l}_\alpha$ becomes antiparallel to $\mathbf{J}^+$. Therefore, the sign of Δ is positive according to (1).

Even in this simple case, the majority of the parameters in expression (5) for Δ are not known precisely. Therefore, all the estimates of D given below only demonstrate that one can obtain a correct order of magnitude for the effect using reasonable educated guesses concerning these parameters. We choose the level-density parameter to be $a = A/8 \approx 30$ MeV^{-1}. For the moment of inertia of the system, $\mathcal{J}$, we take half the rigid-body value with a deformation of $\beta_2 \approx 1.4$ at the scission point. Although $\mathcal{J}$ is known to be only half the rigid-body value for low-lying states because of the pairing-correlation effect, the role of these correlations decreases with increasing excitation. Therefore, this might be a slightly underestimated value of $\mathcal{J}$, but it is still good for our order-of-magnitude estimates. As a reasonable guess for the orbital angular momentum l_α, we take $1\hbar$, since, from a comparison of multiplicities for gamma rays emitted by fragments in binary and ternary fission, it is known that ternary particles carry away about 0.1 of the total angular momentum of $(10{-}14)\hbar$ carried by γ emission. As a reasonable guess of the prescission excitation energy E_f^* of the system, we take 6 MeV. Inserting all these values into Eqs. (5), (8), and (9), we find, for the case of $J^+ = 3$, that

$$D(J^+) \approx +5.5 \times 10^{-3}. \qquad (10)$$

Let us now estimate the effect of an isolated $J^- = 2$ resonance. Recall that, in this case, the compound-nucleus polarization is $P(J^-) = -1/3 \cdot P_n$ and is directed against the neutron polarization. Therefore, Δ would be negative; under the same assumptions as those for J^+, we obtain

$$D(J^-) \approx -4.5 \times 10^{-3}. \qquad (11)$$

Taking into account the contributions of both resonances (and neglecting the interference effects), we obtain the net result

$$D = \frac{\sigma(J^+)P(J^+)\Delta + \sigma(J^-)P(J^-)\Delta}{2\sigma(J^+)[1+P(J^+)] + 2\sigma(J^-)[1+P(J^-)]}. \qquad (12)$$

Thus, we see that, depending on the relative contributions of $\sigma(J^\pm)$, we obtain, for D, the values between the rough estimates in (10) and (11).

IV. Let us now consider the more realistic case of the double neck rupture (see [7]), in which case the first rupture separates a heavy fragment and a light "prefragment," which then emits a ternary particle. In this case, the theoretical difficulties increase even more. The main trouble is how the initial spin J and polarization of the compound nucleus is shared between the light and heavy fragments and the angular momenta of their relative motion:

$$\mathbf{J} = \mathbf{J}_1 + \mathbf{J}_2 + \mathbf{L}_f.$$

This problem was considered by Barabanov and Grechukhin [8], who introduced the coefficient $\mu_{11}(J_1)$ characterizing the transfer of the initial polarization $P(J)$ to one of the fragments (transmission coefficient), so that the fragment polarization can be represented as

$$P_1(J_1) \approx \mu_{11}(J_1)P(J).$$

According to estimates based on various models of the prescission process, this coefficient ranges between -0.1 and $+0.1$. Unfortunately, those calculations were performed for the compound-nucleus polarization directed along the fission axis. Therefore, one of the nearest future problems is to apply this formalism to the case of interest to us, where the polarization direction is perpendicular to the fission axis. There are, however, some indications that the order of magnitude of μ_{11} in our case would be the same. For the time being, we can simply assume that the initial polarization of the compound nucleus is approximately equally shared between those three

components. Then, we assume that the projection of the light-prefragment spin onto the z axis is $J_{1z} = M_1 \approx 1\hbar$ and that the transmission coefficient μ_{11} is

$$\mu_{11} \approx J/3J_1.$$

Here, $J_1 \approx (5\text{–}7)\hbar$ is the total spin of the fission fragments, which was estimated from the experiments with γ emission from the fragments and was explained by either the collective bending modes of the compound system at scission or by a postscission Coulomb excitation. The same experiments also show that the direction of this spin is perpendicular to the fission axis. Since this "additional" $\mathbf{J}_1$ is directed isotropically around the scission axis, it would not on average change the value $J_{1z} = M_1$, but would rather decrease the polarization of the fragment by the factor μ_{11}.

Otherwise, our general idea of the triple-correlation origin remains the same. One should only replace the level density of the entire system by the product of the fragment level densities and take into account the coefficient μ_{11} in calculating the polarization of the light fragment in expressions (2) and (4)–(8). Another difference is that the radius vector $\mathbf{r}_\alpha$ now issues from the center of mass of the light prefragment (see Fig. 3). This means that, if μ_{11} is positive (i.e., the direction of light-fragment polarization coincides with that of the compound nucleus), the values of Δ would change signs.

We should also replace the total prescission excitation energy E_f^* of the system in (9) by the average excitation energy $\langle E_{\rm LF}^* \rangle$ of the light fragment. It should be recalled that, in [9], the anticorrelation was found between the average excitation energy $\langle E_f^* \rangle$ of the system and the final energy E_α of the outgoing α particle:

$$\langle E_f^* \rangle \approx \langle E_{\max}^* \rangle - 0.4E_\alpha. \qquad (13)$$

Here, $\langle E_{\max}^* \rangle \approx 30$ MeV is the average fissioning-system internal excitation energy corresponding to $E_\alpha = 0$. Now, the total excitation energy E_f^* of the system is the sum of the fragment excitation energies:

$$E_f^* = E_{\rm LF}^* + E_{\rm HF}^*.$$

The mechanism behind the anticorrelation in (13) has yet to be clarified. Therefore, we can consider two possibilities. One of them is to assume that the ratio of the excitation energies of the fragments in this sum is constant, $E_{\rm LF}^*/E_{\rm HF}^* \approx 1$. Then, we obtain the dependence of the effect on E_α in the form

$$D \sim 1/\sqrt{15 - 0.2E_\alpha}.$$

This dependence is shown in Fig. 1 by the dotted curve (which is normalized to the experimental value at $E_\alpha = 16$ MeV).

The other possibility is to consider the excitation energies of the fragments as independent quantities and to suppose that E_α changes with $E_{\rm LF}^*$ for fixed $E_{\rm HF}^* \approx 15$ MeV. In this case, we obtain the dependence of the effect on E_α in the form

$$D \sim 1/\sqrt{15 - 0.4E_\alpha}.$$

This dependence is shown in Fig. 1 by the solid curve. The curve is again normalized at the experimental point $E_\alpha = 16$ MeV. Below, this value of E_α is also taken in the estimates of the average coefficients D.

Assuming again $l_\alpha = 1$ and half the rigid-body value for the light-fragment moment of inertia $\mathcal{J}_1$, we find for the $J^+ = 3$ compound resonance and $J_1 = 5$ that

$$D = -\frac{P(J^+)\mu_{11}\Delta}{2[1 + P(J^+)\mu_{11}]} = -\frac{J^+}{3J_1} \qquad (14)$$
$$\times \frac{\hbar^2 l_\alpha M_1 \sqrt{a}}{\mathcal{J}_1 \sqrt{\langle E_{\rm LF}^* \rangle}} \frac{P(J^+)}{2[1 + P(J^+)\mu_{11}]} \approx -2 \times 10^{-3}.$$

For the $J^- = 2$ compound resonance, we obtain

$$D = \frac{P(J^-)\mu_{11}\Delta}{2[1 + P(J^-)\mu_{11}]} = \frac{J^-}{3J_1} \qquad (15)$$
$$\times \frac{\hbar^2 l_\alpha M_1 \sqrt{a}}{\mathcal{J}_1 \sqrt{\langle E_{\rm LF}^* \rangle}} \frac{P(J^-)}{2[1 + P(J^-)\mu_{11}]} \approx 1 \times 10^{-3}.$$

Those values of D were obtained under the assumption of the independent variation of the fragment excitations in Eq. (13) (our second assumption). If the ratio of these energies is fixed, the values of D in Eqs. (14) and (15) would be larger by a factor of about 1.4.

Finally, taking into account the contribution from both resonances, we get

$$D = -\frac{\sigma(J^+)P(J^+)\mu_{11}\Delta + \sigma(J^-)P(J^-)\mu_{11}\Delta}{2\sigma(J^+)[1 + P(J^+)\mu_{11}] + 2\sigma(J^-)[1 + P(J^-)\mu_{11}]}. \qquad (16)$$

As in the preceding case, we find that the net effect D depends on the relative contribution of $\sigma(J^+)$ and $\sigma(J^-)$ and varies in the range between the approximate values in Eqs. (14) and (15).

In the case of a ^{235}U target, the values of $\sigma(J^+ = 4)$ and $\sigma(J^- = 3)$ are already known [10]. Substituting them into Eq. (15), we obtain $D \approx -0.7 \times 10^{-3}$, that is, a correct order of magnitude but a wrong sign of the effect. Since the polarization-transmission coefficients of [8] might also be negative, this means most probably that, instead of our simplified estimate of μ, one should perform more detailed calculations of this quantity.

V. Thus, we have shown that the suggested approach might reproduce both a correct order of magnitude of the observed effect and the character of its dependence on E_α observed experimentally.

ACKNOWLEDGMENTS

I am grateful to G. Petrov, A. Barabanov, and F. Goennenwein for stimulating discussions.

This work was supported by INTAS (grant no. 99-00229) and the Russian Foundation for Basic Research (project no. 99-02-17275).

REFERENCES

1. P. Jesinger, A. Koetzle, A. Gagarski, *et al.*, in *Nuclear Fission and Fission-Product Spectroscopy*, Ed. by G. Fioni *et al.*, AIP Conf. Proc. **447**, 395 (1998).
2. P. Jesinger, A. Koetzle, F. Goennenwein, *et al.*, ILL Annual Report (Grenoble, 1999), p. 59.
3. F. Goennenwein, private communication.
4. R. Blin-Stoyle, *Fundamental Interactions and the Nuclei* (North-Holland, Amsterdam, 1973).
5. V. E. Bunakov and L. B. Pikelner, Prog. Part. Nucl. Phys. **39**, 337 (1997).
6. A. Bohr and B. Mottelson, *Nuclear Structure* (Benjamin, New York, 1969), Vol. 1.
7. V. Rubchenya and S. Yavshits, Z. Phys. A **329**, 217 (1988).
8. A. L. Barabanov and D. P. Grechukhin, Yad. Fiz. **47**, 648 (1988) [Sov. J. Nucl. Phys. **47**, 411 (1988)].
9. P. Heeg, M. Mutterer, M. Panicke, *et al.*, in *Proceedings of the Conference on 50 Years with Nuclear Fission, Gaithersburg, 1989* (American Nuclear Society, La Grange Park, 1989), Vol. 1, p. 299.
10. A. Popov, private communications.

Physics of Atomic Nuclei, Vol. 65, No. 4, 2002, pp. 621–627. From Yadernaya Fizika, Vol. 65, No. 4, 2002, pp. 653–659.

Influence of a Continuum on Cluster-Decay Processes*

D. S. Delion** **and J. Suhonen**[1)]

National Institute of Physics and Nuclear Engineering, Bucharest-Măgurele, Romania

Received August 31, 2001

Abstract—A microscopic approach to cluster decay including single-particle states in a continuum is given. The equations of motion describing cluster-like states are derived within the multistep shell-model approach. The lowest collective two-particle eigenmodes are used as building blocks for α-like states. Good agreement with low-lying states in ^{212}Po is obtained. The spectroscopic factor for the α decay between ground states is reproduced. It is shown that only by including the continuum part of the single-particle spectrum is the decay width for α- and cluster-decay processes reproduced. The α-like structure of the lowest states in ^{212}Po is analyzed, and strong high-lying resonances are predicted.

1. INTRODUCTION

Although the first study in theoretical nuclear physics was devoted to α decay and provided a nice explanation in terms of the Coulomb barrier penetration of a preformed α particle [1], a microscopic description of cluster formation at the nuclear surface is still an open problem. The usual shell-model configuration space used in estimating the cluster probability is not able to reproduce the absolute value of the half-life for the transition between ground states (g.s.) [2]. This deficiency is connected with the asymptotic exponential decrease of single-particle (s.p.) wave functions for bound states [3]. The problem of considering the continuum part of the spectrum in microscopic calculations is rather involved, but it is very important, especially for drip-line nuclei [4]. An attempt at reproducing half-lives would be the inclusion of s.p. narrow resonances lying in a continuum [5–7], so-called Gamow states. Although the true asymptotic behavior of the wave functions is achieved, the value of the half-life has not yet been reproduced. We will show that the inclusion of the background components is able to reproduce the total decay width because an important part of the clustering process proceeds through such states. To this aim, we use, for the diagonalization of the Woods–Saxon s.p. mean field, a harmonic-oscillator (h.o.) basis with two constants, which is very suitable for treating states in a continuum together with the discrete part of the spectrum.

Narrow s.p. Gamow resonances can become a useful tool for analyzing high-lying α-like four-particle states that were observed long ago as resonances in α-particle anomalous large-angle scattering (ALAS) and which are associated with so-called "quasimolecular states." Such states were mainly observed and analyzed in α scattering on light nuclei like ^{16}O [8], ^{40}Ca [9], or ^{28}Si [10], but it is also interesting to look for such states in heavy nuclei such as ^{208}Pb [11]. We will show that such resonances can indeed be built on top of Gamow s.p. resonances and that they have a structure similar to that of low-lying α-decaying states. As an example, we chose the ^{212}Po nucleus, which exhibits a nice α-like structure on top of the doubly magic nucleus ^{208}Pb.

2. THEORETICAL BACKGROUND

The cluster-decay rate for the process $B \to A + C$ connecting two spherical nuclei is given by the standard quantum-mechanical prescription

$$\Gamma \equiv \sum_l \Gamma_l = \lim_{r\to\infty} \hbar v \sum_l |g_l(r)|^2, \qquad (2.1)$$

where v is the relative velocity of the emitted cluster C and the daughter nucleus A and $g_l(r)$ is the lth component of the wave function describing their relative motion in some spherical potential according to the Schrödinger equation

$$\left[-\frac{\hbar^2}{2\mu}\frac{d^2}{dr^2} + \frac{\hbar^2 l(l+1)}{2\mu r^2}\right] g_l(r) + V(r) g_l(r) = E_C g_l(r). \qquad (2.2)$$

*This article was submitted by the authors in English.

[1)]Department of Physics, University of Jyväskylä, Finland.

**e-mail: delion@theor1.theory.nipne.ro

1063-7788/02/6504-0621$22.00

Table 1. Low-lying energies in ^{212}Po (in MeV) for various thresholds of the metric-matrix eigenvalues (in parentheses)

$J^\pi_{a_4}$	$E_{\rm exp}$ [23]	$E(0.05)$	$E(0.2)$	$E(0.5)$
0^+_1	0.000	0.000	0.000	0.000
2^+_1	0.727	0.949	0.952	0.952
4^+_1	1.132	1.087	1.090	1.081
6^+_1	1.355	1.081	1.144	1.135
8^+_1	1.476	1.131	1.174	1.166
2^+_2	1.513	1.203	1.203	2.398
1^+_1	1.621	1.907	1.909	1.901
2^+_3	1.679	1.783	1.995	2.423
0^+_2	1.801	2.080	2.091	2.081
2^+_4	1.806	2.248	2.253	2.607

This set of equations can be integrated by proceeding from large distances, where each component is a spherical outgoing Coulomb wave:

$$\lim_{r\to\infty}[g_l(r)] = C_l[G_l(r) + iF_l(r)]. \qquad (2.3)$$

Narrow resonances have a very small imaginary part of the cluster energy E_C, and the regular Coulomb functions $F_l(r)$ have vanishing values inside the barrier; therefore, the constants C_l are virtually real-valued. These values are determined by matching the outgoing solution to the Schrödinger equation with the internal solution at some radius R,

$$g_l(R)/R = \mathcal{F}_l(R), \qquad (2.4)$$

where

$$\mathcal{F}_l(R) = \int [\Psi_C(\xi_C)\Psi_A(\xi_A)Y_l(\hat{R})]^* \times \Psi_B(\xi_B)d\xi_C d\xi_A d\hat{R} \qquad (2.5)$$

is the microscopic cluster-formation amplitude. Here, the notation is standard—in particular, ξ are internal coordinates. From (2.4), one thus obtains

$$\Gamma_l = \hbar v\left[\frac{R}{G_l(R)}\right]^2 |\mathcal{F}_l(R)|^2 \equiv P_l F_l. \qquad (2.6)$$

This quantity is the product of two functions strongly depending on the matching radius R, but it should be a constant with respect to this radius. Therefore, the internal and external wave functions should also have the same logarithmic derivatives $f_l(R) \equiv g'_l(R)/g_l(R) = G'_l(R)/G_l(R)$, and this is just the condition for a resonance state in a potential $V(r)$.

The modulus squared of the formation amplitude $\mathcal{F}_l$ in (2.5) has the meaning of the cluster probability inside the parent wave function. In order to evaluate the overlap integral (2.5), the wave function for the parent nucleus Ψ_B should be expanded in terms of the same building blocks as the cluster internal wave function Ψ_C. For intance, the α-particle wave function is the product of the proton–proton (pp) and neutron–neutron (nn) h.o. functions [12]. Therefore, the parent wave function is a superposition of the products of the two-body components and the daugther wave function taken as a vacuum,

$$|\Psi_B\rangle \equiv P^\dagger_{\alpha_4}|0\rangle = \sum_{\alpha_2\beta_2} X(\alpha_2\beta_2;\alpha_4)(P^\dagger_{\alpha_2}P^\dagger_{\beta_2})_{\alpha_4}|0\rangle, \qquad (2.7)$$

where the index has the meaning of the angular momentum, parity, eigenvalue, and isospin projection: $\alpha_k \equiv (J^\pi_{a_k}, \tau)$, $k = 2, 4$. Summation contains pp–nn ($\tau, \tau' = +1, -1$) and pn–pn ($\tau, \tau' = 0, 0$) terms. For instance, ^{212}Po is a typical example of the α-like structure built on top of the doubly magic nucleus ^{208}Pb. For the core state $|0\rangle = |^{208}\rangle$Pb, these two kinds of terms correspond to the couplings $(^{210}\mathrm{Po}\otimes{}^{210}\mathrm{Pb})_{\alpha_4}$ and $(^{210}\mathrm{Bi}\otimes{}^{210}\mathrm{Bi})_{\alpha_4}$, respectively.

The microscopic treatment of ^{212}Po is given in [13], where the equations of motion were written by using a representation that is equivalent to (2.7). This procedure is related to the multistep shell-model (MSM) procedure [14–16]. Using the TDA equations of motion for the two-particle and four-particle systems, respectively,

$$[H, P^\dagger_{\alpha_2}] = E_{\alpha_2}P^\dagger_{\alpha_2}, \quad [H, P^\dagger_{\alpha_4}] = E_{\alpha_4}P^\dagger_{\alpha_4}, \qquad (2.8)$$

one obtains, by using a symmetrized double commutator, the set of equations

$$\sum_{\alpha'_2\beta'_2} H(\alpha_2\beta_2;\alpha'_2\beta'_2)X(\alpha'_2\beta'_2;\alpha_4) = E_{\alpha_4}\sum_{\alpha'_2\beta'_2} I(\alpha_2\beta_2;\alpha'_2\beta'_2)X(\alpha'_2\beta'_2;\alpha_4), \qquad (2.9)$$

where the metric and Hamiltonian matrices are given by the following overlap integrals:

$$I(\alpha_2\beta_2;\alpha'_2\beta'_2) \equiv \langle 0|(P_{\beta_2}P_{\alpha_2})_{\alpha_4}(P^\dagger_{\alpha'_2}P^\dagger_{\beta'_2})_{\alpha_4}|0\rangle,$$

$$H(\alpha_2\beta_2;\alpha'_2\beta'_2) \equiv \frac{1}{2}\langle 0|[(P_{\beta_2}P_{\alpha_2})_{\alpha_4}, H, (P^\dagger_{\alpha'_2}P^\dagger_{\beta'_2})_{\alpha_4}]|0\rangle = \frac{1}{2}(E_{\alpha_2} + E_{\beta_2} + E_{\alpha'_2} + E_{\beta'_2})I(\alpha_2\beta_2;\alpha'_2\beta'_2). \qquad (2.10)$$

In this way, the interaction is involved only in the first, two-particle step. In the second, four-particle step, only two-particle energies appear in the equation of

Table 2. Quartet structure of low-lying α-like states in terms of two-particle pairs (second column) (the amplitude is given in the third column; given are also the spectroscopic factors of the pp–nn (the fourth column) and pn–pn (the fifth column) four-particle terms in the quartet operator defined by Eq. (27); given in the sixth and seventh columns are the hindrance factors of the $J^{\pi}_{a_4}$ states)

$J^{\pi}_{a_4}$	$J(pp), J(nn)$	X	S_1	S_2	HF_1	HF_2
0^+_1	$0^+_1(pp), 0^+_1(nn)$	1.084	1.19(−2)	8.49(−7)	1.00	1.00
2^+_1	$0^+_1(pp), 2^+_1(nn)$	1.091	1.38(−3)	5.16(−8)	0.12	0.06
4^+_1	$0^+_1(pp), 4^+_1(nn)$	1.092	7.49(−4)	1.39(−9)	0.07	0.00
6^+_1	$0^+_1(pp), 6^+_1(nn)$	1.092	4.44(−4)	1.02(−8)	0.04	0.01
8^+_1	$0^+_1(pp), 8^+_1(nn)$	1.092	3.33(−4)	5.36(−9)	0.02	0.00
2^+_2	$2^+_1(pp), 0^+_1(nn)$	1.092	1.54(−3)	6.44(−8)	0.04	0.73

motion. The set of Eqs. (2.9) can be solved by using the eigenstates of the metric matrix [17] as an orthonormalized basis.

In order to analyze the emission of heavier clusters like ^{10}Be, ^{14}C, or ^{16}O, one can extend the MSM technique to a chain of calculations by using, in the next steps, together with pairs, α clusters as new building blocks [18, 19]:

$$P^{\dagger}_{\alpha_N}|0\rangle = \sum_{\alpha_m\beta_n} X(\alpha_m\beta_n;\alpha_N)(P^{\dagger}_{\alpha_m}P^{\dagger}_{\beta_n})_{\alpha_N}|0\rangle, \qquad (2.11)$$

$$N = m + n.$$

3. NUMERICAL APPLICATION FOR ^{212}Po $\rightarrow$ ^{208}Pb + α

The s.p. spectrum is obtained by integrating the Schrödinger equation for the Woods–Saxon (WS) potential with a universal parametrization [20]. First, we have computed bound states and resonances in a continuum using the "Gamow" code [21]. Two-particle states were treated by using the surface delta interaction [22]. The calculated spectrum is in good agreement with experimental data [17]. The result of the calculation for four-body states is given in Table 1, which also displays the experimental energies in the second column. Given in the next three columns are the eigenvalue computed by solving Eq. (2.9). They correspond to different minimal accepted eigenvalues $D_{\min}$ of the metric matrix written in parentheses. Although only the lowest two-particle states were included in calculation, the agreement with the experimental low-lying part of the spectrum is quite satisfactory, somewhere between that in [13] and that in [24].

Table 2 (second column) presents the structure of the four-particle states in terms of the most important two-particle pairs. One can see that the first six low-lying states have practically one major component. It is important to stress the fact that the low-

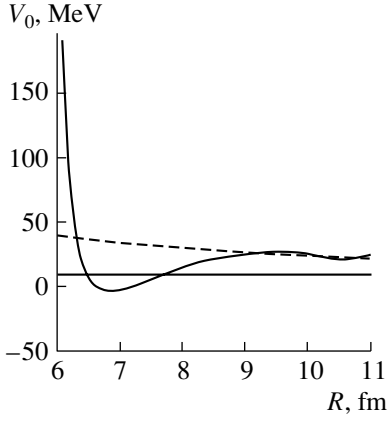

Fig. 1. Local equivalent potential computed by using the formation amplitude as a wave function. The dashed curve represents the α–daughter Coulomb potential. The horizontal solid line shows the energy of the emitted α particle.

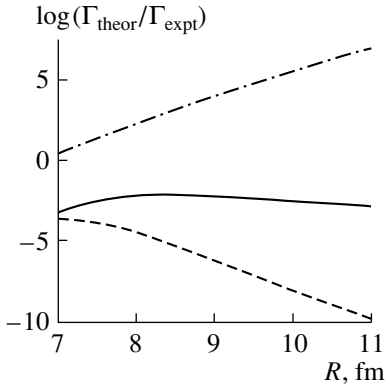

Fig. 2. Quantities $\log(\Gamma_{\text{theor}}/\Gamma_{\text{expt}})$ (solid curve), $\log(F_0)$ (dashed curve), and $\log(P_0/\Gamma_{\text{expt}})$ (dash-dotted curve) versus the distance R between the center of mass of the α particle and the daughter nucleus ^{208}Pb.

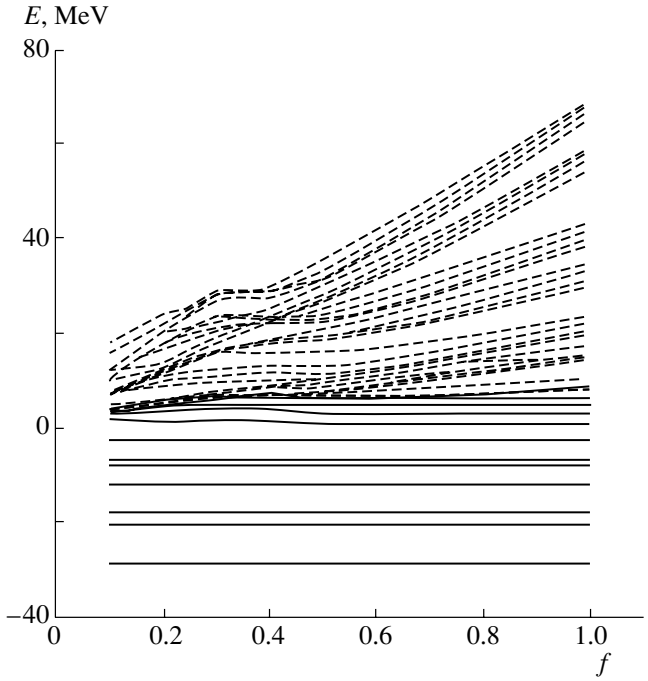

Fig. 3. Some single-particle levels versus the ratio $f \equiv \lambda_2/\lambda_1$ of the h.o. parameters.

est monopole two-particle components $0_1^+(pp)$ and $0_1^+(nn)$, entering into the four-particle wave function, are the only ones having, in their structure, Gamow resonances in a continuum [17].

It is of interest to see which would be the equivalent local potential if one considers the α-particle-formation amplitude as a wave function satisfying the Schrödinger equation (2.2). In Fig. 1, we depict this equivalent potential for $l = 0$ (solid curve). One can clearly see the molecular shape of this local equivalent potential. This kind of local potential was used as a phenomenological interaction to reproduce quasimolecular resonances in the α-particle-scattering data [10]. The dashed curve represents the pure Coulomb potential between the daughter and the α particle. The Coulomb barrier at this point is around 25 MeV. The horizontal solid line denotes the energy of the emitted α particle, $E_\alpha = 8.95$ MeV.

The integral of the formation probability F_l defines the so-called spectroscopic factor (SF) S_i. Given in the fourth and fifth columns of Table 2 are the SF for the pp–nn ($i = 1$) and pn–pn ($i = 2$) four-particle components of the wave function (2.7). One can observe that the total g.s.-to-g.s. SF has the right order of magnitude [25]. The so-called hindrance factors HF_i are given in the sixth and seventh columns. They are defined as a mean value on the interval (8–10) fm of the ratio of the formation probabilities corresponding to some eigenstate and the g.s. The states given in Table 2 have $HF_1 > 0.01$.

In the region of the geometric-touching radius $R_{\text{c.m.}} = 9$ fm, the decay width, as can be seen from Fig. 2 (solid curve), is virtually constant, proving the validity of our calculation. According to Eq. (2.6), the decay width is the product of two terms that have behave oppositely: the formation probability F_0 (dashed curve in Fig. 2) decreases, while the penetrability P_0 (dash-dotted curve in Fig. 2) increases. It is important to observe from the same figure that the decay width is underestimated by two orders of magnitude. This means that the inclusion of narrow Gamow resonances is not sufficient for reproducing the absolute value of the decay width. The role of the "background" is also very important, because the probability of an α-cluster formation at the nuclear surface is proportional to the density of the s.p. components in the continuum. This can be achieved by using a mixed nonorthogonal h.o. basis in the diagonalization procedure, whereby the number of shells needed in the expansion is reduced and, whereby, at the same time, a better description of the decay process is obtained. For this purpose, we represented the radial s.p. wave functions as [26]

$$u_l(r) = \sum_{2n_1+l=N_1\le N_0} c_{n_1 l}^{(1)} \mathcal{R}_{n_1 l}^{(\lambda_1)}(r) + \sum_{2n_2+l=N_2>N_0} c_{n_2 l}^{(2)} \mathcal{R}_{n_2 l}^{(\lambda_2)}(r), \qquad (3.1)$$

where λ_1 is the h.o. parameter coresponding to the h.o. potential that fits the WS interaction in the region

Table 3. High-lying monopole ($0^+_{a_4}$) states with a large hindrance factor for the $pp-nn$ channel (HF_1, last column)[the spectroscopic factor of the pp–nn quartet operator (2.7) is given in the fifth column].

a_4	E, MeV	$J(pp), J(nn)$	X	S_1	HF_1
141	6.332	$0^+_4(pp), 0^+_1(nn)$	−0.667	1.34(−03)	14.33
		$0^+_3(pp), 0^+_2(nn)$	0.242		
		$0^+_1(pp), 0^+_6(nn)$	0.614		
316	12.181	$0^+_1(pp), 0^+_8(nn)$	1.063	1.34(−03)	14.33
		$0^+_2(pp), 0^+_8(nn)$	−0.366		
356	14.494	$0^+_7(pp), 0^+_1(nn)$	1.036	2.66(−03)	1.48
383	16.541	$0^+_3(pp), 0^+_8(nn)$	−1.030	1.43(−04)	2.93
		$0^+_2(pp), 0^+_8(nn)$	−0.136		
438	19.338	$0^+_4(pp), 0^+_8(nn)$	1.002	6.88(−04)	7.89
458	20.396	$0^+_7(pp), 0^+_5(nn)$	−0.987	6.44(−04)	1.70
472	21.662	$0^+_7(pp), 0^+_6(nn)$	1.001	1.02(−03)	1.09
475	21.979	$0^+_7(pp), 0^+_7(nn)$	1.002	2.84(−04)	1.28
476	22.100	$0^+_6(pp), 0^+_8(nn)$	1.000	2.05(−04)	2.70
507	27.486	$0^+_7(pp), 0^+_8(nn)$	1.001	7.09(−04)	21.98
510	31.499	$0^+_8(pp), 0^+_8(nn)$	1.000	8.97(−05)	4.28

Table 4. As in Table 3, but for $2^+_{a_4}$ states

a_4	E, MeV	$J(pp), J(nn)$	X	S_1	HF_1
171	4.334	$2^+_{11}(pp), 0^+_8(nn)$	1.033	0.54(−04)	1.48
		$2^+_{11}(pp), 2^+_{19}(nn)$	−0.114		
409	11.034	$0^+_7(pp), 2^+_{19}(nn)$	1.009	0.18(−03)	5.08
432	12.020	$2^+_{16}(pp), 0^+_8(nn)$	0.812	0.18(−03)	5.08
		$2^+_{16}(pp), 2^+_{19}(nn)$	0.589		
485	18.087	$0^+_{11}(pp), 2^+_{19}(nn)$	1.000	0.35(−03)	13.32
487	18.585	$0^+_{11}(pp), 2^+_{21}(nn)$	1.000	0.20(−03)	1.28

of the discrete spectrum, while λ_2 corresponds to an h.o. potential that describes better the continuum part of the spectrum. Figure 3 shows some s.p. levels versus the ratio $f \equiv \lambda_2/\lambda_1$. One can see that the bound states and narrow resonances have relatively stable positions, while the density of other states in a continuum becomes higher with decreasing f. In this way, one obtains a quasicontinuum description of the background. The optimal value of the parameter f is taken in such a way as to obtain the right value of the total decay width (2.6) by using a minimal amount of major shells. Figure 4 shows that, if one considers only $N_0 = 6$ major shells, the total decay width is not reproduced (dash-dotted curve). The same happens if one takes $N = 9$ shells with $f = 1$ (dashed curve), while, in the case of $f = 0.2$ (solid curve) for the last three shells, one obtains nearly a plateau beyond the geometric-touching point, reproducing the experimental value.

As was indicated above, narrow s.p. Gamow resonances play an important role in some low-lying states that have a strong overlap with the α-particle wave function and which are called α-like states. They should also play an important role in some high-lying states seen as resonances in the scattering of α particles on the daughter nucleus, especially above the Coulomb barrier. Table 3 presents the monopole α-like four-particle states having $HF_1 > 1$ (last col-

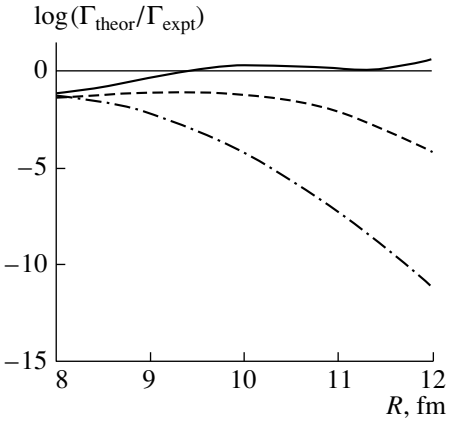

Fig. 4. Total decay width if one considers $N_0 = 6$ major shells (dash-dotted curve), $N = 9$ shells with $f = 1$ (dashed curve) and $f = 0.2$ (solid curve) for the last three shells.

umn). States above the barrier have energies greater than $16(= 25 - 9)$ MeV. The excitation energies are relative to the g.s. energy in ^{212}Po.

To obtain such high-lying states, we performed a diagonalization by considering the two-particle states with energies less than 20 MeV and $J = 0$, ..., 4. Despite a very large number of eigenstates, only very few have large overlaps with the α-particle wave function, i.e., large values of HF_1 and spectroscopic factors. All these states contain at least one of the states involving Gamow resonances in their structure, as can be seen from the third column of Table 3. High-lying α-like quadrupole states are given in Table 4. As in the preceding case, these states have two-particle monopole components carrying Gamow resonances and only two of them are above the Coulomb barrier.

4. CONCLUSION

We have analyzed the influence of states in a continuum on cluster-decay processes. As an example containing basic ideas, we have considered the α decay of ^{212}Po. We have used the MSM technique to describe α-like structures in terms of two-body states as main building blocks. This is a very appropriate procedure to be extended in a straightforward way to the emission of heavier clusters. In order to construct the two-particle pp, nn, and pn states in ^{210}Po, Pb, and Bi nuclei, we have first considered, in the s.p. spectrum, only bound states and narrow Gamow resonances in a continuum. As a residual two-body potential, we have used a surface delta interaction. It is very satisfactory that low-lying states in ^{212}Po can be reproduced by using only the lowest two-particle eigenstates of these three nuclei as building blocks. Spurious components with small eigenvalues of the metric matrix were eliminated in order to take into account the Pauli exclusion principle. We have analyzed the α-cluster content of the wave function for all four-particle eigenstates. We have found that the first lowest states have an α-particle-formation amplitude commensurate with that of the g.s. and called them α-like states. We have also found some high-lying monopole and quadrupole eigenstates strongly overlapping with the α-cluster wave function. All of them have, in their structure, monopole two-particle states of pp or nn type, with important Gamow resonance components. States above the Coulomb barrier should be observed as resonances in α-particle scattering on ^{208}Pb. Moreover, the equivalent local potential derived by evaluating the α-particle-formation amplitude for the transition between the ground states and interpreted as a wave function satisfying the Schrödinger equation has a "pocket" molecular shape. Similar potentials were used in calculations reproducing resonances in the elastic scattering of α particles. The majority of such resonances were observed in light nuclei around Ca; therefore, our future purpose is to extend the multistep shell-model calculation to this region.

It turned out that the spectroscopic factor of the pp–nn component is much greater than that of the pn–pn component owing to the difference in the proton and neutron single-particle structures. In addition, the pp–nn component has a right order of magnitude. If one considers only bound and resonance s.p. states, the absolute value of the g.s.-to-g.s. decay width is underestimated by two orders of magnitude. The inclusion of the background components by using a very efficient quasicontinuum representation, in terms of an h.o. basis with two constants, corrects for this deficiency.

REFERENCES

1. G. Gamow, Z. Phys. **51**, 204 (1928).
2. I. Tonozuka and A. Arima, Nucl. Phys. A **323**, 45 (1979).
3. T. Fliessbach and S. Okabe, Z. Phys. A **320**, 289 (1985).
4. J. Dobaczewski, W. Nazarewicz, T. R. Werner, *et al.*, Phys. Rev. C **53**, 2809 (1996).
5. F. A. Janouch and R. J. Liotta, Phys. Rev. C **27**, 896 (1983).
6. G. Dodig-Crnkovic, F. A. Janouch, R. J. Liotta, *et al.*, Phys. Scr. **37**, 523 (1988).
7. S. M. Lenzi, O. Dragun, E. E. Maqueda, *et al.*, Phys. Rev. C **48**, 1463 (1993).
8. P.-H. Heenen, Nucl. Phys. A **272**, 399 (1976).
9. N. Takigawa and S. Y. Lee, Nucl. Phys. A **292**, 173 (1977).
10. P. Manngård, PhD Thesis (Åbo Akademi, Åbo, 1996).
11. A. R. Barnett and J. S. Lilley, Phys. Rev. C **9**, 2010 (1974).

12. H. J. Mang, Annu. Rev. Nucl. Sci. **14**, 1 (1964).
13. P. Schuck, R. Wittman, and P. Ring, Lett. Nuovo Cimento **17**, 107 (1976).
14. R. J. Liotta and C. Pomar, Nucl. Phys. A **362**, 137 (1981); **382**, 1 (1982).
15. G. Dodig-Crnkovic, F. A. Janouch, R. J. Liotta, *et al.*, Nucl. Phys. A **444**, 419 (1985).
16. G. Dodig-Crnkovic, F. A. Janouch, and R. J. Liotta, Nucl. Phys. A **501**, 533 (1989).
17. D. S. Delion and J. Suhonen, Phys. Rev. C **61**, 024304 (2000).
18. D. S. Delion, A. Insolia, and R. J. Liotta, Phys. Rev. Lett. **78**, 4549 (1997).
19. R. G. Lovas, R. J. Liotta, A. Insolia, *et al.*, Phys. Rep. **294**, 265 (1998).
20. J. Dudek, Z. Szymanski, and T. Werner, Phys. Rev. C **23**, 920 (1981).
21. T. Vertse, K. F. Pal, and Z. Balogh, Comput. Phys. Commun. **27**, 309 (1982).
22. P. J. Brussaard and P. W. M. Glaudemans, *Shell-Model Applications in Nuclear Spectroscopy* (North-Holland, Amsterdam, 1977).
23. R. B. Firestone, V. S. Shirley, S. Y. F. Chu, *et al.*, *Table of Isotopes* (Wiley-Interscience, New York, 1996), CD-ROM, 8th ed., Version 1.0.
24. D. Strottman, Phys. Rev. C **20**, 1150 (1979).
25. R. Blendowske, T. Fliessbach, and H. Walliser, Nucl. Phys. A **464**, 75 (1987).
26. D. S. Delion, A. Insolia, and R. J. Liotta, Phys. Rev. C **54** 292, (1996).

Physics of Atomic Nuclei, Vol. 65, No. 4, 2002, pp. 628–629. From Yadernaya Fizika, Vol. 65, No. 4, 2002, pp. 660–661.

Pionic Fusion Study of the Halo Nucleus ^{6}He, the Reaction $d + {}^4\mathrm{He} \rightarrow {}^6\mathrm{He} + \pi^+$ at CELSIUS*

M. Andersson, Chr. Bargholtz, Kj. Fransson, E. Fumero, L. Gerén, L. Holmberg, K. Lindh, L. Mårtensson, I. Sitnikova, P.-E. Tegnér, G. Weiss, and K. Wilhelmsen Rolander**

Department of Physics, Stockholm University, Sweden

Received August 31, 2001

Abstract—The halo nucleus ^{6}He has been studied in a pionic fusion experiment at the CELSIUS storage ring facility in Uppsala. The ^{6}He nuclei were produced in reactions with a deuteron beam incident on a ^{4}He jet target 0.9–5.4 MeV above threshold in the center-of-mass frame. The ^{6}He ions were detected in a ΔE–E solid-state detector telescope inserted into the CELSIUS ring. The aim of the experiment was to investigate, in particular, the high-momentum part of the halo wave function by measuring the total and differential cross sections of the reaction $d + {}^4\mathrm{He} \rightarrow {}^6\mathrm{He} + \pi^+$. © *2002 MAIK "Nauka/Interperiodica".*

The nuclide ^{6}He is the simplest two-neutron halo nucleus. Most experiments on ^{6}He so far have concentrated on the low-momentum part of the halo wave function [1–3]. The high-momentum part of the wave function is less well known. The aim of this experiment was to investigate the high-momentum part of the wave function by producing ^{6}He, in its ground state, in the pionic fusion reaction $d + {}^4\mathrm{He} \rightarrow {}^6\mathrm{He} + \pi^+$, close to threshold. A measurement very close to threshold has the advantage that only low-angular momenta contribute to the reaction. Results of theoretical estimates have shown high sensitivity to both the reaction mechanism and different models of ^{6}He. The isobaric analog state of the ground state of ^{6}He at 3.56 MeV excitation energy in ^{6}Li has been studied in an earlier pionic fusion experiment [4]. The results from this measurement reflect a sensitivity to the structure of the halo.

The experiment was done at the CELSIUS accelerator and storage ring at The Svedberg Laboratory in Uppsala. The electron-cooled circulating ion beam, in combination with thin internal targets, ensures small momentum spread and high luminosity. This makes it ideally suited for studies of nuclear reactions close to threshold.

In this experiment a deuteron beam was used together with a ^{4}He gas-jet target with a nominal thickness of 1.6×10^{14} atom/cm^2. The measurements were done at three different beam energies, 217.7, 218.6, and 224.5 MeV, corresponding to $E_{\mathrm{c.m.}} = 0.9$, 1.5, and 5.4 MeV above threshold in the center-of-mass frame. The reaction products were detected in a zero-degree spectrometer [5]. The spectrometer uses the quadrupole and dipole magnets of the CELSIUS ring to focus the ^{6}He ions onto a charged-particle telescope inside the beam tube, 6.1 m downstream from the target. The radial position of the telescope is continuously adjustable in order to match the momenta of the reaction products. For these measurements, a transmission (ΔE) detector of 1.0 mm silicon and a stopping (E) detector of 1.7 mm high-purity germanium were used. The stopping detector is position-sensitive with its contacts divided into 18 horizontal strips of 2-mm width on one side and 66 vertical, 1-mm-wide strips on the other side. From the position and energy information, the emission angle can be deduced.

Very close to threshold heavy-reaction products

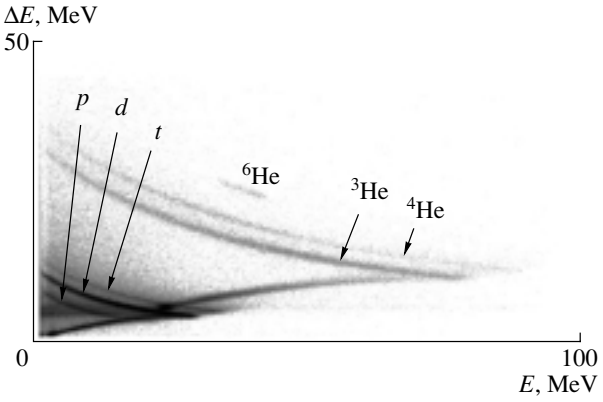

ΔE–E spectrum recorded at 217.7 MeV beam energy. Different ions are identified.

*This article was submitted by the authors in English.

**e-mail: geren@physto.se

carry most of the beam momentum and therefore travel close to the beam. Hence forward and backward scattered ions in the center of mass are simultaneously detected in the telescope. Simulations assuming an isotropic angular distribution of ^{6}He show an acceptance of 60% at a beam energy of 217.7 MeV and 30% at a beam energy of 218.6 MeV.

The energy deposited in each detector was summed to obtain the full energy of the ^{6}He ions. A $\Delta E{-}E$ spectrum recorded at 217.7 MeV energy is shown in the figure. The ^{6}He events are well separated from all other charged particles. A similar spectrum recorded at a beam energy below the absolute threshold for the reaction will be used to further reduce the background.

Preliminary results from the reaction $d + {}^4\mathrm{He} \rightarrow {}^6\mathrm{He} + \pi^+$ show an anisotropic angular distribution of ^{6}He with a larger forward than backward peak. This would indicate that the pion is emitted preferentially in the direction of the heavier particle in the initial system. A similar asymmetry was found for the analog reaction $\alpha + d \rightarrow {}^6\mathrm{Li}^* + \pi^0$ [4]. However, preliminary results seem to indicate that the cross section for the $d + {}^4\mathrm{He} \rightarrow {}^6\mathrm{He} + \pi^+$ reaction increases with energy, whereas for the analog reaction the total cross section decreased with about 40% over 0.7 MeV.

ACKNOWLEDGMENTS

The authors are greatly indebted to the CELSIUS group for providing excellent experimental conditions for this experiment. We wish to thank Davor Protic and the personnel at the detector laboratory in Jülich for manufacturing the germanium detector. This work was supported in part by the Swedish Natural Science Research Council.

REFERENCES

1. M. J. G. Borge *et al.*, Nucl. Phys. A **560**, 664 (1993).
2. T. Aumann *et al.*, Phys. Rev. C **59**, 1252 (1999).
3. A. A. Korsheninnikov *et al.*, Nucl. Phys. A **617**, 45 (1997).
4. M. Andersson *et al.*, Phys. Lett. B **481**, 165 (2000).
5. Chr. Bargholtz *et al.*, Nucl. Instrum. Methods Phys. Res. A **390**, 160 (1997).

Physics of Atomic Nuclei, Vol. 65, No. 4, 2002, pp. 630–636. From Yadernaya Fizika, Vol. 65, No. 4, 2002, pp. 662–668.

Angular Correlations in Ternary Fission Induced by Polarized Neutrons*

P. Jesinger, A. Kötzle, F. Gönnenwein, M. Mutterer[1], J. von Kalben[1], G. V. Danilyan[2], V. S. Pavlov[2], G. A. Petrov[3], A. M. Gagarski[3], W. H. Trzaska[4], S. M. Soloviev[5], V. V. Nesvizhevski[6], and O. Zimmer[6]**

Physikaliches Institut, Tübingen, Germany

Received August 31, 2001

Abstract—Ternary fission induced by cold polarized neutrons was studied for the two isotopes ^{233}U and ^{235}U at the Institut Laue–Langevin in Grenoble, France. In particular two types of angular correlations between the spin of the incoming neutrons and the emission directions of both, the fission fragments (FF) and the ternary particles (TP), were investigated. For FF and TP detectors facing the target at right angles to the neutron beam, first, for longitudinally polarized neutrons a triple correlation between spin and the emission of outgoing particles was explored and, second, for transversally polarized neutrons parity violating asymmetries in the emission of FFs and TPs were analyzed. Nonzero expectation values for the triple correlation were oberserved in the present experiments for the first time. © *2002 MAIK "Nauka/Interperiodica".*

1. INTRODUCTION

With the discovery of parity nonconserving (PNC) asymmetries in the angular distributions of fission fragments (FF) for reactions induced by polarized neutrons, it was demonstrated that, surprisingly, even in this complex nuclear reaction effects usually traced to the weak interaction can be unraveled [1]. PNC effects could further be shown to be a useful tool to explore the mechanism of more complicated phenomena like ternary fission just by comparing the sizes of angular asymmetries of fragments for ternary and binary fission [2, 3]. In ternary fission, besides the two familiar fission fragments, an additional light-charged particle appears which in 90% of all cases is an α particle. Evidently, in ternary fission new types of angular correlations between the emission directions of the outgoing particles and the spin direction of the neutrons being captured in fissile nuclei become observable. In fact, it was proposed more recently that ternary fission may even be an appropriate testing ground for time reversal invariance [4] (TRI). The correlation to be studied in fission is modeled on the correlation in the emission of electrons and antineutrinos in the decay of polarized neutrons which is investigated in the search for a violation of TRI.

The correlation at hand is a triple correlation between the direction of the spin of the neutron inducing fission and the directions of emission of one of the FFs (conventionally the light fragment, LF) and the ternary particles (TP). The observable to be measured reads

$$B = \hat{\boldsymbol{\sigma}} \cdot [\hat{\mathbf{p}}_{\mathrm{LF}} \times \hat{\mathbf{p}}_{\mathrm{TP}}]\,. \qquad (1)$$

In Eq. (1) $\hat{\boldsymbol{\sigma}}$ is the spin vector of the neutron, while $\hat{\mathbf{p}}_{\mathrm{LF}}$ and $\hat{\mathbf{p}}_{\mathrm{TP}}$ are the momenta of the light fragment and the ternary particle, respectively, all vectors being unit vectors. Formally the observable B violates TRI. However, it has always been stressed by theory that, in general, a nonzero expectation value for an observable like B does not by itself prove a violation of TRI [5]. Instead, interactions between particles in the entrance or exit channel may mimic TRI. By contrast, experiments on parity violation do not suffer from this ambiguity. In fission PNC is observed for reactions with polarized neutrons as a nonvanishing expectation value for the observable

$$A_{\mathrm{LF}}^{\mathrm{PNC}} = \hat{\boldsymbol{\sigma}} \cdot \hat{\mathbf{p}}_{\mathrm{LF}}. \qquad (2)$$

The observable in Eq. (2) is a pseudoscalar signaling PNC in case a nonzero average value is observed. PNC according to Eq. (2) may be studied for both, binary, and ternary fission, where in the latter reaction simply the presence of a TP is requested.

*This article was submitted by the authors in English.

[1]Institut für Kernphysik, Darmstadt;
e-mail: mutterer@hrz1.tu-darmstadt.de
[2]ITEP, Moscow, Russia; e-mail: danilyan@vitep5.itep.ru
[3]PNPI, Gatchina, Russia;
e-mail: gpetrov@hep486.pnpi.spb.ru
[4]Accelerator Laboratory, Jyväskylä, Finland;
e-mail: trzaska@phys.jyu.fi
[5]Khlopin Radium Institute, St. Petersburg, Russia;
e-mail: soloviev@atom.nw.ru
[6]ILL, Grenoble, France; e-mail: nesvizh@ill.fr
**e-mail: goennenwein@uni-tuebingen.de

In experiments to be reported here the triple correlation B and the PNC observable $A_{\rm LF}^{\rm PNC}$ were investigated in ternary fission of U isotopes.

2. EXPERIMENTAL SETUP

The experiments on ternary fission were carried out for (n, f) reactions with ^{233}U and ^{235}U as targets and a neutron beam from the ILL reactor in Grenoble. The neutron beam was available at the exit of a curved neutron guide facing a cold neutron source. The spectrum of cold neutrons was rather broad with an average wavelength of 4.5 Å. With a supermirror polarizer the polarization achieved was $(95 \pm 1)\%$, and the flux density was 6×10^8 n/cm^2 s. The neutron beam was running horizontally. The target and the detectors for FFs and TPs facing the target were placed in a common plane oriented perpendicularly to the beam. The two main FFs were intercepted by two multiwire proportional counters (MWPC) mounted symmetrically on opposite sides of the beam on a common axis with the target. The timing signals from the MWPCs were used to derive the time-of-flight (TOF) difference between two correlated FFs. The TOF difference allows one to separate reasonably well light and heavy fragments. The TPs were detected by PIN diodes. Each PIN diode was 3×3 cm^2 in size, and 16 diodes were assembled to form an array. Two such arrays were positioned again on opposite sides of the beam and at right angles to the axis defined by the MWPCs and the target. This arrangement of detectors exploits the fact that the emission of TPs is roughly peaked at right angles relative to the fission axis established by the momenta of the two receding FFs. The diodes had to be protected from αs due to the radioactivity of the targets. Since αs from ternary fission have an average energy of about 16 MeV they are readily distinguished from the αs from target radioactivity. Some of the diodes were furthermore equipped for particle identification by analyzing the signal rise time [6]. A novel technique enabled a clear-cut separation of αs from H isotopes, the by far most abundant ternary particles.

With properly chosen magnetic guiding fields between the polarizer and the U target the spin of the neutron beam may be rotated in any direction wanted. For measuring the triple correlation of Eq. (1) the spin was oriented longitudinally along the beam. The observable B is thus close to ± 1, giving the experiment maximum sensitivity. For the PNC experiments, on the other hand, the neutron spin was turned perpendicularly to the beam and pointing towards the FF detectors. Now the observable $A_{\rm LF}^{\rm PNC}$ from Eq. (2) is close to ± 1 optimizing the detection of PNC asymmetries.

In both types of experiments the asymmetries are expected to be very small and giving rise to only small deviations from angular isotropy. Therefore, the two experiments for the triple correlation and the PNC asymmetry are evaluated, respectively, in terms of the two probability distributions

$$W(\hat{\mathbf{p}}_{\rm LF}, \hat{\mathbf{p}}_{\rm TP})\, d\Omega_{\rm LF} d\Omega_{\rm TP} \sim (1 + DB) P(\hat{\mathbf{p}}_{\rm LF}, \hat{\mathbf{p}}_{\rm TP})\, d\Omega_{\rm LF} d\Omega_{\rm TP}, \quad (3)$$

$$W(\theta, \varphi) d\Omega_{\rm LF} \sim \left(1 + \alpha_{\rm LF}^{\rm PNC} A_{\rm LF}^{\rm PNC}\right) d\Omega_{\rm LF}. \quad (4)$$

It should be stressed that in deriving Eq. (3) or (4) the spin vector $\hat{\boldsymbol{\sigma}}$ is kept fixed, either parallel or perpendicular to the beam direction, respectively. The factor $P(\hat{\mathbf{p}}_{\rm LF}, \hat{\mathbf{p}}_{\rm TP})$ in Eq. (3) takes into account the angular distribution of the TP relative to the direction of flight of the light FF. In Eq. (4) it has to be noted that the observable $A_{\rm LF}^{\rm PNC}$ is just equal to $\cos\theta$ with θ being the angle between the spin vector $\hat{\boldsymbol{\sigma}}$ and the fission axis $\hat{\mathbf{p}}_{\rm LF}$. The coefficients D and $\alpha_{\rm LF}^{\rm PNC}$ are taken to be constants measuring the size of the triple correlation and the PNC asymmetry, respectively. It can be shown that simple relations hold between these constants and the corresponding expectation values $\langle B \rangle$ and $\langle A_{\rm LF}^{\rm PNC} \rangle$ of the observables, namely,

$$\langle B \rangle \approx D/3 \quad \text{and} \quad \langle A_{\rm LF}^{\rm PNC} \rangle = \alpha_{\rm LF}^{\rm PNC}/3. \quad (5)$$

While taking the experimental data use was made of the spin flip technique. Every second the neutron spin was flipped by 180°. From the number of counts N_+ and N_- in the two spin positions the above constant asymmetry coefficients are obtained as the difference of counts normalized to the sum of counts, viz., $(N_+ - N_-)/(N_+ + N_-)$. The experimental setup allowed one to measure in parallel the coefficients for four independent combinations of detectors yielding four independent values for the coefficients. In addition data were taken for two settings of the guide fields inverting the spins at the target position and hence also the signs of the coefficients. The guide fields were inverted typically once per day. Thus a total of eight independent measurements is available for evaluation. Finally, it was checked that for a depolarized neutron beam the asymmetries indeed vanish within experimental uncertainty.

More details on the experiment and its evaluation may be found in a recent publication [7].

3. EXPERIMENTAL RESULTS

In the experiments on triple correlations in ternary fission unexpected effects were observed for both U isotopes studied. The correlation coefficients D as obtained from the raw data for α particles as TPs are shown in Figs. 1 and 2 for the isotopes ^{233}U and ^{235}U,

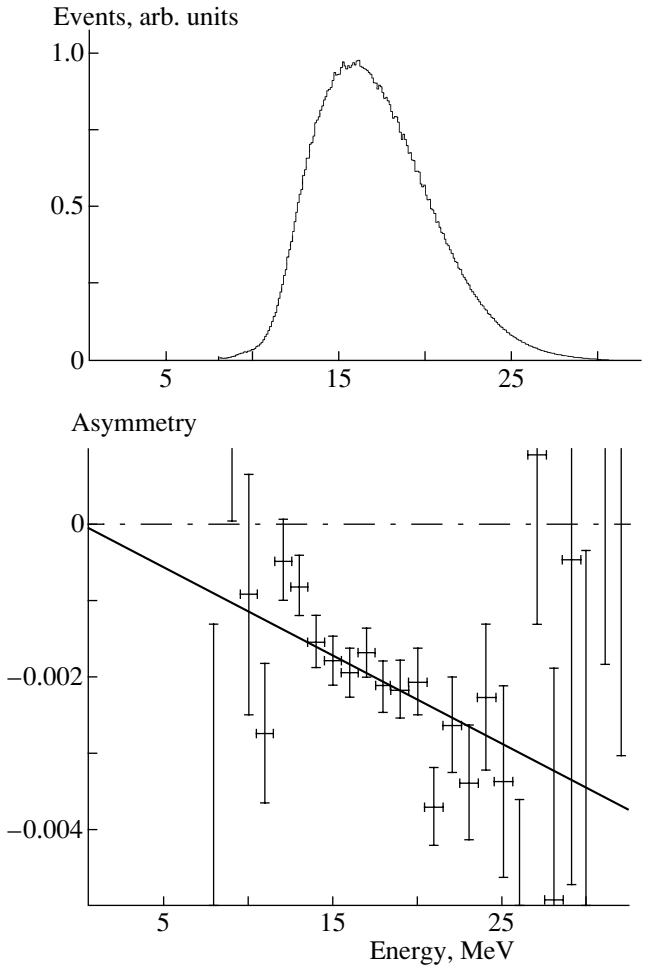

Fig. 1. ^{233}U target. Top panel: energy distribution of ternary α particles corrected for energy loss in absorber foil. Bottom panel: triple correlation coefficient D as a function of α energy. The straight line is a linear fit to the data.

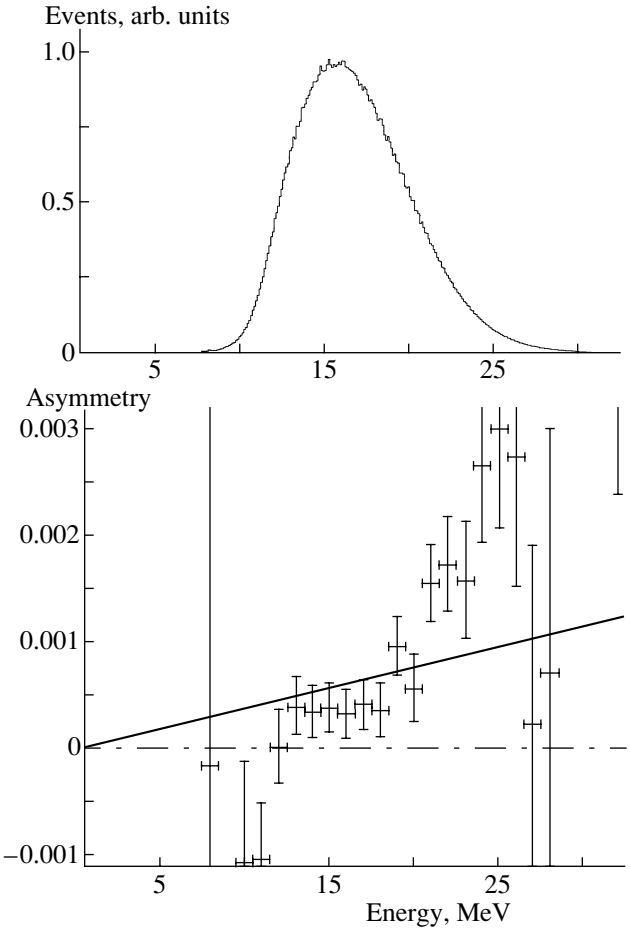

Fig. 2. ^{235}U target. Top panel: energy distribution of ternary α particles corrected for energy loss in absorber foil. Bottom panel: triple correlation coefficient D as a function of α energy. The straight line is a linear fit to the data.

respectively. The correlation coefficient D is plotted as a function of the α-particle energy in the bottom panels of the figures. For comparison the energy spectra of α particles measured in the present experiments are given in the top panels. The α detectors were calibrated with an ^{241}Am source, and the spectra were corrected for the energy loss in the Al foil protecting the PIN diodes. The spectra are well known in the literature to be to good approximation Gaussian in shape with average energies of 15.9 ± 0.2 MeV and with an FWHM of 10 ± 0.5 MeV for thermal neutron induced fission of all isotopes investigated so far [8]. The energy loss correction amounted up to almost 10 MeV and, as is evident from Figs. 1 and 2, the present spectra are severely truncated at lower α energies when compared to the actual spectra. These latter spectra extend down to α energy zero. About 25% of ternary αs are missed in the present setup.

Probably the most striking feature of the correlation depicted in Figs. 1 and 2 is the large size of D which comes close to $\pm 4 \times 10^{-3}$ at the upper limit of the α-energy spectrum. The different signs of the correlation for the two U isotopes under study is likewise noteworthy. Furthermore, the pronounced dependence of the correlation on the α-particle energy catches the eye. This strong energy dependence makes it impossible to find reproducible values for the energy-averaged correlation $\langle D \rangle$ from the raw data of different experiments with different low-energy cutoffs of α detection. Instead, the dependence of D on the full range of α energies has to be taken into account. To this purpose the shape of the function for the correlation D vs. α energy has to be known. The present experiments, unfortunately, do not allow one 4to uniquely determine the precise shape of this function. As a first approach a linear fit to the data has been chosen which is shown in Figs. 1 and 2.

Having discovered that the triple correlation coefficient D varies as a function of α-particle energy, the question arises whether a similar variation also obtains as a function of the angle of emission of the α particle relative to the fission axis. The granulated PIN diode arrays of the experiments to be reported here enable one to determine the correlation D vs. the angle θ between α particle and light fragment momenta. Results of this analysis for the reaction $^{233}\mathrm{U}(n,f)$ are depicted in Fig. 3. The top panel shows the angular distribution of α particles in the angular range covered by the diodes of the arrays. The angular distribution is in good agreement with literature data [9]. The panel on bottom of Fig. 3 represents the energy averaged correlation $\langle D\rangle$ as a function of the angle θ. Evidently, within statistical uncertainty the correlation stays virtually constant for the range of angles accessible to measurement.

Several corrections have to be applied to the raw data before quoting a final result for the triple correlation. There are some trivial ones like, first, corrections for the geometry of the experimental setup chosen (finite size and position of detectors and target), second, finite resolving power in the separation of light and heavy fragments, third, finite polarization of the neutron beam and, fourth, chance coincidences. More details on how these corrections were implemented are given elsewhere [10]. A much more delicate question is how the averaging over α-particle energy has to be performed since quite a sizable fraction of all ternary α particles escape detection at low energies. For the present purpose it has been chosen to rely on the linear fit to the data for the correlation coefficient D shown in Figs. 1 and 2 and its extrapolation to zero energy. It should be stressed that this linear fit and especially its extrapolation is not very convincing and furthermore in conflict with the predictions of recent theoretical models of the triple correlation [11]. In any case, any assumption on the dependence of the correlation D on α-particle energy will introduce a systematic uncertainty or error which is difficult to assess precisely. The errors quoted in the following are, therefore, only the statistical errors.

Final results for the energy-averaged triple correlation coefficients $\langle D\rangle$ are given separately for α particles and tritons. For ternary fission in the $^{233}\mathrm{U}(n,f)$ reaction the correlations are, respectively,

$$\langle D\rangle_\alpha = (-2.52 \pm 0.14) \times 10^{-3}, \qquad (6)$$
$$\langle D\rangle_t = (-1.99 \pm 0.63) \times 10^{-3}.$$

For the $^{235}\mathrm{U}(n,f)$ reaction the corresponding results for α particles and tritons are, respectively,

$$\langle D\rangle_\alpha = (+0.83 \pm 0.11) \times 10^{-3}, \qquad (7)$$
$$\langle D\rangle_t = (+0.60 \pm 0.41) \times 10^{-3}.$$

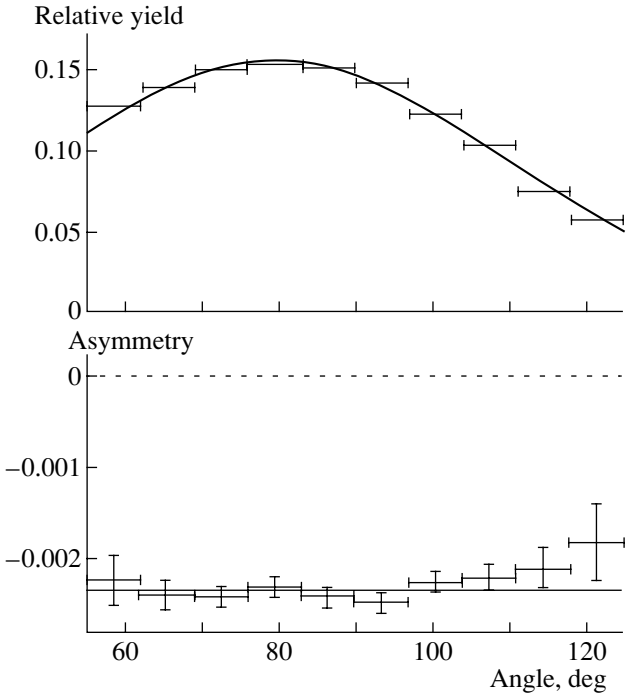

Fig. 3. $^{233}\mathrm{U}$ target. Top panel: ternary α-particle yield as a function of the angle between light fission fragment and ternary particle. Bottom panel: triple correlation coefficient $\langle D\rangle$ averaged over energy as a function of the angle between light fission fragment and ternary particle.

In the results laid down in Eqs. (6) and (7) it is remarkable that the correlation has the same size for the two main contributors to TPs, α particles and tritons. The observation holds within statistical uncertainty for both reactions studied. Since unlike the α particles the tritons carry spin, the result appears to indicate that the correlation depends on neither particle type nor particle spin of the TP emitted.

PNC effects in neutron induced fission being discussed since decades, only a shorthand report on the present PNC investigation will be given. With the experimental setup described for the measurement of the triple correlation staying untouched, the experiment is switched to a PNC study by turning the spin of the neutron beam from longitudinal to transverse and pointing towards the FF detectors. The basic equations for the PNC asymmetry in the angular distribution of FFs have already been quoted in Eqs. (2) and (4). PNC effects were measured for ternary fission of the $^{233}\mathrm{U}(n,f)$ reaction only. Moreover, the statistics accumulated did not allow one to disentangle PNC asymmetries for FFs accompanied by either α particles or tritons. A new and notable result is here that the PNC asymmetry as quantified by the coefficient $\alpha_{\mathrm{LF}}^{\mathrm{PNC}}$ in Eq. (4) is independent of the energy of the TPs. The final result, corrected similarly to the triple correlation above and averaged

over energy, is

$$\langle \alpha_{\rm LF}^{\rm PNC} \rangle = (0.37 \pm 0.10) \times 10^{-3}. \qquad (8)$$

The present result for ternary fission is remarkably close to the value for the asymmetry found for binary fission of the same ^{233}U target nucleus investigated in the same neutron beam of the ILL which has been measured to be [12]

$$\langle \alpha_{\rm LF}^{\rm PNC} \rangle = (0.400 \pm 0.017) \times 10^{-3}. \qquad (9)$$

The equality of PNC asymmetries of fragments in binary and ternary fission is well known from previous work [3] where the ratio of asymmetries for ternary to binary fission is reported to be (1.05 ± 0.10) for the reaction at hand.

A further result of the present experiment should be noted in passing. With the same setup as used in the investigation of PNC effects for the FFs, i.e., for transverse polarization of the neutron beam with the spin pointing towards the FF detectors, the left–right asymmetry of TPs in ternary fission can be determined by observing the count rates in the TP detectors positioned at right angles to neutron spin and neutron momentum. The observable in question is

$$A_{\rm TP}^{\rm LR} = \hat{\mathbf{p}}_{\rm TP} \cdot [\hat{\boldsymbol{\sigma}} \times \hat{\mathbf{p}}_n]\,. \qquad (10)$$

It measures the asymmetry in the emission $\hat{\mathbf{p}}_{\rm TP}$ of TPs with respect to an oriented plane formed by neutron spin $\hat{\boldsymbol{\sigma}}$ and neutron momentum $\hat{\mathbf{p}}_n$. In analogy to Eqs. (3) and (4) the asymmetry is parametrized by the ansatz

$$W(\theta,\varphi) d\Omega_{\rm TP} \sim \left(1 + \alpha_{\rm TP}^{\rm LR} A_{\rm TP}^{\rm LR}\right) d\Omega_{\rm TP}. \qquad (11)$$

In Eq. (11) the polar angles (θ, φ) specify the emission direction of the TPs relative to the oriented normal to the plane $(\hat{\boldsymbol{\sigma}}, \hat{\mathbf{p}}_n)$. The constant $\alpha_{\rm TP}^{\rm LR}$ in the above equation is called the left–right asymmetry coefficient which quantifies the size of the asymmetry. In analogy to Eq. (5) the relation $\langle A_{\rm TP}^{\rm LR} \rangle = \alpha_{\rm TP}^{\rm LR}/3$ between the expectation value of the observable and the coefficient holds.

For the ^{233}U(n,f) reaction induced by cold neutrons the left–right asymmetry coefficient for ternary particles averaged over TP energy is found to be

$$\langle \alpha_{\rm TP}^{\rm LR} \rangle = -(0.08 \pm 0.08) \times 10^{-3}. \qquad (12)$$

The result indicates that within statistical uncertainty TPs from ternary fission exhibit no left–right asymmetry.

4. DISCUSSION

The observable B from Eq. (1) with the particular feature to invert sign when time is reversed has been investigated for ternary fission induced by cold polarized neutrons in the fissile isotopes ^{233}U and ^{235}U. The experiments to be reported here are novel. Though originally motivated by the idea that possibly the experiments could probe TRI it became evident very quickly that, as predicted by theory, in a complex reaction like fission TRI is not directly linked to a nonvanishing expectation value for the observable B. From experiment this conclusion is strongly supported by the mere size of the correlation as quantified by the correlation coefficient D approaching $\pm 4 \times 10^{-3}$. Most probably the effect observed is much too large to be traced to a violation of TRI and, hence, an alternative interpretation has to be found.

Looking for an interaction in the ternary fission process which could bring forth the correlation discovered, attention has to be drawn to the fact that the dependence on the energy of the TP is quite different for the triple correlation and the PNC effect for FF. While the size of the triple correlation varies markedly with the energy of the TP, the PNC asymmetry is independent of the TP energy. As to the PNC effect, it is now well established that it becomes prominent in nuclear fission due to an enhancement of the mixing of states with opposite parities in the compound nucleus. It is further generally accepted that angular distributions, either parity conserving or not, are settled in the course of low-energy fission at the saddle point. Hence, PNC asymmetries in the angular distributions of FFs probe the early stages of fission up to the saddle point. This statement allows one to draw some conclusions from the PNC effect in ternary fission. As confirmed by the present experiments, the PNC effect has the same size, in both binary and ternary fission. The equality is interpreted to show that the TPs of ternary fission appear at a late stage of fission, i.e., close to or right at scission, since then all PNC effects are already established when the TPs come into existence. It is, hence, not surprising that the PNC effects for the FFs are also independent of the energies of the TPs as observed for the first time in the present experiments.

By contrast to the PNC effects, the triple correlation does depend on TP energy (Figs. 1, 2) and this is taken as a strong indication that the correlation originates near the scission point, i.e., at the final stage of the fission process. Different scenarios are then conceivable. In any case the polarization of the compound nucleus following capture of a polarized neutron has to be taken into account. As a first idea it is then obvious to imagine a spin–orbit interaction between the polarized fissioning nucleus and the ejected TP, either electromagnetic or—more probably—nuclear in character [13]. The spin–orbit interaction adds to the Coulomb interaction exerted by the two nascent FFs on the TP. The Coulomb force is held responsible for the focusing of the TP roughly at right angles to

the fission axis. More precisely, due to the asymmetry in mass and charge split of the FFs, the TP is slightly pushed by the Coulomb force toward the light FF and the average opening angle between the light FF and the TP is 83°. The angular distribution measured in the present experiments clearly exhibits this feature as shown in the top panel of Fig. 3. The additional spin–orbit interaction should become manifest as a further shift, widening or narrowing down the opening angle between light FF and TP away from the average 83°, depending on the direction of neutron and hence also nuclear spin. This prediction can be checked experimentally. In fact, in the case where the spin–orbit interaction is operative, the correlation coefficient D should have opposite signs for angles smaller or larger than the average angle 83° since, when flipping the spin, the event rate, e.g., drops for angles smaller but increases for angles larger than the average opening angle and vice versa. However, as demonstrated in the bottom panel of Fig. 3, experiment clearly tells that the correlation coefficient D is independent of the emission angle of the TP. The spin–orbit interaction thus appears to be ruled out as a factor behind the triple correlation observed.

A more elaborate model for the triple correlation has been proposed by Bunakov [11]. The model is described in detail in a companion paper and only the main ideas are sketched here. Basically it is assumed that the fissioning system is sufficiently equilibrated at the scission point and therefore a stastistical model should be a valid approach. It is then argued that the spin of the polarized compound nucleus is transferred onto the two FFs and that, for the detector setup chosen in the present experiments, the orbital angular momentum of, say, an α particle enters into the angular momentum balance with the TP orbital angular momentum being parallel or antiparallel to the nuclear spin. If now in the level density of nuclei a dependence on angular momentum is taken into account, a nonvanishing triple correlation with the observed order of magnitude emerges in the statistical approach.

Even more gratifying is that the dependence of the triple correlation on TP energy is surprisingly well reproduced. The dependence is traced to a correlation between the intrinsic excitation energy at scission and the kinetic energy of the TP. The link between these two energies is understood by noting that the dumbbell shape of a fissioning nucleus at scission may vary between very compact and very deformed configurations. While on average the intrinsic energy at scission is expected to be about 6 MeV, for compact shapes the intrinsic energy is known to be close to zero ("cold fission") while the TP energy will be large due to the stronger Coulomb repulsion in a compact scission configuration. By contrast, for deformed scission shapes the intrinsic energy will be larger than average and the TP energy smaller than average. Thus there is a correlation between the two energies at hand which is mediated by the scission configuration.

The mechanism behind the triple correlation should be very similar for ternary fission of any polarized nucleus. Therefore, the size of the effect could be expected to have the same order of magnitude for all fission reactions. However, the polarization of the compound nucleus and the transfer of the polarization onto the FFs enter as further crucial parameters when the FF spin is coupled to the orbital angular momentum of the TP. The polarization picked up by a nucleus following capture of a polarized neutron is governed by the capture states and these change rapidly with neutron energy. For given neutron spin the polarization can even change sign. Hence, the opposite signs of the correlation coefficient D measured for the two isotopes ^{233}U and ^{235}U in the present experiments is likewise within the scope of the correlation model proposed.

Finally, as a comment to the investigation of left–right asymmetries of TPs in ternary fission it may be conjectured that this asymmetry should be zero. The reason is that, similar to the PNC asymmetry, also the left–right asymmetry is settled by the interference of compound nucleus levels at an early stage of fission. This is at least the view advanced for the interpretation of left–right asymmetries of FFs in binary fission. But at this early stage of the process the TPs have not yet come into view. The experimental result, with the left–right asymmetry being according to Eq. (12) compatible with nil for the TPs is, hence, not surprising.

Evidently, there is much work still ahead to get a comprehensive survey on all conceivable correlations and asymmetries in ternary fission. Of course, as a natural extension of the present work, the dependence of correlations and asymmetries should be studied for a larger choice of fissile nuclei, both as a function of the energy of neutrons inducing fission and as a function of masses and energies of FFs and TPs.

Besides the correlations studied here, it should also be interesting to analyze for ternary fission the PNC asymmetries of TPs and the left–right asymmetries of FFs which are complementary to those reported from the present experiments. Likewise the forward–backward asymmetries of both FFs and TPs could give further insight into the mechanism of ternary fission.

ACKNOWLEDGEMENTS

Technical support by the ILL, Grenoble, and financial support by the BMBF, Bonn; the RFBR, Moscow; and INTAS, Bruxelles, is gratefully acknowledged.

REFERENCES

1. G. V. Danilyan *et al.*, Pis'ma Zh. Éksp. Teor. Fiz. **26**, 197 (1977) [JETP Lett. **26**, 186 (1977)].
2. V. E. Bunakov and V. P. Gudkov, Z. Phys. A **321**, 271 (1985).
3. F. Gönnenwein *et al.*, Nucl. Phys. A **567**, 303 (1994).
4. K. Schreckenbach *et al.*, in *Time Reversal Invariance and Parity Violation in Neutron Reactions*, Ed. by C. R. Gould *et al.* (World Sci., Singapore, 1994), p. 187.
5. E. Henley and B. Jacobson, Phys. Rev. **113**, 225 (1959); V. E. Bunakov and L. B. Pikelner, Prog. Part. Nucl. Phys. **39**, 337 (1997).
6. M. Mutterer *et al.*, IEEE Trans. Nucl. Sci. **47**, 756 (2000).
7. P. Jesinger *et al.*, Nucl. Instrum. Methods Phys. Res. A **440**, 618 (2000).
8. F. Gönnenwein, in *Seminar on Fission, Pont d'Oye IV*, Ed. by C. Wagemans *et al.* (World Sci., Singapore, 2000), p. 59.
9. C. Wagemans in *The Nuclear Fission Process*, Ed. by C. Wagemans (CRC Press, Boca Raton, 1991); M. Mutterer and J. P. Theobald, in *Nuclear Decay Modes*, Ed. by D. Poenaru (Inst. of Physics Publ., Bristol, 1996), Chap. 12.
10. P. Jesinger, PhD Thesis (University of Tübingen, 2001).
11. V. E. Bunakov, Yad. Fiz. **65**, 648 (2002) [Phys. At. Nucl. **65**, 616 (2002)].
12. A. Kötzle *et al.*, Nucl. Instrum. Methods Phys. Res. A **440**, 750 (2000).
13. A. L. Barabanov, private communication.

Physics of Atomic Nuclei, Vol. 65, No. 4, 2002, pp. 637–640. From Yadernaya Fizika, Vol. 65, No. 4, 2002, pp. 669–672.

Nonlinear Evolution of the Axisymmetric Nuclear Surface*

V. G. Kartavenko[1),2)], K. A. Gridnev[**], and W. Greiner[2)]

Institute of Physics, St. Petersburg State University, Petrodvorets, Russia

Received August 31, 2001

Abstract—We consider a uniformly charged incompressible nuclear liquid bounded by a closed surface. It is shown that the evolution of an axisymmetric surface $\Gamma(\mathbf{r},t) \equiv \sigma - \Sigma(z,t) = 0$, $\mathbf{r} = (\sigma,\phi,z)$ can be approximately reduced to the motion of a curve in the (σ,z) plane. A nonlinear integro-diffrerential equation for the contour $\Sigma(z,t)$ is derived. The contour $\Sigma(z,t)$ and the local curvature are found to be a direct correspondence, which makes it possible to use methods of differential geometry to analyze the evolution of an axisymmetric nuclear surface. © *2002 MAIK "Nauka/Interperiodica".*

1. MOTIVATION

The nonlinear dynamics of a nuclear surface is an object of special interest for the following reasons. First, the nuclear density decreases considerably in the surface region, where density fluctuations and clustering may be of importance. Second, various types of instability may develop in the surface region and lead to fragmentation processes at low (fission, nucleon transfer) and high (multifragmentation, breakup, etc.) energies. Finally, the liquid-drop concept [1] has been intensively used in macro- [2] and microphysics [3] for over a century. In any complicated systems, the nonlinear dynamics of shapes inevitably leads to mathematical problems in describing global geometric quantities such as a surface or an enclosed volume in various dimensions (polymers, cell membranes, 3D droplets).

Application of the soliton concept to nonlinear nuclear hydrodynamics opened yet new possibilities in this field (see, e.g., the review in [4] and [5–8] for recent references). However, any extension of nonlinear dynamics from $1+1$ to $2+1$ and $3+1$ dimensions runs into difficulties of a fundamental character. The crucial point is to reduce the dimension of the problem at hand. The simplest two-dimensional nonlinear liquid objects were considered in [9]. It was shown that the 2D pure vortical motion of an inviscid nuclear liquid can be reduced to the 1D evolution of the contour bounding this drop. An extension to semi-3D geometry was performed in [10]. The equations of motion describing a localized vortex on a spherical nuclear surface—a bounded region of constant vorticity surrounded by irrotational flux—were reduced to the 1D nonlinear evolution of the boundary.

Here, we consider a uniformly charged incompressible nuclear 3D fluid bounded by a closed surface. It is shown that the evolution of an axisymmetric surface $\Gamma(\mathbf{r},t) \equiv \sigma - \Sigma(z,t) = 0$, $\mathbf{r} = (\sigma,\phi,z)$ can be approximately reduced to the motion of a curve in the (σ,z) plane.

2. FRAMEWORK

The evolution of a one-body Wigner phase-space distribution function is analyzed instead of a full many-body wave function. Integrating the kinetic equation

$$\frac{\partial f}{\partial t} + \frac{\mathbf{p}}{m}\frac{\partial f}{\partial \mathbf{r}} - \frac{\partial V}{\partial \mathbf{r}}\frac{\partial f}{\partial \mathbf{p}} = I_{\rm rel}, \qquad (1)$$

$$H_W = \frac{p^2}{2m} + V(\mathbf{r})$$

over momentum space with various polynomial weighting functions of the variable $\mathbf{p}$, one arrives at an infinite chain of equations for local collective observables, including the density, the collective velocity, the pressure, and an infinite set of tensorial functions of the time and spatial coordinates, which are defined as moments of the distribution function in momentum space:

the particle density $n(\mathbf{r},t) \equiv g\int d\mathbf{p}\, f(\mathbf{r},\mathbf{p},t)$ and the mass density $\rho(\mathbf{r},t) = m\, n(\mathbf{r},t)$, where we consider a proton and a neutron as different states of the same particle (the spin–isospin degeneracy of $g = 4$);

the collective current and velocity of nuclear matter, $\rho(\mathbf{r},t)\mathbf{u}(\mathbf{r},t) = g\int d\mathbf{p}\,\mathbf{p} f(\mathbf{r},\mathbf{p},t)$;

*This article was submitted by the authors in English.

[1)]Bogoliubov Laboratory of Theoretical Physics, Joint Institute for Nuclear Research, Dubna, 141980 Russia.

[2)]Institut für Theoretische Physik der J. W. Goethe Universität Frankfurt am Main, Frankfurt am Main, Germany.

[**]e-mail: gridnev@nuclpc1.phys.spbu.ru

the pressure tensor $P_{ij}(\mathbf{r},t) = (g/m)\int d\mathbf{p} \times q_i q_j f(\mathbf{r},\mathbf{p},t), \mathbf{q} = \mathbf{p} - m\mathbf{u}$;

tensors of various order describing energy–momentum transfer,

$$P_{ijk}(\mathbf{r},t) = \frac{g}{m^2}\int d\mathbf{p} q_i q_j q_k f(\mathbf{r},\mathbf{p},t), \qquad (2)$$

$$P\underbrace{_{ij\ldots k}}_{n}(\mathbf{r},t) = \frac{g}{m^{n-1}}\int d\mathbf{p}\,\underbrace{q_i q_j \ldots q_k}_{n} f(\mathbf{r},\mathbf{p},t),$$

and integrals related to relaxation terms,

$$\int d\mathbf{p} I_{\rm rel} = 0, \quad \int d\mathbf{p}\mathbf{p} I_{\rm rel} = 0, \qquad (3)$$

$$R_{ij} \equiv \frac{g}{m}\int d\mathbf{p}\, q_i q_j I_{\rm rel}, \ldots .$$

Truncating this chain, one arrives at the "fluid-dynamics" level of the description of nuclear processes,

$$\frac{\partial \rho}{\partial t} + \sum_k \frac{\partial}{\partial x_k}(u_k \rho) = 0, \qquad (4)$$

$$\rho\frac{Du_i}{Dt} + \sum_k \frac{\partial P_{ik}}{\partial x_k} + \frac{\rho}{m}\frac{\partial V}{\partial x_i} \qquad (5)$$

$$+ \rho\left(\Omega_i \sum_k \Omega_k x_k - \Omega^2 x_i\right)$$

$$+ \rho\sum_{s,j}\varepsilon_{isj}\left(2\Omega_s u_j + \frac{d\Omega_s}{dt}x_j\right) = 0,$$

$$\frac{DP_{ij}}{Dt} + \sum_k\left(P_{ik}\frac{\partial u_j}{\partial x_k} + P_{jk}\frac{\partial u_i}{\partial x_k} + P_{ij}\frac{\partial u_k}{\partial x_k}\right) \qquad (6)$$

$$+ 2\sum_{s,m}\Omega_m(\varepsilon_{jms}P_{is} + \varepsilon_{ims}P_{js})$$

$$+ \sum_k \frac{\partial}{\partial x_k}P_{ijk} = R_{ij}.$$

Here, we have used the standard notation

$$\frac{D}{Dt} \equiv \frac{\partial}{\partial t} + \sum_k u_k \frac{\partial}{\partial x_k}$$

for the operator giving the matter derivative or the rate of change at a point locally moving with the fluid. The hydrodynamic set of Eqs. (4)–(6) describes evolution in a rotating nuclear system. The linear transformation

$$x_i = \sum_{j=1}^{3} T_{ij} X_j$$

relates the coordinates of a point (X_1, X_2, X_3) in an inertial frame and (x_1, x_2, x_3) in a moving reference frame with a common origin. The orientation of the moving frame with respect to the inertial frame will be assumed to be time-dependent, $T_{ij}(t)$, representing an orthogonal transformation, and the vector

$$\Omega_i = \frac{1}{2}\sum_{j,k,m}\varepsilon_{ijk}\,(dT/dt)_{jm}\,T^{+}_{mk}$$

represents a general time-dependent rotation.

Let us restrict ourselves to the simplest possible motion of a nuclear liquid. We consider a uniformly charged (with a total charge Ze) incompressible nuclear "liquid" confined in a volume V bounded by a closed surface S obeying the equation $\Gamma(\mathbf{r},t) \equiv \sigma - \Sigma(z,t) = 0$, $r = (\sigma,\phi,z)$, where (σ,ϕ,z) are the cylindrical coordinates of a point. The geometry of the problem places the origin at the center of mass ($\int d\mathbf{r}\,\rho(\mathbf{r},t) \times \mathbf{u}(\mathbf{r},t) = 0$). The mean-field potential and the related tensors can be decomposed into nuclear and Coulomb terms $V(\mathbf{x},t) = V_{\rm nucl}(\mathbf{x},t) + V_{\rm coul}(\mathbf{x},t)$. The nuclear potential can be derived as the first variation of the short-range interaction-functional (as usual, for effective density-dependent Skyrme forces) with respect to the density, $V_{\rm nucl}(\mathbf{x},t) \equiv \delta\mathcal{E}[n]/\delta n$. This gives the nuclear potential as a function of the density $n(\mathbf{r},t) = n_0\eta(\mathbf{r},t)$. The incompressibility of nuclear matter implies $n_0 = (2p_{\rm F}^3)/(3\pi\hbar^3)$, where n_0 and $p_{\rm F}$ are, respectively, the density of nuclear matter and the Fermi momentum. Bearing in mind that the effective mean-field potential is approximately constant in the interior of nuclei and that it has a sharp coordinate dependence in the surface region, we replace it by the surface term [11] $\gamma_s {\rm div}\hat{\mathbf{n}}$, where $\hat{\mathbf{n}} = \nabla\Gamma/|\nabla\Gamma|$ is the unit outward normal to S and the surface tension γ_s is related to the mass formula coefficient as $b_s = 4\pi r_0^2\gamma_s \sim 22$ MeV. In both cases, the contour $\Sigma(z,t)$ defines completely the nuclear potential on the nuclear surface,

$$V_{\rm coul}(\mathbf{x},t) = \left(\frac{Z}{A}e\right)^2 n_0 \int d\mathbf{x}'\,\frac{\eta(\mathbf{x}',t)}{|\mathbf{x}-\mathbf{x}'|} \qquad (7)$$

$$= \left(\frac{Z}{A}e\right)^2 n_0 \int\limits_{z_{\rm min}}^{z_{\rm max}} dz' \int\limits_0^{\Sigma(z',t)} d\sigma'\sigma' I(\sigma,\sigma',z'),$$

$$I(\sigma,\sigma',z') = \int\limits_0^{2\pi} d\phi \frac{1}{\sqrt{\sigma^2 + \sigma'^2 - 2\sigma\sigma'\cos\phi}}.$$

Concerning pressure tensors, we will not solve the kinetic Eq. (1), but will use the fact that this simplest picture can be reproduced under the assumption that

the distribution functions $f(\mathbf{r},\mathbf{p},t)$ has the factorized form

$$f^0(\mathbf{r},\mathbf{p}) = (2\pi\hbar)^{-3}\eta^0(\mathbf{r})\phi^0(\mathbf{p}), \qquad (8)$$
$$f(\mathbf{r},\mathbf{p},t) = (2\pi\hbar)^{-3}\eta(\mathbf{r},t)\ \phi(\mathbf{r},\mathbf{p},t),$$

where $\eta(\mathbf{r},t) \equiv \theta(\Gamma(\mathbf{r},t))$ $[\eta^0(\mathbf{r}) \equiv \theta(\Gamma^0(\mathbf{r}))]$ is a step function that is equal to unity inside the surface $\Gamma(\mathbf{r},t)$ $[\Gamma^0(\mathbf{r})]$ and to zero outside it. The distribution function $f^0(\mathbf{r},\mathbf{p})$ describes an equilibrium spherically symmetric state $\{\Gamma^0(\mathbf{r}) \equiv \sigma - \sqrt{R_0^2 - z^2}$, where R_0 is the radius of a sphere of the equivalent volume $[4R_0^3 = 3\int dz\Sigma(z,t)^2]\}$. The distribution function $f(\mathbf{r},\mathbf{p},t)$ corresponds to a dynamical picture. Both distribution functions describe a homogeneous distribution of nuclear matter within the volume bounded by a narrow surface. The momentum-dependent parts of the distribution functions could be parametrized as

$$\phi^0(\mathbf{p}) = \theta(p_\mathrm{F}^2 - p^2), \qquad (9)$$
$$\phi\left(\mathbf{r},\mathbf{p},t\right) = \theta(p_\mathrm{F}^2 - \sum_{i,j}(\delta_{ij} + \alpha_{ij}(t))q_iq_j\Big).$$

The form chosen for the momentum-dependent part of $f(\mathbf{r},\mathbf{p},t)$ ($f^0(\mathbf{r},\mathbf{p})$) ensures that it yields the current density with the collective velocity $\mathbf{u}(\mathbf{r},t)$ ($\mathbf{u}^0 = 0$). Of course, the symmetry of the problem is defined by the symmetry of all effective forces and of the initial state. In a fluid at rest, there are only normal stresses, which are independent of the direction of the normal to the surface element across which it acts and the equilibrium pressure tensor has a spherically symmetric form via the symmetry of the equilibrium distribution function, $P_{ij}^0(\mathbf{r}) = (2/5)\epsilon_\mathrm{F}\eta^0(\mathbf{r})n_0\delta_{ij}$. There is no reason to expect these results to be valid for a moving fluid, where the tangential stresses are generally nonzero and where the normal component of the stress acting across a surface element depends on the direction of the normal to the element. The simple notion of a pressure acting equally in all directions is often lost in a moving fluid. Deformations of Cartesian space define a deformation in momentum space, and vice versa. We only consider a motion with $\mathbf{\Omega} = 0$ and assume that the tensor α_{ij} is diagonal. The dynamical pressure tensors are $P_{ij}(\mathbf{r},t) = (2/5)(1 + \alpha_{ii})^{-1}\epsilon_\mathrm{F}n_0\eta(\mathbf{r},t)\delta_{ij}$. These equations show that the introduction of the functions $\alpha_{ii}(t)$ in the expression for $\phi(\mathbf{r},\mathbf{p},t)$ take into account the deformation of the Fermi surface.

In the cylindrical coordinates, the main hydrodynamical set of equations takes the form

$$\frac{\partial u_\sigma}{\partial t} + u_\sigma\frac{\partial u_\sigma}{\partial\sigma} + u_z\frac{\partial u_\sigma}{\partial z} = F_\sigma, \qquad (10)$$
$$\frac{\partial u_z}{\partial t} + u_\sigma\frac{\partial u_z}{\partial\sigma} + u_z\frac{\partial u_z}{\partial z} = F_z,$$
$$\frac{\partial u_\sigma}{\partial\sigma} + \frac{\partial u_z}{\partial z} + \frac{u_\sigma}{\sigma} = 0,$$

where u_σ and u_z (F_σ and F_z) are the projections of the velocity (forces) onto the axes σ and z, respectively.

The boundary conditions are

$$\hat{\mathbf{n}}\Xi\hat{\mathbf{n}} = -\gamma_s\left(\frac{1}{C_1} + \frac{1}{C_2}\right), \quad \hat{\mathbf{n}}\Xi\hat{\mathbf{t}} = 0, \qquad (11)$$

where Ξ is the stress tensor, which can be calculated by using all the above formulas for the pressure tensor and the mean-field potentials, and C_1 and C_2 are the principal radii of curvature. A direct evaluation yields

$$\frac{1}{C_1} + \frac{1}{C_2} = \frac{1}{\Sigma(1+\Sigma_z^2)^{1/2}} - \frac{\Sigma_{zz}}{(1+\Sigma_z^2)^{3/2}}, \qquad (12)$$
$$\Sigma_z \equiv \frac{\partial\Sigma}{\partial z}, \quad \Sigma_{zz} \equiv \frac{\partial^2\Sigma}{\partial z^2},$$

$$\hat{\mathbf{n}} = \frac{\hat{e}_\sigma - \Sigma_z\hat{e}_z}{\sqrt{1+\Sigma_z^2}}, \quad \hat{\mathbf{t}} = \frac{\Sigma_z\hat{e}_\sigma + \hat{e}_z}{\sqrt{1+\Sigma_z^2}}, \qquad (13)$$
$$\hat{e}_\sigma = \frac{\hat{\mathbf{n}} + \Sigma_z\hat{\mathbf{t}}}{\sqrt{1+\Sigma_z^2}}, \quad \hat{e}_z = \frac{-\Sigma_z\hat{\mathbf{n}} + \hat{\mathbf{t}}}{\sqrt{1+\Sigma_z^2}}.$$

The final integro-differential equation of motion for a contour accumulates the coupled set of Eqs. (10)–(12):

$$\frac{D\Sigma(z,t)}{Dt} = \frac{\partial\Sigma(z,t)}{\partial t} \qquad (14)$$
$$+ u_z(\Sigma,z,t)\frac{\partial\Sigma(z,t)}{\partial z} = u_\sigma(\Sigma,z,t).$$

The evolution of the surface $\Gamma(\sigma,z,t)$ as a motion of a 2D spatial curve in the (σ,z) plane is a particular choice of a general 3D curve dynamics,

$$\mathbf{u} = u_t\hat{\mathbf{t}} + u_n\hat{\mathbf{n}} + u_b\hat{\mathbf{b}}, \qquad (15)$$

where the tangent $\hat{\mathbf{t}}$, the normal $\hat{\mathbf{n}}$, and the binormal $\hat{\mathbf{b}} \equiv \hat{\mathbf{t}} \times \hat{\mathbf{n}}$ form the Frenet–Serret triad [12] obeying the equations of differential geometry:

$$\hat{\mathbf{t}} \equiv \frac{d\mathbf{r}}{ds}, \quad \frac{d\hat{\mathbf{t}}}{ds} = \frac{d^2\mathbf{r}}{ds^2} = \kappa\hat{\mathbf{n}}, \quad \kappa = \left|\frac{d^2\mathbf{r}}{ds^2}\right|, \qquad (16)$$
$$\frac{d\hat{\mathbf{b}}}{ds} = -\tau\hat{\mathbf{n}}, \quad \tau = \kappa^{-2}\Big(\frac{d\mathbf{r}}{ds} \times \frac{d^2\mathbf{r}}{ds^2}\Big)\cdot\frac{d^3\mathbf{r}}{ds^3},$$
$$\frac{d\mathbf{n}}{ds} = -\kappa\hat{\mathbf{t}} + \tau\hat{\mathbf{b}}.$$

Here, κ is the curvature and τ is the torsion of the curve at the arclength position s and time t. A direct evaluation yields

$$\frac{ds}{dz} = \sqrt{1+\Sigma_z^2}, \quad \tau = 0, \quad \kappa = \frac{\Sigma_{zz}}{1+\Sigma_z^2}.$$

The axial symmetry of the problem constrains the evolution to the $(\hat{\mathbf{n}}, \hat{\mathbf{t}})$ plane and $(z \leftrightarrow s)$ and $[\Sigma(z,t) \leftrightarrow \kappa(s,t)]$ equivalence. This describes the evolution of an axisymmetric surface in purely geometric terms of the curvature and the arclength. The integro-differential form of Eqs. (10)–(14) leads to strong nonlocality as a consequence of the long-range part of the interaction.

3. SUMMARY

We have considered a uniformly charged incompressible nuclear liquid bounded by a closed surface. It has been shown that the evolution of an axisymmetric surface $\Gamma(\mathbf{r},t) \equiv \sigma - \Sigma(z,t) = 0, \mathbf{r} = (\sigma, \phi, z)$ can be approximately reduced to the motion of a curve in the (σ, z) plane. A nonlinear integro-differential equation for the contour $\Sigma(z,t)$ has been derived. It has been shown that $\Sigma(z,t)$ and the local curvature are in direct correspondence, which makes it possible to use methods of differential geometry to analyze the evolution of an axisymmetric nuclear surface.

The objective of this short report was only to present the main line. The extended article is in preparation.

ACKNOWLEDGMENTS

This work was supported in part by the Russian Foundation for Basic Research and Deutsche Forschungsgemeinschaft.

REFERENCES

1. J. W. S. Rayleigh, Proc. R. Soc. London **29**, 71 (1879).
2. S. Chandrasekhar, *Ellipsoidal Figures of Equilibrium* (Yale Univ. Press, New Haven, 1969).
3. J. M. Eisenberg and W. Greiner, *Nuclear Models (Collective and Single-Particle Phenomena)* (North-Holland, Amsterdam, 1970).
4. V. G. Kartavenko, Fiz. Élem. Chastits At. Yadra **24**, 1469 (1993) [Phys. Part. Nucl. **24**, 619 (1993)].
5. R. E. Apfel *et al.,* Phys. Rev. Lett. **78**, 1912 (1997).
6. A. Ludu and J. P. Draayer, Phys. Rev. Lett. **80**, 2125 (1998).
7. V. G. Kartavenko, K. A. Gridnev, and W. Greiner, Int. J. Mod. Phys. E **7**, 287 (1998).
8. V. G. Kartavenko, A. Săndulescu, and W. Greiner, Int. J. Mod. Phys. E **8**, 381 (1999).
9. V. G. Kartavenko, J. Phys. G **19**, L83 (1993).
10. V. G. Kartavenko, K. A. Gridnev, J. Maruhn, and W. Greiner, J. Phys. G **22**, L19 (1996).
11. C. E. Rosenkilde, J. Math. Phys. (N.Y.) **8**, 84 (1967); **8**, 88 (1967); **8**, 98 (1967).
12. V. I. Smirnov, *A Course of Higher Mathematics* (GITTL, Moscow, 1957; Addison-Wesley, Reading, 1964), Vol. 2, Chap. V.

Physics of Atomic Nuclei, Vol. 65, No. 4, 2002, pp. 641–644. From Yadernaya Fizika, Vol. 65, No. 4, 2002, pp. 673–676.

Band Interaction in ^{162}Dy, ^{168}Er, and ^{172}Yb*

E. P. Grigoriev**

Institute of Physics, St. Petersburg State University, Petrodvorets, Russia

Received October 31, 2001

Abstract—Coriolis interaction between levels of two rotational bands in ^{172}Yb with $K^\pi = 2^+$ and 3^+ and in ^{168}Er between levels with $K^\pi = 0^-$, 1^-, and 2^- is studied. The values of the interaction parameters are obtained. The mutual influence of two bands in ^{162}Dy with $\Delta K = 2$, $K_i^\pi = 0_2^+$ and 2_1^+ due to Coriolis interaction is demonstrated. © *2002 MAIK "Nauka/Interperiodica".*

1. INTRODUCTION

The wave functions of the unified model define the energy of the excited states of nuclei and their other properties [1]. It is necessary to know experimental data on band energies, transition probabilities, moments, and other quantities to identify the quadrupole-vibrational, octupole-vibrational, or two-quasiparticle type of the band excitation. The wave functions of many states are complex—they contain two or more components. The effects of Coriolis mixing of two states are observed when $\Delta K = 1$ rotational bands are close or when they intersect. The mixing affects, first of all, the shift of rotational levels. We used this effect to consider the pairs of $\Delta K = 1$ bands in ^{172}Yb and ^{168}Er and the pair of bands with $\Delta K = 2$ in ^{162}Dy.

The term $H_{\rm rot}$ in the Hamiltonian and Wigner function D^J_{MK} define the eigenenergies of band levels, $E = (\hbar^2/2\mathcal{J})J(J+1)$. This formula may be violated because of a pairing reduction, an increase in the spin, and band interaction. The pairing reduction leads to a decrease in the inertia parameter $A = \hbar^2/2\mathcal{J}$ in the ground-states band from $A = 12$–30 keV, which follows from the energy of the $2^+ \to 0^+$ transition to the approximately rigid-body value $A \approx 7$ keV if $J > 20\hbar$. The same tendency takes place in bands built on the excited head levels. The band interaction, the second reason, creates irregularity in the behavior of A in the band. It is necessary to find the reason for irregularities if they are discovered in experiments.

We considered four cases of two-band interaction and A anomalies. For three of them, $\Delta K = 1$ and irregularities are associated with Coriolis interaction. We can understand the energy of levels if we take into account the mixing of the bands with K and $K+1$. The fourth example considered here is that of the intersection of $K_i^\pi = 2_1^+$ and 0_2^+ bands in ^{162}Dy. The analysis contains the following limitations: (i) The moments of inertia are the same for two bands. (ii) Other bands do not affect the bands under consideration. The observed energy of two levels with spin J is defined by the terms [1]

$$E_{K,K+1} = \frac{1}{2}[\epsilon_{0,K} + A_K J(J+1) + \epsilon_{0,K+1} + A_{K+1}J(J+1)] \pm \frac{1}{2}([\epsilon_{0,K+1} + A_K J(J+1) - \epsilon_{0,K} - A_{K+1}J(J+1)]^2 + 4W^2_{K,K+1})^{1/2},$$

where $\epsilon_{0,K}$ and $\epsilon_{0,K+1}$ are the energy of unreal $J = 0$ noninteracting levels of the bands with K and $K+1$, $W_{K,K+1}$ is the matrix element of the band interaction, and $A_K = A_{K+1}$. It is important to define the interaction parameter B in the term $W_{K,K+1} = B[J(J+1) - K(K+1)]^{1/2}$ and its dependence on the structure of interacting bands. The high quality of experimental data is needed for this aim, and we obtained new results using part of them [2–4]. We used the above formulas to determine three interaction parameters and evaluated the energies of levels in five rotational bands.

2. CORIOLIS INTERACTION IN THE $K^\pi = 2^+$ AND 3^+ LEVELS IN ^{172}Yb

Two pair of bands with $K^\pi = 2^+$ and 3^+ are known up to an excitation energy of 2 MeV in ^{172}Yb [2]. A smooth decrease in $A(J)$ with increasing J is observed in low-level bands with 1172.39-keV, 3_1^+ and 1465.88-keV, 2_1^+ head levels.

For the second pair of the bands, the experimental and calculated values of the energy of the levels and the parameters $A(J)$ are shown in Table 1. A large gap between the 2^+ and 3^+ levels and an increase in

*This article was submitted by the author in English.

** e-mail: epgrig@nuclepc1.phys.spbu.ru

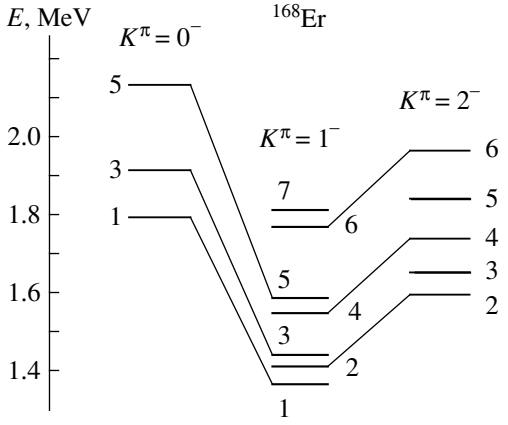

Fig. 1. Positions of low-lying rotational bands with $K^\pi = 0^-$, 1^-, and 2^- in ^{168}Er.

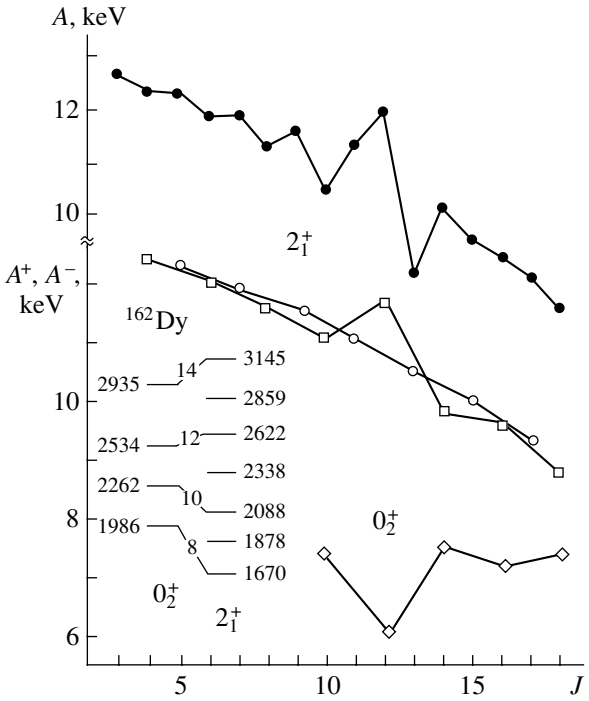

Fig. 2. Inertia parameters $A(J \to J-1)$ (•), $A^+(J \to J-2)$ (□ and ◇, even spin), and $A^-(J \to J-2)$ (○, odd spin) in ^{162}Dy versus J.

parameter A with increasing J are features peculiar to the band with $K^\pi = 2^+$.

We consider this agreement to be rather good, bearing in mind the above assumptions. We obtained the agreement of energy values within approximately 4 keV for 5^+ levels and within 15 keV for 6^+ levels.

The parameter value of $B = 6.86$ keV corresponds to the mixing of the two quasiparticle states 3^+, $p[411]\downarrow - p[404]\downarrow$ and 2^+, $p[411]\downarrow + p[411]\uparrow$, 7.7%. Identification was made in [3]. Errors in calculating B are less than 0.01 keV, but the influence of other bands may change this value of B. Specific calculations are required for obtaining an actual value, but such calculations are to be done not only in the two-band approximation.

3. CORIOLIS INTERACTION OF THE $K_i^\pi = 0_1^-$ AND 1_1^- BANDS IN ^{168}Er

Between the head levels of the $K^\pi = 0^-$ and 1^- bands in ^{168}Er, there is a large gap of $\Delta E = 426$ keV (Fig. 1 [4]). In spite of this, a strong signature splitting takes place in the $K = 1$ band between levels with even and odd spins, and we suppose that this may be due to the influence of the $K^\pi = 0^-$ band, which consists of only odd spin levels. We can see in Table 2 that the experimental values of the parameter A in the $K = 1$ band are 11–16 keV for odd-spin levels and only 2–5 keV for odd-spin levels.

The $K = 0$ band does not affect the spin 2^-, 4^-, ... levels in the $K = 1$ band. The odd-spin levels in $K = 1$ band go down, while, in the $K = 0$ band, they go up because of the repulsion of the levels.

The results of our calculation show that energies of $J = 5$ levels and $J = 7$ levels agree with experimental values within 8 and 19 keV, respectively. The difference of the calculated and experimental values of the energy of $J^\pi = 2^-$, 4^-, and 6^- levels does not exceed 5 keV. The reduction of their energy may be associated with the interaction with the $K^\pi = 2^-$ band, the bandhead energy of the 2^- level being 1569.45 keV.

The interaction-parameter value of $B = 35.44$ keV is rather large. The structure of the band was defined in [5]: 0^-, $n[512]\uparrow - n[642]\uparrow$, 25% and 1^-, $n[512]\uparrow - n[633]\uparrow$, 72%.

The second $K_i^\pi = 1_2^-$ band is known (the bandhead energy is 1936.40 keV, its spin–parity being 1^-); its signature splitting is about 1 keV. We expect that the interaction with a known 0^- band may increase energies of odd-spin levels. However, we observe a decrease in the energies of these levels, just as in the low-lying 1^- band. This may be explained by the influence of higher $K^\pi = 0^-$ levels, for example, those at 2137 and 2417 keV [6].

4. CORIOLIS INTERACTION OF THE $K_i^\pi = 1_1^-$ AND 2_1^- BANDS IN ^{168}Er

The $K^\pi = 0^-$ band does not affect even-spin levels in the $K^\pi = 1^-$ and other bands. Nevertheless, the inertia parameters $A^+(J \to J-2)$ increase with increasing J (Table 3). We assume that this effect is associated with the influence of the $K^\pi = 2^-$ band, where there are irregularities in the dependence $A(J)$.

Table 1. Experimental E_{expt} and calculated E_{calc} values of the energy of levels and values of inertia parameter A for bands with $K_i^\pi = 2_2^+$ and 3_2^+ in ^{172}Yb (in keV) [the parameters used to calculate E_{calc} are the following (in keV): $\epsilon_0(K=2) = 1549.0$, $\epsilon_0(K=3) = 1530.8$, $A(K=2) = A(K=3) = 11.94$, and $B = 6.86$]

J	$K^\pi = 2^+$			$K^\pi = 3^+$		
	E_{expt}	E_{calc}	A	E_{expt}	E_{calc}	A
2	1608.49	1619.7	–	–	–	–
3	1700.64	≡1700.64	15.36	1662.81	≡1662.81	–
4	1803.11	≡1803.11	12.80	1749.21	≡1749.21	10.80
5	1927.02	1928.8	12.39	1862.80	1859.2	11.36
6	2075.27	2077.8	12.35	2007.98	1993.5	12.10

Table 2. Experimental E_{expt} and calculated E_{calc} values of the energy of levels and values of the inertia parameter A for bands with $K_i^\pi = 0_1^-$ and 1_1^- in ^{168}Er (in keV) [the parameters used to calculate E_{calc} are the following (in keV): $\epsilon_0(K=0) = 1760.12$, $\epsilon_0(K=1) = 1344.83$, $A(K=0) = A(K=1) = 10.018$, and $B = 35.44$]

J	$K^\pi = 0^-$			$K^\pi = 1^-$		
	E_{expt}	E_{calc}	A	E_{expt}	E_{calc}	A
1	1786.11	≡1786.11	–	1358.90	≡1358.90	–
2	–	–	–	1403.74	1403.93	11.21
3	1913.90	≡1913.90	12.78	1431.47	≡1431.47	4.62
4	–	–	–	1541.71	1545.18	13.78
5	2129.24	2137.24	11.96	1574.12	1568.76	3.24
6	–	–	–	1760.76	1765.57	15.55
7	–	2450.27	–	1795.32	1776.65	2.47

Table 3. Experimental E_{expt} and calculated E_{calc} values of the energy of levels and values of the inertia parameter A for bands with $K_i^\pi = 1_1^-$ and 2_1^- in ^{168}Er (in keV) [the parameters used to calculate E_{calc} are the following (in keV): $\epsilon_0(K=1) = 1143.85$, $\epsilon_0(K=2) = 1306.04$, $A(K=1) = A(K=2) = 10.275$, and $B = 8.49$]

J	$K=1$			$K=2$			
	E_{expt}	E_{calc}	A^+	E_{expt}	E_{calc}	A^+	A
1	1358.90	1364.4	–	–	–	–	–
2	1403.74	≡1403.74	–	1569.75	≡1569.75	–	–
3	1431.47	1466.0	–	1633.46	1630.4	–	10.67
4	1541.71	≡1541.71	9.86	1541.71	≡1541.71	10.70	10.71
5	1574.12	1670.7	–	1820.48	1826.3	–	10.13
6	1760.76	1759.2	9.96	1949.64	1953.7	10.48	10.76
7	1795.32	1896.6	–	–	2104.0	–	–

The calculations were performed for the interaction between even-spin levels of the $K^\pi = 1^-$ and 2^- bands. At fixed energies of the $J = 2$ and 4 levels, the difference of the experimental and calculated energies for $J = 6$ levels is 1.5 keV for the $K = 1$ band and 4 keV for the $K = 2$ band. The difference of 3 keV and 6 keV for 3^- and 5^- levels in $K = 2$ band may be connected with the influence of $K = 0$ band.

The band-mixing parameter $B = 8.49$ keV is significantly less than that for the $K = 0$ and $K = 1$ bands: $B = 35.44$ keV. The structure of the bands was established in [5]: 1^-, $n[633]\uparrow - n[512]\uparrow$, 72% and 2^-, $n[633]\uparrow - n[521]\uparrow$, 27%.

5. INTERACTION OF $K_i^\pi = 2_1^+$ AND 0_2^+ BANDS IN ^{162}Dy

The 0_2^+ and 2_1^+ rotational bands in ^{162}Dy [7] are shown in Fig. 2. They intersect at the energy of 2.44 MeV and the spin values of $J = 11$ and 12. Here, some other mechanism of mixing should take place because there is no Coriolis interaction between $\Delta K = 2$ levels.

On the top of Fig. 2, the signature splitting in the $K^\pi = 2^+$ γ-vibrational band is shown. At $J = 12$, there is the largest amplitude of signature splitting, and we see the inversion of the spin position after $J = 11$. Up to $J = 12$, higher positions have values A for odd J; after $J = 12$, they have values of A for even J. The dependence of the parameters $A^+(J \to J-2) = \Delta E/2(2J+1)$ and A^- for even-spin and for odd-spin levels, respectively, is shown in the lower part of Fig. 2. We can see the anomaly in the dependence $A^+(J)$ in both bands at $J = 12$. The lowest value for the 0_2^+ band corresponds to the influence of the 2_1^+ band. A smooth dependence for odd-spin levels means that the anomaly is associated with the interaction of even-spin levels in both bands as they intersect.

To understand the repulsion mechanism, it is necessary to know the structure of intersecting bands and the energy and the structure of the 1^+ states if Coriolis effect takes place here. The interaction parameters calculated for other bands may be useful for their analysis.

ACKNOWLEDGMENTS

I am grateful to V.O. Sergeev for an enlightening discussion and comments.

REFERENCES

1. A. Bohr, K. Dan. Vidensk. Selsk. Mat. Fys. Medd. **26** (14) (1952).
2. B. Singh, Nucl. Data Sheets **75**, 199 (1995).
3. E. P. Grigoriev and V. G. Soloviev, *Structure of Even Deformed Nuclei* (Nauka, Moscow, 1974).
4. V. S. Shirley, Nucl. Data Sheets **71**, 261 (1994).
5. V. G. Soloviev, A. V. Sushkov, and N. Yu. Shirikova, Fiz. Élem. Chastits At. Yadra **27**, 1643 (1996) [Phys. Part. Nucl. **27**, 667 (1996)].
6. V. G. Soloviev, A. V. Sushkov, and N. Yu. Shirikova, Fiz. Élem. Chastits At. Yadra **31**, 786 (2000) [Phys. Part. Nucl. **31**, 385 (2000)].
7. R. G. Helmer and C. W. Reich, Nucl. Data Sheets **87**, 317 (1999).

Physics of Atomic Nuclei, Vol. 65, No. 4, 2002, pp. 645–652. From Yadernaya Fizika, Vol. 65, No. 4, 2002, pp. 677–684.

Cold and Hot Binary and Ternary Fission Yields in the Spontaneous Fission of ^{252}Cf*

J. H. Hamilton[**], A. V. Ramayya, J. K. Hwang, G. M. Ter-Akopian[1),2)], A. V. Daniel[1),2)], J. O. Rasmussen[3)], S.-C. Wu[3)], R. Donangelo[3),4)], C. J. Beyer, J. Kormicki, X. Q. Zhang, A. M. Rodin[1)], A. S. Fomichev[1)], G. S. Popeko[1)], J. Kliman[1)], L. Krupa[1)], M. Jandel[1)], Yu. Ts. Oganessian[1)], G. Chubarian[5)], D. Seweryniak[6)], R. V. F. Janssens[6)], W. C. Ma[7)], R. B. Piercey[7)], W. Greiner[8)], and J. D. Cole[9)]**

Department of Physics, Vanderbilt University, Nashville, USA

Received July 20, 2001

Abstract—The spontaneous fission (SF) of ^{252}Cf has been studied via γ–γ–γ coincidence and light charged particle—γ–γ coincidence with Gammasphere. The yields of correlated Mo–Ba pairs in binary fission with 0–10 neutron emission have been remeasured with an uncompressed cube. The previous hot fission mode with 8–10 neutron emission seen in the Mo–Ba split is found to be smaller than earlier results but still present. New $0n$ binary SF yields are reported. By gating on the light charged particles detected in ΔE–E detectors and γ–γ coincidence with Gammasphere, the relative yields of correlated pairs in alpha ternary fission with zero to $6n$ emission are observed for the first time. The peak occurs around the $\alpha 2n$ channel. A number of correlated pairs are identified in ternary fission with ^{10}Be as the light charged particle. We observed only cold, $0n$ ^{10}Be and little, if any, hot, xn ^{10}Be channels.

1. INTRODUCTION

Studies of prompt γ rays emitted in spontaneous fission (SF) with large detector arrays have given new insights into the fission process [1–5]. From γ–γ–γ coincidence studies of the prompt γ rays emitted in the SF of ^{252}Cf with Gammasphere, yields of individual correlated pairs in binary and ternary fission were determined for the first time for 0 to 10 neutron emission [2–4]. Earlier we reported an ultrahot fission mode in the Mo–Ba split in the ^{252}Cf SF [2]. By using an uncompressed γ–γ–γ cube, problems in the fission data analysis from complexity in the spectra in the 8–10 neutron emission yields were overcome. The new Mo–Ba yields show a reduced yield for the ultrahot mode. These data also allowed the extraction of more accurate zero neutron emission yields in cold binary fission. A new experiment was carried out in which the light charged particles (LCP) involved in ternary fission were detected in an LCP–γ–γ coincidence mode. From gating on the α particles and a γ ray, the relative 0 to $6n$ yields associated with α ternary fission were extracted. Gamma rays associated with new correlated pairs in coincidence with high-energy ^{10}Be particles also were identified. These data give new insights into fission. In contrast to α ternary SF, only the $0n$ mode is observed for ^{10}Be.

2. A NEW DETERMINATION OF THE Ba–Mo YIELD MATRIX FOR ^{252}Cf

We carried out pioneering work on the quantitative determination of yield matrices, using γ–γ and γ–γ–γ coincidence data to extract yields of particular fragment pairs in the SF of ^{252}Cf [2–4]. One interesting finding was that $\approx 0.5\%$ of the ^{252}Cf Ba–Mo split proceeds via a "hot fission" mode, where as many as 10 neutrons are emitted [2, 3]. This latter feature stimulated some theoretical speculations and also some scepticism, since the hot fission mode

*This article was submitted by the authors in English.

[1)]Flerov Laboratory of Nuclear Reactions, Joint Institute for Nuclear Research, Dubna, Russia.
[2)]Joint Institute for Heavy Ion Research, Oak Ridge, USA.
[3)]Lawrence Berkeley National Laboratory, USA.
[4)]Instituto de Física, Universidade Federal do Río de Janeiro, Brazil.
[5)]Cyclotron Institute, Texas A & M University, USA.
[6)]Argonne National Laboratory, USA.
[7)]Department of Physics, Mississippi State University, USA.
[8)]Institut für Theoretische Physik, J.W. Goethe Universität, Frankfurt M., Germany.
[9)]Idaho National Engineering and Environmental Laboratory, USA.
**e-mail: hamilton@nucax1.phy.vanderbilt.edu

Table 1. Pairwise percentage yields of Mo–Ba fission fragments [10]

Mo\Ba	138	140	141	142	143	144	145	146	147
102		<0.01		<0.01	0.03(1)	0.09(1)	0.17(1)	0.21(1)	0.05(1)
103		0.02(1)	0.04(2)	0.05(1)	0.18(2)	0.59(1)	0.70(2)	0.46(1)	0.18(1)
104	0.003(2)	0.06(1)	0.05(1)	0.23(1)	0.46(2)	1.25(1)	0.77(1)	0.46(1)	0.05(1)
105	<0.01	0.06(1)	0.12(2)	0.56(1)	0.89(3)	1.28(2)	0.53(2)	0.14(1)	<0.01
106	0.004(2)	0.14(1)	0.20(1)	0.87(1)	0.83(2)	0.73(1)	0.14(1)	0.04(1)	
107	0.02(1)	0.23(1)	0.29(2)	0.44(1)	0.31(2)	0.18(1)	0.03(1)		
108	0.004(1)	0.19(1)	0.14(2)	0.14(1)	0.05(1)	0.02(1)			

(called Mode 2) has been reported only in the Ba–Mo pairs in ^{252}Cf and not in ^{248}Cf SF [6]. There have been some theoretical efforts to understand how this hot fission could arise [4, 7, 8]. In the present work we used our 1995 Gammasphere data, taken by the GANDS95 collaboration [2]. The analysis was carried out with uncompressed triple coincidence spectra. This differs from the previous analysis, where either uncompressed double coincidence spectra or compressed triple coincidence spectra were used. In both of these methods one faces problems because of the vast number of γ rays in the spectrum and particularly because of the degeneracy of several γ rays in the 8–10 neutron emission yields for Mo–Ba.

In this new analysis, using the uncompressed three-dimensional data, we remeasured the pair yields of Ba ($Z = 56$) with Mo ($Z = 42$) partners. Because ^{104}Mo and ^{108}Mo have $2^+ \to 0^+$ transitions that are too close in energy to resolve and their $4^+ \to 2^+$ transitions are barely resolvable with peak-fitting routines, we have generally chosen to double-gate on the Ba fragments and measure the $2^+ \to 0^+$ intensities in the Mo partners (and $4^+ \to 2^+$, where the $2^+ \to 0^+$ are unresolvable). The Ba double gates are on the $4 \to 2 \to 0$ cascade and the $3 \to 2 \to 0$ cascade, the latter being significant in the heavier bariums where octupole deformation is reported [9]. The odd-A nuclei are special cases discussed in a separate publication. Their yields in our triple-coincidence analysis fall rather smoothly into the yield patterns of their even–even neighbours. In the yield calculations we have taken into account that Compton suppression is not complete and that, also, Compton scattering on the walls of the chamber and into a detector occur and that true continuum gammas are simultaneously present. Rather than using one of the existing gamma efficiency curves for Gammasphere, as determined off-line with radioactive standards in a single mode, we checked the efficiency curves with rotational cascades in the actual experiment, double-gating on two transitions high in the rotational band and measuring the intensities of the lower transitions in the band. Thus, these efficiency measurements involved coincidence efficiencies and take into account Compton suppression, "time-walk," and other factors at the high count rates of the actual experiment.

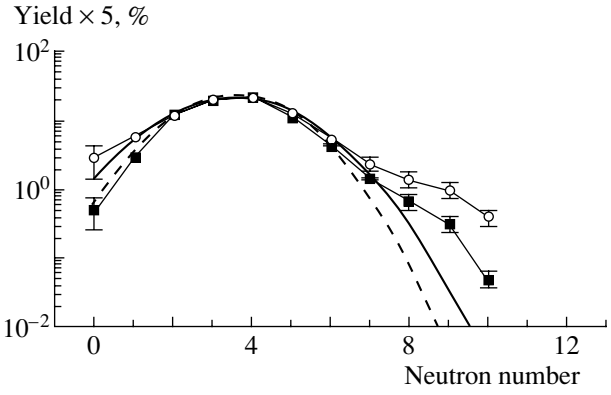

Fig. 1. Ba–Mo fission yields vs. the number of prompt fission neutrons. Closed squares and open circles connected with thin lines, respectively, show data obtained in the present work and reported in papers [2, 3]. The dashed and thick solid curves approximate these data with Gaussians.

In Table 1 we give the fission yields in percent. The columns are labeled by the Ba mass numbers and the rows by the Mo mass numbers. The numbers in parentheses after each value are the statistical standard deviations (s.d.), taken as the square root of the sum of the squares of the peak fit of the value and the average of the squares of the two shifted-gate background subtractions. We have summed the $4^+ \to 2^+ \to 0^+$ cascade and the $3^- \to 2^+ \to 0^+$ cascade contributions of the Ba gates and the $2^+ \to 0^+$ and the $2^+_\gamma \to 0^+$ Mo peaks in the resulting spectra to give yields in Table 1 as close as possible to twofold coincidence yields. Our yields are normalized so that the sum of ^{106}Mo yields matches that of Ter-Akopian *et al.* [2, 3].

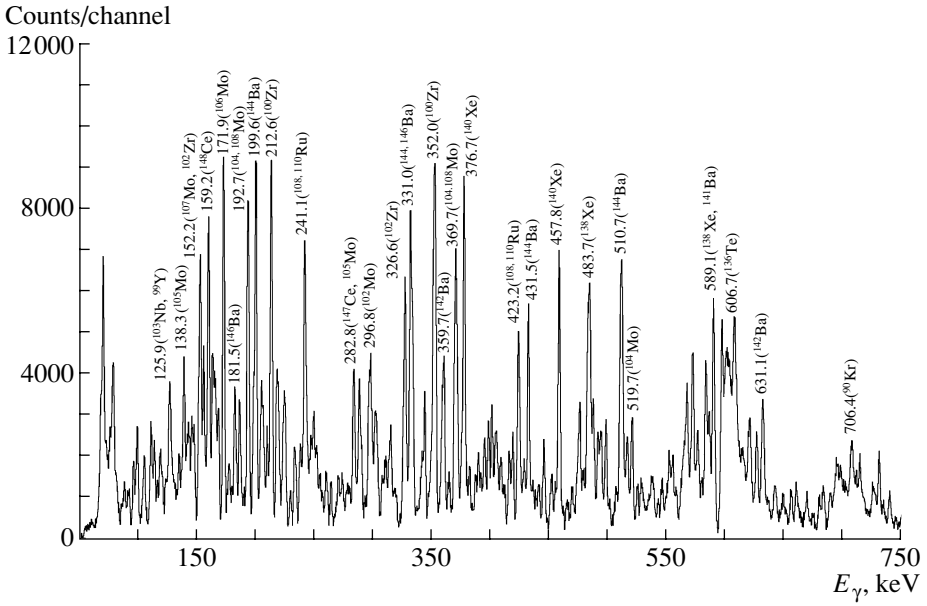

Fig. 2. Spectrum of γ rays detected in coincidence with α particles emitted in the ternary fission of ^{252}Cf. Peaks of γ rays emitted by various fragments formed in the ternary α-particle fission are labeled in the spectrum.

Figure 1 shows semilog plots of the summed Ba–Mo fission yields vs. neutron-emission number found in our work and in the previous work [2, 3]. One sees that the hot fission mode is still present but its intensity is reduced by about a factor of 3 from the 14% reported earlier [2]. Since work was completed, Biswas *et al.* [11] also reported analogous data that show a similar small irregularity around eight neutrons lost. They reported they could not observe a 10-neutron loss. We do report one such cell, ^{104}Mo–^{138}Ba, but with a large s.d., as $(0.003 \pm 0.002)\%$.

3. COLD BINARY SF

Since the neutronless binary events are much smaller than those with neutrons emitted, double-gating techniques have been employed to extract the yields for the cold binary fission. No direct measurements of yields of correlated pairs in cold binary fission had been made prior to our work. Earlier we reported the first results for the correlated pairs in cold binary fission in ^{252}Cf [1, 3] and ^{242}Pu [12]. Subsequently we extracted additional and more accurate yields of cold binary fission [4] from Gammasphere data with 72 detectors.

The cold binary fission yields are shown in Table 2 along with the theoretical values predicted by Sandulescu *et al.* [13]. In Table 2, the first reports of the cold binary fission of an odd-Z–odd-Z fragmentation is shown for the Tc–Cs pair and of an even-Z–odd-A pair. The overall agreement with the theory is generally good, including the predicted enhancement of the odd-Z and odd-A cases.

4. LCP TERNARY FISSION

More recently, another experiment was performed incorporating charged particle detectors to detect ternary particles in coincidence with γ rays in Gammasphere. The energy spectrum of charged particles

Table 2. Average cold binary fission yields from gates on two light fragment and two heavy fragment transitions (results of two different predictions made in [13] are presented in columns 4 and 5)

Fragments	A_L/A_H	$Y_{\rm exp}$	$Y_{\rm th}$	$Y_{\rm th}^{\rm (ren)}$
Zr/Ce	100/152	0.010(2)	0.38	0.004
	102/150	0.020(4)	2.82	0.033
	103/149	0.030(6)	4.21	0.049
	104/148	0.010(2)	1.03	0.012
Mo/Ba	104/148	0.010(2)	0.47	0.005
	106/146	0.040(8)	0.61	0.007
	107/145	0.070(14)	3.07	0.036
	108/144	0.030(6)	7.45	0.087
Tc/Cs	109/143	0.090(18)	11.03	0.128
Ru/Xe	110/142	0.060(12)	3.78	0.044
	111/141	0.10(2)	7.12	0.083
	112/140	0.020(4)	0.59	0.007
	114/138	0.020(4)	1.17	0.014
Pd/Te	116/136	0.050(20)	2.35	0.027

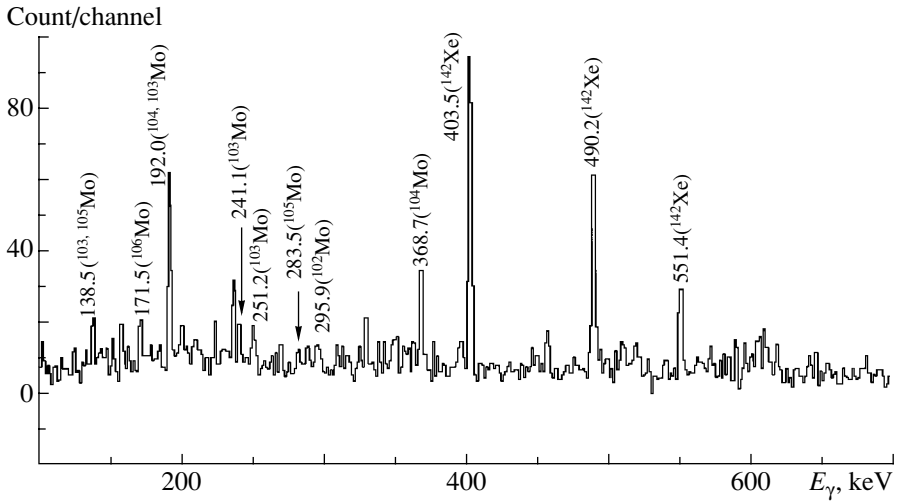

Fig. 3. The same spectrum as in Fig. 2 with a condition that, in addition to the coincidence with ternary α particles the γ rays should be also in coincidence with the $2^+ \rightarrow 0^+$ transition in ^{142}Xe.

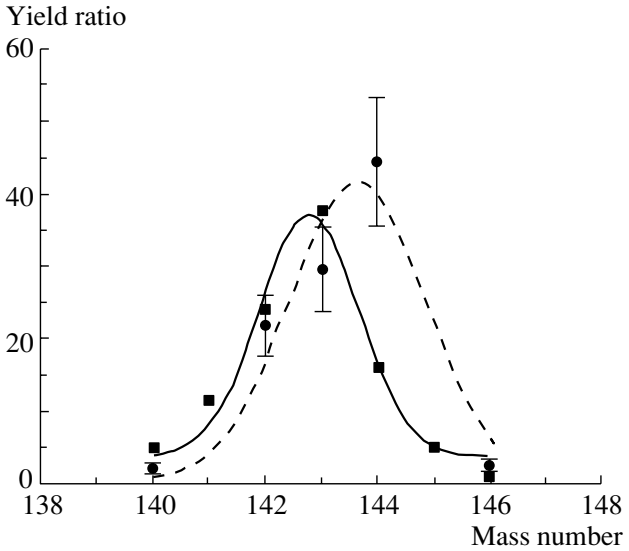

Fig. 4. Yield distribution vs. the number of prompt neutrons obtained for binary (closed squares) and ternary α (closed circles) fission resulting in Ba isotopes emitted as heavy fragments in coincidence with the partner ^{106}Mo and ^{102}Zr, respectively. The solid and dashed curves show Gaussian approximations with average neutron emission equal, respectively, 3.2 and 2.4.

emitted in the spontaneous fission of ^{252}Cf was measured by using two ΔE–E Si detector telescopes installed at the center of the Gammasphere array at Argonne National Laboratory. With the position resolution of the strip detector (2-mm-wide strips), the ΔE–E telescopes provided unambiguous Z and A identification for all the LCP of interest. The energy calibration of the telescopes was performed with ^{224}Ra and ^{228}Th radioactive sources. The γ spectrum in coincidence with ternary α particles is shown in Fig. 2. In this spectrum, one can easily see the γ transitions for various partner nuclei where a ternary α particle is emitted. For example, Xe and Mo isotopes are partners, where α and xn are emitted. Now, imposing an additional condition that the α-gated γ spectrum should be also in coincidence with the $2^+ \rightarrow 0^+$ transition in ^{142}Xe, one gets a very clean spectrum as shown in Fig. 3. Various α, xn fission channels are marked on the spectrum. From the analysis of the γ-ray intensities in these types of spectra, one can calculate the yield distributions. The yield distributions both for binary and ternary α channel from 0 to $6n$ emission are shown in Fig. 4 for two particular channels. These are the first relative 0–$6n$ yields for any ternary α SF. Note the peak of the

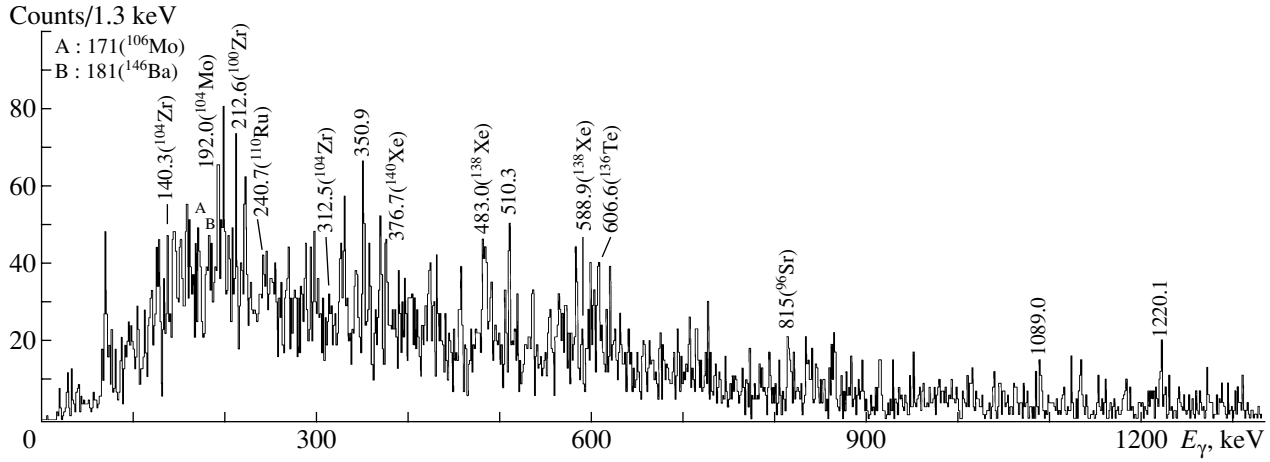

Fig. 5. Gamma spectrum gated on ^{10}Be particles. Several peaks are marked with several isotopes related to the present work. (It is hard to assign the right isotopes to each peak because of the expected γ-ray multiplicity in this spectrum.)

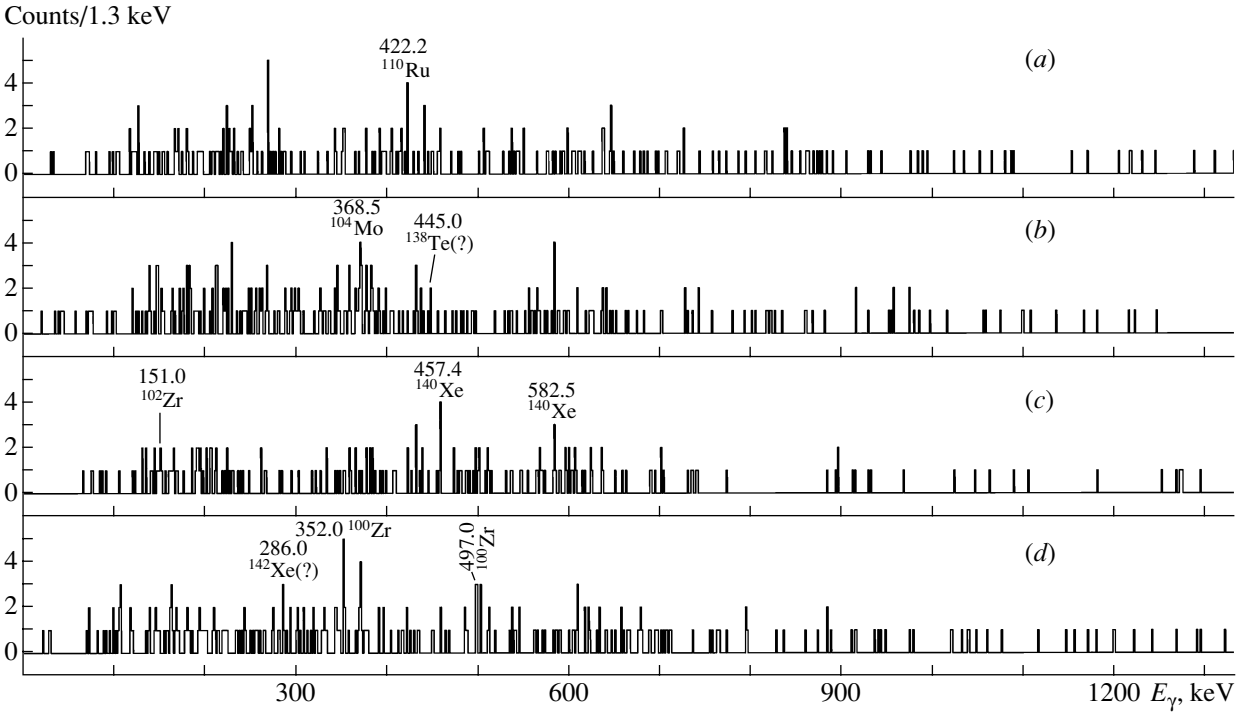

Fig. 6. Coincidence spectra gated on the ^{10}Be particle and (*a*) 240.7 keV (^{110}Ru), (*b*) 192.0 keV (^{104}Mo), (*c*) 376.7 keV (^{140}Xe), and (*d*) 212.6 keV (^{100}Zr) transitions.

neutron emission yields for Ba–α–^{102}Zr is shifted up about 0.5 u from the Ba–^{106}Mo binary yield and so the average neutron emission in this α ternary SF channel is shifted down by about 0.8n. About 20% of the α yield is from ^{5}He ternary fission in ^{252}Cf SF.

5. IDENTIFICATION OF THE COLD ^{10}Be TERNARY SF PAIRS OF ^{252}Cf

Ternary fission is a very rare process that occurs roughly only once in every 500 SF dominated by α ternary fission. Roughly, the ^{10}Be particles are emitted once per 10^5 SF. The maximum yield in the binary SF is located around three to four neutrons. We now find that the α ternary fission is, mostly, accompanied by $\approx$2 to 3 neutrons.

In neutronless ternary SF, the two larger fragments have very low excitation energy and high kinetic energies. Experimentally it is not easy to identify the γ transitions of the cold or hot ^{10}Be ternary SF

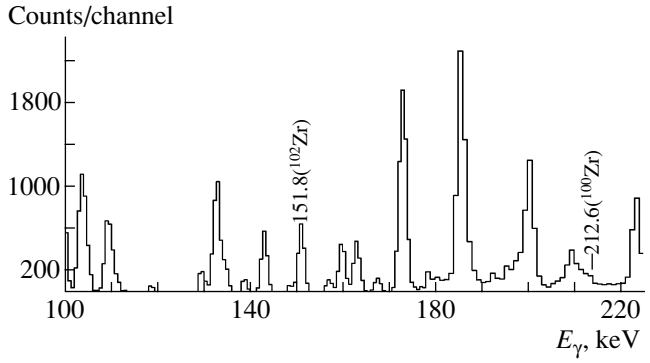

Fig. 7. Coincidence spectrum double-gated on 376.7 and 457.3 keV transitions in ^{140}Xe. See 151.2 (^{102}Zr) and 212.6 (^{100}Zr).

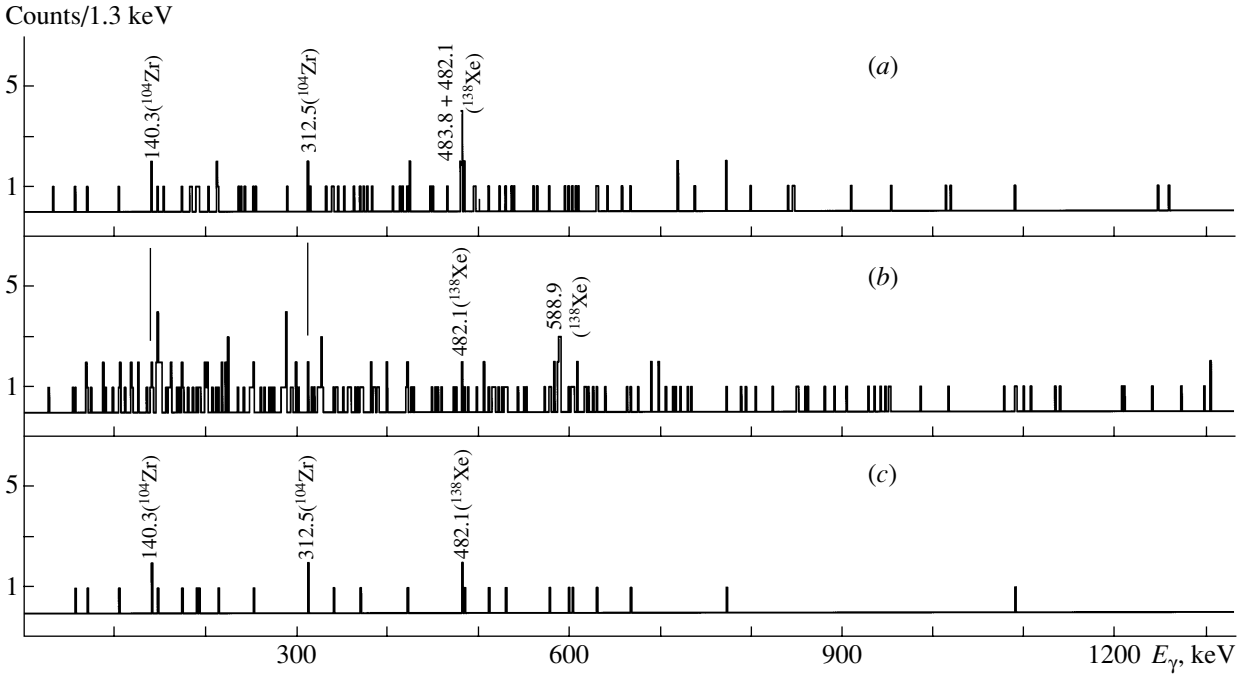

Fig. 8. Coincidence spectra gated on the ^{10}Be particle and (*a*) 588.9 keV (^{138}Xe) and (*b*) 483.8 keV (^{138}Xe) transitions. (*c*) Coincidence spectrum with "AND" gate of 588.9 and 483.8 keV (^{138}Xe) transitions, and gated on ^{10}Be. This logical "AND" gate takes arithmetic minimum of two spectra for each channel in the Radware program [16].

pair because it is a very rare process. The first case of neutronless ^{10}Be ternary SF in ^{252}Cf was reported from a $\gamma-\gamma-\gamma$ coincidence spectrum where the pairs are ^{96}Sr and ^{146}Ba without neutrons emitted [5]. In our LCP$-\gamma-\gamma$ data, the cover foils allowed only the high energy tail of the ^{10}Be energy spectrum to be observed in the particle detector and their partners established from the 3*D* cube data. In the present work, the neutronless (cold) ^{10}Be ternary spontaneous fission pairs of ^{252}Cf are identified for two other fragment pairs of ^{104}Zr$-^{138}$Xe and ^{106}Mo$-^{136}$Te from the analysis of the $\gamma-\gamma$ matrix gated by the ^{10}Be particles. Also, several isotopes related to the ^{10}Be ternary SF are observed.

From the $\Delta E-E$ plot, the ^{10}Be charged particles are selected as a gate to make the $\gamma-\gamma$ matrix. Here we selected a narrow time gate of a width of $\approx$80 ns between the γ rays and the ^{10}Be charged particles. Also, we did not subtract the background spectrum from the full projection of the $\gamma-\gamma$ matrix because of poor statistics. The high efficiency of Gammasphere enables coincidence relationships to be established even with the low-statistics data associated with a small ^{10}Be ternary SF yield. The γ spectrum gated on the ^{10}Be charged particles is shown in Fig. 5. Several peaks are marked with isotopes related to

Table 3. Fragments identified from the coincidence relationship between γ rays and ^{10}Be ternary particle (* identified in $\gamma-\gamma-\gamma$ data and ** in LCP$-\gamma-\gamma$ data)

Identified isotopes (β_2 [14, 15])	Observed γ rays, keV	Partner isotopes (β_2 [14, 15])
$^{100}_{40}$Zr (0.321)	212.6, 352.0, 497.0	$^{142}_{54}$Xe (0.145)*
$^{102}_{40}$Zr (0.421)	151.8, 326.2	$^{140}_{54}$Xe (0.1136)*
$^{104}_{40}$Zr (0.381)	140.3, 312.5	$^{138}_{54}$Xe(0.0309)**
$^{104}_{42}$Mo (0.325) (or $^{108}_{42}$Mo)	192.0, 368.5	$^{138}_{52}$Te (0.000) (or $^{134}_{52}$Te)
$^{106}_{42}$Mo (0.353)	171.6 with 606.6 (^{136}Te)	$^{136}_{52}$Te (0.000)**
$^{110}_{44}$Ru (0.303) (or $^{108}_{44}$Ru)	240.7, 422.2	$^{132}_{50}$Sn (0.000) (or $^{134}_{50}$Sn)
$^{136}_{52}$Te (0.000)	606.6, 424.0	$^{106}_{42}$Mo (0.353)**
$^{138}_{54}$Xe (0.0309)	588.9, 483.8, 482.1	$^{104}_{40}$Zr (0.381)**
$^{140}_{54}$Xe (0.1136)	376.7, 457.4, 582.5	$^{102}_{40}$Zr (0.421)*

the present work. It is sometimes hard to assign the right isotopes from the energies of the peaks alone because the same energy transition may be present in one or more isotopes. For example, the strong 212-keV peak in the spectrum can come from several sources such as ^{100}Zr, ^{111,113}Rh, and ^{147}La. So next, in the ^{10}Be gated $\gamma-\gamma$ matrix, we set a gate on the 212.6 keV energy in ^{100}Zr. There we can see the 352.0 ($4^+ \to 2^+$) and 497.0 ($4^+ \to 2^+$) keV transitions in ^{100}Zr. Four examples are shown in Fig. 6 to identify ^{110}Ru (or ^{108}Ru), ^{104}Mo (or ^{108}Mo), ^{140}Xe, and ^{100}Zr, respectively. But the identification of the γ transitions belonging to these partner fragments is not clear in those spectra. From the $\gamma-\gamma-\gamma$ cube we could clearly establish coincidence for ^{100}Zr–^{142}Xe and ^{102}Zr–^{140}Xe. Also, by double gating on the 376.7 and 457.3 keV γ rays in ^{140}Xe (Fig. 7), we can see clearly the zero neutron channel ^{102}Zr and probably the ^{100}Zr $2n$ channel, which is weaker by a factor of 5–10 if present. The identification of several isotopes related with the ^{10}Be emission is made by the observation of two or three transitions in coincidence belonging to each isotope and from the $\gamma-\gamma-\gamma$ cube. All isotopes and the related γ transitions identified in the present work are tabulated in Table 3. In Table 3, partner fragments pertaining to the cold (neutronless) channel are shown, some of which are confirmed as noted. Quadrupole deformations for each isotope are taken from [14, 15]. From these examples, we can see that the statistics of the coincident spectrum with a single gate on the lowest gamma transition does not depend on the statistics of the gated peak shown in Fig. 1 because of complexity of the γ-ray multiplicity and the enhanced population of the low-lying levels in the ^{10}Be SF.

Two fragment pairs, ^{138}Xe–^{104}Zr and ^{136}Te–^{106}Mo with no neutrons emitted show γ rays produced from both pair fragments in the ^{10}Be gated coincidence spectrum with a single γ gate. In other words, the 171.6 keV transition of ^{106}Mo is observed in the coincidence spectrum with a single gate on the 606.6 keV transition of ^{136}Te. Also, the 140.3 and 312.5 keV transitions in ^{104}Zr are observed in the coincidence spectrum with a single gate on the 588.9 keV transition of ^{138}Xe. For a single gate set on the 588.9 keV transition ($2^+ \to 0^+$) in ^{138}Xe, the coincidence spectrum is shown in Fig. 8. The $4^+ \to 2^+$ and $2^+ \to 0^+$ transitions in ^{104}Zr and the 483.8 and 482.9 keV doublet transitions ($6^+ \to 4^+$ and $4^+ \to 2^+$) in ^{138}Xe show up clearly. To find the real peaks coincident with both the 588.9 and 483.8 keV transitions, we set the "AND" gate of 588.9 and 483.8 keV transitions as shown in Fig. 8. This logical "AND" gate takes arithmetic minimum of two spectra for each channel in the Radware program [16]. Then only three transitions of energies 140.3 keV ($2^+ \to 0^+$) and 312.5 keV ($4^+ \to 2^+$) in ^{104}Zr and 482.1 keV ($6^+ \to 4^+$) transition in ^{138}Xe show up clearly in Fig. 8. Although the three peaks in Fig. 8*c* contain only two counts, the background is less than 0.01/channel in Fig. 8. The 140.3 and 312.5 keV transitions do not exist in the level scheme of ^{138}Xe. Since the $\gamma-\gamma$ matrix is gated by ^{10}Be particles, 140.3 and 312.5 keV transitions belong to the partner nucleus ^{104}Zr. However, 109.0 and 146.8 keV transitions in ^{103}Zr (^{10}Be + $1n$ channel) and the 151.8 and 326.2 keV transitions in ^{102}Zr (channel ^{10}Be + $2n$) do not show up clearly. In another case of ^{136}Te–^{106}Mo, also, the channels ^{10}Be + $1n$ and ^{10}Be + $2n$ are not observed. This could be caused by the larger feeding to the ground state but more likely by small yields in the channels ^{10}Be + n and ^{10}Be + $2n$. The

hot fission mode can excite the fragments up to higher level energies than the cold fission. Therefore, SF yields of the channels $^{10}\mathrm{Be}+n$ and $^{10}\mathrm{Be}+2n$ have to be smaller than the neutronless (cold) ^{10}Be SF yield. The present results indicate that the cold (neutronless) process is dominant in the ternary SF accompanying a heavy third particle such as ^{10}Be with high kinetic energy.

In our work, we are gating only on the high kinetic energy part of the ^{10}Be particles. The ^{104}Zr isotope is highly deformed with a β_2 value of around 0.4 [15, 16] and the ^{138}Xe nucleus is very spherical. Therefore, the ^{10}Be particle seems to be emitted from the breaking of $^{148}\mathrm{Ce} = {}^{138}\mathrm{Xe}+{}^{10}\mathrm{Be}$ at scission which would enhance the ^{10}Be kinetic energy. Increased deformation at the scission point increases excitation energy for the third ternary particle and two heavy fragments. Therefore, the possibility of observing the exciated levels in both the fragments increases when both of them are deformed at the scission point such as ^{104}Zr (deformed)–^{148}Ce(^{138}Xe+^{10}Be) (deformed). Actually, the neutronless binary fission yield for the ^{148}Ce–^{104}Zr pair is as high as 0.05(3) per 100 SF of ^{252}Cf [17]. These cases are very similar to the one we reported earlier for the pair ^{96}Sr (spherical shape) and ^{146}Ba (deformed shape) [5].

In the α ternary fission we see the cold, zero, neutron fission but $2n$ and $3n$ channels are much stronger. However, for the cold ^{10}Be ternary SF pairs identified from the γ–γ matrix gated on ^{10}Be charged particles and the 3D data, we find the zero neutron channel clearly much stronger than $1n$ and $2n$. This is a very unique discovery in the study of cold (zero neutron) fission processes.

ACKNOWLEDGMENTS

Research at Vanderbilt University and Mississippi State University is supported in part by the US Department of Energy under grant nos. DE-FG05-88ER40407 and DE-FG05-95ER40939. Work at Idaho National Engineering and Environmental Laboratory is supported by the US Department of Energy under contract no. DE-AC07-76ID01570. Work at Argonne National Laboratory is supported by the Department of Energy under contract no. W-31-109-ENG-38. Work at JINR (Dubna) and J.W. Goethe University (Frankfurt) is partly supported by grants from the Russian Foundation for Basic Research (grant no. 98-02-04134) and DFG (346RUS) 113/484/O(R).

REFERENCES

1. J. H. Hamilton *et al.*, J. Phys. G **20**, L85 (1994).
2. G. M. Ter-Akopian, J. H. Hamilton, Yu. Ts. Oganessian, *et al.*, Phys. Rev. Lett. **77**, 32 (1996).
3. G. M. Ter-Akopian *et al.*, Phys. Rev. C **55**, 1146 (1997).
4. A. V. Ramayya, J. H. Hamilton, J.K. Hwang, *et al.*, in *Heavy Elements and Related New Phenomena,* Ed. by R. K. Gupta and W. Greiner (World Sci., Singapore, 1999), Vol. 1, p. 477.
5. A. V. Ramayya, J. K. Hwang, J. H. Hamilton, *et al.*, Phys. Rev. Lett. **81**, 947 (1998).
6. N. Schultz, private communication.
7. Yu. U. Pyatkov *et al.*, Nucl. Phys. A **624**, 140 (1997).
8. R. Donangelo, J. O. Rasmussen, M. O. Stoyer, *et al.*, Int. J. Mod. Phys. E **7**, 669 (1998).
9. J. H. Hamilton, S. J. Zhu, A. V. Ramayya, *et al.*, in *Nuclear Structure 98, Gatlinburg, USA, 1998,* Ed. by C. Baktash (American Inst. of Physics, New York, 1999), p. 473.
10. S.-C. Wu, R. Donangelo, A. V. Daniel, *et al.*, Phys. Rev. C **62**, 041601 (2000).
11. D. C. Biswas, R. K. Choudhury, M. Cinausero, *et al.*, Eur. Phys. J. A **7**, 189 (2000).
12. Y. X. Dardenne, R. Aryaeinejad, S. J. Asztalos, *et al.*, Phys. Rev. C **54**, 206 (1996).
13. A. Sandulescu, A. Florescu, F. Carstoiu, *et al.*, Int. J. Mod. Phys. E **7**, 625 (1998).
14. S. Raman, C. H. Malarkey, W. T. Milner, *et al.*, At. Data Nucl. Data Tables **36**, 1 (1987).
15. P. Moller, J. R. Nix, W. D. Myers, *et al.*, At. Data Nucl. Data Tables **59**, 185 (1995).
16. D. C. Radford, Nucl. Instrum. Methods Phys. Res. A **361**, 297 (1995).
17. J. H. Hamilton, A. V. Ramayya, S. J. Zhu, *et al.*, Prog. Part. Nucl. Phys. **35**, 635 (1995).

Physics of Atomic Nuclei, Vol. 65, No. 4, 2002, pp. 653–657. From Yadernaya Fizika, Vol. 65, No. 4, 2002, pp. 685–689.

Anisotropic α Decay*

D. S. Delion[1], A. Insolia, and R. J. Liotta[2]**

Department of Physics and Astronomy, University of Catania and INFN, Catania, Italy

Received September 3, 2001

Abstract—A microscopic approach to the problem of anisotropic α decay in deformed nuclei is presented. Nuclear wave functions are calculated within the BCS approach, and the WKB semiclassical approximation is used for the penetration through the deformed Coulomb barrier. Results are compared with recent experimental data obtained at CERN by the ISOLDE and NICOLE collaborations. The predictions of the model for well-deformed nuclei are in very good agreement with experimental findings.
© *2002 MAIK "Nauka/Interperiodica".*

1. INTRODUCTION

It was shown long ago that, in odd-mass actinides at very low temperature, alpha particles are emitted preferentially with respect to the direction of the total nuclear spin [1–5]. Recently, new experiments [6] have renewed interest in this problem by reporting anisotropic emission in some At, near spherical isotopes, in connection with several theoretical descriptions of this effect.

Preferential emission of alpha particles from deformed nuclei was first explained by Hill and Wheeler [7] and then by Bohr, Fröman, and Mottelson [8] in terms of the penetration of an alpha cluster through a deformed Coulomb barrier. It was thus found that, since, for a prolate nucleus, the barrier at the poles is thinner than at the equator, the probability of penetrating through the barrier is larger along the nuclear-symmetry axis. More recently, Berggren [9] proposed an *alpha + core* model in order to explain observed anisotropies for almost spherical At isotopes. The quadrupole–quadrupole interaction acting between the already existing structureless alpha cluster and an odd-mass core was diagonalized within a weak-coupling scheme. The strength of the interaction was adjusted to obtain the energy of the emitted alpha particle. Several solutions with pronounced anisotropy were obtained on the basis of this model [10]. No good comparison with available data was obtained. Buck *et al.* [11] describe the alpha decay of odd-mass nuclei within a similar model in which the depth of the alpha–core potential (taken as a square well), the alpha-formation probability, and the number of nodes in the radial wave function are fitted to experimental data. Rowley *et al.* [12] followed the same philosophy, diagonalizing the quadrupole–quadrupole interaction in an extreme-cluster-model basis. Stewart *et al.* [13], using either semiclassical or coupled-channels transmission matrices without any formation mechanism, also calculated anisotropic α emission.

The traditional Hill and Wheeler line was adopted in [14, 15], but use was made there of a realistic deformed mean field with a large *configuration space + pairing* residual interaction in computing the alpha-cluster-preformation amplitude inside a nucleus. The penetration through a deformed Coulomb barrier was estimated within the WKB approximation [8]. The anisotropy was explained mainly by the effect of the deformed barrier (see [16] for an overview on the microscopic approach to the alpha-decay problem).

The objective of the present article is to give a short account of our work on anisotropic alpha-particle emission from odd-mass nuclei at low temperatures. We will discuss some predictions of [14, 15], as well as some more recent calculations, yet unpublished, in connection with the experimental results obtained by Schuurmans *et al.* on anisotropy in At, Fr, and Pa isotopes [17, 18]. We will show that our predictions were very well confirmed by recent experimental findings in well-deformed nuclei.

2. MICROSCOPIC DESCRIPTION OF ANISOTROPY

The mechanism used in [14, 15] to describe the emission of an alpha particle involves a classical two step process [19]: first, four nucleons cluster at a point of the nuclear surface with a given formation

*This article was submitted by the authors in English.

[1]Institute of Physics and Nuclear Engineering, Bucharest, Romania; e-mail: delion@theor1.theory.nipne.ro

[2]KTH—Institute of Physics, Stockholm, Sweden; e-mail: liotta@msi.se

**e-mail: Antonio.Insolia@catania.infn.it

amplitude; afterward, this object penetrates through the Coulomb barrier.

Let us consider the decay process

$$B(I_i, K_i, M_i) \to A(I_f, K_f, M_f) + \alpha, \qquad (1)$$

where K_i (K_f) and M_i (M_f) are the projections of the initial (final) total angular momenta in, respectively, the intrinsic and the laboratory frame [19].

We describe the parent and daughter nuclei within the BCS approximation; that is, the wave function for a nucleus X (A or B) is

$$|\phi^X\rangle = a^+_{k\Omega}|(\mathrm{BCS})\rangle^X_\pi \otimes |(\mathrm{BCS})\rangle^X_\nu, \qquad (2)$$

where π (ν) labels proton (neutron) degrees of freedom. The operator $a^+_{k\Omega}$ is the creation operator for an unpaired nucleon with projection Ω on the intrinsic symmetry axis, and k stands for the other quantum numbers. In the case of favored transitions of an odd-mass nucleus, the quantum numbers $k\Omega$ of the odd nucleon remain unchanged during the decay process.

The formation amplitude can be written as [14, 15]

$$F(R,\vartheta,\varphi) = \sum_L F_L(R,\vartheta,\varphi) \qquad (3)$$

$$= \sum_L \int d\xi_\alpha d\xi_A [\phi_\alpha(\xi_\alpha)\phi^A(\xi_A) \times Y_L(R,\vartheta,\varphi)]^*_{J_B M_B} \phi^B(\xi_B),$$

where R is the distance between the cluster and the daughter nucleus and ξ represents the internal coordinates. The intrinsic wave function for the alpha particle has a standard Gaussian form. Additional details on the evaluation of the multidimensional integral in Eq. (3) can be found in [14, 15].

Experimentally, nuclei are typically first produced, then separated, implanted into a foil of a ferromagnet material (cooled down to a few 10^{-2} mK) and eventually oriented by applying a strong magnetic field. The anisotropy is thus measured with respect to the direction of the applied magnetic field [17, 18].

If full alignment is not achieved in orienting the implanted isotopes, the conditions are such that one has to perform averaging over the initial distribution of the angular-momentum projections M_i. The total width is given by

$$\Gamma(\vartheta,\varphi) = \frac{\hbar v}{4\pi}\left(\frac{R}{G_0(E,R)}\right)^2 \sum_l F_l^2 W(\vartheta), \qquad (4)$$

where F_l is the partial-wave formation amplitude for the emitted alpha particle; i.e.,

$$F_l = \exp\left\{-\frac{2l(l+1)}{\chi}\sqrt{\left(\frac{\chi}{kR}-1\right)}\right\} \qquad (5)$$

$$\times \sum_\Omega (-1)^\Omega \langle I_i K_i l - \Omega | I_f K_f\rangle \sum_{l'} K^\Omega_{ll'} a_{l'\Omega}(R).$$

The matrix element $K_{ll'}$, as well as the quantities χ and $G_0(E,R)$, is defined as in [14] (see also [8] for additional details). The microscopic formation amplitude enters into the calculation through the amplitude $a_{l'\Omega}(R)$ in Eq. (4).

The function W in (4) determines the angular distribution of the emitted particle. After recoupling l and l' to the angular momentum L of the emitted alpha particle and under the assumption that the nucleus involved is axisymmetric, one gets

$$W(\vartheta) = \sum_L A_L P_L(\cos\vartheta), \qquad (6)$$

where the amplitudes A_L are given in terms of the F_l amplitudes of Eq. (5) [15].

3. NUMERICAL CALCULATIONS AND DISCUSSION

We will apply the above formalism to a few selected cases of the anisotropic α decay of odd–even nuclei. In particular, we will discuss ^{241}Am, At isotopes, ^{221}Fr, and the ^{227,229}Pt isotopes.

3.1. Application to the α Decay of ^{241}Am

In this section, we present an application of the formalism developed above to the case of the favored transition [15]

$$^{241}\mathrm{Am} \to ^{237}\mathrm{Np} + \alpha, \qquad (7)$$

for which $K_i = K_f = I_i$, the Nilsson quantum numbers of both the parent and daughter nuclei being $5/2^-[523]$. The deformed Woods–Saxon potential is diagonalized by using 18 major shells [20]. The deformation parameters were chosen to be $\beta_2 = 0.22$, $\beta_3 = 0$, and $\beta_4 = 0.08$. The total width was computed according to the above formalism. We obtained $\Gamma_{\mathrm{theor}} = 2.09 \times 10^{-34}$ MeV, which is quite close to the experimental value of $\Gamma_{\mathrm{expt}} = 3.34 \times 10^{-34}$ MeV. As to the case of even–even nuclei [15, 16], the absolute alpha-decay widths for odd nuclei are given within the right order of magnitude. For instance, in the case of $^{243}\mathrm{Am} \to ^{239}\mathrm{Np} + \alpha$, we obtained $\Gamma_{\mathrm{theor}} = 1.17 \times 10^{-33}$ MeV, which is to be compared with the experimental value of $\Gamma_{\mathrm{expt}} = 1.96 \times 10^{-33}$ MeV. However, the main goal of our analysis is to determine the influence of deformation on the angular distributions of emitted alpha particles.

The model predicts a large enhancement of the anisotropy versus quadrupole deformation. The role

of deformations with multipolarities higher than the quadrupole one is much less important [15]. The influence of the intrinsic structure of the parent and daughter wave functions can be estimated by studying the angular distribution versus the angular-momentum transfer L. We found that, if only the $L = 0$ component is included, the total width Γ versus ϑ shows a variation that is 10% smaller than that in the case where all L components are included. This result evinces the important role of the barrier deformation. As a matter of fact, the $L = 0$ part of the formation amplitude is isotropic, in which case the calculated anisotropy must be entirely attributed to the barrier. A similar feature was found in axially deformed even–even nuclei [14]. Although higher L contributions seem to give rise to a small effect, one should bear in mind that, without the inclusion of deformations and without a large basis included in the calculation of single-particle states, one would fail to reproduce the absolute value of the width by many orders of magnitude [16].

The function $W(\vartheta)$ is a relevant quantity in dealing with the anisotropy in alpha-decay processes. Once the microscopic formation amplitude has been calculated, one can easily expand the function W in terms of even-order Legendre polynomials, as is shown in Eq. (6).

We found that, in the case where all nuclei are assumed to be aligned with the maximum projection of the total angular momentum in the laboratory frame, M_i, the coefficients A_L have the same phase [15].

Applying the reduction procedure of [3], we can compare the calculated W values with the experimental data [3] at $1/T = 90.5\ \mathrm{K}^{-1}$. We did this and obtained the results presented in Table 1.

The agreement can be considered to be remarkable, especially if one considers that the absolute normalization is given by the formation amplitude entering into the evaluation of the coefficients A_L.

3.2. At Isotopes

With the basis and the residual interaction previously discussed, we now proceed to evaluate the absolute decay widths and the coefficients W versus the deformation parameters for At isotopes. An important motivation for this study is the comparison with recent experimental data obtained at ISOLDE (CERN) [17].

For many At isotopes (from the odd-proton nucleus ^{207}At with $I_i = I_f = 9/2^-$), we have calculated the dependence of the amplitudes A_L and of the anisotropy of the decay on the deformation parameter β_2. We have found, within our model [15], that the amplitudes A_L [as well as the coefficients $W(\vartheta)$] are almost similar for different isotopes. The only relevant parameter is the nuclear deformation.

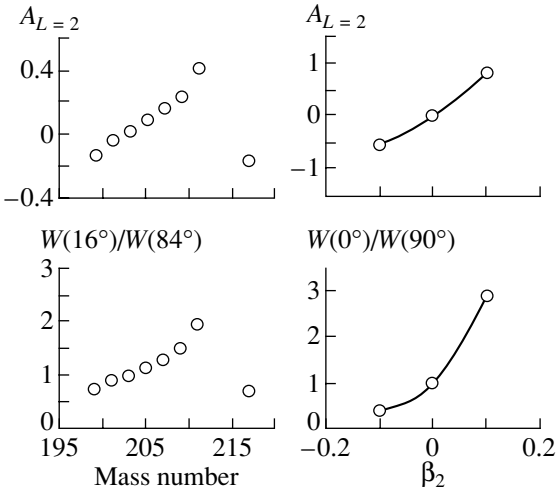

Predictions from [15] for the amplitudes A_L (right upper panel) and anisotropy versus deformation (right lower panel) for a typical case of ^{207}At; experimental results of [17] for the same quantities (left panels). The results seem to suggest that the anisotropy increases with increasing prolate deformation.

In the right panels of the figure, we present our predictions from [15] for the amplitudes A_L and the anisotropy versus the deformation for a typical case. In the left panels of the figure, the experimental results of [17] are displayed. Our results seem to suggest that the anisotropy increases with increasing prolate deformation. This is a possible key to interpret the experimental data [17]. We agree that this interpretation brings about the problem associated with the possibility that the deformation increases as one approaches ^{211}At. Some criticism has been raised against this interpretation; a different interpretation of the data from [17] was proposed.

Anyway, the data of [17] suggest (in terms of the model) a sharp change in the nuclear properties (deformation from a prolate to an oblate case, for instance) to justify a dramatic decrease in the measured anisotropy ratio down to values smaller than unity.

It is worth mentioning that the model has no free parameter and that the anisotropic ratio is strongly

Table 1. Function $W(\vartheta)$ at $\vartheta = 0$ and $\vartheta = \pi/2$ versus the measured anisotropy for the favored transition $^{241}\mathrm{Am} \to {}^{237}\mathrm{Np} + \alpha(\Omega^\pi = 5/2^-)$

ϑ	W_{theor}	W_{expt}
0	1.500	1.610
$\pi/2$	0.736	0.714

Table 2. Deformations and experimental and computed coefficients A_2 for $^{221}_{87}$Fr and for the Pa isotopes indicated in the table [18]

Isotope	β_2	β_3	$A_2^{\rm th}$	$A_2^{\rm exp}$
$^{221}_{87}$Fr	−0.069	0.0	−0.215	−0.375
	0.120	0.15	−0.373	
$^{227}_{91}$Pa	0.168	0.0	0.649	0.696
	−0.068	0.1	0.748	
$^{229}_{91}$Pa	0.185	0.0	0.733	1.13
	0.185	0.08	0.808	

dependent on the deformation (see, for instance, the results in [15] for almost spherical Rn isotopes, with appreciable differences between cases of ^{207}Rn and ^{207}At nuclei, which have the same mass number, so that any difference should be attributed only to different properties of the odd neutron and proton orbital entering into the problem).

A general comment is in order: we can say that the coefficient A_2 is positive (in the phase with $A_0 = 1$) for prolate deformations and negative (opposite phase) for oblate ones. The other coefficients A_L with $L \neq 2$ are virtually negligible. The values of A_4 are one order of magnitude smaller than A_2. In spite of this, it is interesting to note that A_4 is positive and symmetric with respect to the deformation parameter β_2. A similar qualitative and even quantitative behavior is found for other At isotopes. Actually, all the features discussed above are essentially the same even for the odd–neutron case of ^{207}Rn ($I_i = I_f = 5/2$) and the other Rn isotopes.

3.3. The Case of ^{221}Fr and Pa Isotopes

Finally, it is of great interest to quote the most recent results of Schuurmans *et al.* [18] for well-deformed nuclei. For ^{221}Fr, a $K = 1/2$ ground state was assumed with a prolate deformation [18], while a previous calculation [14, 15] used an oblate ground state with $K = I = 5/2$ (displayed in the first line of Table 2 as a theoretical prediction for $A_2^{\rm theor}$). For Pa isotopes, a prolate ground state was taken for the favored $5/2^- \to 5/2^-$ ($^{227}_{91}$Pa $\to \alpha +$ $^{223}_{89}$Ac) and $5/2^+ \to 5/2^+$ ($^{229}_{91}$Pa $\to \alpha +$ $^{225}_{89}$Ac) transitions. The results are reported in Table 2 (adapted from [18]).

The agreement between the microscopic model and the experimental data is excellent. The calculation of the total widths gives $\Gamma = 0.64 \times 10^{-25}$ MeV and $\Gamma = 0.29 \times 10^{-28}$ MeV for the $^{227}_{91}$Pa and $^{229}_{91}$Pa, respectively.

As was already discussed explicitly for the ^{241}Am case, the $L = 0$ part in the formation amplitude is the largest contribution. The neglect of higher multipoles in the formation amplitude produces anisotropy only slightly smaller (10–20% in relation to the case in which all multipolarities are included). This shows that the main role is played by the penetration through the deformed barrier. The effect is therefore expected to be larger for very well deformed nuclei.

4. CONCLUDING REMARKS

A realistic microscopic approach to calculating the formation amplitude for the alpha-decay problem in axisymmetric deformed nuclei has been constructed within the well-known approach by Mang and Rasmussen (see, e.g., [19] and references therein). It is worthwhile to stress the main ingredients of the alpha-width calculation for deformed nuclei: (a) the use of a realistic deformed mean field, (b) a large shell-model space, (c) an exact diagonalization of the deformed mean field, and (d) no cut (within the selected large basis) in calculating the alpha-formation amplitude. The predicted absolute values of the total alpha widths are reproduced within 10–30% [16].

In the model, we performed a systematic microscopic calculation of quantities related to alpha-particle emission from oriented odd-mass nuclei; in particular, we have done this for $_{85}$At, $_{86}$Rn, $_{87}$Fr, and $_{91}$Pa isotopes.

We have found that the probability of emitting an alpha particle in the polar direction with respect to the corresponding probability in the equatorial direction is strongly dependent on the emission angle. For prolate deformations, this ratio is above unity, while, for oblate deformations, it is less than one. We have also found that deformations higher than quadrupole deformation can play an important role in some cases. Even in the region of near spherical nuclei, the anisotropy was found to be measurable. In addition, we have found that the main role in the observed anisotropy is due to deformed-barrier penetration. This has been recently confirmed experimentally in the case of well-deformed nuclei [18]. A different interpretation was suggested for the case of quasispherical nuclei [18].

In this study, we have emphasized the importance of anisotropies in alpha-decay processes as a tool for extracting intrinsic deformation parameters in nuclei.

REFERENCES

1. S. H. Hanauer, J. W. T. Dabbs, L. D. Roberts, *et al.*, Phys. Rev. **124**, 1512 (1961); Q. O. Navarro, J. O. Rasmussen, and D. A. Shirley, Phys. Lett. **2**, 353 (1962).

2. A. J. Soinski, R. B. Frankel, Q. O. Navarro, *et al.*, Phys. Rev. C **2**, 2379 (1970).
3. A. J. Soinski and D. D. Shirley, Phys. Rev. C **10**, 1488 (1974).
4. D. Vandeplassche, E. van Walle, C. Nuytten, *et al.*, Phys. Rev. Lett. **49**, 1390 (1982).
5. F. A. Dilmanian *et al.*, Phys. Rev. Lett. **49**, 1909 (1982).
6. J. Wouters *et al.*, Phys. Rev. Lett. **56**, 1901 (1986); Nucl. Instrum. Methods Phys. Res. B **26**, 463 (1987); N. G. Nicolis *et al.*, Phys. Rev. C **41**, 2118 (1990).
7. D. L. Hill and J. D. Wheeler, Phys. Rev. **89**, 1102 (1953).
8. P. O. Fröman, K. Dan. Vidensk. Selsk. Mat. Fys. Medd. **1** (3) (1957); A. Bohr, P. O. Fröman, and B. Mottelson, K. Dan. Vidensk. Selsk. Mat. Fys. Medd. **29** (10) (1955).
9. T. Berggren, Phys. Lett. B **197**, 1 (1987); Hyperfine Interact. **43**, 407 (1988).
10. T. Berggren, Phys. Rev. C **50**, 2494 (1994).
11. B. Buck, A. C. Merchant, and S. M. Perez, J. Phys. G **18**, 143 (1992).
12. N. Rowley, G. D. Jones, and M. W. Kermode, J. Phys. G **18**, 165 (1992).
13. T. L. Stewart *et al.*, Phys. Rev. Lett. **77**, 36 (1996); Nucl. Phys. A **611**, 332 (1996).
14. A. Insolia, P. Curutchet, R. J. Liotta, *et al.*, Phys. Rev. C **44**, 545 (1991); D. S. Delion, A. Insolia, and R. J. Liotta, Phys. Rev. C **46**, 1346 (1992).
15. D. S. Delion, A. Insolia, and R. J. Liotta, Phys. Rev. C **46**, 884 (1992); **49**, 3024 (1994).
16. R. G. Lovas, R. J. Liotta, A. Insolia, *et al.*, Phys. Rep. **294**, 265 (1998); D. S. Delion, A. Insolia, and R. J. Liotta, Phys. Rev. C **54**, 292 (1996).
17. NICOLE and ISOLDE Collab. (P. Schuurmans *et al.*), Phys. Rev. Lett. **77**, 4720 (1996); NICOLE and ISOLDE Collab. (J. Krause *et al.*), Phys. Rev. C **58**, 3181 (1998).
18. NICOLE and ISOLDE Collab. (P. Schuurmans *et al.*), Phys. Rev. Lett. **82**, 4787 (1999).
19. R. G. Thomas, Prog. Theor. Phys. **12**, 253 (1954); H. J. Mang, Annu. Rev. Nucl. Sci. **14**, 1 (1964).
20. R. Bengtsson *et al.*, Phys. Scr. **39**, 196 (1989); S. Cwiok *et al.*, Comput. Phys. Commun. **46**, 379 (1987).

Physics of Atomic Nuclei, Vol. 65, No. 4, 2002, pp. 658–663. From Yadernaya Fizika, Vol. 65, No. 4, 2002, pp. 690–695.

Dripline Nuclei*

B. Jonson**

Experimentell Fysik, Chalmers Tekniska Högskola och Göteborgs Universitet, Sweden

Received August 31, 2001

Abstract—A review of some recent experimental studies of dripline nuclei is given. The main emphasis is devoted to light nulcei and especially to the occurrence of halo states. © *2002 MAIK "Nauka/Interperiodica".*

1. INTRODUCTION

Current nuclear physics focuses on exploring nucleonic matter under extreme conditions, which can be created in modern accelerator laboratories. The opportunities offered by beams of exotic nuclei for research in the areas of nuclear structure physics and nuclear astrophysics are exciting, and worldwide activity in the construction of different types of radioactive beam facilities bears witness to the strong scientific interest in the physics that can be probed with such beams [1]. With access to exotic nuclei at the very limits of nuclear stability, the physics of the neutron and proton driplines have been in focus. The driplines are the limits of the nuclear landscape, where additional protons or neutrons can no longer be kept in the nucleus—they literally drip out. In the vicinity of the driplines, the structural features of the nuclei change compared to nuclei closer to the beta-stability line. It was among neutron-rich light nuclei that a threshold phenomenon, nuclear halo states, was discovered about 15 years ago. Since then, the halo phenomenon has been studied extensively, both experimentally and theoretically, and is now a well-established structural feature of many light dripline nuclei [2–6]. The low binding energy of particles or clusters of particles, combined with high beta-decay energy in the dripline regions, gives rise to exotic nuclear decay modes, such as beta-delayed particle emission and particle radioactivity. The normal nuclear shell closures may disappear and be replaced by new magic numbers. Examples are the recent observations of the breakdown of the $N = 8$ shell closure for ^{12}Be [7, 8] and the new magic number at $N = 16$ [9]. In this review, I shall present some recent studies relevant to the physics of dripline nuclei.

2. DRIPLINE NUCLEI

There has over the past decades been a rapid development of different techniques to study nuclei at the driplines. As defined above the driplines are the edges of the nuclear landscape on the two sides of the peninsula of stable nuclear speices. But let me first point to another development that has been striking. The heaviest elements had been identified up to $Z = 112$ after many years of hard work at GSI and Dubna. Recently there has, however, been a development that is amazingly fast: There are now indications that elements $Z = 114$ [10] and $Z = 116$ [11] have been found at Dubna.

The proton dripline has been reached up to the element Bismuth. This has been done by studies of proton radioactivity, and ground-state proton emitters from ^{105}Sb to ^{185m}Bi [12] have been identified at present. The $N = Z$ line has been reached up to ^{100}Sn, and nuclides with very large proton excess have been observed and studied for many of the lighter elements. Some of the most striking results are the detailed spectroscopic study of the $T_Z = -5/2$ nucleus ^{31}Ar [13] and the recent obsrevation of the doubly-magic $T_Z = -4$ nucleus ^{48}Ni [14].

3. EXPERIMENTAL STUDIES OF HALO STATES

A halo state is a bound state very close to the continuum—the threshold for particle emission. For this reason, the properties of other states of the same nucleus are only of indirect relevance to it. A halo state may be studied via its diagonal matrix elements, accessible through measurements such as nuclear moments or elastic scattering. So far, however, the main body of information has come from its nondiagonal matrix elements, i.e., in processes where the halo is destroyed or created. This is the case for nuclear breakup processes and beta decays, where especially

*This article was submitted by the author in English.

** e-mail: bjn@fy.chalmers.se

the former method has been widely utilized. The momentum distributions of both the halo particles and core fragments have been studied. The distributions revealed narrow momentum widths, which are interpreted as corresponding to the wide spatial size of the halo ground state. There are, however, important steps to take before the measured distributions may be interpreted. It must first be understood how to bridge the gap between experiment and theory—the experimental filter. This has to be included in order to correct the distortions of the picture and must be known in order to make a meaningful comparison. Interpretation is, however, still not completely straightforward, and the reaction mechanism and final-state interactions have to be taken into account.

Two-body halos. In general, two-body nuclear halos are limited to weakly bound nucleon-core systems in relative s or p states [15]. The simplest example is given by ^{11}Be, which to a good approximation may be viewed as a neutron coupled to the quadrupole-deformed ^{10}Be core. The neutron separation energy is 504 keV, and both the ground state, an $1s_{1/2}$ intruder, and the $0p_{1/2}$ first excited state at 320 keV are well-developed halo states. The contribution of core excitations to the ground-state wave function was recently determined from analysis of a $^{11}\mathrm{Be}(p,d)^{10}\mathrm{Be}$ reaction performed in inverse kinematics using a 35.3 MeV/u ^{11}Be beam [16, 17]. The results show a dominant $1s_{1/2}$ component in the ^{11}Be ground state wave function with a 16% $[0d_{5/2}\otimes 2^+]_{1/2^+}$ particle-rotation admixture. A similar result is obtained by comparing cross sections from measured coincidences between ^{10}Be and γ rays [18] after breakup of 60 MeV/u ^{11}Be and from a β-NMR measurement of the nuclear magnetic moment, $\mu(^{11}\mathrm{Be}) = -1.6816(8)\mu_N$ [19].

Several experiments have identified ^{19}C as a one-neutron halo nucleus [20, 21]. The neutron separation energy has been determined from Coulomb dissociation experiments as $S_n = 530 \pm 130$ keV [22]. The $1s_{1/2}$ and $0d_{5/2}$ orbitals are expected to be close in energy, and the ground-state spin has been suggested as either $1/2^+$ ($[1s_{1/2} \otimes {}^{18}\mathrm{C}(0^+)]^{1/2^+}$) or $5/2^+$ ($[0d_{5/2} \otimes {}^{18}\mathrm{C}(0^+)]^{5/2^+}$). In both these cases, contribution from core excitation $^{18}\mathrm{C}(2^+)$ is expected. The presence of the $0d_{5/2}$ component in the wave function results in a less pronounced halo [23, 24] for ^{19}C. The energy sequence between the s and d orbitals is not yet known, but the best present evidence points to the most likely ground state spin as being $1/2^+$ [22, 25, 26].

Three-body halos. The two-neutron halo nuclei have received the most attention among the halo systems. This is due to their Borromean character [2], where the three-body system is bound and its pair-wise subsystems are unbound. The most studied nuclei of this type are ^{6}He, ^{11}Li, and ^{14}Be. Much effort has gone into the experimental determination and theoretical interpretation of the momentum distribution of fragments from breakup reactions. It must be generally expected that for three-body halos the two-body subsystems have a low-lying continuum structure, so final-state interactions become important. But it is also known that knowledge on the two-body substructure can be gained from reactions with three-body systems. An example is provided by single-nucleon stripping experiments, with beams of ^{11}Be and ^{11}Li [27] showing that the ground state of ^{10}Li is an $1s_{1/2}$ intruder state, as in ^{11}Be.

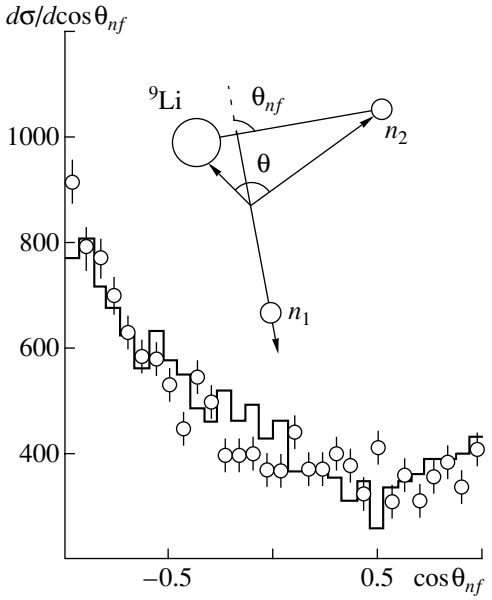

Fig. 1. Distribution of the decay neutrons from ^{10}Li formed in ^{11}Li neutron knockout reactions [32]. The insert shows a schematic diagram of the reaction, where θ_{nf} is the angle between the momentum direction of ^{10}Li reconstructed as a sum of the momenta of the ^{9}Li fragment and the decay neutron and the direction of the n+^{9}Li relative momentum $\mathbf{p}_{nf}$. The distribution asymmetry is due to a linear term in $\cos\theta_{nf}$ and shows that there are contributions from interfering s and p states.

Experiments on three-body halo systems, where the core and one of the neutrons are detected, are referred to as one-neutron knockout (or stripping) reactions. In the sudden approximation, the momentum transfer to the $(A-1)$ system can be neglected in experiments with high beam energy. In the projectile rest frame we have $\mathbf{p}_{n_1} + \mathbf{p}_{n_2} + \mathbf{p}_{\mathrm{C}} = 0$. The momentum transferred to the $(A-1)$ system is then equal to the momentum of the ejected neutron $\mathbf{p}_{n_1}$ with the opposite sign and will therefore reflect the

internal neutron momentum distribution. This is only valid to a certain extent, however. An example is given in an experiment with a beam of 224 MeV/u ^{6}He, where the ^{5}He fragments after one-neutron knockout were studied [28]. The Fourier transformation of the wave function from a three-body cluster model [29] showed too large a momentum width. The reason for this is that the knockout process gives a "wound" in the wave function, and only the remaining part of it should be taken into account. This was done by using a cylindrical-shaped cut [30], and in this way the momentum distribution could be reproduced.

Early theoretical calculations [31] showed that an approximately equal admixture of $(1s_{1/2})^2$ and $(0p_{1/2})^2$ components in the ground state of ^{11}Li gave the best fit to the experimentally measured narrow momentum distribution measured for ^{9}Li recoils after its breakup. The presence of this admixture was recently demonstrated in an experiment with a 287 MeV/u beam of ^{11}Li where the recoil momentum of $\mathbf{p}(^{10}\mathrm{Li}) = \mathbf{p}(^9\mathrm{Li} + n)$ was determined from a complete kinematics experiment performed at GSI [32]. A fit to these data using spherical Hankel functions for the s and p neutrons gives a $(45 \pm 10)\%$ admixture of $(1s_{1/2})^2$ in the ^{11}Li ground state.

In a one-neutron stripping experiment with a 240 MeV/u ^{6}He beam [33] a large spin alignment of the ^{5}He fragment was observed. The angular distribution of the $\mathbf{p}_{\alpha n}$ vector on polar angles in a coordinate system with the z axis parallel to the direction of the $\mathbf{p}_{^5\mathrm{He}}$ momentum shows an anisotropy, which can be described by a correlation function $W(\theta_{\alpha n}) = 1 + 1.5\cos^2\theta_{\alpha n}$. The correlation coefficient is smaller than expected for a pure $(0p_{3/2})^2$, indicating a 7% admixture of $(0p_{1/2})^2$ [34] in the ^{6}He ground-state wave function.

For ^{11}Li, a similar analysis [32] of the distribution of the decay neutrons from the ^{10}Li fragments gave a skew angular distribution (Fig. 1). This is a model independent way to demonstrate the mixing of s and p states in the ^{11}Li ground state wave function.

The heaviest Be isotope ^{14}Be has recently been studied in kinematically complete experiments at GANIL [35] and at GSI [36]. The results are consistent with a large $(1s_{1/2})^2$ admixture in the ground state. An analysis of the skew angular distribution of the decay neutron from ^{13}Be shows that the ^{14}Be ground-state wave function also has contributions from different parity states and gives evidence of a contribution from the $0d_{5/2}$ state.

4. THE $A = 8$ ISOBARIC CHAIN

The $A = 8$ dripline nuclei are ^{8}He and ^{8}B. ^{8}He is a nucleus that best may be described as a five-body cluster consisting of an α core surrounded by four valence neutrons [37]. On the other side of the isobar, the last bound nucleus before the dripline is ^{8}B, which has been shown to be a one-proton halo nucleus, and which is well described in a $(p + {}^3\mathrm{He} + \alpha)$-picture [38, 39]. A similar cluster structure has been suggested for ^{8}Li [38].

The ^{8}He nucleus has a larger two-neutron separation energy than its neighbor, the ^{6}He Borromean nucleus. Its radius is also slightly smaller and early on it was pointed out that its structure is better described as a five-body cluster than a "double" Borromean system. The first experimental indication of a predominant $\alpha + 4n$ structure came from a compilation of cross section data at 790 MeV/u [40] and from experiments on its beta decay. In the latter experiments it was found that almost half of the GT sum-rule strength is concentrated in a state at 9.3 MeV in ^{8}Li, which decays with the emission of tritons together with ^{5}He $(\alpha + n)$. This shows that the ground state of ^{8}He has a large overlap with an $(\alpha + t + n)$ in ^{8}Li [41]. In a recent study of 227 MeV/u ^{8}He breaking up in a carbon target [30], the decay channels up to σ_{-2n} were detected. The difference in interaction cross section between ^{8}He and ^{4}He exceeds the sum of the cross sections of the measured channels by more than 50%. This excess is due to the $\alpha + 4n$ breakup and gives another sign of the five-body structure of ^{8}He. The excitation energy spectrum from the $(^6\mathrm{He} + n + n)$-channel in the same experiment [30] shows a broad distribution of up to about 3.5 MeV. The interpretation of this structure is a relatively narrow 2^+ state with an overlapping broader, higher-lying 1^- state. The interpretation of the dipole state is further supported in an experiment with a lead target which shows an increased excitation probability of the 1^- state [42].

The proton-rich nucleus ^{8}B with $S_p = 138$ keV has been shown to be a one-proton halo nucleus. The first experiments performed at the FRS at GSI [43, 44] revealed a narrow momentum distribution of the ^{7}Be fragments (FWHM value of 91 ± 5 MeV/c) and a large one-proton removal cross section, $\sigma_{-1p} = 98 \pm 6$ mb, in breakup reactions of 1440 MeV/u ^{8}B in a carbon target. The data [44] were reproduced in a model [38, 39] where the ^{8}B wave function was calculated in an extended three-body model $(\alpha + {}^3\mathrm{He} + p)$ with explicit inclusion of the binary $^7\mathrm{Be} + p$ channel. The model [39] predicts a sizeable fraction of core excitation $[^7\mathrm{Be}^*(1/2^-) \otimes 0p_{3/2}]_{2^+}$. In a recent study

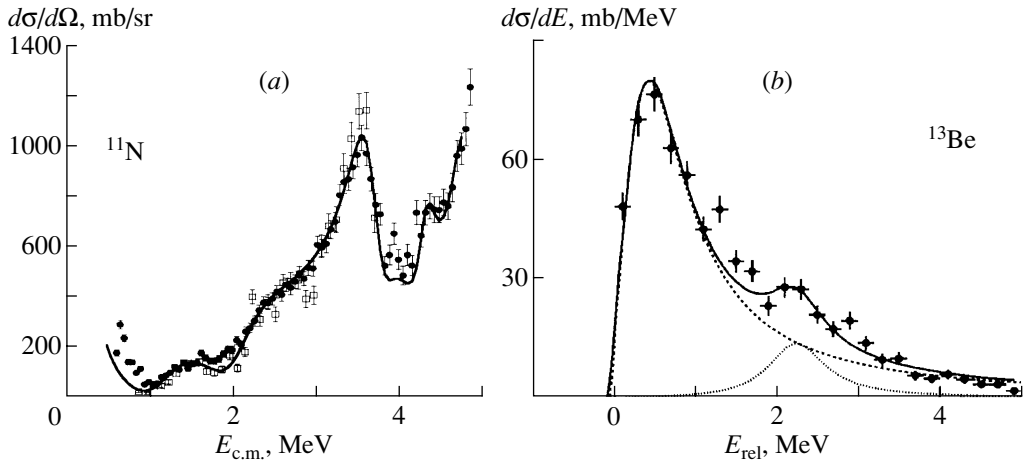

Fig. 2. (*a*) Excitation function of ^{11}N with data from GANIL (filled circles) and MSU (open squares). The curve is a potential model fit with added resonances [55]. (*b*) Relative energy spectrum of ^{12}Be and the decay neutron after one-neutron knockout in ^{14}Be. The solid curve is a fit assuming the ground state to be a neutron in a $l = 0$ motion relative to the core at very low energy with another resonance at 2.3 MeV [36].

[45], the experiments were extended to include measurements of gamma rays in coincidence with the ^{7}Be fragments. A Doppler shifted line, with a center-of-mass energy of 429 keV corresponding to the first excited state in ^{7}Be, could clearly be observed and its intensity shows good agreement with the predicted 15.6% core excitation [39].

5. UNBOUND NUCLEI AT THE DRIPLINE

The relative kinetic energy distribution of α-particle and neutrons from one-neutron knockout reactions in ^{6}He is strongly influenced by the unbound ^{5}He ($I^\pi = 3/2^-$) system [28]. This resonance is comparatively long lived ($\Gamma = 600$ keV, corresponding to a lifetime of more than 300 fm/c) and it therefore decays far away from the reaction zone. The measured spectrum was found to reproduce the expected shape of the ^{5}He, and from an event-mixed correlation function it was shown that the peak in the distribution is a real resonance.

The ground state of ^{7}He is known [46] to have $I^\pi = 3/2^-$, corresponding to a $0p_{3/2}$ orbital according to the standard shell-model prediction. The spin-orbit partner of the ground state was only recently observed in an experiment where ^{7}He was produced in a one-neutron knockout reaction from ^{8}He [30, 47]. The relative energy spectrum of $^6\mathrm{He} + n$ showed a distribution that in a sequential fragmentation model could be fitted with the known ground state resonance and a resonance at $E_r = 1.2$ MeV ($\Gamma = 1.0$ MeV), which is interpreted as the $0p_{1/2}$ spin-orbit partner of the ground state. A second excited state in ^{7}He at an energy 3 MeV above the threshold was observed [48–50] earlier. The decay of this resonance goes mainly into $\alpha + 3n$, which indicates that it is a $5/2^-$ state with probable structure $[^6\mathrm{He}(2^+) \otimes 0p_{1/2}]_{5/2^-}$ [48].

In a recent experiment at MSU [51], ^{9}He was produced from a beam of ^{11}Be. The relative velocity spectrum between ^{8}He and a neutron showed a narrow peak around zero velocity. This is interpreted as an $1s_{1/2}$ ground state in ^{9}He with a scattering length of $a_s = -25$ fm. This adds one more case to the intruder s states in the $N = 7$ isotones, where ^{11}Be was the first case to be observed [52].

It has been shown [53–56] that the $1s_{1/2}$ intruder state also is the ground state of the unbound nucleus ^{11}N—the mirror of ^{11}Be. The results from a resonance scattering experiment performed at GANIL are shown in Fig. 2, where ^{11}N was produced with a radioactive beam of ^{10}C in the reaction $^{10}\mathrm{C} + p \rightarrow {}^{11}\mathrm{N}$. Reactions of this type will certainly be frequently utilized in the investigations of unbound nuclei in the vicinity of the driplines when the new generation of radioactive beam facilities becomes operational.

Theoretical models for ^{11}Li need as input the structure of the low lying states in ^{10}Li. The current experimental situation is that it is quite clear the ground state of ^{10}Li is a $1s_{1/2}$ neutron coupled to the $I^\pi = 3/2^-$ ground state of ^{9}Li. Some of the main experiments are as follows:

(1) The momentum distribution of neutrons in coincidence with ^{9}Li fragments in proton- and neutron-removal reactions from ^{11}Be and ^{11}Li, respectively,

revealed a narrow width that can only be understood if the ground state of ^{10}Li is an s state [27, 31].

(2) The relative velocity distribution of ^{9}Li and neutrons was studied, where the ^{10}Li was produced from an ^{18}O beam [57] and more recently from a ^{11}Be beam [51]. The data are consistent with an s state as the ground state, with a scattering length similar to the one found in [27].

(3) The relative energy spectrum of $^{9}\mathrm{Li} + n$ after one-neutron removal [58] reveals a structure that is consistent with a 2^- state as the ground state. A more recent result [36] confirms the low energy state and also shows a state at about 0.7 MeV, which is interpreted as the $[0p_{1/2} \otimes 3/2^-]_{1^+}$ state.

From this it is clear that ^{10}Li belongs to the group of isotones with a $1s_{1/2}$ intruder as the ground state. The exact energy of the scattering state in the ground state and the position of the p state remains to be determined. Future experiments with radioactive beams as the $d(^{9}\mathrm{Li}, ^{10}\mathrm{Li})p$ reaction for a direct study of the excited states in ^{10}Li or via its isobaric analog states in resonance scattering, $^{9}\mathrm{Li} + p \rightarrow {}^{10}\mathrm{Be}$ (see Fig. 2a) may shed light on this problem.

The relative energy spectrum of $^{12}\mathrm{Be} + n$ obtained from one-neutron knockout reaction data from ^{14}Be measured at GSI [36] is shown in Fig. 2b. The structure at low energy shows that the ground state of ^{13}Be is dominated by a s-motion of the neutron versus the core [59].

6. SUMMARY AND OUTLOOK

In this review, I have given some examples of recent results from a subfield of nuclear physics that is remarkably active at present. It is clear that, to a large extent, the discovery of halo states sparked this interest, but the halo phenomenon is only one of many new elements that have added to the nuclear paradigm for experiments with radioactive nuclear beams. We are still only in the initial stages of exploring the outer parts of the nuclear landscape, and the next generation of experiments with radioactive nuclear beams will undoubtedly provide new possibilities for research with very good chances of discovering unexpected phenomena. High priority should be given to systematic investigations of nuclei spanning the region from stability towards the edges of the nuclear landscape. At the same time there is a need for strong interaction with theory, so that further steps can be taken in carrying out calculations on as fundamental a level as possible.

A few of the burning issues that may be addressed in the years to come can be mentioned. First, it is clear that continued investigations of the structure of halo states not only need better detection techniques and more intensity, but also access to heavier systems. The continuum structure of neutron-rich nuclei in particular is important for a full understanding of these nuclei. The role of the binary subsystems in Borromean nuclei has to be understood in more detail. In this context, unbound nuclei in the vicinity of the dripline could provide essential information. The structural changes in the dripline regions that already have been observed in several cases need more investigation and further mapping. The role of fusion reaction to reach far away from stability with high cross sections should also be investigated. These examples are of direct relevance to halo physics, but other important subjects that RNB physics should address are the exploration of the position of the neutron dripline for heavier elements, the exploration of exotic nuclei with large isospin, the $N = Z$ line up to ^{100}Sn, superheavy elements, and studies of the r- and rp-process paths. On the theory side, better understanding is needed of the connection between cluster and few-body models to shell-model and mean-field theories.

REFERENCES

1. NuPECC Report on Radioactive Nuclear Beam Facilities (2000).
2. M. V. Zhukov *et al.*, Phys. Rep. **231**, 151 (1993).
3. K. Riisager, Rev. Mod. Phys. **66**, 1105 (1994).
4. P. G. Hansen, A. S. Jensen, and B. Jonson, Annu. Rev. Nucl. Part. Sci. **45**, 591 (1995).
5. I. Tanihata, J. Phys. G **22**, 157 (1996).
6. B. Jonson and K. Riisager, Philos. Trans. R. Soc. London, Ser. A **356**, 2063 (1998).
7. A. Navin *et al.*, Phys. Rev. Lett. **85**, 266 (2000).
8. I. Iwasaki *et al.*, Phys. Lett. B **481**, 7 (2000).
9. A. Ozawa *et al.*, Phys. Rev. Lett. **84**, 5493 (2000).
10. Yu. Ts. Oganessian *et al.*, Phys. Rev. Lett. **83**, 3154 (1999).
11. Yu. Ts. Oganessian *et al.*, Phys. Rev. C **63**, 011301(R) (2001).
12. P. J. Woods and C. N. Davids, Annu. Rev. Nucl. Part. Sci. **47**, 541 (1997).
13. H. O. U. Fynbo *et al.*, Nucl. Phys. A **677**, 38 (2000).
14. B. Blank *et al.*, Phys. Rev. Lett. **84**, 1116 (2000).
15. K. Riisager, D. V. Fedorov, and A. S. Jensen, Europhys. Lett. **69**, 547 (2000).
16. S. Fortier *et al.*, Phys. Lett. B **461**, 22 (1999).
17. J. S. Winfield *et al.*, Nucl. Phys. A (in press).
18. T. Aumann *et al.*, Phys. Rev. Lett. **84**, 35 (2000).
19. W. Geithner *et al.*, Phys. Rev. Lett. **83**, 3792 (1999).
20. D. Bazin *et al.*, Phys. Rev. C **57**, 2156 (1998).
21. T. Baumann *et al.*, Phys. Lett. B **439**, 256 (1998).
22. T. Nakamura *et al.*, Phys. Rev. Lett. **83**, 1112 (1999).
23. D. Ridikas *et al.*, Nucl. Phys. A **628**, 363 (1998).
24. M. Smedberg and M. V. Zhukov, Phys. Rev. C **59**, 2048 (1999).
25. J. A. Tostevin and J. S. Al-Khalili, Phys. Rev. C **59**, R5 (1999).

26. P. Banerjee and R. Shyam, Phys. Rev. C **61**, 047301 (2000).
27. M. Zinzer *et al.*, Phys. Rev. Lett. **75**, 1719 (1995).
28. D. Aleksandrov *et al.*, Nucl. Phys. A **633**, 234 (1998).
29. B. V. Danilin *et al.*, Yad. Fiz. **53**, 71 (1991) [Sov. J. Nucl. Phys. **53**, 45 (1991)].
30. K. Markenroth *et al.*, Nucl. Phys. A (in press).
31. I. J. Thompson and M. V. Zhukov, Phys. Rev. C **49**, 1904 (1994).
32. H. Simon *et al.*, Phys. Rev. Lett. **83**, 496 (1999).
33. L. V. Chulkov *et al.*, Phys. Rev. Lett. **79**, 201 (1997).
34. L. V. Chulkov and G. Schrieder, Z. Phys. A **359**, 231 (1997).
35. M. Labiche *et al.*, Phys. Rev. Lett. (in press).
36. H. Simon, PhD Thesis (TU Darmstadt, 1999).
37. M. V. Zhukov *et al.*, Phys. Rev. C **50**, R1 (1994).
38. L. V. Grigorenko *et al.*, Phys. Rev. C **57**, R2099 (1998).
39. L. V. Grigorenko *et al.*, Phys. Rev. C **60**, 044312 (1999).
40. I. Tanihata *et al.*, Phys. Lett. B **289**, 261 (1992).
41. L. Grigorenko *et al.*, Nucl. Phys. A **607**, 277 (1996); **614**, 567 (1997).
42. M. Meister *et al.*, to be published.
43. W. Schwab *et al.*, Z. Phys. A **350**, 283 (1995).
44. M. H. Smedberg *et al.*, Phys. Lett. B **452**, 1 (1999).
45. The FRS Collab. (in press).
46. F. Ajzenberg-Selove, Nucl. Phys. A **490**, 1 (1988).
47. M. Meister *et al.* (in press).
48. A. A. Korsheninnikov *et al.*, Phys. Rev. Lett. **82**, 3581 (1999).
49. H. G. Bohlen *et al.*, Prog. Part. Nucl. Phys. **42**, 17 (1999).
50. M. G. Gornov *et al.*, Russ. Acad. Sci. Bull., Phys. Ser. **62**, 1781 (1998).
51. P. G. Hansen, private communication.
52. D. J. Millener *et al.*, Phys. Rev. C **28**, 497 (1983).
53. L. Axelsson *et al.*, Phys. Rev. C **54**, R1511 (1996).
54. A. Lépine-Szily *et al.*, Phys. Rev. Lett. **80**, 1601 (1998).
55. K. Markenroth *et al.*, Phys. Rev. C **62**, 034308 (2000).
56. J. M. Oliveiera *et al.*, Phys. Rev. Lett. **84**, 4056 (2000).
57. M. Thoennessen *et al.*, Phys. Rev. C **59**, 111 (1999).
58. M. Zinzer *et al.*, Nucl. Phys. A **619**, 151 (1997).
59. H. Simon *et al.* (in press).

Physics of Atomic Nuclei, Vol. 65, No. 4, 2002, pp. 664–668. From Yadernaya Fizika, Vol. 65, No. 4, 2002, pp. 696–700.

Superheavy Hydrogen ^{5}H and Spectroscopy of ^{7}He*

A. A. Korsheninnikov[1)], M. S. Golovkov[1)], A. Ozawa, K. Yoshida, I. Tanihata, Z. Fulop, K. Kusaka, K. Morimoto, H. Otsu, H. Petrascu, F. Tokanai, D. D. Bogdanov[2)], M. L. Chelnokov[2)], A. S. Fomichev[2)], V. A. Gorshkov[2)], Yu. Ts. Oganessian[2)], A. M. Rodin[2)], S. I. Sidorchuk[2)], S. V. Stepantsov[2)], G. M. Ter-Akopian[2)], R. Wolski[2)], W. Mittig[3)], P. Roussel-Chomaz[3)], H. Savajols[3)], E. A. Kuzmin[4)], E. Yu. Nikolskii[4)], B. G. Novatskii[4)], and A. A. Ogloblin[4)]**

RIKEN, Saitama, Japan

Received July 20, 2001

Abstract—Data on the spectroscopy of ^{5}H and ^{7}He from recent experiments with radioactive beams in Dubna and in RIKEN are presented. © *2002 MAIK "Nauka/Interperiodica".*

The neutron-rich nuclei ^{5}H and ^{7}He have been investigated in numerous experiments for 30 years. However, the existence of ^{5}H as a well-defined resonance has yet to be proven conclusively. The ^{7}He ground state, which decays into $n + {}^6$He, was very well established experimentally, but many attempts at observing an excited state of ^{7}He has proven to be futile. We performed a spectroscopic study of ^{5}H and ^{7}He using radioactive beams.

In a search for ^{5}H, we applied an experimental method that is similar to the missing-mass method, but which involves detecting an unstable recoil particle. The usual missing-mass experiment studies a binary reaction $A(b,c)D$, and measurement of the recoil particle c allows one to obtain the excitation spectrum for the residual nucleus D. If the residual system D is very neutron-rich, then, generally speaking, the particle c is very proton-rich and can be even unstable, like, e.g., ^{6}Be, which decays into $p + p + \alpha$, or like the ^{2}He singlet state, which decays into $p + p$. To deal with the unstable recoil nucleus c, one needs to detect all particles from its decay. Having kinematically complete information about the unstable system c, one can determine the excitation energy in the residual system D and study its spectroscopy. Of course, the residual system D can also be unstable.

To detect all particles from the decay of the unstable recoil c, we constructed the RIKEN telescope, which represents a stack of solid-state detectors (Fig. 1). Each detector is position-sensitive (strip-detector); it allows one to determine the coordinates of all particles detected in coincidence—that is, to measure their angles. Energy depositions and energy losses are measured for each particle as well. The detectors have an annular hole, and a beam goes through this hole. With the aid of this telescope, decay products of the unstable recoil c can be detected at small angles in the laboratory frame. This corresponds to measurements under inverse kinematics, which is typical of many experiments with secondary beams.

In a search for ^{5}H, we studied the reaction p (^{6}He, ^{2}He)^{5}H. A secondary beam of ^{6}He with an energy of 36A MeV was obtained from a primary beam of ^{13}C by using the ACCULINA fragment separator at JINR (Dubna). The experimental scheme is shown in Fig. 1. Two plastic scintillators were used to identify each particle of the secondary beam and to measure its energy by the time-of-flight method. The trajectory of ^{6}He was measured by two multiwire proportional chambers. For a target, we used a cryogenic target taken from GANIL (France) and filled with a hydrogen gas at a temperature of 35 K and a pressure of 10 atm. The target thickness was 6×10^{21} proton/cm^2. Two protons from the decay of ^{2}He were detected in coincidences by the RIKEN telescope. Apart from protons, we also detected tritons from the decay process $^5\mathrm{H} \to t + n + n$ using a downstream telescope that consisted of a large-area SSD detector and a BGO crystal.

*This article was submitted by the authors in English.

[1)]On leave from the Russian Research Centre Kurchatov Institute, Moscow, Russia.

[2)]JINR, Dubna, Moscow oblast, 141980 Russia.

[3)]GANIL, CAEN, France.

[4)]Russian Research Centre Kurchatov Institute, pl. Kurchatova 1, Moscow, 123098 Russia.

**e-mail: alexei@postman.riken.go.jp

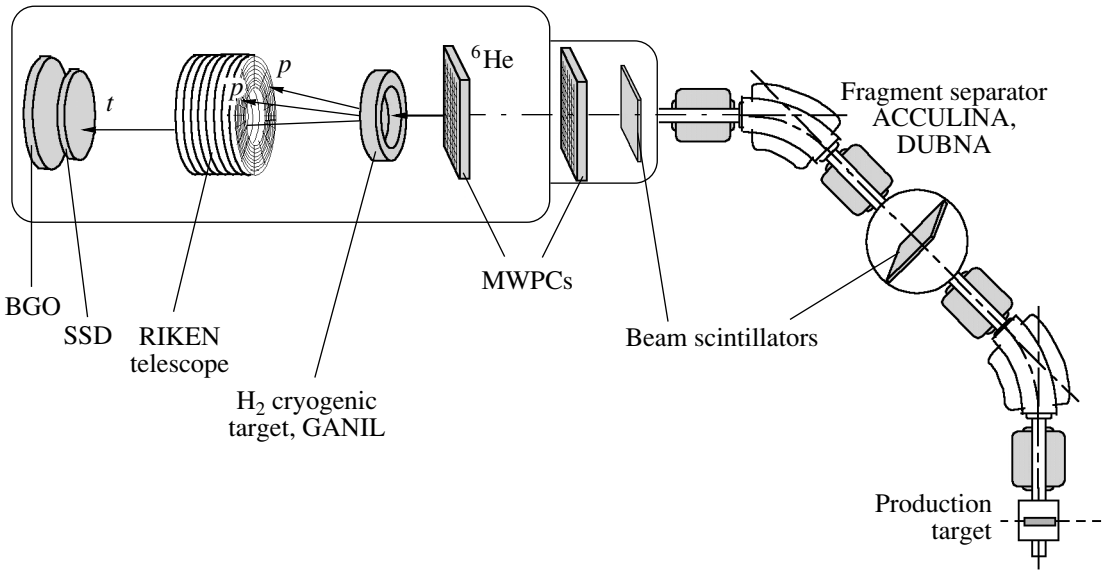

Fig. 1. Experimental setup for search for ^{5}H.

Figure 2 shows a preliminary result for the ^{5}H spectrum extracted from $p+p$ coincidences and measured in coincidences with tritons from the decay of the ^{5}H system, $p(^6\mathrm{He}, ppt)$. The spectrum is shown versus the energy of ^{5}H above the $t+n+n$ decay threshold. The background from measurements with the empty target (instead of the target filled with hydrogen) is negligible in this spectrum. A cutoff at about 7 MeV reflects the detection limit due to the acceptance of the RIKEN telescope.

In the spectrum in Fig. 2, a peak at about 2 MeV, which is a good candidate for the resonance ^{5}H, attracts attention. The analysis of the data is still in progress. On the other hand, the spectra obtained for various reaction channels, $p(^6\mathrm{He}, pt)^3\mathrm{H}$ and $p(^6\mathrm{He}, t)^4\mathrm{He}$, show proper peaks corresponding to the residual nuclei ^{3}H and ^{4}He, confirming the reliability of the results obtained.

Prior to the present conference we found out that, very recently, calculations of ^{5}H were performed within a $t+n+n$ three-body model [1]. In that investigation, the $t+n+n$ continuum was taken into account, in contrast to previous calculations of ^{5}H within the oscillator shell model. The calculations in [1] show the resonance $^5\mathrm{H}(1/2^+)$ in the energy region, which is consistent with our observation of the peak at about 2 MeV.

Let us now address the spectroscopy of ^{7}He. The reaction $p(^8\mathrm{He}, d)^7\mathrm{He}$ was studied in [2]. A secondary beam of ^{8}He at $50A$ MeV was produced by the RIPS fragment separator (RIKEN). For a proton target, use was made of CH_2; background measurements with a carbon foil and an empty target were also performed. The experimental setup used is shown in Fig. 3. Deuterons were detected by the RIKEN telescope at small angles in the laboratory frame, which correspond to a large cross section. Particles emitted from the decay of ^{7}He were detected in addition to the deuterons. Neutrons were measured by the neutron walls of plastic scintillators, while charged particles were bent in a dipole magnet and detected by a drift chamber and a plastic scintillators' hodoscope. These parts of the detection system allowed us to investigate the spectra of deuterons detected in coincidences with

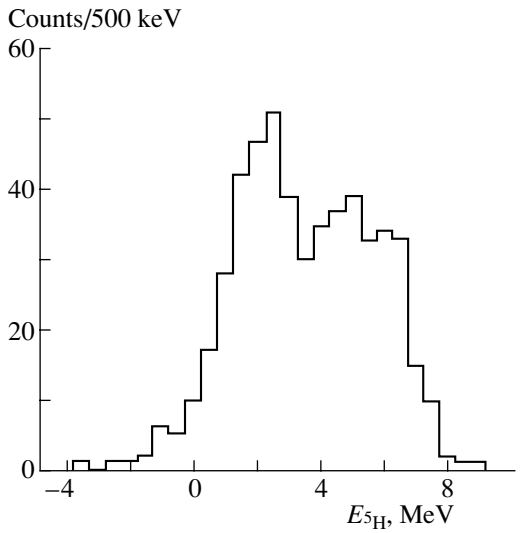

Fig. 2. Missing-mass spectrum of ^{5}H from the reaction $p(^6\mathrm{He}, ppt)$.

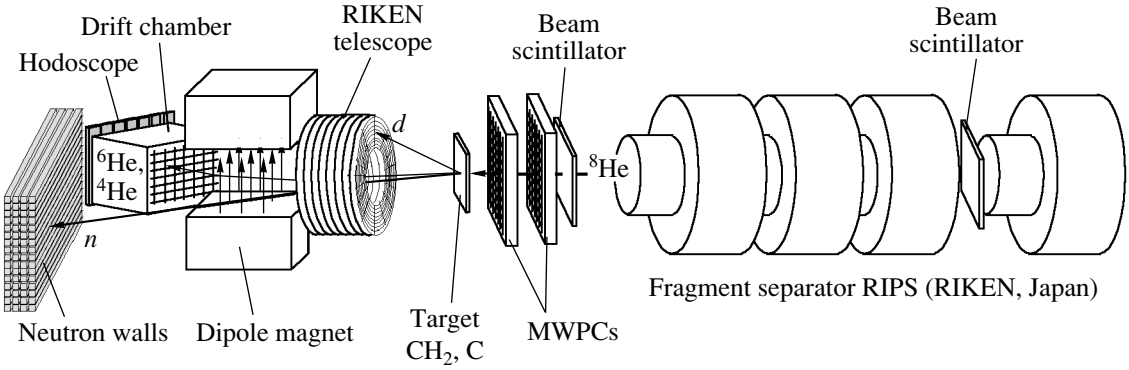

Fig. 3. Experimental setup for the spectroscopy of ^{7}He.

^{6}He, ^{4}He, and neutrons. Other detectors in Fig. 3, beam scintillators and multiwire proportional chambers, were used to identify each beam particle, to measure its energy, and to perform its tracking.

As a result, the deuteron spectra were obtained for the reactions $p(^8\mathrm{He}, d)$, $p(^8\mathrm{He}, d^6\mathrm{He})$, $p(^8\mathrm{He}, d^4\mathrm{He})$, $p(^8\mathrm{He}, dn)$, $p(^8\mathrm{He}, dn^6\mathrm{He})$, and $p(^8\mathrm{He}, dn^4\mathrm{He})$. These spectra show the well-known ground state of ^{7}He at the energy of $E_{n-^6\mathrm{He}} = 0.44$ MeV above the $n+^6$He decay threshold and an excited state of ^{7}He at $E_{n-^6\mathrm{He}} \sim 3.3$ MeV in addition to it.

As an example, we show two spectra in Figs. 4 and 5. A strong peak in Fig. 4 corresponds to the ground state of ^{7}He. This peak is not seen in Fig. 5 in the spectrum of deuterons detected in $d + n +^4$He coincidences, because the ground state of ^{7}He cannot decay into an α particle (see the decay scheme in Fig. 6). Instead, Fig. 5 displays another peak that corresponds to the excited state found for ^{7}He.

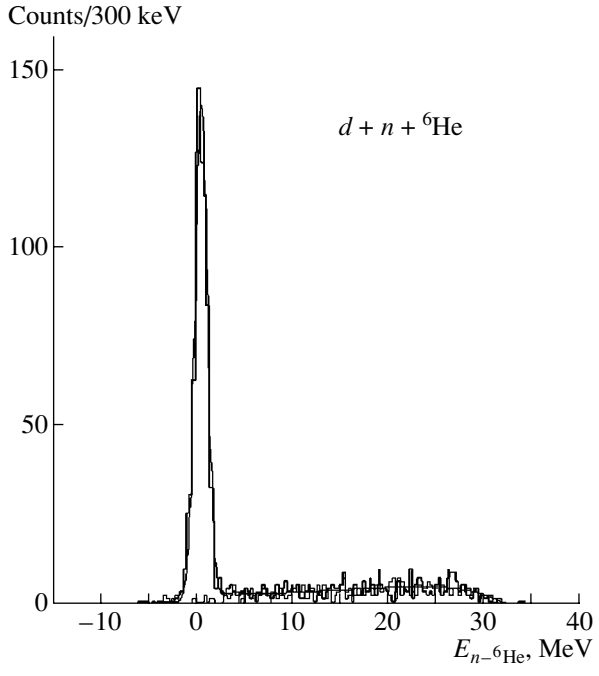

Fig. 4. Spectrum of deuterons from the reaction $p(^8\mathrm{He}, dn^6\mathrm{He})$. The spectrum is shown versus energy above the $n + ^6$He decay threshold.

The decay scheme of ^{7}He is shown in Fig. 6. The most interesting experimental finding is that the revealed excited state of ^{7}He decays predominantly into $^4\mathrm{He} + 3n$, despite a greater $^6\mathrm{He} + n$ decay energy. This reflects an unusual structure of this state.

We investigated the structure of the excited state found in our study within the $\alpha + 3n$ four-body model. We considered various ways to arrange three valence neutrons in the low-lying orbitals $P3/2$, $P1/2$, and $S1/2$ relative to the α particle. For each such case, we considered all possible spin–parities of the total system $\alpha + 3n$. The antisymmetrization of three valence neutrons was taken into account. After that, coupling of angular momenta and spins in the system $\alpha + 3n$ can be analyzed for each particular case. We investigated the spin–parity of the subsystem $\alpha + 2n$, which is the subsystem ^{6}He inside ^{7}He*.

For example, it turns out that the $J^\pi = 1/2^-$ ^{7}He excited state, which is formed by two neutrons in the $P3/2$ orbital relative to α particle and one neutron in the $P1/2$ orbital, contains the ^{6}He subsystem produced by the $(P3/2)^2$ pair of neutrons with a norm of 100% for the spin–parity of ^{6}He $J^\pi = 0^+$. This means that this excited state is prepared for decay into $^6\mathrm{He}_{\mathrm{g.s}} + n$. Furthermore, the latter is the most preferable decay from the point of view of penetration through a barrier due to the highest decay energy. Thus, this state $^7\mathrm{He}^*(1/2^-)$ should decay mainly into $^6\mathrm{He}_{g.s} + n$.

Finally, two candidates attracted our attention upon investigating the subsystem ^{6}He inside ^{7}He*. These are excited states $^7\mathrm{He}^*(5/2^-)$ and $^7\mathrm{He}^*(3/2^-)$.

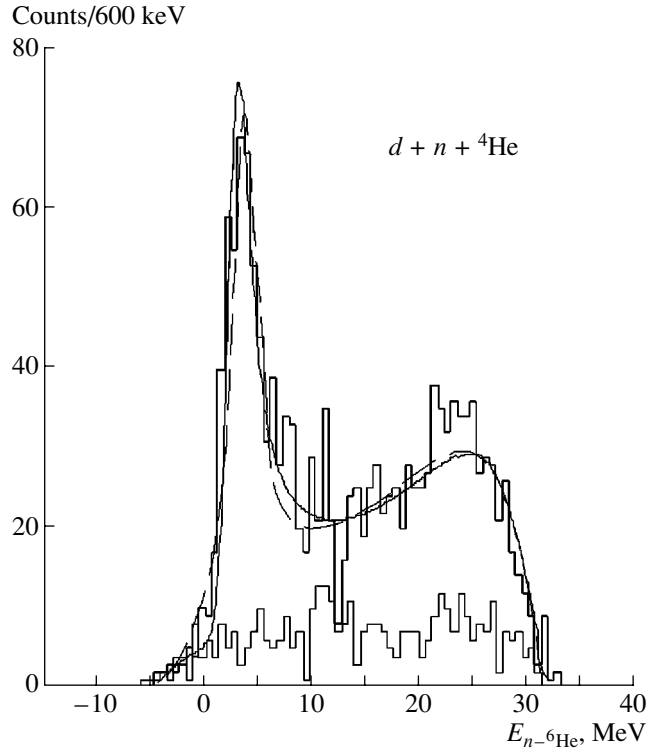

Fig. 5. Spectrum of deuterons from the reaction $p({}^8\mathrm{He}, dn{}^4\mathrm{He})$. The upper histogram, with a pronounced peak, corresponds to the measurements with a CH_2 target. The lower, structureless, histogram, which was obtained with carbon and empty targets, shows the total background from materials other than protons in the target.

These states are not prepared for decay into $^6\mathrm{He}_{g.s} + n$, but they contain the subsystem ^{6}He with a spin–parity of 2^+. Thus, these states should decay into $^6\mathrm{He}^*(2^+) + n$ with the subsequent decay $^6\mathrm{He}^*(2^+) \to {}^4\mathrm{He} + n + n$. It is consistent with the experimental observation of decay of the ^{7}He excited state found there into $^4\mathrm{He} + 3n$.

The $^7\mathrm{He}^*(5/2^-)$ state has a configuration involving a neutron excited into the $P1/2$ orbital and coupled to the ^{6}He subsystem, which itself is in an excited 2^+ state and which is produced by two $P3/2$ neutrons. The $^7\mathrm{He}^*(3/2^-)$ state includes the same configuration of neutrons. Thus, one can expect that, owing to spin–orbit forces, the $5/2^-$ state should be located at a lower energy, while the $3/2^-$ state should be pushed higher into a continuum and should be broader. In other words, $^7\mathrm{He}^*(5/2^-)$ seems to remain the only candidate for the observed excited state of ^{7}He decaying into $^4\mathrm{He} + 3n$. This conclusion is supported by the calculations performed in [3] within the resonating-group method. In particular, the phase shifts for $n + {}^6\mathrm{He}^*(2^+)$ scattering in $5/2^-$ and $3/2^-$ states were calculated in [3]. It was found that the $3/2^-$ phase shift does not show any resonance, while the $5/2^-$ phase shift shows a resonantlike structure.

Thus, the structure of the revealed $^7\mathrm{He}^*$ level should represent a neutron in an excited state coupled to the ^{6}He core, which itself is in an excited 2^+ state. The population of such an unusual state in our experiment is consistent with the structure of ^{8}He used as a projectile. It was noticed in [4] that the ground state of ^{8}He contains mainly the ^{6}He subsystem in a 2^+ excited state. Indeed, we arrived

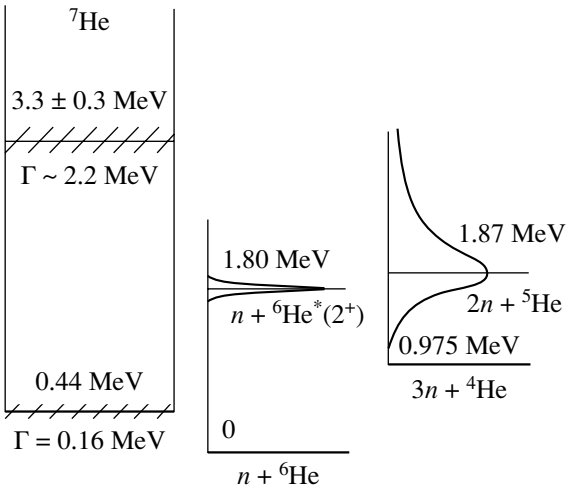

Fig. 6. Decay scheme of ^{7}He.

at the same conclusion about $^8\mathrm{He}_{g.s.}$ as that drawn in [4] by investigating the ^{6}He subsystem within $^7\mathrm{He}^*$ along the lines adopted above. Namely, an analysis of the antisymmetrized $^8\mathrm{He}(0^+)$ wave function on the basis of the $4n + \alpha$ five-body model involving four neutrons in the $P3/2$ orbital relative to the α core leads to the following norms for various J^π in the ^{6}He subsystem: $P(0^+) = 17\%$, $P(1^+) = 0$, $P(2^+) = 83\%$, and $P(3^+) = 0$.

In summary, we have studied the reaction $p(^6\mathrm{He}, pp)^5\mathrm{H}$ via correlation measurements. Preliminary results show a peak that is a good candidate for the resonance ^{5}H at an energy about 2 MeV above the $t + n + n$ decay threshold. In studying the reaction $p(^8\mathrm{He}, d)^7\mathrm{He}$, we have observed an excited state of ^{7}He, which decays into $^4\mathrm{He} + 3n$. Most likely, this state has a structure involving a neutron in the excited $P1/2$ state coupled to the ^{6}He core, which itself is in an 2^+ excited state. A tentative spin assignment for this state is $J^\pi = 5/2^-$.

REFERENCES

1. N. B. Shul'gina, B. V. Danilin, L. V. Grigorenko, *et al.*, Phys. Rev. C **62**, 014312 (2000).
2. A. A. Korsheninnikov, M. S. Golovkov, A. Ozawa, *et al.*, Phys. Rev. Lett. **82**, 3581 (1999).
3. J. Wurzer and H. M. Hofmann, Phys. Rev. C **55**, 688 (1997).
4. M. V. Zhukov, private communication.

Physics of Atomic Nuclei, Vol. 65, No. 4, 2002, pp. 669–673. From Yadernaya Fizika, Vol. 65, No. 4, 2002, pp. 701–705.

Transition Quadrupole Moments in Superdeformed Bands*

B. Buck, A. C. Merchant, and S. M. Perez**[1)]**

Department of Physics, University of Oxford, Theoretical Physics, UK

Received August 31, 2001

Abstract—We propose a method to select core and cluster in a binary component description of atomic nuclei. The choice is based on the mismatch between measured binding energies and the underlying trend supplied by the liquid drop model. A key point is that the charge to mass ratios of parent, core, and cluster should be as nearly equal as possible. This approach reinforces our earlier conclusions concerning the occurrence of exotic clustering in actinide nuclei and also reveals a competing binary mode in these nuclei in which the cluster charge and mass are substantially larger than those corresponding to an exotic decomposition. In fact, this additional mode corresponds to superdeformation, and we predict that it should be widespread across the Periodic Table. In binary models, the transition quadrupole moments Q_t of superdeformed (SD) bands depend strongly on the charge and mass splits, but are rather insensitive to other details. Indeed, given the cluster charge $\langle Z_2 \rangle$, Q_t can be determined algebraically. We compare calculations of transition quadrupole moments with the measured values for the 41 SD bands in 21 even–even nuclei for which experimental data are available. The mass range is from $A \sim 60$ to $A \sim 240$ and the values of Q_t vary from ~ 3 to ~ 30 e b. A good level of agreement is obtained. © *2002 MAIK "Nauka/Interperiodica".*

1. INTRODUCTION

The cluster model of nuclear structure is well established for light nuclei up to ^{44}Ti [1–4], and we have further shown that a binary cluster description of actinide and medium mass nuclei reproduces many of their properties with astonishing precision [5–7]. Thus we have been able to account for the band structure, detailed spectra, electromagnetic decays and half-lives for exotic and alpha emission in many isotopes in the trans-Pb [6] and Ba–Nd [7] regions. We have often been guided in our choices of cluster decomposition by knowledge of the observed exotic decay modes; however, in order to justify these selections more plausibly, and with a view to applying the model to other parts of the periodic table, we have now developed simple methods for deciding the optimum binary cluster structures (if any) for all even–even nuclei.

We often find that very large clusters are indicated by our method. This provides an intuitively appealing description for superdeformed (SD) states. As an application of our cluster selection procedure we point out here that it enables us to obtain a systematic understanding of the measured values of the transition quadrupole moment Q_t for the 41 SD bands in 21 even–even nuclei listed in [8, 9]. The result for Q_t follows from a simple algebraic formula which requires only the identification of the two components into which a given nucleus is to be decomposed and a radius parameter common to all the 41 cases considered.

2. CLUSTER SELECTION

We suggest [10] that likely binary clusterizations of a given parent nucleus can be identified from the local maxima of the function $D(Z_1, A_1, Z_2, A_2)$ defined by

$$D(Z_1, A_1, Z_2, A_2) = [B_E(Z_1, A_1) - B_L(Z_1, A_1)] + [B_E(Z_2, A_2) - B_L(Z_2, A_2)], \quad (1)$$

where B_E is an experimentally determined binding energy and B_L is the corresponding liquid drop value for each of the fragments of (charge, mass) (Z_i, A_i) with $i = 1, 2$ into which the parent of (charge, mass) (Z_T, A_T) may be divided. This means we are searching for the largest deviations of the summed binding energies of the two fragments from the underlying trend, as given by liquid drop values. A convenient form for B_L is [11]

$$B_L = a_v A - a_s A^{2/3} - a_c \frac{Z^2}{A^{1/3}} - a_a \frac{(A-2Z)^2}{A} + \delta, \quad (2)$$

*This article was submitted by the authors in English.

[1)]Department of Physics, University of Cape Town, Private Bag, Rondebosch, South Africa; e-mail: perez@physci.uct.ac.za

**e-mail: a.merchant1@physics.ox.ac.uk

1063-7788/02/6504-0669$22.00

Transition quadrupole moments

Nucleus	Q_t(calc.), e b	Q_t(exp.) [8, 9] (for different observed bands), e b
^{60}Zn = ^{48}Cr + ^{12}C	2.5 ± 0.1	2.75 ± 0.45
^{62}Zn = ^{50}Cr + ^{12}C	2.6 ± 0.1	$2.7^{+0.7}_{-0.5}$
^{80}Sr = ^{68}Ge + ^{12}C	3.2 ± 0.1	$2.7^{+0.7}_{-0.6}$; $2.2^{+0.6}_{-0.5}$; $2.8^{+1.1}_{-0.8}$; $3.6^{+2.0}_{-1.1}$
^{82}Sr = ^{70}Ge + ^{12}C	3.3 ± 0.2	4.5 ± 0.9
^{84}Zr = ^{56}Fe + ^{28}Si	5.9 ± 0.2	5.2 ± 0.8
^{86}Zr = ^{58}Fe + ^{28}Si	6.0 ± 0.2	$4.6^{+0.7}_{-0.6}$; 4.0 ± 0.3; $3.8^{+0.6}_{-0.5}$; and $5.4^{+2.2}_{-1.1}$
^{132}Ce = ^{100}Ru + ^{32}Si	9.5 ± 0.3	7.4 ± 0.4; 7.3 ± 0.3; 7.6 ± 0.4
^{134}Nd = ^{102}Pd + ^{32}Si	9.8 ± 0.3	6.8 ± 0.3; 6.4 ± 0.4
^{142}Sm = ^{88}Sr + ^{54}Cr	13.6 ± 0.5	11.7 ± 0.1; $13.2^{+0.8}_{-0.7}$
^{146}Gd = ^{90}Zr + ^{56}Cr	14.2 ± 0.5	12 ± 2
^{148}Gd = ^{88}Sr + ^{60}Fe	14.7 ± 0.5	14.6 ± 0.2; 14.8 ± 0.3; 17.8 ± 1.3
^{150}Gd = ^{88}Sr + ^{62}Fe	14.8 ± 0.5	$17.0^{+0.5}_{-0.4}$; $17.4^{+0.5}_{-0.4}$; 16.2 ± 0.4; and $15.0^{+0.6}_{-0.4}$; 16.8 ± 1.2
^{152}Dy = ^{88}Sr + ^{64}Ni	15.6 ± 0.6	17.5 ± 0.5
^{154}Dy = ^{88}Sr + ^{66}Ni	15.7 ± 0.6	$15.9^{+3.1}_{-2.1}$
^{190}Hg = ^{142}Nd + ^{48}Ca	17.1 ± 0.6	$17.7^{+1.0}_{-1.2}$; 17.6 ± 1.5
^{192}Hg = ^{140}Ce + ^{52}Ti	18.1 ± 0.6	20.2 ± 1.2; 19.5 ± 1.5
^{194}Hg = ^{140}Ce + ^{54}Ti	18.4 ± 0.7	17.7 ± 0.4; 17.6 ± 0.6; 17.6 ± 0.8
^{194}Pb = ^{144}Nd + ^{50}Ti	18.3 ± 0.7	$20.1^{+0.3}_{-0.5}$
^{196}Pb = ^{144}Nd + ^{52}Ti	18.6 ± 0.7	$19.5^{+0.4}_{-0.3}$
^{236}U = ^{134}Te + ^{102}Zr	29.3 ± 1.1	32 ± 5
^{238}U = ^{134}Te + ^{104}Zr	29.5 ± 1.1	29 ± 3

where

$$a_v = 15.56 \text{ MeV}, \quad a_s = 17.23 \text{ MeV}, \qquad (3)$$
$$a_c = 0.697 \text{ MeV}, \quad a_a = 23.285 \text{ MeV}.$$

The pairing term δ in Eq. (2) is taken as $12/\sqrt{A}$ (MeV) because in this paper we consider only the fragmentation of even–even nuclei into even–even fragments. In addition, electric dipole transitions in even–even nuclei are found to be very weak, suggesting that attention should be restricted to fragments obeying the condition

$$\frac{Z_1}{A_1} = \frac{Z_2}{A_2} = \frac{Z_T}{A_T} \qquad (4)$$

as closely as possible, so that the calculated dipole transition rates, which involve the operator $(Z_1/A_1 - Z_2/A_2)$, are very small. This implies that the centers of charge and mass in the nucleus almost coincide. In general, no single choice of cluster can satisfy this dipole constraint exactly. However, if we are willing to consider that the nuclear state is a superposition of several possible cluster partitions then it becomes feasible to satisfy Eq. (4) by using effective or average cluster charges and masses [10].

Initially we applied the dipole constraint by selecting a specific cluster charge Z_2 and finding a corresponding cluster mass A_2 such that

$$\frac{A_2}{Z_2} \le \frac{A_T}{Z_T} \le \frac{(A_2+2)}{Z_2}. \qquad (5)$$

We then assigned weights (probabilities) $p(A_2)$ and $p(A_2+2)$ to the two isotopic masses, with the sum of the weights equal to unity and the mean mass given by $\langle A_2 \rangle = A_T Z_2/Z_T$. Hence this superposition obeys the dipole constraint exactly. The mean neutron number would then be $\langle N_2 \rangle = N_T Z_2/Z_T$. It is thus now possible to calculate the similarly weighted mean deviations $\langle D(1,2) \rangle$ and to plot them against the even integer values of the cluster charge Z_2.

A similar procedure was also applied to mixtures of adjacent cluster isotones. That is, we chose particular

values of N_2 and found the corresponding masses A_2 satisfying the relation

$$\frac{A_2}{N_2} \leq \frac{A_T}{N_T} \leq \frac{(A_2+2)}{N_2}. \quad (6)$$

Again the appropriate probabilities $p(A_2)$ and $p(A_2+2)$ were assigned, so that now the mean mass was $\langle A_2 \rangle = A_T N_2/N_T$ and the dipole condition fulfilled. This leads to mean values of the cluster charge given by $\langle Z_2 \rangle = Z_T N_2/N_T$.

However, it is preferable to have a method of interpolating exactly between the above results for isotopes and isotones. That is, we wish to choose arbitrary mean values for the plotting parameter $\langle Z_2 \rangle$ and for each choice to find the weighted combinations of clusterings which ensure the correct mean $\langle Z_2 \rangle$, along with the effective $\langle N_2 \rangle$ implied by the dipole rule. Thus, after selecting some value of $\langle Z_2 \rangle$, the required value of $\langle N_2 \rangle$ will be given by $\langle N_2 \rangle = N_T \langle Z_2 \rangle / Z_T$, equivalent to the dipole condition.

Given $\langle Z_2 \rangle$ and $\langle N_2 \rangle$ we can determine clusters with adjoining values of Z_2 and of N_2 which bracket the above mean values and have probabilities consistent with them. Thus, using

$$Z_2 + 2 \geq \langle Z_2 \rangle \geq Z_2, \quad N_2 + 2 \geq \langle N_2 \rangle \geq N_2, \quad (7)$$

we easily find that the weighting probabilities are given by

$$\begin{aligned} p(Z_2+2) &= (1/2)[\langle Z_2 \rangle - Z_2], \quad (8)\\ p(Z_2) &= (1/2)[(Z_2+2) - \langle Z_2 \rangle],\\ p(N_2+2) &= (1/2)[\langle N_2 \rangle - N_2],\\ p(N_2) &= (1/2)[(N_2+2) - \langle N_2 \rangle]. \end{aligned}$$

We now consider that a nucleus could be composed of a superposition of up to four different cluster configurations, with weights which are products of the above probabilities. The mean binding for assigned $\langle Z_2 \rangle$ and $\langle N_2 \rangle$ takes the form

$$\begin{aligned} \langle D(1,2) \rangle &= \langle D(\langle Z_2 \rangle, \langle N_2 \rangle) \rangle \quad (9)\\ &= \sum_{Z_2, N_2} p(Z_2) p(N_2) D(Z_2, N_2). \end{aligned}$$

To keep things as simple as possible, we use the even–even cluster closest to the peak indicated by a plot of this average in what follows.

The figure shows $D(Z_1, A_1, Z_2, A_2)$ as a function of cluster charge $\langle Z_2 \rangle$ for six nuclei representative of the mass regions where SD bands have been reported. The behavior illustrated is completely typical of most of the nuclei we have examined to date, which leads us to expect bands of strongly deformed states essentially everywhere (although at excitation energies which we are, at present, unable to determine).

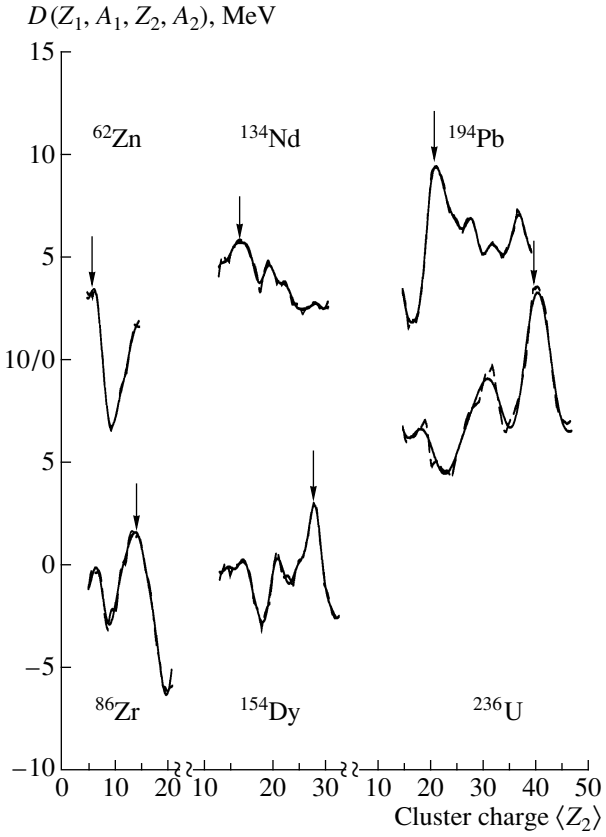

Calculations of $\langle D(Z_1, A_1, Z_2, A_2) \rangle$ as a function of cluster charge $\langle Z_2 \rangle$ for ^{62}Zn, ^{86}Zr, ^{134}Nd, ^{154}Dy, ^{194}Pb, and ^{236}U. Arrows indicate the preferred cluster charge. Dashed curve—full calculation using Eq. (9); full curve—calculation using a Fourier based filtering technique to remove small scale structure (such structure is physically meaningless, since our input was restricted to even–even nuclei, implying minimum Z and N steps of 2 units). Both curves were obtained from procedures identical to those described in [10].

Collective motion of these structures gives rise to SD bands in the parent nuclei. The SD clusterizations presented in the table result from a straightforward application of the above criteria.

Experiment often shows several SD bands in a given nucleus, sometimes with similar values of Q_t, but also with different ones. This can be understood in our model as follows. We expect several bands with very similar quadrupole deformations associated with any given cluster structure because excitations of cluster or core or both can all produce closely related bands with comparable excitation energies. The significance of the lesser maxima of $D(Z_1, A_1, Z_2, A_2)$ is currently under investigation, but we strongly suspect that bands associated with these clusterings may be present as well. This would lead to the coexistence of several clusterizations in the same nucleus marked out by their different quadrupole deformations.

3. TRANSITION QUADRUPOLE MOMENTS

There is a well-known relationship between the charge radii of a given nucleus and the core and cluster into which it is decomposed (see, for example, [12]) of the form:

$$(Z_1 + Z_2)\langle R^2\rangle = Z_1\langle R_1^2\rangle + Z_2\langle R_2^2\rangle + \alpha_2\langle r_{L,L}^2\rangle, \quad (10)$$

where (Z_i, A_i) are as defined in the previous section; $\langle R^2\rangle$, $\langle R_1^2\rangle$, and $\langle R_2^2\rangle$ are mean square charge radii for the parent, core, and cluster nuclei, respectively;

$$\alpha_2 = \frac{Z_1A_2^2 + Z_2A_1^2}{(A_1 + A_2)^2}, \quad (11)$$

$$\langle r_{L,L}^2\rangle = \int_0^\infty r^2|\chi_L(r)|^2\,dr,$$

with $\chi_L(r)$ being the radial wave function for the relative motion of cluster and core with angular momentum L ($L = 0$ for positive parity bandheads in even–even nuclei). For an internally unexcited even–even cluster and core, the total angular momentum is identical to the relative orbital angular momentum of the two bodies and so the transition quadrupole moment for states $J = L + 2$ and $J = L$ is simply

$$Q_t = 2\alpha_2\langle r_{L+2,L}^2\rangle, \quad (12)$$

$$\langle r_{L+2,L}^2\rangle = \int_0^\infty r^2\chi_L^*(r)\chi_{L+2}(r)\,dr.$$

Cluster bands are characterized by a large value of the quantum number $G = 2n + L$, so that the radial wave functions for states with low angular momentum L have a large number of nodes n. Clearly, the radial functions for states with $J = L + 2$ and $J = L$ differ in their node number by one. However, we have previously shown that [6], even up to rather high L values, such pairs of radial functions are practically identical, except very close to the origin ($r = 0$) where the extra node is accommodated. It is therefore a good approximation to replace $\langle r_{L+2,L}^2\rangle$ by $\langle r_{L,L}^2\rangle$ and write

$$Q_t \approx 2[(Z_1 + Z_2)\langle R^2\rangle - Z_1\langle R_1^2\rangle - Z_2\langle R_2^2\rangle] = 2R_0^2[Z_TA_T^{2/3} - Z_1A_1^{2/3} - Z_2A_2^{2/3}], \quad (13)$$

where the mean square charge radius of each of the nuclei has been related to its mass by $\langle R_i^2\rangle = R_0^2A_i^{2/3}$. Equation (13) enables us to evaluate Q_t once the core-cluster binary decomposition of the parent nucleus has been chosen and a value for R_0 specified.

We take $R_0 = 1.07 \pm 0.02$ fm, determined from elastic electron scattering by Ravenhall [13] as the radius parameter of a Fermi density distribution for heavy nuclei. The resulting values for Q_t are compared with experiment in the table. We note the large number of magic proton and neutron values amongst the cores and clusters in the table (reflecting the associated increase in stability). Thus, there are magic proton numbers in the isotopes of Ca and Ni of 20 and 28, respectively. Also there are magic neutron numbers in ^{48}Ca, ^{88}Sr, ^{134}Te, ^{140}Ce, and ^{142}Nd of 28, 50, 82, 82, and 82, respectively.

We see from the table that, except for ^{132}Ce and ^{134}Nd, the clusterization indicated by the highest maximum of the appropriate D plot gives a good description of the transition quadrupole moment of at least one experimental SD band in each of the 21 nuclei examined. However, the naive geometric picture of two more or less equal clusters, in touching contact, giving rise to a 2 : 1 major to minor axis ratio is not borne out. Rather, we usually find a considerable asymmetry between core and cluster, and in some cases it is so great that it corresponds to what we have previously called "exotic" clustering (because it involves a light ion, such as ^{14}C, seen to be emitted in exotic nuclear decay). Thus, although all cases examined are undoubtedly strongly deformed, many of them do not seem to be superdeformed in the 2 : 1 axis ratio sense in which this term is often employed.

To calculate other properties of SD states, more detailed calculations are necessary. In principle this is a relatively straightforward task. Once core and cluster have been identified, we can solve a Schrödinger equation for their relative motion using a universal form for the ion–ion potential [14]. A value for the relative motion quantum number $G = 2n + L$ can also be assigned from systematic considerations [15]. Then energies and wave functions are available for the calculation of whichever observables are desired. However, the details of such calculations depend on the precise excitation energy of the bandhead and the value of G employed. To attain maximum accuracy in these matters it is best to fine-tune the potential radius and G value so as to reproduce the experimental excitation energies of a couple of states of known angular momentum. Because linking transitions between SD and ND bands are rarely seen, this information is not often available (although we have performed such calculations for ^{60}Zn [16], ^{194}Hg, ^{236}U, and ^{240}Pu [15], some of the rare examples where it is possible). We hope that this situation will gradually improve as more experimental data are gathered.

4. CONCLUSIONS

We have applied a principle of maximum stability to determine the most favoured core-cluster decom-

positions of the 21 even–even nuclei for which transition quadrupole moments Q_t of superdeformed bands have been measured. Once the clustering was specified, we used a simple algebraic formula to calculate Q_t, viz., Eq. (13). The single adjustable parameter R_0 was taken as 1.07 ± 0.2 fm from Ravenhall's fits to elastic electron scattering from heavy nuclei [13]. A generally good account was given of the data. The final clusterizations seem to indicate that although all the bands studied are certainly strongly deformed, they do not all have major to minor axis ratios as large as $2:1$.

ACKNOWLEDGMENTS

A.C.M. would like to thank the UK Engineering and Physical Science Research Council (EPSRC) for financial support. S.M.P. would like to thank the South African Foundation for Research, and the University of Cape Town, for financial support.

REFERENCES

1. A. Arima *et al.*, Adv. Nucl. Phys. **5**, 345 (1972).
2. K. Wildermuth and Y. C. Tang, in *A Unified Theory of the Nucleus* (Academic, New York, 1977), p. 1.
3. H. Furutani *et al.*, Prog. Theor. Phys. Suppl. **68**, 193 (1980).
4. S. Ohkubo, Prog. Theor. Phys. Suppl. **132**, 1 (1998).
5. B. Buck, A. C. Merchant, S. M. Perez, *et al.*, J. Phys. G **20**, 351 (1994).
6. B. Buck, A. C. Merchant, and S. M. Perez, Phys. Rev. Lett. **76**, 380 (1996); Phys. Rev. C **58**, 2049 (1998); **57**, R2095 (1998); **59**, 750 (1999).
7. B. Buck, A. C. Merchant, and S. M. Perez, Nucl. Phys. A **652**, 211 (1999); **657**, 267 (1999).
8. B. Singh, R. B. Firestone, and S. Y. Frank Chu, Nucl. Data Sheets **78**, 1 (1996).
9. X. L. Han and C. L. Wu, At. Data Nucl. Data Tables **73**, 43 (1999).
10. B. Buck, A. C. Merchant, M. J. Horner, *et al.*, Phys. Rev. C **61**, 24314 (2000).
11. W. S. C. Williams, in *Nuclear and Particle Physics* (Clarendon Press, Oxford, 1991), p. 60.
12. B. Buck and A. A. Pilt, Nucl. Phys. A **280**, 133 (1977).
13. D. G. Ravenhall, Rev. Mod. Phys. **30**, 430 (1958).
14. B. Buck, A. C. Merchant, and S. M. Perez, Nucl. Phys. A **614**, 129 (1997).
15. B. Buck, A. C. Merchant, and S. M. Perez, Nucl. Phys. A (in press).
16. B. Buck, A. C. Merchant, and S. M. Perez, Phys. Rev. C **61**, 14310 (2000).

Physics of Atomic Nuclei, Vol. 65, No. 4, 2002, pp. 674–677. From Yadernaya Fizika, Vol. 65, No. 4, 2002, pp. 706–709.

Interpretation of Airy Minima in $^{16}O + {}^{16}O$ and $^{16}O + {}^{12}C$ Elastic Scattering in Terms of a Barrier-Wave/Internal-Wave Decomposition*

F. Michel**, **F. Brau**[1)], **G. Reidemeister**[2)], **and S. Ohkubo**[3)]

Faculté des Sciences, Université de Mons-Hainaut, Belgium

Received August 31, 2001

Abstract—The observation of refractive effects in $^{16}O + {}^{16}O$ and $^{16}O + {}^{12}C$ elastic scattering data has definitively established the fact that the optical potential for some light heavy-ion systems is relatively transparent and that its real part is deep. Most of the interpretations of the rainbow features of these data rely on the so-called nearside–farside decomposition of the scattering amplitude. Starting from recent optical model analyses of $^{16}O + {}^{16}O$ and $^{16}O + {}^{12}C$ elastic scattering around 100 MeV incident energy as an example, we present an alternative interpretation based on the barrier-wave/internal-wave decomposition first proposed by Brink and Takigawa. This method, which complements the nearside–farside approach, demonstrates clearly the exceptional transparency of the $^{16}O + {}^{16}O$, and to a lesser extent $^{16}O + {}^{12}C$, interactions at the investigated energies and makes possible the extraction of the two contributions whose interference explains the Airy oscillations seen in the farside amplitude. © *2002 MAIK "Nauka/Interperiodica".*

The observation in $^{16}O + {}^{16}O$, $^{16}O + {}^{12}C$, and $^{12}C + {}^{12}C$ elastic scattering data of distinctive refractive effects [1–3], like strong Airy minima, superimposed on more classic diffractive features, has definitively established the fact that the real part of the light heavy-ion nucleus–nucleus optical potential is deep, and that—in some favorable cases—the light heavy-ion interaction displays some transparency [1]. This refractive behavior shows up, e.g., in analyses carried out very recently for the $^{16}O + {}^{16}O$ [4, 5] and the $^{16}O + {}^{12}C$ [6, 7] systems.

Semiclassical approaches [8] are often used to interpret the optical model calculations results. The semiclassical analyses presented in this context have nearly invariably been performed within the framework of the nearside–farside decomposition of the elastic scattering amplitude proposed 25 years ago by Fuller [9]. In this approach, the scattering amplitude is decomposed into nearside and farside components, which are obtained simply from the partial wave expansion of $f(\theta)$,

$$f(\theta) = f_{\mathrm{R}}(\theta) + \sum_{\ell} a_\ell P_\ell(\cos\theta), \qquad (1)$$

by replacing the usual Legendre polynomials $P_\ell(\cos\theta)$ by combinations $\tilde{Q}_\ell^{(-)}$ and $\tilde{Q}_\ell^{(+)}$ of Legendre polynomials and Legendre functions of the second kind, Q_ℓ,

$$P_\ell(\cos\theta) \to \tilde{Q}_\ell^{(\pm)} \qquad (2)$$
$$= \frac{1}{2}[P_\ell(\cos\theta) \mp i\frac{2}{\pi}Q_\ell(\cos\theta)],$$

and by decomposing the Rutherford amplitude into its nearside and farside components $f_{\mathrm{R},N}(\theta)$ and $f_{\mathrm{R},F}(\theta)$ [9]. The nearside and farside contributions correspond in a semiclassical picture to trajectories with positive and negative deflection angles, respectively (Fig. 1). The ratios to the Rutherford cross section of the nearside (σ_N) and farside (σ_F) contributions to the unsymmetrized $^{16}O + {}^{16}O$ elastic scattering cross section at 124 MeV are presented as an example in Fig. 2. This is one of the incident energies where a minimum is observed in the experimental angular distribution at 90° [4, 10] and in the excitation function at the same angle [11]; if a minimum is found at 90° in the symmetrized cross section $\sigma_S(\theta) = |f(\theta) + f(\pi - \theta)|^2$, such a minimum is guaranteed to exist also in the unsymmetrized cross section [12]. Here

*This article was submitted by the authors in English.

[1)]Faculté des Sciences, Université de Mons-Hainaut, Belgium; e-mail: Fabian.Brau@umh.ac.be

[2)]Faculté des Sciences, Université Libre de Bruxelles, Belgium; e-mail: greidem@ulb.ac.be

[3)]Department of Applied Science and Environment, Kochi Women's University, Japan; e-mail: ohkubo@is.kochi-wu.ac.jp

**e-mail: Francis.Michel@umh.ac.be

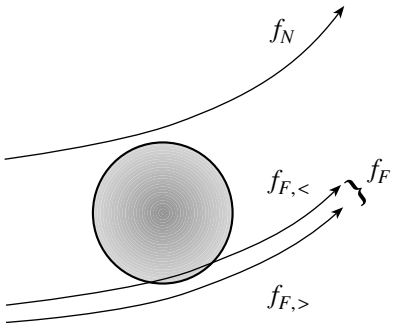

Fig. 1. Classical trajectories contributing to the nearside (f_N) and farside (f_F) components of the elastic scattering amplitude; the latter generally contains contributions from deeply penetrating ($f_{F,<}$) and more peripheral ($f_{F,>}$) trajectories.

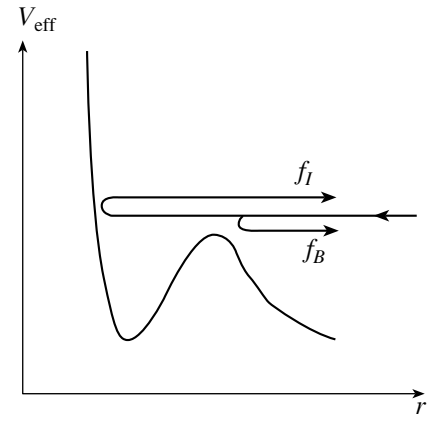

Fig. 3. Classical trajectories contributing to the barrier-wave (f_B) and internal-wave (f_I) components of the elastic scattering amplitude.

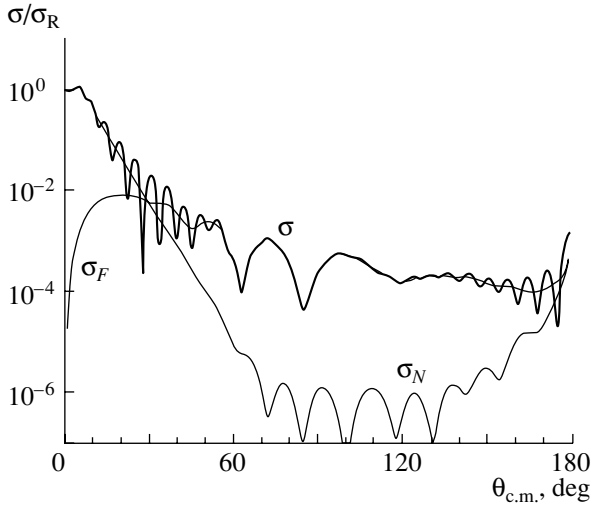

Fig. 2. Nearside (σ_N) and farside (σ_F) contributions to the unsymmetrized $^{16}O + {}^{16}O$ optical model angular distribution at 124 MeV.

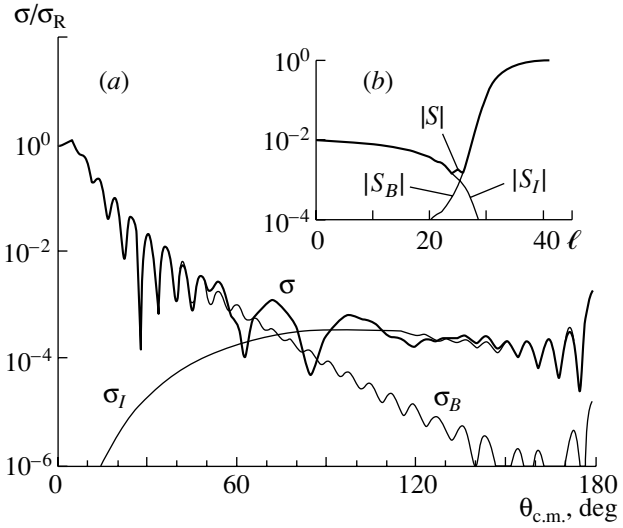

Fig. 4. (*a*) Barrier-wave (σ_B) and internal-wave (σ_I) contributions to the unsymmetrized $^{16}O + {}^{16}O$ optical model angular distribution at 124 MeV; (*b*) moduli of the barrier-wave (S_B) and internal-wave (S_I) components of the elastic S matrix.

and in the following, calculations are carried out with the phenomenological potential of Nicoli *et al.* [4].

While the forward angle Fraunhofer oscillations are readily understood in the nearside–farside picture in terms of an interference between f_N and f_F, the Airy minima, which are observed here around 60°, 90°, and 120° in the farside contribution to the amplitude, can only be explained if one assumes [1, 13, 14] that two different ranges of angular momenta, $\ell_<$ and $\ell_>$, contribute to f_F (Fig. 1). This interpretation, which is suggested by the general behavior of the classical deflection function, is substantiated by the fact that an increase of the absorption, which affects preferentially the lower-ℓ contribution, tends to smooth out these minima.

We found that another decomposition of the scattering amplitude in terms of barrier-wave and internal-wave components, originally introduced by Brink and Takigawa [15], complements the information supplied by the nearside–farside approach and sheds additional light on light heavy-ion scattering in an incomplete absorption context. This method, which proved very useful in understanding the anomalous features seen in some light-ion elastic scattering systems at low energy [8, 15, 16]—providing for the first time clear evidence for transparency in the scattering of composite nuclear projectiles like the α-particle—has to our knowledge been practically ignored in the context of light heavy-ion scattering.

The internal-wave/barrier-wave decomposition makes sense only for potentials which are deep

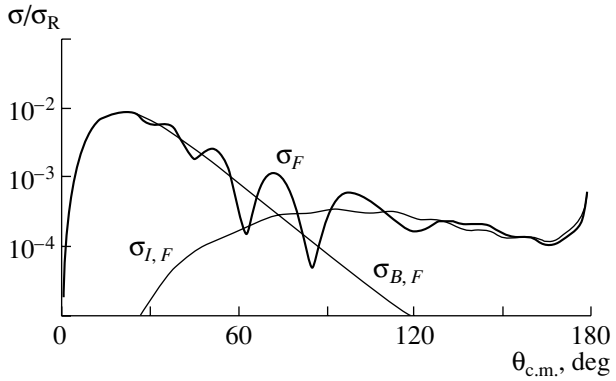

Fig. 5. Barrier-wave ($\sigma_{B,F}$) and internal-wave ($\sigma_{I,F}$) contributions to the farside component (σ_F) of the unsymmetrized $^{16}O + {}^{16}O$ optical model angular distribution at 124 MeV.

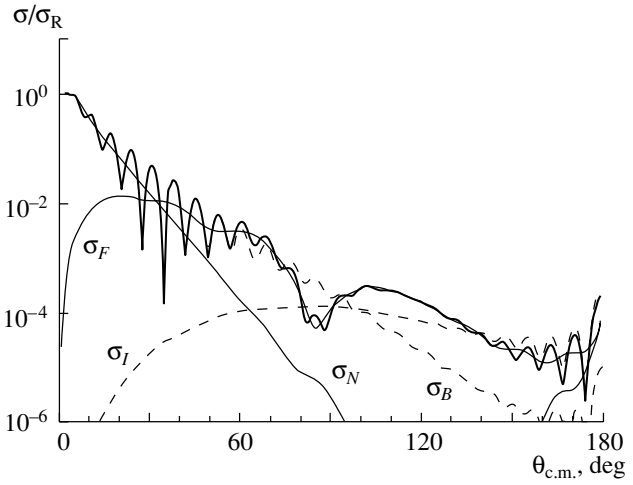

Fig. 6. Nearside/farside (σ_N/σ_F) and barrier-wave/internal-wave (σ_B/σ_I) components of the $^{16}O + {}^{12}C$ optical model cross section at 132 MeV.

enough for the effective potentials active in the scattering at the considered energy to display a "potential pocket"; the scattering amplitude $f(\theta)$ can then be split into barrier-wave $f_B(\theta)$ and internal-wave $f_I(\theta)$ components, corresponding, respectively, to the part of the incident flux which is reflected at the barrier of the effective potential and that which penetrates the nuclear interior and reemerges after reflection at the most internal turning point (Fig. 3).

Although the barrier-wave/internal-wave decomposition was initially introduced within a semiclassical frame [15], it was shown by Albiński and Michel [17] that, by investigating the response of the elastic scattering amplitude to small modifications of the optical potential inside of the barrier radius, this decomposition can be carried out for many systems in an accurate way using any conventional optical model code. We used this method for decomposing the $^{16}O + {}^{16}O$ elastic scattering amplitudes at the energies investigated by Nicoli *et al.* between 75 and 124 MeV [4]. The result of the barrier-wave/internal-wave decomposition at 124 MeV is presented in Fig. 4*a*. The barrier-wave contribution σ_B is seen to decrease steadily with angle and to account for the diffractive oscillations observed up to 50°, while the internal-wave contribution σ_I dominates the scattering beyond about 120° and behaves smoothly up to that angle. The deep minima seen in the unsymmetrized cross section around 60° and 90°, and the shallower one around 120°, are interpreted here as resulting from a strong interference between the barrier-wave and internal-wave amplitudes f_B and f_I. The presence of a strong internal-wave contribution in the intermediate angle region is seen to be essential for the reproduction of these minima, and more generally for a correct description of the cross section beyond 50°; since the internal-wave contribution arises from that part of the incident flux which probes the nuclear interior, this result demonstrates clearly the remarkable transparency of the $^{16}O + {}^{16}O$ interaction at the studied energy. The moduli of the barrier-wave and internal-wave contributions to the S-matrix are displayed in Fig. 4*b*.

While we interpret the minima around 60° and 90° as being due to an interference between the barrier-wave and internal-wave contributions to the scattering amplitude, these minima have repeatedly been interpreted in previous works (see, e.g., [1]) as resulting from an interference in the farside amplitude between the contributions of the two ranges of angular mo-

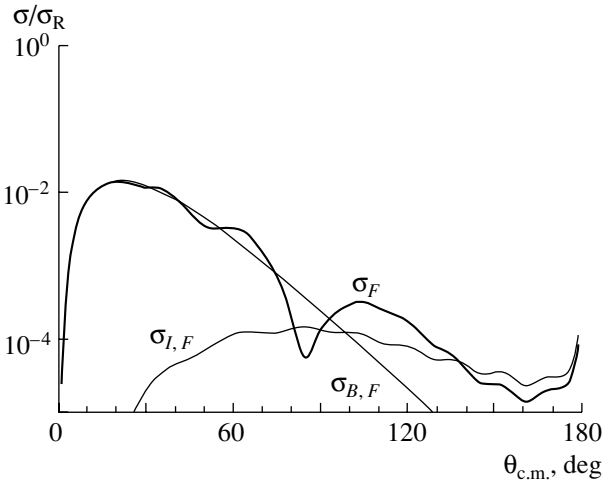

Fig. 7. Barrier-wave ($\sigma_{B,F}$) and internal-wave ($\sigma_{I,F}$) contributions to the farside component (σ_F) of the $^{16}O + {}^{12}C$ optical model angular distribution at 132 MeV.

menta $\ell_<$ and $\ell_>$ alluded to above. The contributions $\sigma_{F,<}$ and $\sigma_{F,>}$ of these two ranges to the farside cross section have sometimes been extracted in an approximate way using the so-called interpolated-envelope technique [13, 18]. These two contributions can be obtained in a more natural and more rigorous way by performing a nearside–farside decomposition of the barrier-wave and internal-wave amplitudes themselves; this decomposition is performed in an automatic way by replacing the Legendre polynomials by the functions $\tilde{Q}_\ell^{(-)}$ and $\tilde{Q}_\ell^{(+)}$ in the partial wave series for the barrier-wave and internal-wave amplitudes. The farside contributions $\sigma_{B,F} = |f_{B,F}|^2$ and $\sigma_{I,F} = |f_{I,F}|^2$ to the barrier-wave and internal-wave cross sections σ_B and σ_I are presented in Fig. 5; σ_F is seen to have been split into two components varying smoothly with angle—and which furthermore originate from different ranges of angular momenta since the barrier-wave and internal-wave contributions are nearly decoupled in angular momentum space (Fig. 4*b*). These two components $\sigma_{I,F}$ and $\sigma_{B,F}$ thus appear to be nothing else than the cross sections $\sigma_{F,<}$ and $\sigma_{F,>}$.

For symmetric systems like $^{16}O + {}^{16}O$, the structure of the unsymmetrized angular distributions predicted by the optical model calculations at large angles is difficult to observe in the experimental data. It is thus interesting to examine asymmetric systems which are not affected by Mott interference to investigate further the merits of our approach. We have performed similar calculations for $^{16}O + {}^{12}C$ elastic scattering at 132 MeV incident energy [6]; in contrast to $^{16}O + {}^{16}O$, the $^{16}O + {}^{12}C$ experimental angular distribution displays a prominent Airy minimum around $\theta = 80°$, which appears to be of second order and which is well described by optical model calculations carried out with a deep real potential [6]. Figure 6 presents the barrier-wave/internal-wave and nearside–farside cross sections calculated with this potential. Absorption is seen to be somewhat larger than in the $^{16}O + {}^{16}O$ case, since the difference between the internal-wave and barrier-wave contributions at large angles does not exceed one order of magnitude (it reaches two orders of magnitude in $^{16}O + {}^{16}O$); another indication of stronger absorption is that the modulus of the internal S-matrix at low angular momenta is about twice smaller here than in the latter case. The barrier-wave and internal-wave contributions to the full farside cross section are presented in Fig. 7.

In summary, we have shown that a barrier-wave/internal-wave decomposition of the elastic scattering amplitude complements the often used nearside–farside decomposition and sheds new light on the exceptional transparency of some light heavy-ion systems like $^{16}O + {}^{16}O$ or $^{16}O + {}^{12}C$. In particular, the Airy minima observed in the angular distributions appear here to be due to an interference between the contribution of the flux reflected at the barrier and that of the flux which probes the nuclear interior and reemerges in the entrance channel. Moreover, the two contributions to the farside amplitude introduced in the nearside–farside approach to explain the occurrence of these Airy minima are obtained in a natural and unambiguous way from the barrier-wave/internal-wave decomposition. Further investigation of light heavy-ion scattering along these lines might help to clarify the mechanism of the nucleus–nucleus interaction and thus pave the way to a better understanding of the cluster structure of the unified nuclear system.

REFERENCES

1. M. E. Brandan and G. R. Satchler, Phys. Rep. **285**, 143 (1997).
2. M. S. Hussein and K. W. McVoy, Prog. Part. Nucl. Phys. **12**, 103 (1984).
3. M. E. Brandan, M. S. Hussein, K. W. McVoy, *et al.*, Comments Nucl. Part. Phys. **22**, 77 (1996).
4. M. P. Nicoli, F. Haas, R. M. Freeman, *et al.*, Phys. Rev. C **60**, 064608 (1999).
5. Dao T. Khoa, W. von Oertzen, H. G. Bohlen, *et al.*, Nucl. Phys. A **672**, 387 (2000).
6. A. A. Ogloblin, D. T. Khoa, Y. Kondō, *et al.*, Phys. Rev. C **57**, 1797 (1998).
7. M. P. Nicoli, F. Haas, R. M. Freeman, *et al.*, Phys. Rev. C **61**, 034609 (2000).
8. D. M. Brink, *Semi-Classical Methods for Nucleus–Nucleus Scattering* (Cambridge Univ. Press, Cambridge, 1985).
9. R. C. Fuller, Phys. Rev. C **12**, 1561 (1975).
10. Y. Kondō, Y. Sugiyama, Y. Tomita, *et al.*, Phys. Lett. B **365**, 17 (1996).
11. M. L. Halbert, C. B. Fulmer, S. Raman, *et al.*, Phys. Lett. B **51B**, 341 (1974).
12. N. Rowley, H. Doubre, and C. Marty, Phys. Lett. B **69B**, 147 (1977).
13. K. W. McVoy, H. M. Khalil, M. M. Shalaby, *et al.*, Nucl. Phys. A **455**, 118 (1986).
14. K. W. McVoy and M. E. Brandan, Nucl. Phys. A **542**, 295 (1992).
15. D. M. Brink and N. Takigawa, Nucl. Phys. A **279**, 159 (1977).
16. F. Michel, S. Ohkubo, and G. Reidemeister, Prog. Theor. Phys. Suppl., No. 132, 7 (1998).
17. J. Albiński and F. Michel, Phys. Rev. C **25**, 213 (1982).
18. H. M. Khalil, K. W. McVoy, and M. M. Shalaby, Nucl. Phys. A **455**, 100 (1986).

Physics of Atomic Nuclei, Vol. 65, No. 4, 2002, pp. 678–682. From Yadernaya Fizika, Vol. 65, No. 4, 2002, pp. 710–714.

Nuclear-Rainbow Scattering and Nucleus–Nucleus Potentials at Short Distances*

W. von Oertzen[1], A. Blažević, H. G. Bohlen, Dao T. Khoa[2], F. Nouffer, P. Roussel-Chomaz[3], W. Mittig[3], and J. M. Casandjian[3]

Hahn-Meitner-Institut, Berlin, Germany

Received August 31, 2001

Abstract—The elastic scattering of strongly bound nuclei at energies of 10 to 70 MeV per nucleon shows the phenomenon of "rainbow scattering." A nuclear rainbow appears because of deflection to negative angles. This process involves a strong overlap of nuclear densities, with values of up to twice the saturation density of nuclear matter. The $^{16}O + {}^{16}O$ system is studied with a high precision over a wide energy range from 7 to 70 MeV per nucleon in several laboratories. Primary Airy maxima and higher order Airy structures are observed. At all energies, excellent fits are obtained with deep potentials as deduced from the double-folding model involving a nucleon–nucleon interaction weakly dependent on the density. It is shown that Pauli blocking expected at low energies is strongly reduced if the local momenta are calculated self-consistently. Systematics confirms a refractive origin of large-angle scattering, at low energies inclusive. Thus, nuclear-rainbow scattering yields unique information about the properties of cold nuclear matter at higher densities. © *2002 MAIK "Nauka/Interperiodica".*

1. NUCLEAR-RAINBOW SCATTERING

Refractive nuclear (rainbow) scattering has been a subject of increased attention over the last decades, because it became possible to establish that deep potentials are needed to describe the systematics of heavy-ion scattering. At lower energies, the angular distributions were originally fitted with rather shallow potentials; however, the use of the double-folding model produced very deep real parts of the optical potential for $^{16}O + {}^{16}O$ scattering [1–6], as well as for α-particle scattering [7, 8]. New precise and complete data revealed a very clear sensitivity of large-angle scattering to the details of the real potential at short distances. At these short distances, where there are large density overlaps of scattered nuclei, the double-folding potential is very sensitive to the details of the effective nucleon–nucleon interaction (based on the Paris M3Y interaction [2, 9, 10]), and it has been shown that a consistent description can only be obtained with a distinct, but small density dependence [2, 3, 9, 10]. The same effective interaction gives, in Hartree–Fock calculations, a soft equation of state of cold nuclear matter [4, 9, 10], with the incompressibility parameter taking values in the range $K \simeq 220$–250 MeV with an accuracy of $\pm 15\%$.

We give a brief survey of recent experimental results for elastic $^{16}O + {}^{16}O$ scattering over a wide range of energies. Precise data have now been measured up to large angles at nine energy values in the range $E_{\rm lab} = 75$–124 MeV at IreS [5] and at $E_{\rm lab} =$ 250, 350, 480, 704 and 1120 MeV at the HMI and at GANIL [6]; further data at two energies were measured by Kondo *et al.* [11]. The phenomenology and the quality of the data are shown in Fig. 1 for elastic scattering at higher energies (from 124 to 1120 MeV) and at lower energies. Elastic-scattering data were fitted with an optical potential, where the real part was obtained on the basis of the double-folding model or on the basis of the functional dependence represented by the squared Woods–Saxon form $f_i^2(r)$, where

$$f_i(r) = \left(1 + \exp\left(\frac{r - R_i}{a_i}\right)\right)^{-1}$$

with $i = V$ and W for, respectively, the real and the imaginary part. The latter parametrization gives potential shapes that are very close to double-folding potentials. In addition, a surface term, with the form factor $4a_S \dfrac{d}{dr} f_S(r)$, must be added to the imaginary potential, as was found in [10].

We repeat here the basic facts of rainbow scattering [12, 13]. The rainbow structure appears if the

*This article was submitted by the authors in English.

[1]Also Freie Universität Berlin, Germany; e-mail: oertzen@hmi.de

[2]Institute for Nuclear Science, Hanoi, Vietnam.

[3]GANIL, Caen Cedex, France.

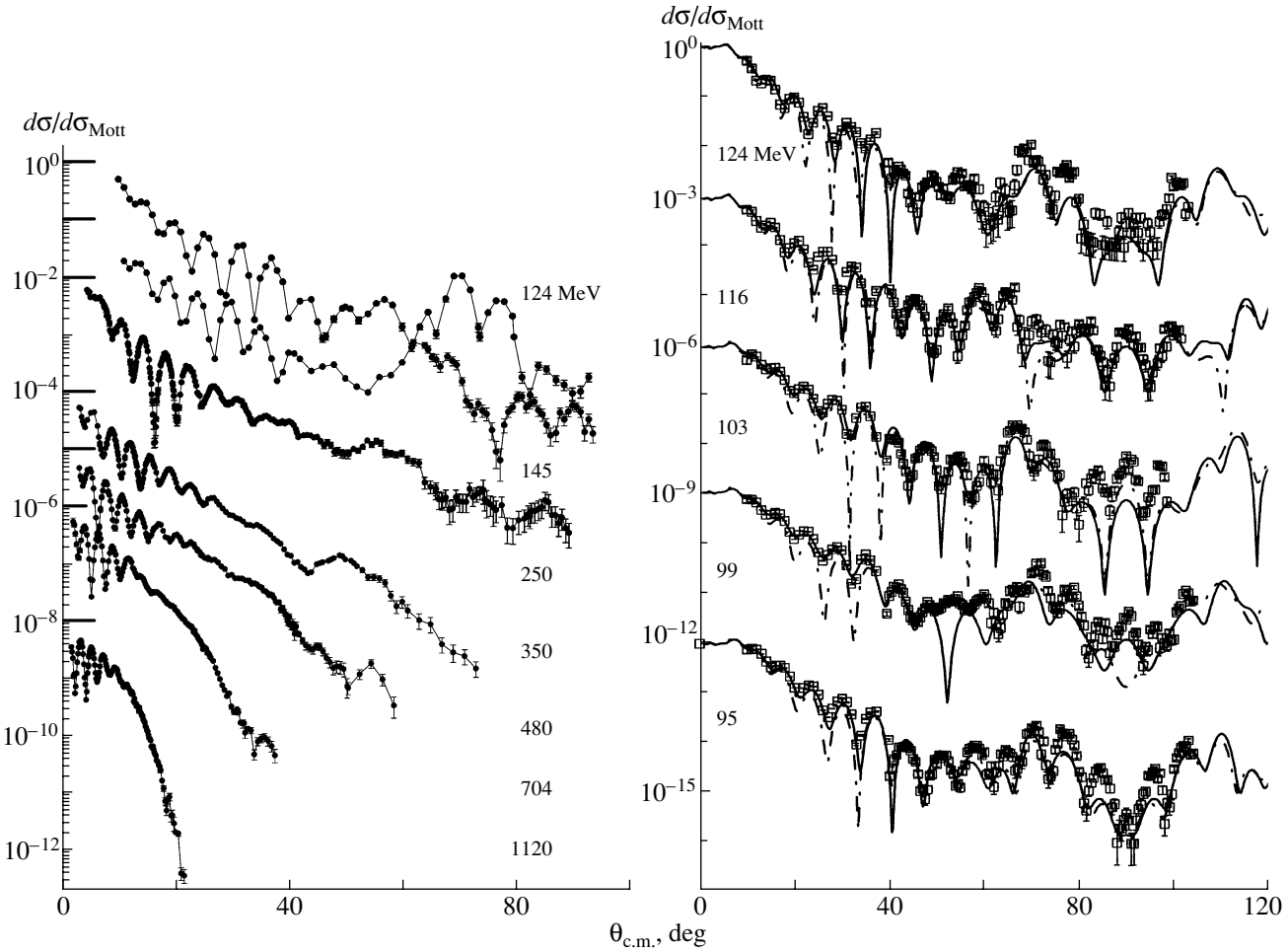

Fig. 1. Differential cross section for elastic $^{16}O + {}^{16}O$ scattering at many energy values (fits to these data are discussed in [5, 9, 10, 14]): (left panel) data for energies $E_{\mathrm{lab}} = 124$ to 1120 MeV (the primary rainbow maximum at $E_{\mathrm{lab}} = 350$ MeV is located at an angle of 55°; it moves to larger angles outside the observation region at lower energies) and (right panel) data for energies from $E_{\mathrm{lab}} = 95$ to 124 MeV [5], with fits obtained with optical model potentials from the double-folding model or with the squared Woods–Saxon potentials.

nuclear potential is sufficiently strong for deflecting particles at "negative angles" and a maximum deflection (rainbow) angle occurs. In this case, a particular oscillating interference structure due to contributions from several impact parameters contributing to the maximum deflection angle will appear, and it will be described by an Airy function (this function is shown in Fig. 2). Higher order maxima, which are refered to as second or third-order Airy structures, appear inside the lighted region. The most remarkable feature of this complete data set for $^{16}O + {}^{16}O$ is the fact that we can follow the evolution of the primary Airy structure from the higher energies of $E_{\mathrm{lab}} = 350$ MeV, where it is well pronounced, down to 124 MeV and lower, where higher order Airy structures appear in the angular range of observation.

2. DOUBLE-FOLDING MODEL AND THE EQUATION OF STATE OF NUCLEAR MATTER

In a systematic analysis, the folded potentials and the squared Woods–Saxon potentials (WS2) were used and found to give equivalent overall fits to elastic-scattering data. We must emphasize the most important point concerning these potentials : The originally (30 years ago) used Woods–Saxon potentials have incorrect radial shapes. This is true, for example, in many cases of α-particle scattering, where only in the last 15 years was it found from a systematic study of scattering states and bound states that the deep potentials [14] of the cited shapes are required. For a further discussion, the potentials

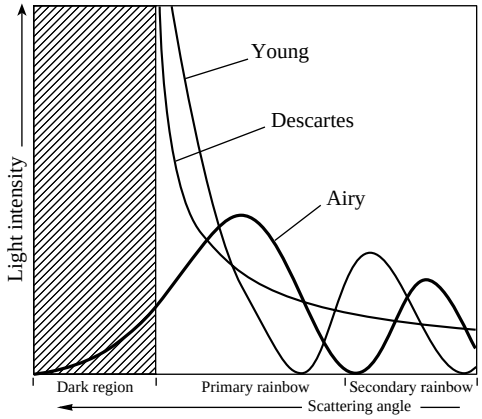

Fig. 2. Airy function describing the rainbow phenomenon. The first intensity maximum appears within the classical lighted region away from the shadow border line. It extends into the shadow and in the lighted region, where higher order maxima and minima occur, which are indeed observed in $^{16}O + {}^{16}O$ scattering at lower energy (see Fig. 1). The "classical" solutions show divergence at the rainbow angle θ_R.

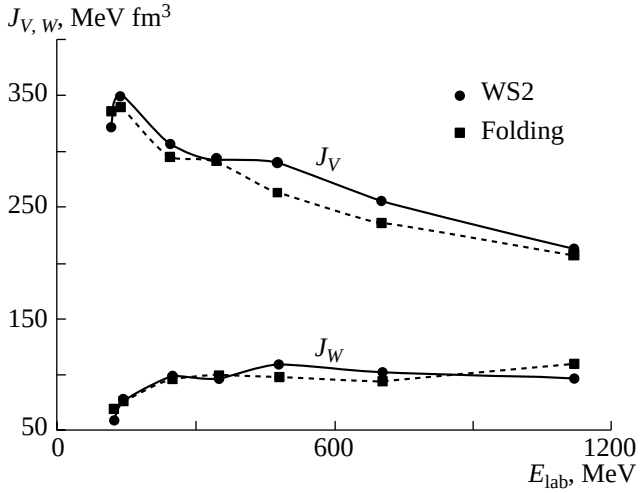

Fig. 3. Volume integrals J_V and J_W of, respectively, the real and the imaginary part of the best-fit real WS2 and folded potentials for the $^{16}O + {}^{16}O$ system at incident energies in the range $E_{lab} = 124–1120$ MeV. The curves are only drawn to guide the eye.

can be classified by their volume integrals

$$J_{V,W} = -\frac{4\pi}{N_A N_B}\int V_{V,W}(r) r^2 dr,$$

which are normalized to the number of interacting nucleon pairs (the nucleon numbers are N_A and N_B for the projectile and the target, respectively). Even in previous studies using the folding model [10] for nucleus–nucleus potentials—in particular, for α-particle scattering on nuclei [7, 8]—it was found that a consistent description is obtained with particular values of the volume integral for nucleon–nucleus potentials [15]. Thus, the criterion for the choice of the potentials was often the value of the volume integral of the real potential per interacting nucleon pair. Values for the volume integrals of $J_V \simeq 300$ MeV fm^3 at $E_{lab} \simeq 30$ MeV per nucleon were obtained in [5, 6] from an analysis for composite particles. The volume integrals for heavier particles could be slightly reduced because of antisymmetrisation effects. We will return to this question later. The systematics of these volume integrals are shown in Fig. 3 over all energies.

An important aspect of the investigation of refractive scattering is a study of the in-medium effective nucleon–nucleon interaction [4, 8–10]. This is achieved by introducing, in the M3Y interaction, a density dependence in such a way that the corresponding Hartree–Fock calculation reproduces the saturation point of nuclear matter [10, 15]. In the double-folding model and in the Hartree–Fock calculation, the exchange part (which is nonlocal) must be treated consistently. In these calculations, different choices of density dependence give different values of the nuclear incompressibility, which is described by the factor K. Examples of such calculations for the equation of state with different values of K are given in Fig.4.

In this approach, the systematics of the nucleon–nucleus potentials, as well as the mean-field potentials of Jeukenne *et al.* [15], are well reproduced [10].

Finally, we return to the question of Pauli blocking effects in the double-folding model. In both heavy-ion and α-particle scattering, very deep squared Woods–Saxon potentials are obtained. This fact could be seen to comply with the Pauli exclusion principle by generating an appropriate number of nodes for the wave function in the interior {the rule $(2N + L) = \sum(n_i + l_i)$ is obeyed [11]}. For the elastic channel, the double-folding model with an effective NN interaction adjusted to the properties of nuclear matter independently gives a potential, as a mean field effect, that is very deep in accordance with the empirical result quoted above. A consistent description of the exchange part of the potential, which is nonlocal, is very important in this concept. It implies that the inclusion of Pauli blocking in the double-folding model must also be done in a self-consistent way. This was recently formulated by Soubbotin *et al.* [16, 17], who calculated a potential based on the Pauli-distorted double-folding model (PDDFM). The main idea is explained in [17] and is illustrated in Fig. 5. Since the relative momentum of nucleons in the potential is determined by the very deep double-folding potential, it increases in the self-consistent description of the

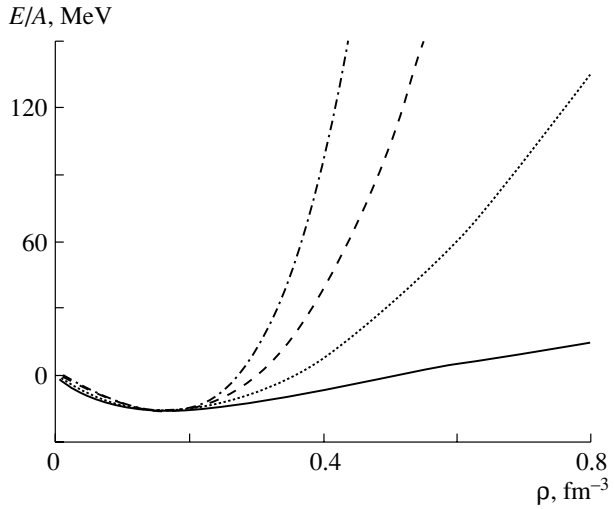

Fig. 4. Results of Hartree–Fock calculations using different versions of the density-dependent M3Y (Paris) interaction (the solid, the dotted, the dashed, and the dash-dotted curve correspond to the DDM3Y1, the BDM3Y1, the BDM3Y2, and the BDM3Y3 version), which yield different values for the incompressibility constant K (150 MeV for DDM3Y1, 210 MeV for BDM3Y1, 330 MeV for BDM3Y2, and 435 MeV for BDM3Y3).

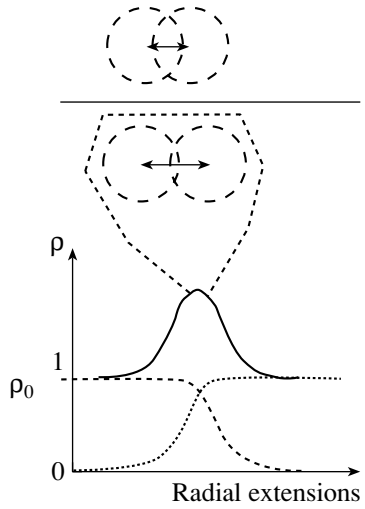

Fig. 5. Illustration of the reduction of Pauli blocking. The local momentum **K** of nucleons during the overlap in the potential becomes high owing to the very strong attractive potential $V(r)$ ($|\mathbf{K}| \sim [E - V(r)]^{1/2}$, where E is the energy of two nuclei in the c.m. frame). In rainbow scattering, overlaps of the densities (ρ) with twice the saturation value (ρ_0) are observed in the elastic channel. The reduced overlap of the Fermi spheres thus occurs owing to the very strong attractive potential created by the mean-field effect in the double-folding model. The circles represent the Fermi spheres in momentum space. The upper part of this figure shows the distance in momentum space with the asymptotic **K** value; the lower part presents the rainbow region with the density overlap and the PDDFM mean field.

local PDDFM potential. The effect of Pauli blocking is thus strongly reduced in the regions of strong overlap.The potentials therefore remain deep over a wide energy range (6–60 MeV per nucleon).

We can thus understand the systematics of nuclear-rainbow scattering down to rather low energies of 7 MeV per nucleon (and even lower energies). The deep potential creates the interference patterns in the angular distributions, which are due to third-order, fourth-order, and higher order Airy structures. The classical studies of low-energy elastic scattering in the $^{12}C + {}^{12}C$ and $^{16}O + {}^{16}O$ systems appear in a completely new light. The structures observed in the excitation functions for the elastic-scattering cross section at 90° are due to the passage of Airy minima in energy (see also [12] for "Airy elephants").

In conclusion, we find that the complete set of data for the $^{16}O + {}^{16}O$ system gives clear criteria for the choice of the particular class of real potentials, which agree well with the results of calculations based on the double-folding model involving a nucleon–nucleon interaction with a weak density dependence, as discussed in [2–4, 8–10]. The related scattering trajectories are deeply penetrating, creating an appreciable density overlap of the two nuclei. Thus, the refractive scattering of strongly bound nuclei is one of the clearest sources of information about the behavior of nuclear matter at higher density.

ACKNOWLEDGMENTS

This work was supported in part by the German Ministry (BMFT) Verbundforschung (contract no. 06OB472D/4).

REFERENCES

1. H. G. Bohlen, E. Stiliaris, B. Gebauer, *et al.*, Z. Phys. A **346**, 189 (1993).
2. D. T. Khoa, W. von Oertzen, *et al.*, Phys. Rev. Lett. **74**, 34 (1995).
3. G. Bartnitzky *et al.*, Phys. Lett. B **365**, 23 (1996).
4. G. Bartnitzky *et al.*, Phys. Lett. B **386**, 7 (1996).
5. M. P. Nicoli, F. Haas, R. M. Freeman, *et al.*, Phys. Rev. C **60**, 064608 (1999).
6. Dao T. Khoa, W. von Oertzen, H. G. Bohlen, *et al.*, Nucl. Phys. A **672**, 387 (2000).
7. S. Ohkubo, Phys. Rev. Lett. **74**, 2176 (1995).
8. D. T. Khoa and W. von Oertzen, Phys. Lett. B **342**, 6 (1995).
9. D. T. Khoa, W. von Oertzen, and H. G. Bohlen, Phys. Rev. C **49**, 1652 (1994).
10. D. T. Khoa and W. von Oertzen, Phys. Lett. B **304**, 8 (1993).
11. Y. Kondo, Y. Sugiyama, *et al.*, Phys. Lett. B **365**, 17 (1996).

12. M. E. Brandan and G. R. Satchler, Phys. Rep. **285**, 143 (1997).
13. J. D. Jackson, Phys. Rep. **320**, 27 (1999).
14. F. Michel, S. Ohkubo, and G. Reidemeister, Prog. Theor. Phys. Suppl., No. 132, 7 (1998).
15. J. P. Jeukenne, A. Lejeune, and C. Mahaux, Phys. Rev. C **16**, 80 (1977).
16. V. B. Soubbotin, W. von Oertzen, *et al.*, Phys. Rev. C **64**, 014601 (2001).
17. K. A. Gridnev, V. B. Soubbotin, W. von Oertzen, *et al.*, Yad. Fiz. **65**, 739 (2002) [Phys. At. Nucl. **65**, 707 (2002)].

Physics of Atomic Nuclei, Vol. 65, No. 4, 2002, pp. 683–688. From Yadernaya Fizika, Vol. 65, No. 4, 2002, pp. 715–720.

Alpha Scattering from Nonclosed Shell Nucleus ^{12}C and Alpha–Nucleus Interaction*

Y. Hirabayashi[1)] and S. Ohkubo**

Department of Applied Science and Environment, Kochi Women's University, Japan

Received July 20, 2001

Abstract—In order to understand the α–nucleus interactions for the $\alpha + {}^{12}\mathrm{C} \sim \alpha + {}^{16}\mathrm{O}$ systems systematically, α scattering from ^{12}C is studied in a microscopic coupled-channel model using a folding potential and realistic microscopic wave functions of ^{12}C. The experimental angular distributions of elastic and inelastic scattering to the 2^+ (4.43 MeV), 3^- (9.64 MeV), and 0_2^+ (7.66 MeV) states in the range of $E_\alpha = 41$–172.5 MeV are analyzed. © *2002 MAIK "Nauka/Interperiodica".*

1. INTRODUCTION

It has been shown that α-clustering is an essential correlation not only in light nuclei but also in medium-weight and heavy nuclei [1, 2]. Many phenomenological and microscopic approaches have been devoted to reveal the spectroscopic properties of the cluster structure of nuclei. Among them, unified description of the α + nucleus system of scattering and bound states has been very powerful in the case when the clustering aspects are not well explored. ^{44}Ti is a typical controversial case where the existence of cluster structure was predicted [3–5] from a careful study of the low-energy properties of the real part of the optical potential determined from a systematic analysis of the experimental data of α scattering from ^{40}Ca. The α-cluster structure in the ^{44}Ti region has been well understood in the microscopic cluster model [6].

On the other hand, α-clustering aspects in the ^{20}Ne region have been thoroughly studied and the spectroscopic properties in the ^{16}O–^{20}Ne region have been well understood. Alpha scattering from target nuclei, ^{16}O [7–10], ^{15}N [10], ^{14}N [11], and ^{14}C [12], have been systematically analyzed, and global optical potentials have been determined. The potentials obtained for hole nuclei, ^{15}N [10] and ^{14}C [12], are very similar to that for the $\alpha + {}^{16}\mathrm{O}$ system [7, 8, 10], which is in accordance with the fact that the α-clustering aspects of the composite system are also a similar supporting weak coupling feature.

One of the long-standing problems is to determine a global potential for the $\alpha + {}^{12}\mathrm{C}$ system. As for the structure of the composite system ^{16}O, all the $T = 0$ energy levels below 12.80 MeV of excitation energy are well understood in the α-cluster model [1]. Also, there are many experimental data on α scattering from ^{12}C in a wide range of incident energies [13–22] . To understand the α^{12}C potential, many theoretical studies have been conducted [23–34].

To our knowledge, to date, nobody has succeeded in making a systematic description of elastic and inelastic α^{12}C scattering in a unified way. The purpose of this paper is to study elastic and inelastic α^{12}C scattering simultaneously in a wide range of incident energies in a microscopic coupled-channel model using a folding potential consistent with a global potential in this mass region. In Section 2, our microscopic coupled-channel model is given, and in Section 3, analysis of the α^{12}C scattering is reported. In Section 4, conclusions are given.

2. MICROSCOPIC COUPLED-CHANNEL MODEL WITH DOUBLE-FOLDING INTERACTIONS

It is important to describe elastic and inelastic α^{12}C scattering simultaneously because the nucleus ^{12}C is strongly deformed and inelastic scattering to the 2^+ (4.43 MeV) and 3^- (9.64 MeV) states are strongly enhanced. Although a conventional collective model is often used in the calculations, it has been known that in ^{12}C, the shell-model-like structure and α-cluster structure coexist. It is desirable to use wave functions for ^{12}C which are as realistic as possible. The coexistence of shell-like states and

*This article was submitted by the authors in English.

1)Center for Information and Multimedia Studies, Hokkaido University, Sapporo, Japan; e-mail: hirabay@hipecs.hokudai.ac.jp

**e-mail: ohkubo@is.kochi-wu.ac.jp

1063-7788/02/6504-0683$22.00

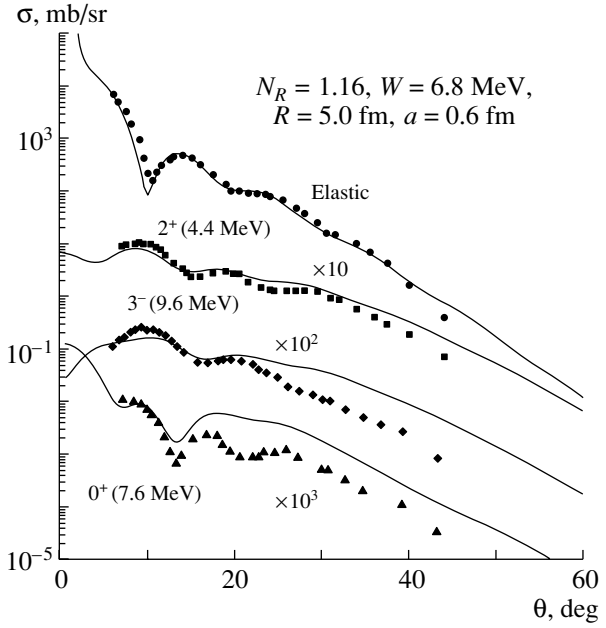

Fig. 1. The experimental data [13] of elastic and inelastic α scattering from ^{12}C at $E_\alpha = 172.5$ MeV are compared with the coupled-channel calculations (solid curves).

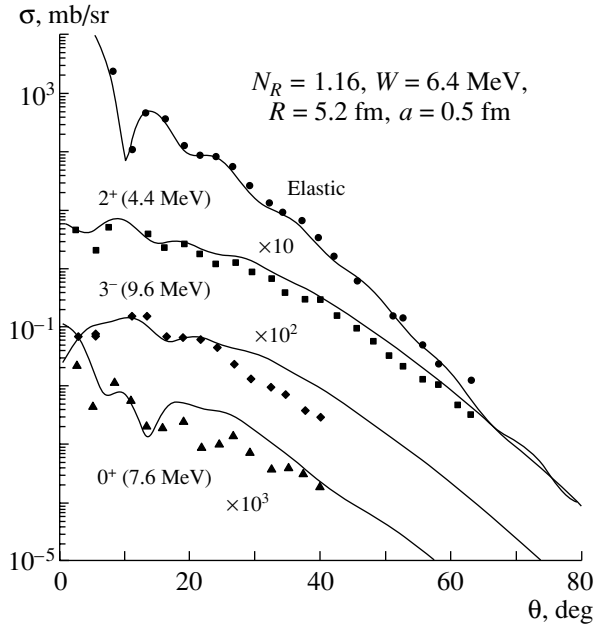

Fig. 2. The experimental data [14] of elastic and inelastic α scattering from ^{12}C at $E_\alpha = 166$ MeV are compared with the coupled-channel calculations (solid curves).

cluster states are well described in a microscopic α-cluster model. In the present calculations, we take the wave functions of ^{12}C calculated in the three-α RGM by Kamimura [35].

It is also better to start from an interaction potential which has as least parameters as possible. In this respect, it is noted that the so-called unique global potentials obtained from a systematic analysis of α scattering from ^{16}O and ^{40}Ca are very similar to the folding potential obtained from DDM3Y [36]: we note that this folding-potential works in the ^{90}Zr and ^{208}Pb regions as well in the systematic description of the angular distributions of α scattering in a wide range of incident energies [37]. Therefore, in the coupled-channel calculations, we take the folding model and the effective interaction DDM3Y.

The total wave function of the $\alpha + {}^{12}$C system is expressed in terms of internal states of ^{12}C as follows:

$$\Psi = \sum_i \varphi(\alpha)\varphi_i(^{12}\mathrm{C})\chi_i(\mathbf{R}), \qquad (1)$$

where $\varphi(\alpha)$ is the intrinsic wave function of the α particle and $\varphi_i(^{12}\mathrm{C})$ is that of the core with spin I and $\chi_i(\mathbf{R})$ is the relative wave function between α and ^{12}C, with i being the ith state of the target. The relative wave function is obtained by solving the following coupled-channel equations:

$$\left[-\frac{\hbar^2}{2\mu}\bigtriangledown^2 + U_{ii}(\mathbf{R}) - (E-\epsilon_i)\right]\chi_i(\mathbf{R}) \qquad (2)$$
$$= -\sum_{j\neq i} U_{ij}(\mathbf{R})\chi_j(\mathbf{R}).$$

The real part of the diagonal and coupling potential in the coupled-channel equation is calculated by double-folding the effective two-body interaction with the nucleon densities of ^{12}C and the α particle:

$$V_{i,j}(\mathbf{R}) \qquad (3)$$
$$= \int \rho_\alpha(\mathbf{r}_\alpha)\rho_{i,j}(\mathbf{r}_T)v(\mathbf{R}-\mathbf{r}_T+\mathbf{r}_\alpha)d\mathbf{r}_T d\mathbf{r}_\alpha,$$

where $\rho_{i,j}$ represents the diagonal ($i=j$) or transition ($i\neq j$) nucleon density of the target ^{12}C [35]. The density of the α particle is taken from [38]. By introducing a phenomenological imaginary potential, the complex coupled potential is given by

$$U_{i,j}(\mathbf{R}) = N_R V_{i,j}(\mathbf{R}) + iW(\mathbf{R})\delta_{i,j}, \qquad (4)$$

where N_R is the normalization factor of the real potential. As for the imaginary potential, a phenomenological Woods–Saxon potential is used. In the coupled-channel calculations, we take into account the five states of ^{12}C; shell-like states 0^+ (0.0 MeV), 2^+ (4.43 MeV), and 3^- (9.64 MeV); and cluster states 0_2^+ (7.66 MeV) and 2_2^+ (10.3 MeV).

3. ANALYSIS OF α^{12}C SCATTERING

Experimental data are analyzed starting from higher energy moving to lower energy because at

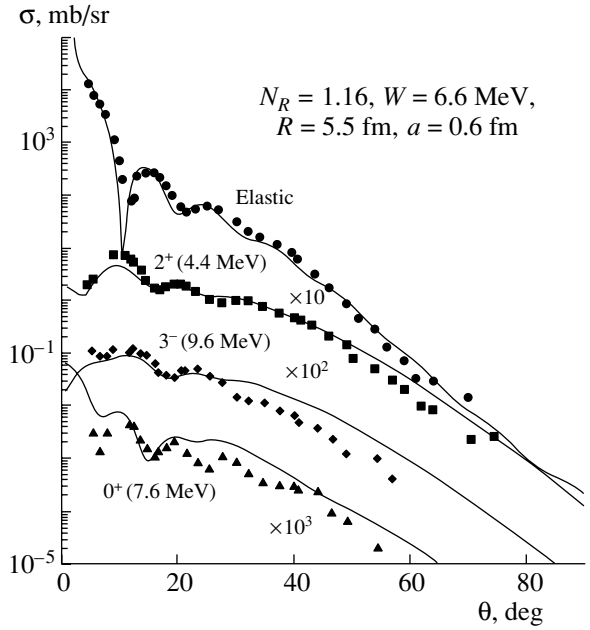

Fig. 3. The experimental data [15] of elastic and inelastic α scattering from ^{12}C at $E_\alpha = 139$ MeV are compared with the coupled-channel calculations (solid curves).

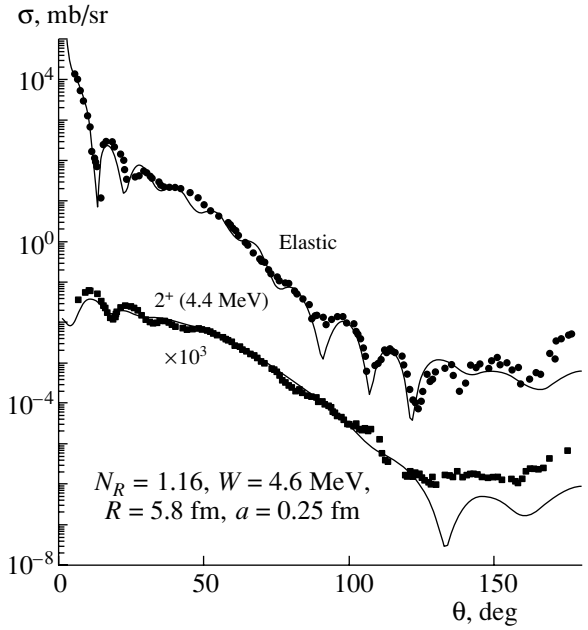

Fig. 4. The experimental data [17] of elastic and inelastic α scattering from ^{12}C at $E_\alpha = 104$ MeV are compared with the coupled-channel calculations (solid curves).

higher energies, the effects of the Pauli principle and resonance are smaller and the reaction mechanism is simpler.

In Fig. 1, the angular distributions at $E_\alpha = 172.5$ MeV obtained for the ground state, 2^+, 3^-, and 0_2^+, in the coupled-channel calculations are compared with the experimental data [13]. The elastic scattering angular distribution is reproduced very well. Inelastic scattering to the 2^+ (4.43 MeV) state is also well reproduced by the calculation. The angular distributions for the 3^- state is reproduced well up to 20°, and the calculation slightly overestimates experimental values at larger angles. As for the cluster state 0^+ (7.6 MeV), the general trend of the angular distribution is reproduced by the calculation.

In Fig. 2, calculated angular distributions at $E_\alpha = 166$ MeV for the ground state, 2^+, 2_2^+, 3^-, and 0_2^+, are displayed in comparison with the experimental data [14]. The fit to the elastic cross sections is very good. The angular distribution for the 2^+ state is also well reproduced. As for the 0_2^+ and 3^- states, which have a very different structure from the ground band, the experimental feature of the angular distribution is well reproduced by the calculation; the slight enhancement of the cross sections for the 3^- state at larger angles is similar to the 172.5-MeV case. The angular distribution for the 0_2^+ state is well reproduced at this energy.

In Fig. 3, the results for $E_\alpha = 139$ MeV are given. The experimental angular distributions [15] of elastic scattering and inelastic scattering to the 2^+ state are reproduced very well by the calculations. The calculated angular distributions for the 0_2^+ and 3^- states also reproduce the essential features of the experimental data, although there is slight overestimation of the cross sections for the 3^- state at larger angles, as was the case for 172.5 and 166 MeV. In the relevant high energy region, the experimental angular distributions for the four states are well reproduced without resorting to a fitting game, although the structures of the states are different. This suggests that not only the wave functions for the states of ^{12}C but also the couplings between the states are well incorporated in the calculations.

The data at $E_\alpha = 104$ MeV were first measured by Hauser *et al.* [16]. They analyzed the data in the forward angles, up to $\theta \sim 100°$, using the Austern–Blair theory and could reproduce the data very well. Also, optical-model analysis was done assuming a bell-shaped potential. They concluded that a repulsive inner core potential added to the larger attractive potential well reproduces the data. They also obtained a similar potential for ^{16}O and ^{14}N, which are very different from the global potential [5]. Specht *et al.* [17] extended the measurement of the angular distributions up to the extreme backward angle, 176°, and they also measured the inelastic angular distribution to the 2^+ (4.43 MeV) state. The inelastic

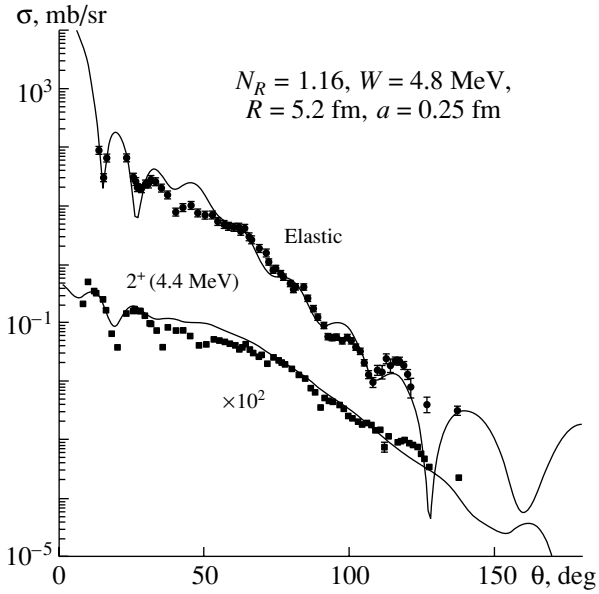

Fig. 5. The experimental data [19] of elastic and inelastic α scattering from ^{12}C at $E_\alpha = 82$ MeV are compared with the coupled-channel calculations (solid curves).

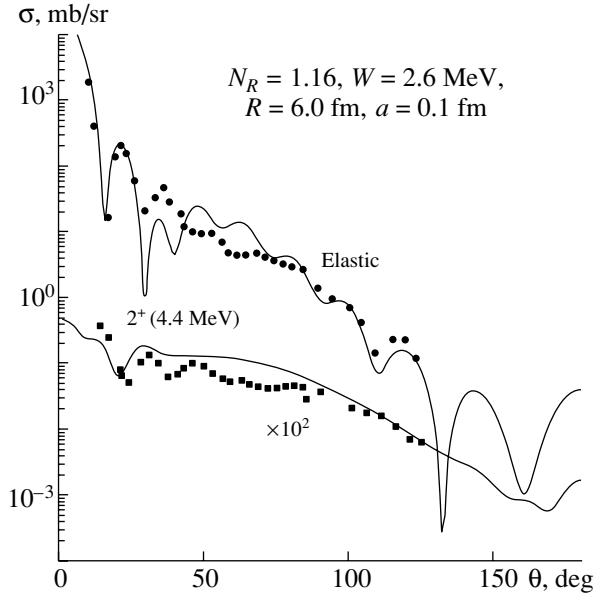

Fig. 6. The experimental data [20] of elastic and inelastic α scattering from ^{12}C at $E_\alpha = 65$ MeV are compared with the coupled-channel calculations (solid curves).

cross sections are greatly enhanced in the backward hemisphere and show a structure similar to elastic scattering. Unfortunately no optical potential model analysis was done. Because the data at high energy and at backward angles could discriminate many potentials that work in the forward angle region, it is very interesting to try to fit the data up to extreme backward angles using an optical potential. Khallaf *et al.* [33] analyzed only elastic data systematically and successfully reproduced the angular distributions at 172.5, 166, 139, and 90 MeV. At 104 MeV, their potential reproduced the slope of the experimental angular distribution, which is similar to the 172.5, 166, and 139 MeV data; however, the pronounced peak in the angular distribution at 100° could not be reproduced and the theoretical result beyond 110° was not compared with the experimental data: also no analysis of the inelastic scattering has been reported. To date, nobody has succeeded in explaining these important data in the potential model.

Normalization factor N_R and volume integral per nucleon pair J_V (in MeV fm^3)

E_α, MeV	N_R	J_V	J_V [28]	J_V [15]
41	0.90	246		
65	1.16	313		
82	1.16	305		
104	1.16	298	393	319
139	1.16	286	353	278
166	1.16	279	326	
172.5	1.16	286		277

In Fig. 4, the experimental angular distributions at $E_\alpha = 104$ MeV [17] are compared with our coupled-channel calculations. The calculation reproduces the behavior of the angular distributions at forward angles, which is consistent with that at higher energies of 172.5, 166, and 139 MeV. Beyond 90°, there appear characteristic oscillations in the elastic angular distributions. The calculation reproduces the oscillatory structure very well. Also in the inelastic scattering, the fall-off stops around 120°, beyond which there appears a plateau: the calculation agrees very well with the experimental data in the forward angles up to 100°, and, interestingly, the calculation increases toward backward angles being consistent with the experimental data. Since the backward data are sensitive to the internal part of the potential, the agreement between the calculations and the data up to backward angles show that the present potential is reasonable at this energy. Therefore, the potential which is consistent with the global potential for the $\alpha + {}^{16}$O system also works for the $\alpha + {}^{12}$C system.

In Fig. 5, experimental data at $E_\alpha = 82$ MeV [19] are compared with the calculations. The behavior of the angular distributions with some oscillatory structure is reproduced by the calculation. The theory shows structure even beyond 120°; it is interesting whether the oscillations are observed in experiment.

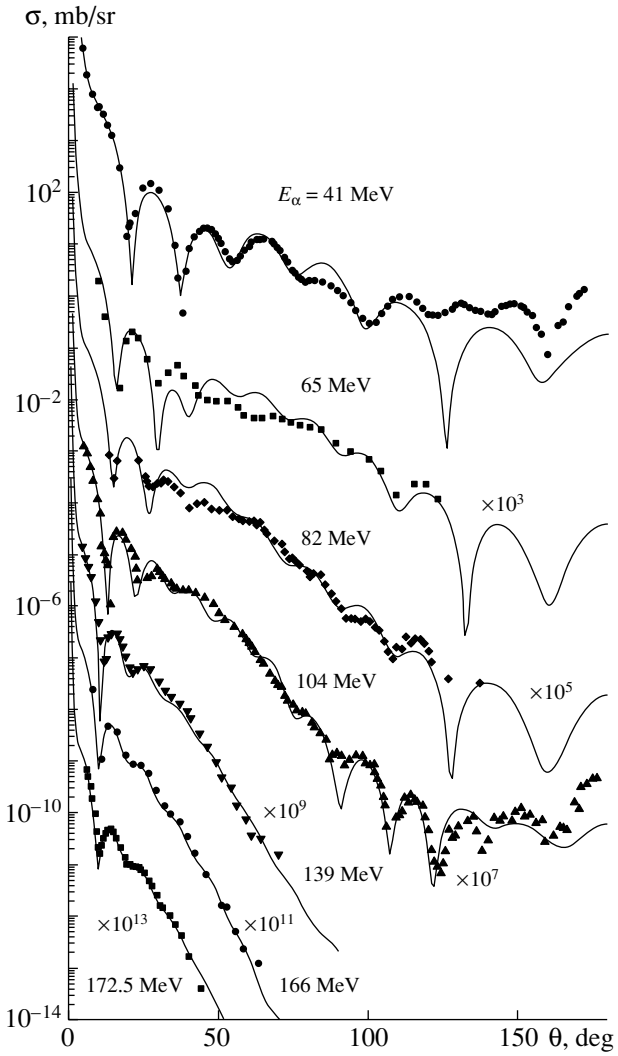

Fig. 7. The experimental angular distributions of elastic α scattering from ^{12}C are compared with the coupled-channel calculations (solid curves).

The angular distribution for inelastic scattering to the 2^+ state shows a structure similar to the 104 MeV data with fall-off up to about 100° following some oscillatory structure. This behavior is essentially well described by our calculation.

In Fig. 6, experimental data at $E_\alpha = 65$ MeV [20] are compared with the calculations. The behavior of the elastic scattering angular distributions is reproduced well by the calculation except around 50°, where the oscillatory structure is slightly exaggerated. The inelastic cross sections are greatly enhanced. The coupled-channel calculation gives the right magnitude of the cross sections and the behavior: the oscillatory structure in the 50°–120° is suppressed in the calculated results. It is noted that a small diffuseness parameter $a = 0.1$ fm is needed. Yasue *et al.* [20] tried to fit the data with a conventional Woods–Saxon potential and a collective form factor but could not get a good agreement: the results are poorer than the present one.

In Fig. 7, the experimental elastic scattering data in the range of $E_\alpha = 41$–172.5 MeV are summarized in comparison with the coupled-channel calculations. The agreement of the calculations with experiment is good in the whole angular range. It should be noted that the potential parameter N_R is kept at 1.16 for all the incident energies (except $E_\alpha = 41$ MeV) and no parameter search has been done. The energy dependence of the real potential is due to that of the DDM3Y. Only imaginary parameters are fitted at each energy.

At $E_\alpha = 41$ MeV [22], the forward oscillatory structure is reproduced by the calculation; however, the agreement deteriorates. Also, we note that a smaller $N_R = 0.9$ is needed. As energy becomes lower, smaller diffuseness parameters are needed for the imaginary potential. At lower energies, effects not included in the present formalism may be involved.

The used parameters of the normalization factor for the real potentials and the volume integrals are given in the table in comparison with other analyses. The energy dependence of the volume integral is consistent with other analyses. It is interesting to investigate whether the difference of the volume integral between the present bare potential and the phenomenological potential of [15] is due to dynamical coupling. On the other hand, the difference between the bare potential and Khoa's folding potential is rather small, suggesting that dynamical polarization due to coupling is rather small at these higher energies.

4. CONCLUSIONS

Alpha-particle scattering from nonclosed shell nucleus ^{12}C was studied by using a folding type deep potential with the use of microscopic α-cluster wave functions for ^{12}C. The angular distributions of elastic and inelastic scattering from 41 to 172.5 MeV were analyzed in the coupled-channel calculations by taking not only the ground-state band but also the α-cluster states, and the agreement of the calculations with the data is fairly good.

The present results show that a deep potential obtained by the folding model works for the description of elastic and inelastic scattering from ^{12}C in a wide range of incident energies employing microscopic α-cluster model wave functions: the potential is consistent with the global ones for the $\alpha + {}^{16}$O, $\alpha + {}^{15}$N, and $\alpha + {}^{14}$N systems. The calculations, however, suggest that at lower energies, some ingredients, which are not included in the present frame, may be needed to improve the fit to the experimental data.

ACKNOWLEDGEMENTS

One of the authors (S.O.) is grateful to F. Michel for useful discussions and collaboration in the initial stage of this work.

S.O. has been supported by a grant-in-aid of the Japan Society for the Promotion of Science (no. 12640288) .

REFERENCES

1. K. Ikeda *et al.*, Prog. Theor. Phys. Suppl., No. 68, 1 (1980).
2. S. Ohkubo, Prog. Theor. Phys. Suppl., No. 132, 1 (1998).
3. F. Michel, G. Reidemeister, and S. Ohkubo, Phys. Rev. Lett. **57**, 1215 (1986).
4. F. Michel, G. Reidemeister, and S. Ohkubo, Phys. Rev. C **37**, 292 (1988).
5. F. Michel, S. Ohkubo, and G. Reidemeister, Prog. Theor. Phys. Suppl., No. 132, 7 (1998).
6. T. Sakuda and S. Ohkubo, Prog. Theor. Phys. Suppl., No. 132, 103 (1998).
7. S. Ohkubo, Y. Kondo, and S. Nagata, Prog. Theor. Phys. **57**, 82 (1977).
8. F. Michel, J. Albiński, P. Belerly, *et al.*, Phys. Rev. C **28**, 1904 (1983).
9. S. Ohkubo, in *Proceedings of the 6th International Conference on Nuclear Reaction Mechanisms,* Ed. by E. Gadioli, Milano Univ. Ric. Sci. Educ. Perman. Suppl., No. 84, 396 (1991).
10. H. Abele and G. Staudt, Phys. Rev. C **47**, 742 (1993).
11. H. Jantsch, H. Abele, R. Neu, *et al.*, in *Proceedings of the 5th International Conference on Clustering Aspects in Nuclear and Subnuclear Systems, Kyoto, Japan, 1988,* Ed. by Y. Sakuragi, T. Wada, and Y. Fujiwara, p. 182.
12. F. Michel and G. Reidemeister, Phys. Rev. C **53**, 3032 (1996); G. Reidemeister and F. Michel, Phys. Rev. C **47**, R1846 (1993).
13. A. Kiss, C. Mayer-Böricke, M. Rogge, *et al.*, J. Phys. G **13**, 1067 (1987).
14. B. Tatischeff and I. Brissaud, Nucl. Phys. A **155**, 89 (1970).
15. S. M. Smith, G. Tibell, A. A. Cowley, *et al.*, Nucl. Phys. A **207**, 273 (1973).
16. G. Hauser, R. Löhken, H. Rebel, *et al.*, Nucl. Phys. A **128**, 81 (1969).
17. J. Specht, G. W. Schweimer, H. Rebel, *et al.*, Nucl. Phys. A **171**, 65 (1971).
18. A. S. Goncharov *et al.*, Yad. Fiz. **54**, 911 (1991) [Sov. J. Nucl. Phys. **54**, 552 (1991)].
19. R. Ceuleneer, F. Michel, G. Reidemeister, *et al.*, unpublished.
20. M. Yasue, T. Tanabe, F. Soga, *et al.*, Nucl. Phys. A **394**, 29 (1983).
21. H. Abele, H. J. Hauser, A. Körber, *et al.*, Z. Phys. A **326**, 373 (1987).
22. N. Baron, R. F. Leonard, and W. M. Stewart, Phys. Rev. C **4**, 1159 (1971).
23. D. A. Goldberg, Phys. Lett. B **55B**, 59 (1975).
24. A. M. Kobos, A. B. Brown, P. E. Hodgson, *et al.*, Nucl. Phys. A **384**, 65 (1982).
25. V. V. Burnov, O. M. Knyazkov, A. A. Shirokova, and K. V. Shitikova, Z. Phys. A **313**, 319 (1983).
26. H. J. Gils, H. Rebel, and E. Friedman, Phys. Rev. C **29**, 1295 (1984).
27. A. K. Chauduri, Nucl. Phys. A **449**, 243 (1986); **459**, 417 (1986).
28. D. T. Khoa, Nucl. Phys. A **484**, 376 (1988); D. T. Khoa, G. R. Satchler, and W. von Oertzen, Phys. Rev. C **56**, 954 (1997).
29. M. El-Azab Farid, J. Phys. G **16**, 461 (1990).
30. R. Lichtenhäler, A. C. C. Villari, A. Lépine-Szily, and L. C. Gomes, Phys. Rev. C **44**, 1152 (1991).
31. E. H. Esmael, S. A. H. Abou Steit, M. E. M. Zedan, and M. Y. M. Hassan, J. Phys. G **17**, 1755 (1991).
32. F. Michel and G. Reidemeister, in *Proceedings of the 6th International Conference "Clusters in Nuclear Structure and Dynamics," Strasbourg, France, 1994,* Ed. by F. Haas, p. 56.
33. S. A. E. Khallaf, A. M. A. Amry, and S. R. Mokhtar, Phys. Rev. C **56**, 2093 (1997).
34. L. C. Chamon, D. Pereira, M. S. Hussein, *et al.*, Phys. Rev. Lett. **79**, 5218 (1997).
35. M. Kamimura, Nucl. Phys. A **351**, 456 (1981); Y. Fukushima and M. Kamimura, in *Proceedings of the International Conference on Nuclear Structure, Tokyo, Japan, 1977,* p. 225.
36. A. M. Kobos, B. A. Brown, R. Lindsay, and G. R. Satchler, Nucl. Phys. A **425**, 205 (1984).
37. S. Ohkubo, Phys. Rev. Lett. **74**, 2176 (1995).
38. G. R. Satchler and W. G. Love, Phys. Rep. **55**, 183 (1979).

Physics of Atomic Nuclei, Vol. 65, No. 4, 2002, pp. 689–696. From Yadernaya Fizika, Vol. 65, No. 4, 2002, pp. 721–728.

Decay Properties of $N \sim Z$ Nuclei*

E. Roeckl**

Gesellschaft für Schwerionenforschung, Darmstadt, Germany

Received July 20, 2001

Abstract—By using heavy-ion induced fusion-evaporation reactions at the on-line mass separator of GSI, the decay properties of neutron-deficient isotopes between ^{56}Ni and ^{100}Sn were investigated. The experimental results will be presented and discussed in comparison with model predictions. © *2002 MAIK "Nauka/Interperiodica".*

1. INTRODUCTION

The study of nuclear decay properties at and near the $N = Z$ line in general, and of nuclei between the double shell closure at ^{56}Ni and ^{100}Sn in particular, meets exceptional phenomena. In addition to β decay and the accompanying emission of β-delayed γ radiation, proton or α emission may occur either as a β-delayed or "Coulomb-delayed" (direct) process, the latter disintegration mode indicating that nuclei beyond the drip lines for proton or α emission have been reached. Nuclei, situated near these borderlines of nuclear stability, are of great current interest to nuclear physics and astrophysics. The latter research link relates to, e.g., the detection of solar neutrinos [1, 2], the *rp* process [3], and the electron-capture cooling of supernovae [4]. As far as nuclear physics is concerned, experiments on direct particle emission give access to binding energies and reduced particle width, while the high energy release in β decay allows one to measure the Gamow–Teller (GT) strength B_{GT} for a large range of excitation energies in the daughter nucleus and thus to stringently test theoretical B_{GT} predictions. The tasks of β-decay measurements are to deduce the experimental B_{GT} distribution as a function of the excitation energy in the daughter nucleus, if possible *completely,* i.e., including (weak) decay branches to high-lying levels, and to investigate whether theoretical calculations are able to reproduce this distribution, with particular emphasis on the possible quenching of the calculated GT strength.

Another interesting feature of β decay is the possibility to determine spin/parity of the parent state if the configuration(s) of the daughter level(s), populated in the decay, is (are) known. This yields another quantity to be compared to (shell) model predictions, represents an important "service" to in-beam spectroscopists in their attempt to establish the γ-ray deexcitation of high-spin levels to, hopefully, well-established low-spin states, and offers, in the case of odd–odd parent nuclei, the chance of studying the structure of low-lying two-quasiparticle states. Odd–odd $N = Z$ nuclei play a special role, as their superallowed $0^+ \rightarrow 0^+$ β decay allows one to accurately determine the weak vector-coupling constant and thus to probe physics beyond the standard model. In this context, it is important to clarify whether β decay of non-0^+ (high-spin) states competes with the superallowed transition.

Based on these motivations, there has been a recent upsurge of both theoretical and experimental work on the decay properties of $N \sim Z$ nuclei, measurements being carried out, in particular, at ISOLDE/CERN [5–8], GANIL [9], and GSI. The present paper deals with work performed in the latter laboratory, where two major facilities are available for the study of $N \sim Z$ nuclei. One is a projectile-fragment separator (FRS) which uses fragmentation reactions induced by relativistic beams from a heavy-ion synchrotron SIS. However, only a few experiments on decay properties near $N \sim Z$ have been carried out on this instrument so far [1, 2, 10], in contrast to the other facility, i.e., the isotope separator on-line (ISOL) to the heavy-ion accelerator UNILAC. It is the research program of ISOL, and, in particular, the recent decay studies of ^{56}Cu, ^{58}Cu, and ^{70}Br and of nuclei near ^{100}Sn, which forms the focus of the present overview. A detailed discussion of the nuclear-physics aspects of these results, as well as of their astrophysical relevance, cannot be given within the scope of this report, but can be found in the references cited throughout the text.

*This article was submitted by the author in English.

**e-mail: e.roeckl@gsi.de

1063-7788/02/6504-0689$22.00

2. EXPERIMENTAL TECHNIQUES

At the ISOL, heavy-ion induced fusion-evaporation reactions are induced by ^{32}S, ^{36}Ar, ^{40}Ca, or ^{58}Ni beams on ^{28}Si, ^{40}Ca, ^{50,52}Cr, or ^{58,60}Ni targets. Forced electron-beam arc discharge (FEBIAD) ion sources [11, 12] or thermal ion sources (TIS) [13], which are chemically selective and yield high release efficiencies, are used to produce mass-separated beams of neutron-deficient iron-to-barium isotopes. The 55-keV ISOL beams are implanted either in a thin carbon foil or in a tape that transports the activity to (or away from) the various detector arrays. Coulomb-delayed or β-delayed protons and α particles are measured by means of ΔE–E telescopes consisting of a thin gas or silicon (Si) ΔE-detector and a thick Si E-detector. The former records the energy loss of β-delayed charged particles, whereas the latter measures their rest energy. Low-energy protons or α particles are stopped in the thin detector, while positrons are recorded in the thick detector to derive an anticoincidence condition and thus to suppress energy-loss events of β-delayed particles.

The *high-resolution* spectroscopy of β-delayed γ rays emitted from mass-separated sources is accomplished by using germanium (Ge) detectors, recently including those of the Euroball-Cluster [14] and Clover type [15]. An exceptionally efficient high-resolution γ-ray detector became available at ISOL in 1996, i.e., a cubelike array of six Euroball-Cluster detectors (Cluster Cube) which comprised 42 Ge crystals and had an absolute photopeak efficiency of 10.2(0.5)% for 1.33-MeV γ rays [16]. In the case of low source strengths, the β-delayed γ rays can be measured in coincidence with positrons recorded in a NE102A plastic-scintillation detector.

As a *low-resolution* but high-efficiency alternative to the γ-ray detectors described above, a total-absorption spectrometer (TAS) is used. The TAS [17] consists of a large NaI crystal surrounding a radioactive source, two small Si detectors above and below the source, and a Ge detector placed above the upper Si detector. By demanding coincidence with signals from the Si detectors, the β^+-decay component for the nucleus of interest is selected, whereas coincidences with characteristic $K_{\alpha,\beta}$ x-rays recorded by the Ge detector can be used to select the EC mode. In this way, the *complete* distribution of the β strength can be determined for neutron-deficient isotopes, including, in particular, high-lying levels of the respective daughter nuclei, and the Q_{EC} value can be deduced from the ratio between the β^+ and EC intensities. Moreover, the TAS enables one to investigate X-rays related to the emission of conversion electrons (from isomeric transitions), with an optional anticoincidence condition on signals from the Si detectors and the NaI crystal in order to suppress (room) background. Last but not least, the TAS can also be used to measure β-delayed protons, detected in one of the Si detectors (or a telescope of Si detectors) operated in coincidence with positrons, x-rays, and/or γ rays. In this way, one can, e.g., distinguish between β^+ and EC transitions preceeding proton emission, determine the $(Q_{\mathrm{EC}} - S_p)$ value for a selected level of the final nucleus populated by proton transitions, deduce information on the lifetime of the proton-emitting levels by means of the proton and x-ray coincidence technique (PXCT) [18], and use proton–γ coincidence data to identify excited states in the final nucleus.

3. RESULTS AND DISCUSSION

3.1. Direct Charged-Particle Decay

In addition to interesting nuclear-structure data such as spectroscopic factors, the line spectra of direct protons and α particles yield the mass difference between the parent and daughter nucleus in a straightforward way, i.e., without the complications involved in, e.g., β-endpoint determination. After the early experiments on ^{147}Tm [19], no further ISOL research on direct proton emitters, except for the search experiment of ^{105}Sb [20], was performed. As the data available for this decay are at variance, a new ISOL experiment with improved granularity and resolution of the proton detector is being prepared.

The island of α emission beyond ^{100}Sn was a favorite ISOL topic in the eighties (see, e.g., [21]). More recently, α and cluster emission from ^{114}Ba was searched for, yielding, however, only upper limits of 3.7×10^{-3} and 3.4×10^{-5} for the respective decay branching ratios [22]. (In a related effort, cluster emission from excited states of ^{116}Ba was studied by measuring ^{58}Ni+^{58}Ni reaction cross sections at ISOL [23].) In the summer of 2000, the decay of ^{114}Ba was reinvestigated at the ISOL. According to results from a *very preliminary* data evaluation [24], displayed in Fig. 1, the α decay of ^{114}Ba was observed as the lowest energy line of ~3.4 MeV, the neighbouring higher energy members of the triplet being ascribed to the known [21] α lines of the daughter ^{110}Xe and the granddaughter ^{106}Te. This result is interesting for the following reasons. First, the increase of the energies along the triple α chain is a textbook example of experimental evidence of a shell closure. Second, and indeed related to the topic of this conference, by summing the three α-decay Q values one can deduce, preliminarily again, an experimental Q value

Beta decay of ^{56}Cu to low-lying ^{56}Ni states [the experimental ^{56}Ni level energies $E_{\rm expt}$, β intensities I_β, and β strengths $B_{\rm GT}^{\rm expt}$, determined from a preliminary data evaluation [27], are compared with shell-model predictions for the level energies ($E_{\rm FPD6}$, $E_{\rm KB3}$) and the β strengths ($B_{\rm GT}^{\rm FPD6}$, $B_{\rm GT}^{\rm KB3}$); the spin/parity/isospin assignments ($I^\pi;T$) were deduced from reaction data [28], except for the 4936, 5483 keV, and 5988 levels, whose configurations were tentatively deduced from a comparison with shell-model predictions]

$E_{\rm expt}$, keV	$E_{\rm FPD6}$, keV [26]	$E_{\rm KB3}$, keV [4]	$I^\pi;T$	$I_\beta^{\rm expt}$, %	$B_{\rm GT}^{\rm expt}$	$B_{\rm GT}^{\rm FPD6}$ [26]	$B_{\rm GT}^{\rm KB3}$ [4]
2700.6(4)	3220	4318	$2^+;0$	−1.2(6.6)	−	−	−
3925.1(5)	4072	4901	$4^+;0$	22.2(6.5)	0.113(33)	0.087	0.128
4935.5(6)	4955	5439	$(3^+);0$	10.2(3.2)	0.084(27)	0.102	0.061
5483.0(5)	5643	5893	$(4^+);0$	10.0(2.1)	0.110(24)	0.46	0.100
5987.9(6)	6463	6069	$(3^+);1$	11.6(1.9)	0.169(29)	0.28	0.21
6431.7(7)	6181	6862	$4^+;1$	67.5(3.7)	2.0	2.002	2.001
6588.6(8)	7938	7452	$(3,4,5)^+$	7.6(1.7)	0.158(36)	0.022	0.034

of ∼19.0 MeV for ^{12}C decay of ^{114}Ba, which is important in obtaining experimentally relevant predictions from cluster-emission calculations. Third, the analysis of time correlations between ^{114}Ba and ^{110}Xe events will hopefully yield the hitherto unknown half-life of the latter nucleus. This result, together with the previously unknown α-branching ratio of ^{110}Xe deduced from the intensities of the two lines, can be used to determine the s-wave α width of this nuclide and thus to extend the corresponding sytematics towards its low-mass end [25].

3.2. Beta Decay

^{56}Cu: Beta decay to doubly magic ^{56}Ni. Compared to the previous ISOL work [26], which represented the first observation of the ^{56}Cu decay, the data on β-delayed γ rays have been improved in statistics by about a factor of 30 in a recent measurement [27]. The experimental results are compiled in the table. Besides the γ transitions of 1225, 2507, 2701, and 2780 keV, that were already observed in the earlier work [26] and used to identify four excited states of ^{56}Ni, additional γ lines of 951, 1010, 1653, 2063, 2235, and 3287 keV were assigned to the decay of ^{56}Cu, respectively. The intensity of the β transition to the 2701-keV 2_1^+ state in ^{56}Ni was found to be zero within the experimental uncertainties (see the table). The experimental $B_{\rm GT}$ values were determined by using the branching ratios and the half-life of 78(15) ms from recent data [27] and a $Q_{\rm EC}$ value of 15 300(140) keV [29]. As the latter was derived from systematical (Coulomb energy) trends, the resulting $B_{\rm GT}$ values represent semi-empirical estimates. A discussion of the Fermi and GT strength for the isobaric analog state at 6432 keV [26] is outside the scope of this paper.

The table also lists results obtained from large-scale shell-model calculations. The first one, called Model C in [26], used the FPD6* interaction to determine the strengths of GT transitions between the $[(f_{7/2})^{-1} \times p_{3/2}]$ $(4^+;\ T=1)$ ground state of ^{56}Cu and the $[(f_{7/2})^{-1} \times p_{3/2}]$ $(3^+,4^+,5^+;\ T=0,1)$ and $[(f_{7/2})^{-1} \times p_{1/2}]$ $(3^+,4^+;\ T=0,1)$ excited states of ^{56}Ni. Up to three particles excited from the $f_{7/2}$ orbital to the $p_{3/2}$, $p_{1/2}$, and $f_{5/2}$ orbitals were taken into account. The second calculation [4] was based on the monopole-corrected KB3 interaction. In both calculations, the global effective quenching of the GT matrix elements was included as determined by Martinez-Pinedo *et al.* [30]. As can be seen from the table, qualitative agreement has been obtained between experimental and theoretical $B_{\rm GT}$ values. However, the *total* $B_{\rm GT}$ value measured for the ^{56}Cu decay amounts to 0.42(0.09) compared to the FPD6* result of 4.29. The FPD6*, as well as the KB3 calculation, predicts most of the GT strength to reside at higher ^{56}Ni excitation energies, which are difficult to experimentally access due to their small phase space. However, even $B_{\rm GT}$ at lower excitation energies are valuable for testing model predictions, also in view of their use for calculating EC rates in supernovae.

^{58}Cu: Beta decay versus charge-exchange reactions. By using the TAS, the β decay of ^{58}Cu was studied. The experimental results obtained for this decay (see Fig. 2), as well as for the superallowed $0^+ \to 0^+$ disintegration of ^{46}V [31], may serve as an example of the response function of the TAS and for the determination of β intensities from TAS spectra. The branching ratio for the transition from the ^{58}Cu ground state to the ^{58}Ni ground state was redetermined with improved accuracy to be 81.2(0.5)%

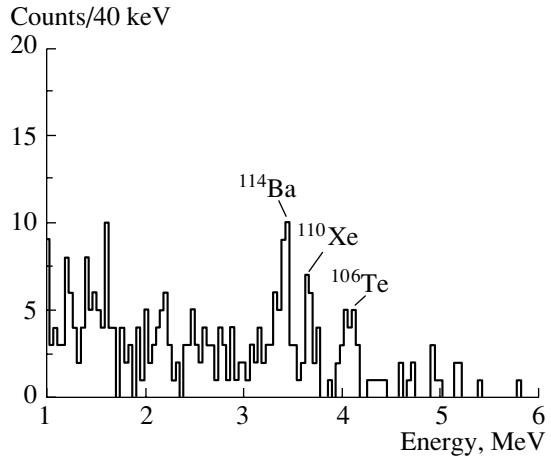

Fig. 1. Triple α chain involving the decays of ^{114}Ba, ^{110}Xe, and ^{106}Te.

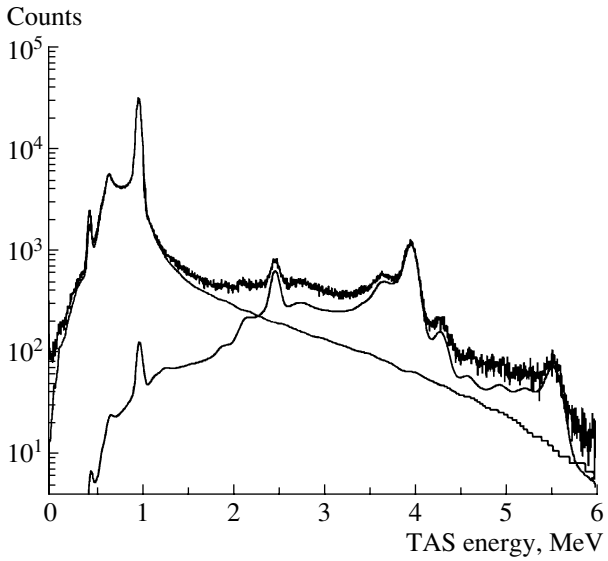

Fig. 2. Total-absorption spectrum of γ rays from the decay of ^{58}Cu decomposed into parts corresponding to the feeding of the ground state and excited levels of ^{58}Ni. The high-energy tail of the 1022 keV peak is due to positrons penetrating into the NaI crystal.

[31], which is of interest for deducing reliable B_{GT} values from cross-section measurements of charge-exchange reactions such as ^{58}Ni(^{3}He, t)^{58}Cu.

^{70}Br and ^{94}Ag: Beta decay of high-spin states of odd–odd $N = Z$ nuclei. As has been mentioned in Section 1, odd–odd $N = Z$ nuclei play a special (fundamental) role in view of their superallowed $0^+ \to 0^+$ β decay. This feature will be discussed here for the cases of ^{70}Br and ^{94}Ag.

There is contradictory information available in the literature concerning the β decay of ^{70}Br. By detection of high-energy positrons, values of 2.2(0.2) s [32] and 79.54(0.59) ms [33] were found, the latter result being in agreement with earlier heavy-ion based studies. Moreover, a recent measurement of β-delayed γ rays [34, 35] did not yield a new half-life value but lead to contradictory conclusions drawn by comparing the γ rays observed with those identified in the β-decay daughter ^{70}Se by in-beam spectroscopy [36]. While in an earlier conference contribution [34] it was concluded that the β-decaying ^{70}Br state has a 5^+ assignment and might be "a quite spherical nucleus," the subsequent publication [35] mentions a 9^+ assignment. At any rate, the discussion of the configuration of this state has to take into account that in-beam work on the neighboring nucleus ^{68}Se has been interpreted by ascribing substantial *oblate* deformation to its ground-state band [37].

In a recent measurement of the ^{70}Br decay [38], an intensity of approximately 100 atoms/s was obtained for the mass-separated and chemically separated ISOL beam of ^{70}Br. This beam intensity is sufficiently high to allow one to obtain, in contrast to [34, 35], very good γ-singles and good γ–γ coincidence data (see Fig. 3). This is indeed an achievement, as ^{70}Br is presumably the lightest bound isotope of bromine. A preliminary data evaluation indicates that the half-life of ^{70}Br is 2.2(0.3) s and that the β-decaying state most probably has a 9^+ assignment. The latter conclusion is again based on a comparison with in-beam data [36]. However, it is clear already now that the level scheme of ^{70}Se will be substantially extended by the new data. Detailed analysis of the rich γ-singles and γ–γ coincidence data, including a search for a short-lived (superallowed) decay component, will hopefully be able to solve the puzzles which may be characterized as "short-lived versus long-lived," "5^+ versus 9^+," and "sphericity versus oblate deformation."

^{94}Ag is the heaviest odd–odd $N = Z$ nucleus with known decay properties. The only information available so far had been gained in an earlier ISOL experiment [39]. The half-life of 0.42(5) ms observed for the β-delayed proton activity was tentatively assigned to the decay of a 9^+ (or 7^+) state in ^{94}Ag, this conclusion being based on a comparison with a shell-model prediction of low-lying ^{94}Ag levels. The latter calculation assumes ^{100}Sn as an inert core and allows the valence protons and neutrons to occupy the $g_{9/2}$, $p_{1/2}$, $p_{3/2}$, and $f_{5/2}$ orbitals [39–41]. A recent ISOL measurement succeeded in detecting β-delayed γ rays of ^{94}Ag for the first time. The preliminary data evaluation [42] yielded a half-life of 0.36(3) ms, which is in agreement with the above-mentioned result obtained for β-delayed protons, and identified several γ transitions

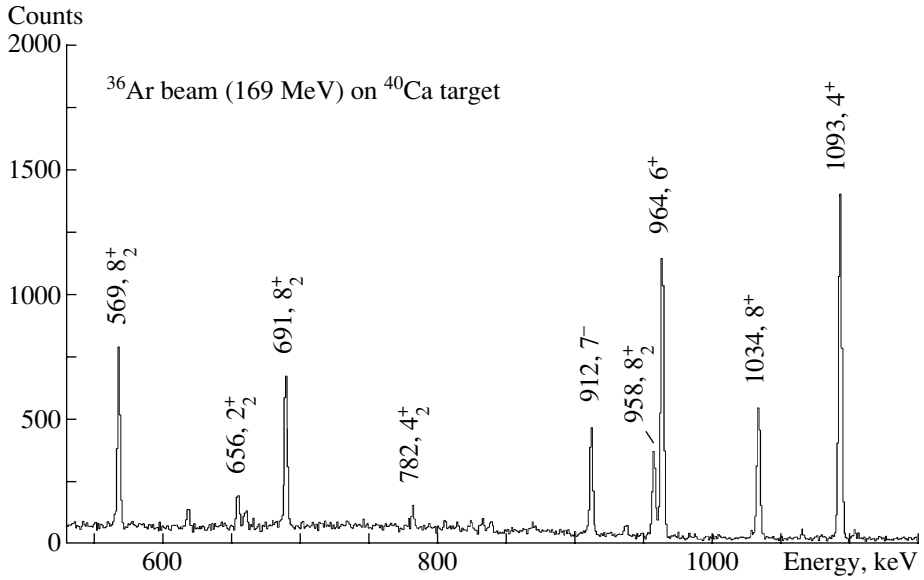

Fig. 3. Gamma-ray spectrum measured at mass $A = 70$ in coincidence with β rays and the 945 keV line, the latter representing a $2^+ \rightarrow 0^+$ transition in ^{70}Se. Beta-delayed γ lines of ^{70}Br are marked by energy and initial spin/parity of the ^{70}Se transitions.

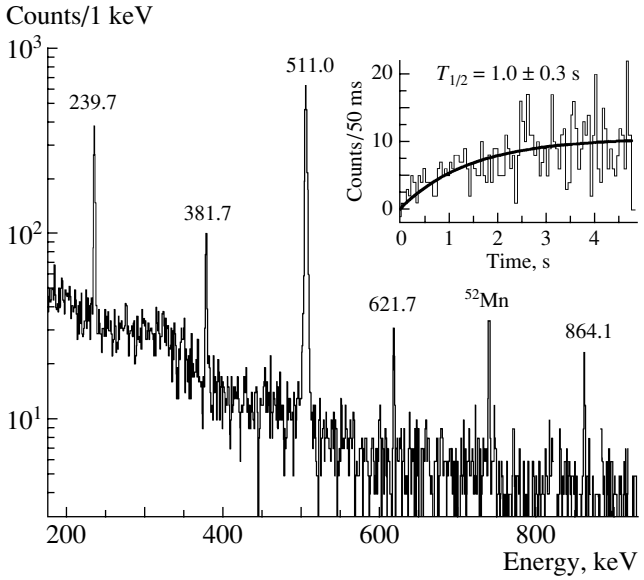

Fig. 4. Beta-coincident gamma-ray spectrum measured at mass $A = 93$. The line marked ^{52}Mn stems from a long-lived contaminant produced in a previous experiment. The inset shows the time dependence of the 240 keV line along with the result of a fit.

known in the daughter nucleus ^{94}Pd from in-beam studies [43].

^{93}Pd, an *rp*-process waiting-point nucleus. By measuring β-delayed protons ($T_{1/2} = 0.7^{+0.2}_{-0.1}$ s) and β-delayed γ rays ($T_{1/2} = 1.0(0.3)$ s), the β-decay of ^{93}Pd was observed [44] for the first time. The averaged half-life of 0.9(0.2) s is at variance with that of $9.3^{+2.5}_{-1.7}$ s, resulting from a preliminary evaluation of FRS data [45] which has meanwhile been superseded [10]. However, it agrees with a shell-model prediction [46] obtained by using a Gross–Frenkel interaction in a $g_{9/2}, p_{1/2}$ model space. By comparing the low-lying ^{93}Pd levels predicted by this model, the four β-delayed γ rays observed (see Fig. 4) can tentatively be assigned to transitions from the first excited $7/2^+$, $9/2^+$, and $13/2^+$ levels of ^{93}Pd to the $9/2^+$ ground state of this nucleus (see Fig. 5).

Furthermore, the β decay of ^{93}Pd is tentatively

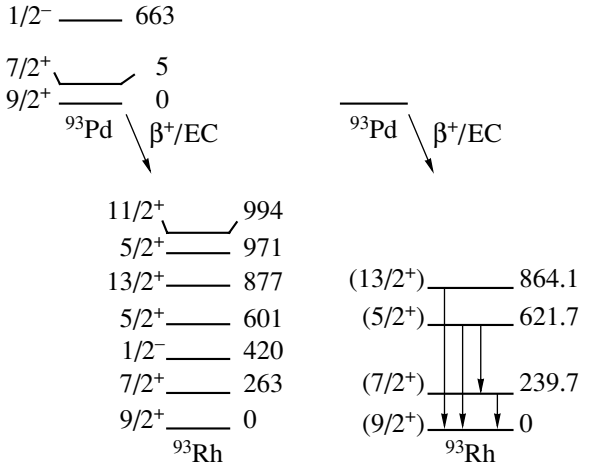

Fig. 5. Comparison of the experimental decay scheme (left panel) to the corresponding shell-model prediction (right panel). The energies are presented in keV.

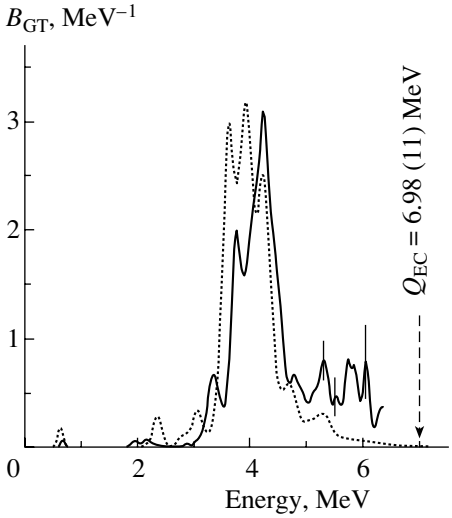

Fig. 6. Comparison of the experimental B_{GT} distribution for ^{97}Ag (solid curve) with the corresponding SNB prediction reduced by a hindrance factor of 4.3 (dotted curve). See text and [47] for details.

interpreted to occur from a low-lying $7/2^+$ and/or a $9/2^+$ state in ^{93}Pd. As ^{93}Pd may represent a waiting-point nucleus of the astrophysical rp process [3], experiments such as this, together with the related shell-model interpretations, may yield valuable input parameters for improved calculations of the rp-process path.

^{97,98}Ag and $^{103-107}$In: Observation of the Gamow–Teller resonance. The β decay of ^{97}Ag, a three proton-hole nucleus with respect to ^{100}Sn, was investigated [47] by using both the TAS and the Cluster Cube. One of the striking results is that the Cluster Cube, even though probably being the most advanced high-resolution detector for β-delayed γ rays available to date, missed about one third of the total GT strength detected by the TAS. The distribution of the GT strength as a function of the ^{97}Pd excitation energy, deduced from the TAS data, shows a pronounced resonance at an energy around 4 MeV with a width of about 1.8 MeV (see Fig. 6). The shape of this GT resonance agrees with that obtained by a shell-model calculation using the SNB Hamiltonian and a model space consisting of active proton orbitals $p_{1/2}$ and $g_{9/2}$ and active neutron orbitals $g_{7/2}$, $d_{5/2}$, $s_{1/2}$, and $h_{11/2}$ [47, 48] (see Fig. 6). The hindrance factor for the total GT strength amounts to 4.3(6) with reference to the SNB calculation (see [47, 48] for details), which agrees with the value of 3.7 expected from further configuration mixing within the SNB model space and from the higher order configuration mixing beyond the SNB model space. By means of the TAS, the GT strength distributions have also been measured for the chain of indium isotopes from ^{103}In [49] to ^{107}In [50]. These data, together with those for ^{98}Cd [51], ^{97}Ag [47], and ^{98}Ag [52], can now be used to establish, for the first time, a mass dependence of the GT hindrance factor near ^{100}Sn.

4. SUMMARY AND OUTLOOK

By using heavy-ion induced fusion-evaporation reactions at the on-line mass separator of GSI, new and interesting data have been obtained for the β decays of ^{56}Cu, ^{70}Br, and of other $N \sim Z$ nuclei below ^{100}Sn. The results have been interpreted through comparison with shell-model predictions, the topics ranging from B_{GT} values of individual daughter levels, the related spin/parity assignment for the parent states, the GT resonance, and its quenching all the way to a waiting-point nucleus of the astrophysical rp process. These investigations are part of an ongoing research program which also includes the following topics.

The experimental knowledge on high-spin states in the even–even $N = Z$ nucleus ^{52m}Fe [53] is very limited in comparison with neighboring nuclei. This is due to the occurrence of a 12^+ "yrast-trap" isomer which predominantly decays by positron emission and whose long half-life of 45.9(0.6) s prevents in-beam measurements from being extended to higher spins. Moreover, the excitation energy of the isomer was poorly known ($E^* = 6820(130)$ keV). In a recent ISOL experiment, the (internal) γ deexcitation of the isomer was observed for the first time, the isomeric energy was measured with significantly higher accuracy ($E^* = 6957.5(0.4)$ keV), and $B(E4)$ values were determined for the $12^+ \to 8^+_1$ (597.1(0.4) keV) and $12^+ \to 8^+_2$ (465.0(0.4) keV) transitions, which offers

a new way of checking shell-model (KB3, FPD6*, etc.) predictions [54].

The β-delayed proton data obtained for ^{57}Zn [55], which probe excited states in the single-proton nucleus ^{57}Cu, were considerably improved, with respect to source purity and energy resolution, over those gained in the one and only previous measurement [56] of this decay. The current evaluation of these data will hopefully allow one to experimentally identify hitherto unknown single-proton states in ^{57}Cu.

In the first study of the ^{61}Ga decay ($T_{1/2} = 140(70)$ ms) [57], the GT population of four excited ^{61}Zn levels ($I^\pi = 1/2^-, 3/2^-$, or $5/2^-$) was observed in addition to the dominant Fermi transition to the ^{61}Zn ground state.

Beta-delayed γ rays of the odd–odd nucleus ^{100}In were measured for the first time. The preliminary evaluation [58] of the high-resolution data yielded a half-life of 6.5(2.2) s in agreement with the previous ISOL result of 6.1(0.9) s, based on β-delayed proton data [59]. The population of the 6_2^+ and 8^+ states in ^{100}Cd, known from in-beam work [60], indicates a tentative spin/parity assignment of 6^+ and/or 7^+ for the β-decaying ^{100}In state(s).

The TAS has recently been used to study the β-delayed proton emission from ^{96}Ag [61]. These data look promising for the determination of lifetimes of proton-unbound ^{96}Pd levels through PXCT (see Section 2) and for the identification of single-proton states in ^{95}Rh ($N = 50$) populated by proton emission. There is preliminary evidence [61] supporting the occurrence of an excited level of ^{95}Rh at 686 keV, which is interpreted, with reference to a shell-model calculation [62], to be the hitherto unobserved $\pi g_{7/2}$ configuration.

All in all, a wealth of β-decay data has become and will continue to become available for $N \sim Z$ nuclei between the double closed-shell nuclei ^{56}Ni and ^{100}Sn. Amongst the ISOL experiments planned for the immediate future, there are a TAS β-strength measurement of ^{52m}Fe, an identification of the β or isomeric decay of ^{99}In, a proton-hole nucleus with respect to ^{100}Sn, and a search for direct proton decay of ^{113}Ba. It is indeed amazing to see the high data quality that can be obtained for nuclei close to the proton drip line, and it is also encouraging to observe what could be called, at least in the authors's judgement, a renaissance in the "interface" between in-beam and decay spectroscopy.

ACKNOWLEDGEMENTS

The author would like to take this occasion to acknowledge with pleasure the fruitful collaboration of many external research groups, in particular, those from Athens, East Lansing, Knoxville, Legnaro, Oak Ridge, St. Petersburg, Valencia, and Warsaw. Their most recent contributions can be seen from the list of references, and it is indeed their efforts that keep the old workhorse ISOL going strong, even after 24 years of on-line service.

This work was supported in part by the Polish Committee of Scientific Research under grant no. KBN 2 P03B 086 17, the program for Scientific Technical Collaboration (WTZ) under project nos. POL 99/009 and RUS 98/672, the CICYT (Spain) under contract no. AEN96-1662, the European Community under contract no. ERBFMGECT950083, the Alexander von Humbolt Foundation, and the US NSF grant nos. PHY-9605207 and PHY-0070911. Nuclear physics research at the University of Tennessee is supported by the US Department of Energy through contract no. DE-FG02-96ER40983. ORNL is managed by UT-Battelle, LLC, for the US Department of Energy under contract no. DE-AC05-00OR22725.

REFERENCES

1. W. Trinder *et al.*, Nucl. Phys. A **620**, 191 (1997).
2. W. Liu *et al.*, Phys. Rev. C **58**, 2677 (1998).
3. H. Schatz *et al.*, Phys. Rep. **294**, 167 (1998).
4. E. Caurier *et al.*, Nucl. Phys. A **653**, 439 (1999).
5. M. Oinonen *et al.*, Phys. Rev. C **56**, 745 (1997).
6. M. Oinonen *et al.*, Eur. Phys. J. A **3**, 271 (1998).
7. Ch. Miehé *et al.*, in *Proceedings of the 2nd International Conference on Exotic Nuclei and Atomic Masses (ENAM 98), Bellaire, USA, 1998,* Ed. by B. M. Sherrill, D. J. Morrissey, and C. N. Davids, AIP Conf. Proc. **455**, 789 (1998).
8. M. Oinonen *et al.*, Phys. Rev. C **61**, 035801 (2000).
9. C. Longour *et al.*, Phys. Rev. Lett. **81**, 3337 (1998).
10. A. Stolz *et al.*, in *Proceedings of the International Workshop on N = Z Nuclei (PINGST 2000), Lund, Sweden, 2000* (Int. Rep. of Lund University, Lund, 2000), p. 113.
11. R. Kirchner *et al.*, Nucl. Instrum. Methods Phys. Res. A **234**, 224 (1985).
12. R. Kirchner *et al.*, Nucl. Instrum. Methods Phys. Res. B **26**, 204 (1987).
13. R. Kirchner, Nucl. Instrum. Methods Phys. Res. A **292**, 203 (1990).
14. J. Eberth *et al.*, Prog. Part. Nucl. Phys. **39**, 29 (1997).
15. J. Gerl *et al.*, in *Proceedings of the Conference on Physics from Large γ-ray Detector Arrays, Berkeley, USA, 1994,* LBL 35687, CONF 940888, UC 413, p. 159.
16. Z. Hu *et al.*, Nucl. Instrum. Methods Phys. Res. A **419**, 121 (1998).

17. M. Karny *et al.*, Nucl. Instrum. Methods Phys. Res. B **126**, 411 (1997).
18. J. C. Hardy *et al.*, Phys. Rev. Lett. **37**, 133 (1976).
19. O. Klepper *et al.*, Z. Phys. A **305**, 125 (1982).
20. M. Shibata *et al.*, Phys. Rev. C **55**, 1715 (1997).
21. D. Schardt *et al.*, Nucl. Phys. A **368**, 153 (1981).
22. A. Guglielmetti *et al.*, Phys. Rev. C **56**, R2912 (1997).
23. M. La Commara *et al.*, Nucl. Phys. A **689**, 43 (2000).
24. Z. Janas *et al.*, GSI Experiment U180 (unpublished result); C. Mazzocchi, submitted to Phys. Lett. B.
25. E. Roeckl, in *Nuclear Decay Modes,* Ed. by D. N. Poenaru (Inst. of Physics Publ., Bristol, 1996), p. 237.
26. M. Ramdhane *et al.*, Phys. Lett. B **432**, 22 (1998).
27. R. Borcea *et al.*, Nucl. Phys. A **695**, 69 (2001).
28. H. Junde, Nucl. Data Sheets **67**, 523 (1992).
29. G. Audi *et al.*, Nucl. Phys. A **624**, 1 (1997).
30. G. Martinez-Pinedo *et al.*, Phys. Rev. C **53**, R2602 (1996).
31. Z. Janas *et al.*, GSI Scientific Report No. GSI-2000-1 (GSI, 2000), p. 13; Eur. Phys. J. A **12**, 143 (2001).
32. B. Vosicki *et al.*, Nucl. Instrum. Methods Phys. Res. B **181**, 307 (1981).
33. R. H. Burch *et al.*, Phys. Rev. C **38**, 1365 (1988).
34. A. Piechaczek *et al.*, in *Proceedings of the International Conference on Perspectives in Nuclear Physics, Gatlinbourg, USA, 1999,* Ed. by J. H. Hamilton, H. K. Carter, and R. B. Piercey (World Scientific, Singapore, 1999), p. 201.
35. A. Piechaczek *et al.*, Phys. Rev. C **62**, 054317 (2000).
36. T. Mylaeus *et al.*, J. Phys. G **15**, L135 (1989).
37. S. M. Fischer *et al.*, Phys. Rev. Lett. **84**, 4064 (2000).
38. J. Döring *et al.*, in *Proceedings of the International Workshop on N = Z Nuclei (PINGST 2000), Lund, Sweden, 2000* (Int. Rep. of Lund University, Lund, 2000), p. 131.
39. K. Schmidt *et al.*, Z. Phys. A **350**, 99 (1994).
40. J. Sinatkas *et al.*, Nucl. Part. Phys. **18**, 1377 (1992); **18**, 1401 (1992).
41. K. Schmidt *et al.*, Nucl. Phys. A **624**, 185 (1997).
42. M. La Commara, private communication.
43. M. Górska *et al.*, Z. Phys. A **353**, 233 (1995).
44. K. Schmidt *et al.*, Eur. Phys. J. A **8**, 303 (2000).
45. E. Wefers *et al.*, in *Proceedings of the "Experimental Nuclear Physics in Europe" Facing the Next Millenium (ENPE 99)," Sevilla, Spain, 1999,* Ed. by B. Rubio, M. Lozano, and W. Gelletly, AIP Conf. Proc. **495**, 375 (1999).
46. H. Herndl and B. A. Brown, Nucl. Phys. A **627**, 35 (1997).
47. Z. Hu *et al.*, Phys. Rev. C **60**, 024315 (1999).
48. B. A. Brown *et al.*, Phys. Rev. C **50**, 2270 (1994).
49. M. Karny *et al.*, Nucl. Phys. A **640**, 3 (1998).
50. M. Karny *et al.*, Nucl. Phys. A **690**, 367 (2001).
51. A. Płochocki *et al.*, Z. Phys. A **342**, 43 (1992).
52. Z. Hu *et al.*, Phys. Rev. C **62**, 064315 (2000).
53. C. A. Ur *et al.*, Phys. Rev. C **58**, 3163 (1998).
54. A. Gadea *et al.*, in *Proceedings of the International Workshop on N = Z Nuclei (PINGST 2000), Lund, Sweden, 2000* (Int. Rep. of Lund University, Lund, 2000), p. 118.
55. A. Jokinen *et al.*, submitted to Eur. Phys. J.
56. D. J. Vieira *et al.*, Phys. Lett. B **60B**, 261 (1976).
57. M. Oinonen *et al.*, Eur. Phys. J. A **5**, 151 (1999).
58. V. Bellguic, private communication.
59. J. Szerypo *et al.*, Nucl. Phys. A **584**, 221 (1995).
60. M. Górska *et al.*, Z. Phys. A **350**, 181 (1994).
61. L. Batist, private communication.
62. I. P. Johnstone and L. D. Skouras, Phys. Rev. C **55**, 1227 (1997).

Physics of Atomic Nuclei, Vol. 65, No. 4, 2002, pp. 697–702. From Yadernaya Fizika, Vol. 65, No. 4, 2002, pp. 729–734.

Inelastic Deuteron Breakup Followed by Fission at Intermediate Energy*

V. A. Rubchenya[1)], W. H. Trzaska, J. Äystö, A. A. Alexandrov[2)], I. D. Alkhazov[1)], K.-T. Brinkmann[3)], A. Evsenin[1)], S. V. Khlebnikov[1)], A. V. Kuznetsov[1)], V. G. Lyapin[1)], M. Mutterer[4)], Yu. E. Penionzhkevich[2)], O. I. Osetrov[1)], Z. Radivojevich, Yu. G. Sobolev[2)], G. P. Tjurin[1)], and D. N. Vakhtin[1)]**

Department of Physics, University of Jyväskylä, Finland

Received July 20, 2001

Abstract—The results of experimental and theoretical studies of the double-differential proton and neutron spectra measured in coincidence with fission fragments in the deuteron-induced reaction on a ^{238}U target at $E_d = 65$ MeV are presented. These spectra measured in the forward direction are analyzed in the plane-wave Born approximation by using the modified model of stripping into a continuum. The pre-neutron emission fission fragment mass distributions were measured for the (d, f), (d, pf), and (d, nf) reaction channels. The enhancement of highly asymmetric mass division in the (d, pf) channel for the low-energy part of the breakup proton spectrum was observed. The (d, pf) channel can be used to imitate the neutron-induced fission at intermediate energy. The fission characteristics were analyzed in the model taking into account nuclear friction and relevant fission modes. © *2002 MAIK "Nauka/Interperiodica".*

1. INTRODUCTION

The investigation of direct reactions induced by deuterons at low energy is a powerful method for exploring the structure of nuclei. For fissioning nuclei, the direct reaction with a deuteron provides possibilities for studying subbarrier resonanses and the structure of the fission barrier. Recently, new pieces of evidence for the existence of hyperdeformed states at the third minimum in the potential energy of ^{236}U were obtained in the reaction $^{235}\mathrm{U}(d, pf)$ [1]. Interest in deuteron-induced reactions at intermediate energy ($E_d > 30$ MeV) is increasing presently. More than fifty years ago, Serber [2] considered the deuteron-breakup process as a source of high-energy neutrons. Powerful neutron sources are very important for multiple practical purposes, such as accelerator-driven systems for nuclear-energy generation and incineration of nuclear waste [3], and for producing beams of neutron-rich radioactive ions by high-energy neutron-induced fission [4].

By analogy with the use of the stripping reaction at low energies for investigating subbarrier fission, one can use (d, pf) reactions to study neutron-induced fission at intermediate energies [5]. The shape of the virtual neutron spectrum relevant to this reaction is determined by direct (stripping or breakup, or both), preequilibrium, and compound mechanisms of the reaction. One of the important problems is the role of the Coulomb breakup mechanism in reactions on heavy nuclei. The importance of the Coulomb breakup of the incident deuteron in the high-energy neutron yield at forward angles was shown in [6]. It is interesting to investigate the role of the Coulomb breakup of deuterons in (d, pf) and (d, nf) reactions on heavy nuclei.

In this article, we report on a study of the double-differential spectra of protons and neutrons measured in coincidence with a fission fragment (FF) in the deuteron-induced reaction on a ^{238}U target at $E_d = 65$ MeV by using the K-130 cyclotron of the Accelerator Laboratory at the University of Jyväskylä. The fission channel is suitable for investigating inelastic deuteron breakup for heavy nuclei at intermediate energies. The mechanism of inelastic breakup followed by fission was analyzed within the stripping-into-continuum model [7] with some corrections. Simultaneously, the FF mass distributions were constructed for the proton-energy bins that correspond to specific bins of the neutron energy. The (d, pf) channel can be used to imitate neutron-induced fission in a wide region of fast-neutron energies. Special attention was paid to exploring extremely asymmetric fission, where the light fragment mass A_L is

*This article was submitted by the authors in English.

[1)]Khlopin Radium Institute, St. Petersburg, Russia.
[2)]Flerov Laboratory of Nuclear Reactions, JINR, Dubna, 141980 Russia.
[3)]Technical University, Dresden, Germany.
[4)]Technical University, Darmstadt, Germany.
**e-mail: rubchen@phys.jyu.fi

Main characteristics of the detectors used: dimensions, angle to the beam direction (θ), time resolution (δT), energy resolution (δE), and position resolution (δX)

Detector	Dimension, cm	θ, deg	δT, ns	δE, %	δX, cm
PSACs	⌀24.3	88–90	0.4	–	0.2
PPAC	⌀3.0	88	0.2	–	–
LCP telescopes	2×2	29, 41, 48, 56, 59, 130, 142	1	5	–
PSND	10×10×100	From 335 to −25	1.0	–	10
	⌀5.5×10×100	From 60 to −120			
		From 150 to −210			

below 80. Fission-fragment mass distributions are analyzed within the theoretical model developed in [8, 9] to describe fission-product yields. The contribution from various fission chances and fission modes, the effect of nuclear shells, odd–even effects, and charge polarization in the fission process are taken into consideration.

2. EXPERIMENTAL METHOD

We used the HENDES array [10] installed at the Accelerator Laboratory (University of Jyväskylä) to measure the double-differential spectra of protons and neutrons in coincidence with two FFs from the $^{238}\mathrm{U}+d$ reaction at $E_d = 65$ MeV. The deuteron beam of intensity 3–5 nA was incident on a 106 μg/cm^2 $^{\mathrm{nat}}$U target placed at the center of the reaction chamber. The reaction chamber housed two gas-filled position-sensitive avalanche counters (PSAC) for recording FFs and six ΔE–E telescopes for recording light charged particles (LCP). Four position-sensitive neutron detectors (PSND) [10, 11] were placed around the reaction chamber. The geometric arrangement of the experiment is shown in Fig. 1.

A common start for TOF measurements was provided by a gas-filled parallel-plate avalanche counter (PPAC, not shown in the figure). The geometric efficiency was 10% of 4π for FF detectors, 4% of 4π for neutron detectors, and 2.5% of 4π for LCP telescopes. The flight path was 25 cm for FF and 60–100 cm for neutrons. The main characteristics of the detectors are presented in the table.

Three of the LCP telescopes positioned at 29°, 41°, and 56° in the vertical plane consisted of 380-μm-thick 2 × 2 cm PIN diodes operated in the fully depleted mode, which were followed by 20-mm-thick CsI(Tl) crystals 20 mm in diameter with a PMT readout. The other two telescopes were made of four 380-μm-thick 2 × 2 cm PIN diodes and 5 × 5 cm CsI(Tl) crystals optically coupled to PIN photodiodes. The energy resolution of the CsI(Tl) telescopes was 5% as measured with a ^{226}Ra α source.

3. RESULTS AND DISCUSSION

The double-differential LCP (d, p, t, and α) spectra were measured at seven angles ranging between 29° and 142°. The proton spectra measured in coincidence with FFs at $\theta = 29°$, 41°, 59°, and 142° are shown in Fig. 2, along with the results of theoretical direct-model calculations.

To estimate the $^{238}\mathrm{U}(d,pf)$ and $^{238}\mathrm{U}(d,nf)$ cross sections in the plane-wave Born approximation, we used the modified formula proposed in [7]. For the (d,pf) channel, the cross section was calculated according to the expression [the modification for the (d,nf) channel is obvious]

$$\frac{d^2\sigma}{dE_p d\Omega_p} = \frac{\mu_{dA}\mu_{pB}}{(2\pi\hbar)^3\mu_{nA}} \times \frac{p_p p}{p_d}\left|F\left(\frac{1}{2}\mathbf{p}_d - \mathbf{p}_p\right)\right|^2 \sigma_{nA}^{\mathrm{fis}}(E_n), \quad (1)$$

where μ_{dA} is the reduced mass of the system formed by the deuteron and the target nucleus, $\mathbf{p}_d$ is the deuteron momentum, μ_{pB} is the reduced mass of the system formed by the proton and the final nucleus, $\mathbf{p}_p$ is the proton momentum, μ_{nA} is the reduced mass of the system formed by the neutron and the target nucleus, $\mathbf{p} = \mathbf{p}_d - \mathbf{p}_p$ is the momentum transfer, F is the deuteron form factor calculated by using the Hulthén-type deuteron wave function, and $\sigma_{nA}^{\mathrm{fis}}(E_n)$ is the cross section for target-nucleus fission induced by neutrons.

The original expression from [7] was modified in two respects. First, the Coulomb field correction was introduced in the local approximation by replacing the

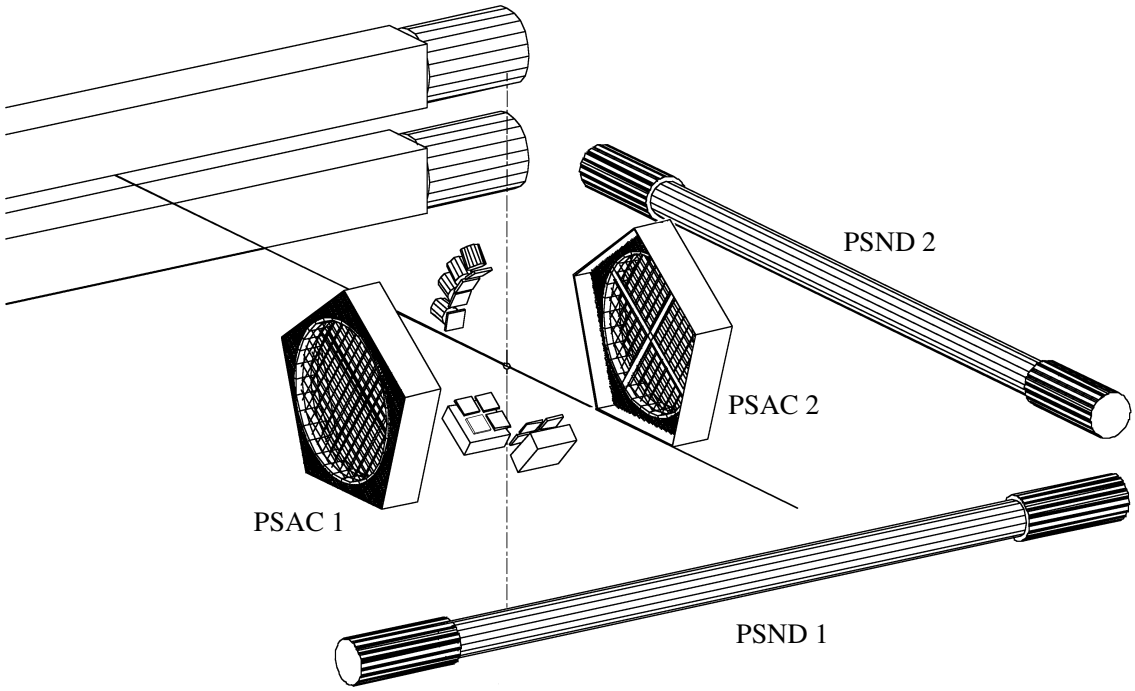

Fig. 1. Experimental layout of HENDES for the ^{238}U$(d, p(n)$ fission) experiment (see text).

deuteron and proton momenta by the "local" momenta:

$$p_d^L = \sqrt{1 - \frac{V_c}{E_d}}\, p_d, \quad p_p^L = \sqrt{1 - \frac{V_c}{E_p}}\, p_p, \qquad (2)$$

$$V_c = 1.44 \frac{Z}{1.5(A^{1/3} + 1)},$$

where Z and A are the charge and mass numbers of the target nucleus. Second, the total cross section calculated in the optical model was used instead of the off-shell total cross section for a nucleon incident on the target nucleus. The probabilities of the formation of a compound nucleus and of its fission were introduced to calculate the (d, pf) and (d, nf) cross sections. One can see from Fig. 2 that the shapes of the proton spectra measured in the forward direction are described by the model near the maximum of the spectra. However, we had to introduce a scaling factor of about 40–50 to ensure coincidence at the maximum of the experimental spectra. The reasons why so large a scaling factor was needed are still unclear. Probably, the contribution of the Coulomb breakup followed by the absorbtion of a neutron may enhance the cross sections. A comparison of the theoretical spectra with experimental ones at large angles shows that the contribution from inelastic breakup is small (the scaling factor for $\theta = 142^\circ$ is 125). The contributions from the evaporation and preequilibrium reaction mechanisms are important at $E_p < 20$ MeV.

The neutron spectra were measured at 20 angles from 10° to 164° by using four PSNDs. The neutron spectra measured in coincidence with FFs at $\theta = 10^\circ$ and 164° are shown in Fig. 3 along with the results of the theoretical calculations at $\theta = 10^\circ$ performed according to formula (1) modified for the (d, nf) channel. The same theoretical model that underestimates the cross section for the (d, pf) channel describes the neutron spectra for $E_n > 20$ MeV at small angles for the (d, nf) channel surprisingly well without any scaling. The processing of neutron data is in progress, and the cross section for inelastic deuteron breakup can be estimated. The calculated value of the total cross section for inelastic breakup in the reaction ^{238}U(d, nf) at $E_d = 65$ MeV is 13.7 mb. Apart from the neutron component originating from deuteron breakup, three more components contribute to the measured neutron spectra: (i) prescission evaporation, (ii) preequilibrium emission from a compound nucleus, and (iii) postscission evaporation from FFs.

The mass and energy distributions of FFs were obtained for certain proton or neutron energy bins of the measured spectra for each LCP and each neutron detector from TOF measurements by an iterative procedure that took into account energy losses in target and detector materials [11]. Prescission neutron emission has been taken into account in processing the FF TOF data. We were primarily interested in the effect that the compound-nucleus excitation energy may have on the far-asymmetric region of the mass

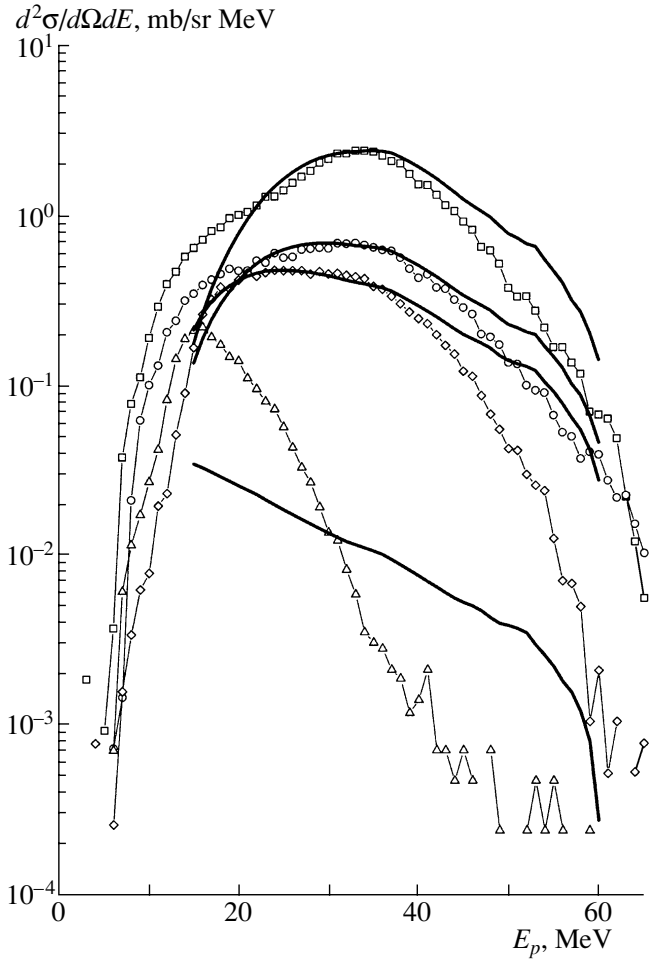

Fig. 2. Measured proton spectra in coincidence with FF at $\theta = 29°$ (squares), $\theta = 41°$ (circles), $\theta = 59°$ (diamonds) and $\theta = 142°$ (triangles) and theoretical direct components (curves).

distribution. For a given proton energy E_p in the reaction $^{238}\mathrm{U}(d, pf)$ at $E_d = 65$ MeV, the energy of a virtual neutron that causes fission is

$$E_n \simeq 62.2 - E_p + 0.0954\sqrt{E_p}\cos\theta_p. \qquad (3)$$

A comparison of the measured pre-neutron-emission FF mass distributions in the (d, pf) channel with the mass distributions obtained in the neutron-induced fission of ^{238}U by using a Los Alamos neutron source [12] has shown suprisingly good agreement between the two methods. The light tail of the FF mass distributions for the (d, f) channel and for two proton energy bins for the (d, pf) channel (symbols) at $\theta_p = 29°$ are displayed in Fig. 4, along with the results of the theoretical calculation for two corresponding proton energies (curves). The experimental results were analyzed within the theoretical model proposed in [8, 9] and used here in a more advanced version. In this version of the model for light-particle-induced fission, the probability of the formation of compound systems for a given angular momentum was calculated by using the optical model. The probability of the formation of a compound nucleus is affected by the emission of fast and preequilibrium light particles. The fission of a compound nucleus having a specific certain excitation energy and a specific spin is calculated on the basis of the dynamical fusion–fission model proposed in [11] for heavy ion reactions. The distributions of the mass and charge number and the excitation energy and the spin of compound nuclei that are to undergo fission have been calculated by means of a Monte Carlo simulation of the fission process. For each particular compound nucleus, the FF characteristics have been calculated by using the semiphenomenological fission model. The influence of nuclear shells, of charge polarization, and of odd–even effects and their dependence on the excitation energy of a compound nucleus have been taken into account. The mass distribution of primary fission fragments is supposed to be determined by the symmetric, two asymmetric, and superasymmetric fission

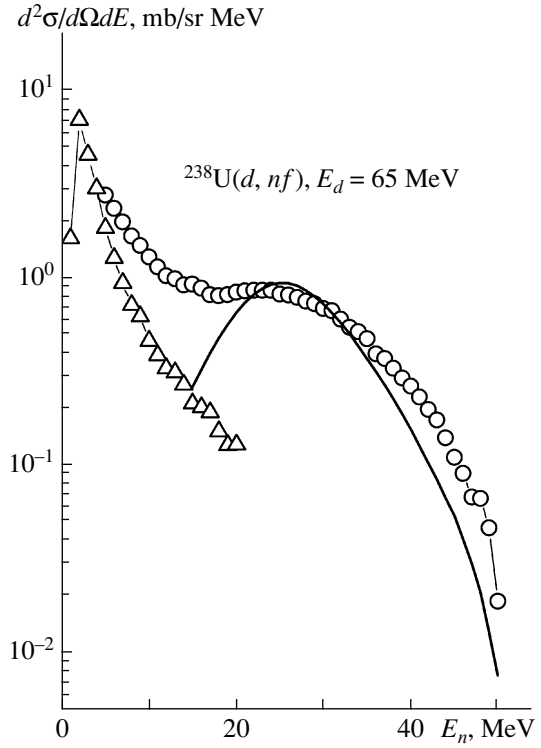

Fig. 3. Measured neutron spectra in coincidence with FFs at $\Theta =$ (circles) 10° (triangles) 164° and results of the theoretical calculations at $\theta = 10°$ that are based on the direct model (curve).

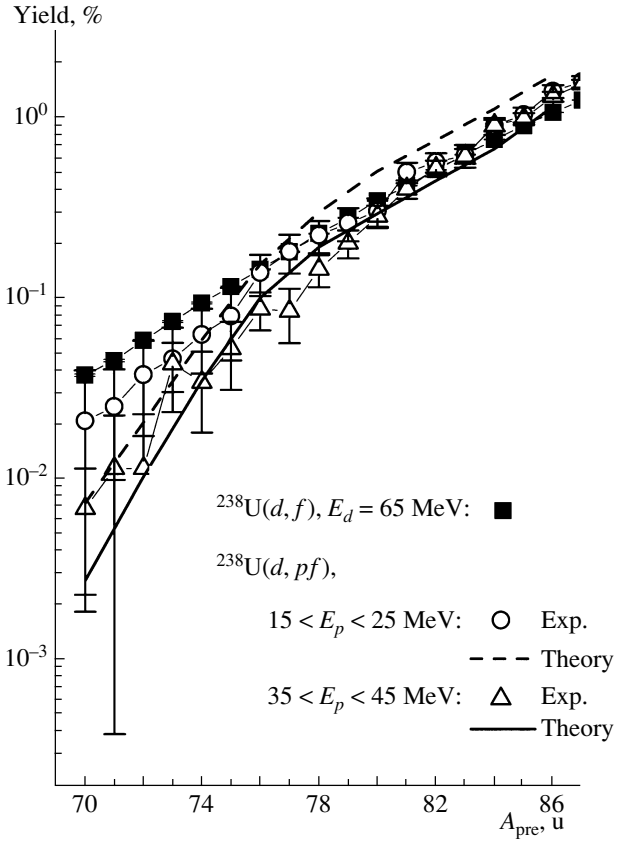

Fig. 4. Measured FF mass distributions (squares) for the (d, f) channel and for two proton energy bins for the (d, pf) channel at (circles) $15 < E_p < 25$ MeV and (triangles) $35 < E_p < 45$ MeV, along with the results of theoretical model calculations for two corresponding proton energies (curves).

modes. One can see from Fig. 4 that the theoretical model satisfactorily describes the experimental data.

4. CONCLUSION

Inelastic deuteron breakup followed by the fission of heavy nuclei at intermediate energy has been measured for the first time. The double-differential spectra of protons and neutrons in coincidence with FFs in the deuteron-induced reactions on a $^{\rm nat}$U target at $E_d = 65$ MeV have been measured. The simplified model of deuteron stripping into a continuum in the plane-wave Born approximation describes the experimental high-energy part of the proton spectra [in the (d, pf) channel] and the neutron spectra [in the (d, nf) channel] at small angles. This model ensures good agreement with experimental cross sections for the reaction ^{238}U(d, nf) at small angles and greatly underestimates the cross section for the reaction ^{238}U(d, pf) at $\theta_p \geq 29°$. The possible contribution of the Coulomb breakup is planned for investigation. We intend to continue this study at a higher deuteron energy and at as small angles of breakup protons as possible.

It has been shown that the (d, pf) channel can be used to measure fission characteristics in high-energy neutron-induced fission. We observed the enhancement of highly asymmetric mass division in the (d, pf) channel for the low-energy part of the proton spectrum in relation to the thermal-neutron-induced fission of heavy nuclei [13]. A model for calculating the fission characteristics in the light-particle-induced fission of heavy nuclei has been developed. This model can be used to predict the cross sections for the formation of exotic nuclides and to evaluate the product yields in fission at intermediate energy.

ACKNOWLEDGMENTS

This work was supported by the Academy of Finland under the Finnish Center of Excellence Programme 2000–2005 (project no. 44875, Nuclear and Condensed Matter Physics Programme at JYFL).

REFERENCES

1. A. Krasznohorkay, M. Hynyadi, M. N. Harakeh, *et al.*, Phys. Rev. Lett. **80**, 2073 (1998).

2. R. Serber, Phys. Rev. **72**, 1008 (1947).
3. C. D. Bowman *et al.*, Nucl. Instrum. Methods Phys. Res. A **320**, 336 (1992).
4. A. C. Mueller, in *Proceedings of International Workshop "Research with Fission Fragments," Benediktbeuern, Germany, 1996,* Ed. by T. von Egidy, F. J. Hartmann, D. Habs, *et al.* (World Sci., Singapore, 1997), p. 48.
5. V. A. Rubchenya *et al.*, in *Proceedings of the Second International Conference "Fission and Properties of Neutron-Rich Nuclei," St. Andrews, Scotland, 1999,* Ed. by J. H. Hamilton, W. R. Philips, and H. K. Carter (World Sci., Singapore, 2000), p. 484.
6. D. Ridikas, W. Mittig, and J. A. Tostevin, Phys. Rev. C **59**, 1555 (1999).
7. R. Lipperheide, Phys. Lett. B **32B**, 555 (1970).
8. M. Huhta *et al.*, Phys. Lett. B **405**, 230 (1997).
9. P. P. Jauho *et al.*, Phys. Rev. C **49**, 2036 (1994).
10. W. H. Trzaska *et al.*, in *Application of Accelerators in Research and Industry,* Ed. by J. L. Duggan and I. L. Morgan (American Inst. of Physics Press, New York, 1997), p. 1059.
11. V. A. Rubchenya *et al.*, Phys. Rev. C **58**, 1587 (1998).
12. C. M. Zöller, PhD Dissertation (Technischen Hochshule, Darmstadt, 1995).
13. I. Tsekhanovich, H. O. Denshlag, M. Davi, *et al.*, Nucl. Phys. A **658**, 217 (1999).

Physics of Atomic Nuclei, Vol. 65, No. 4, 2002, pp. 703–706. From Yadernaya Fizika, Vol. 65, No. 4, 2002, pp. 735–738.

Cluster Structure of ^{48}Cr*

T. Sakuda** **and S. Ohkubo**[1)]**

Department of Physics, Miyazaki University, Japan

Received August 31, 2001

Abstract—The structure of the nucleus ^{48}Cr is investigated by the $^{40}\mathrm{Ca}+\alpha+\alpha$ orthogonality condition model. The energy spectra and electromagnetic transitions are calculated. The observed energies and $E2$ transitions of the yrast band, which show interesting collective behavior, are well reproduced by the cluster model. © *2002 MAIK "Nauka/Interperiodica".*

1. INTRODUCTION

It is well established that α-cluster structure is a stable feature of ^{40}Ca–^{44}Ti nuclei [1]. It is now necessary to study how α-cluster structure persists in nuclei beyond ^{44}Ti. ^{48}Cr is the α nucleus next to ^{44}Ti, and 2α-cluster states may be expected to be in the nucleus. It is very interesting to verify the 2α-cluster states, which could show a greater variety of cluster structure. Furthermore, much attention has been devoted to the yrast states in the ^{48}Cr nucleus [2–4]. They are characterized by the backbend and strong enhancement of $E2$ intraband transitions. Various approaches have been carried out [4–7]. Full fp-shell model calculations are in very good agreement with the experimental energy spectrum [4]. However, large effective charges are needed to get a good agreement for the $E2$ transitions. We want to analyze these features of ^{48}Cr from the viewpoint of α-cluster structure. We will apply the $^{40}\mathrm{Ca}+\alpha+\alpha$ orthogonality condition model for the ^{48}Cr nucleus. The multicluster model is able to span a large model space which includes many shell-model states and various kinds of cluster configurations.

2. ORTOGONALITY CONDITION MODEL FOR THE $^{40}\mathrm{Ca}+\alpha+\alpha$ SYSTEM

The model space is described by a set of wave functions

$$\Phi_J = \sqrt{\frac{4!4!40!}{48!}}\mathcal{A}\{\phi(\alpha)\phi(\alpha)\phi(\mathrm{Ca}) \times [U_{N_{23},l_{23}}(\mathbf{r}), U_{N_1,l_1}(\mathbf{R})]_J\},$$

where ϕ's are the antisymmetrized internal wave functions and $U_{N_{23},l_{23}}(\mathbf{r})$ and $U_{N_1,l_1}(\mathbf{R})$ are harmonic oscillator functions with N_{23} and N_1 quanta for the relative motions. The relative coordinates $\mathbf{r}$ and $\mathbf{R}$ are shown in Fig. 1. We adopt a common oscillator

Table 1. The Pauli-allowed states of the $^{40}\mathrm{Ca}+\alpha+\alpha$ system [they are classified by the $SU(3)$ label (λ,μ) with the multiplicity n]

N	$(\lambda,\mu)^n$
24	$(16,4)\,(12,6)\,(8,8)\,(4,10)\,(0,12)$
25	$(19,3)\,(17,4)\,(15,5)\,(13,6)\,(11,7)\,(9,8)\,(7,9)$ $(5,10)\,(3,11)\,(1,12)$
26	$(22,2)\,(20,3)\,(18,4)^2\,(16,5)\,(14,6)^2\,(12,7)$ $(10,8)^2\,(8,9)\,(6,10)^2\,(4,11)\,(2,12)^2$
27	$(25,1)\,(23,2)\,(21,3)^2\,(19,4)^2\,(17,5)^2\,(15,6)^2$ $(13,7)^2\,(11,8)^2\,(9,9)^2\,(7,10)^2\,(5,11)^2\,(3,12)^2$ $(1,13)$
28	$(28,0)\,(26,1)\,(24,2)^2\,(22,3)^2\,(20,4)^3\,(18,5)^2$ $(16,6)^3\,(14,7)^2\,(12,8)^3\,(10,9)^2\,(8,10)^3\,(6,11)^2$ $(4,12)^3\,(2,13)\,(0,14)$
29	$(29,0)\,(27,1)^2\,(25,2)^2\,(23,3)^3\,(21,4)^3\,(19,5)^3$ $(17,6)^3\,(15,7)^3\,(13,8)^3\,(11,9)^3\,(9,10)^3\,(7,11)^3$ $(5,12)^3\,(3,13)^2\,(1,14)$
30	$(30,0)^2\,(28,1)^2\,(26,2)^3\,(24,3)^3\,(22,4)^4\,(20,5)^3$ $(18,6)^4\,(16,7)^3\,(14,8)^4\,(12,9)^3\,(10,10)^4\,(8,11)^3$ $(6,12)^4\,(4,13)^2\,(2,14)^2\,(0,15)$
31	$(31,0)^2\,(29,1)^3\,(27,2)^3\,(25,3)^4\,(23,4)^4\,(21,5)^4$ $(19,6)^4\,(17,7)^4\,(15,8)^4\,(13,9)^4\,(11,10)^4\,(9,11)^4$ $(7,12)^4\,(5,13)^3\,(3,14)^2\,(1,15)$
32	$(32,0)^3\,(30,1)^3\,(28,2)^4\,(26,3)^4\,(24,4)^5\,(22,5)^4$ $(20,6)^5\,(18,7)^4\,(16,8)^5\,(14,9)^4\,(12,10)^5\,(10,11)^4$ $(8,12)^5\,(6,13)^3\,(4,14)^3\,(2,15)\,(0,16)$
33	$(33,0)^3\,(31,1)^4\,(29,2)^4\,(27,3)^5\,(25,4)^5\,(23,5)^5$ $(21,6)^5\,(19,7)^5\,(17,8)^5\,(15,9)^5\,(13,10)^5\,(11,11)^5$ $(9,12)^5\,(7,13)^4\,(5,14)^3\,(3,15)^2\,(1,16)$

*This article was submitted by the authors in English.

[1)]Department of Applied Science and Environment, Kochi Women's University, Japan; e-mail: ohkubo@yukawa.kyoto-u.ac.jp

**e-mail: sakuda@cc.miyazaki-u.ac.jp

Table 2. Squared components with N oscillator quanta of the wave functions for the yrast band in ^{48}Cr

J^π	$N=24$							$N=26$	$N=28$	$N=30$	$N=32$
	(16, 4) $K=0$	(16, 4) $K=2$	(16, 4) $K=4$	(12, 6)	(8, 8)	(4, 10)	(0, 12)				
0^+	0.414			0.108	0.095	0.064	0.042	0.078	0.166	0.014	0.019
2^+	0.500	0.011		0.098	0.069	0.029	0.012	0.093	0.154	0.016	0.016
4^+	0.402	0.075	0.004	0.104	0.082	0.060	0.001	0.085	0.155	0.015	0.016
6^+	0.451	0.129	0.005	0.090	0.048	0.009	0.000	0.099	0.139	0.016	0.013
8^+	0.281	0.248	0.024	0.113	0.089	0.001	0.000	0.085	0.134	0.013	0.013
10^+	0.238	0.384	0.058	0.089	0.006	0.000	0.000	0.092	0.112	0.012	0.009
12^+	0.111	0.412	0.125	0.158	0.001	0.000	0.000	0.072	0.104	0.008	0.009
14^+	0.067	0.482	0.287	0.003	0.000	0.000	0.000	0.072	0.077	0.007	0.005
16^+	0.015	0.315	0.539	0.000	0.000	0.000	0.000	0.049	0.072	0.004	0.005

constant $a = 0.2815$ fm^{-2} for all clusters. The model wave function is generated as a direct product of the two relative wave functions: $(N_{23}, 0) \times (N_1, 0)$. The Pauli-allowed states are obtained by diagonalizing the norm kernel. The resulting allowed states are listed in the Table 1 and are classified by $SU(3)$ symmetry. The states with the total quanta $N \leq 23$ are not allowed as a matter of course. We can see the $N = 24$ space contains important $(fp)^8$ shell-model states (16, 4). The configurations with a larger value of N have a capacity for presenting the 2α- and also α-cluster states. As for the interactions between clusters, we use the folding potentials with the Hasegawa–Nagata–Yamamoto (HNY) effective two-nucleon interaction (see [1] and references therein). The depth parameters of HNY, $V_0(^3E) = -480$ MeV for the ^{40}Ca–α potential and -522 MeV for the α–α one, are chosen so as to reproduce the energies of the low-lying states in ^{48}Cr. The calculated potentials are shown in Fig. 2 and are similar to the ones used in $^{40}\mathrm{Ca} + \alpha$ and $\alpha + \alpha$ systems but are somewhat shallower.

3. ENERGY SPECTRA

The orthogonality condition model (OCM) equation is solved for the positive-parity states of $J^\pi =$ 0–16 by taking the total quanta $N = 24$–32 for the relative motions. The calculated energy spectra are compared with the experimental data in Fig. 3. The energies are given with respect to the $^{40}\mathrm{Ca} + \alpha + \alpha$ threshold ($E_{\mathrm{th}} = 12.82$ MeV). The yrast band is very well reproduced. These states are mainly the (16, 4)

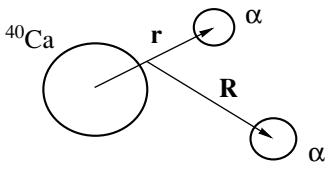

Fig. 1. Relative coordinates of the $^{40}\mathrm{Ca} + \alpha + \alpha$ system.

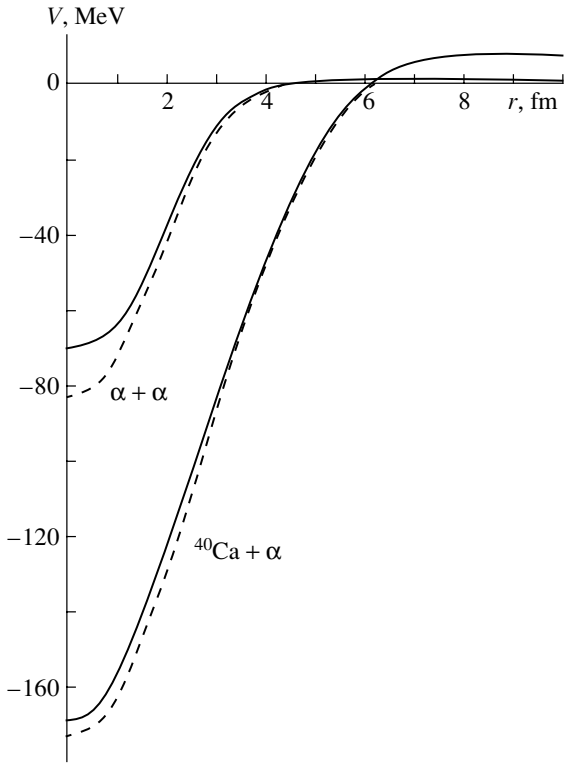

Fig. 2. Folding potentials for the $^{40}\mathrm{Ca} + \alpha$ and $\alpha + \alpha$ in ^{48}Cr (solid curves). For comparison, the corresponding potentials in ^{44}Ti and ^{8}Be are also shown (dashed curves).

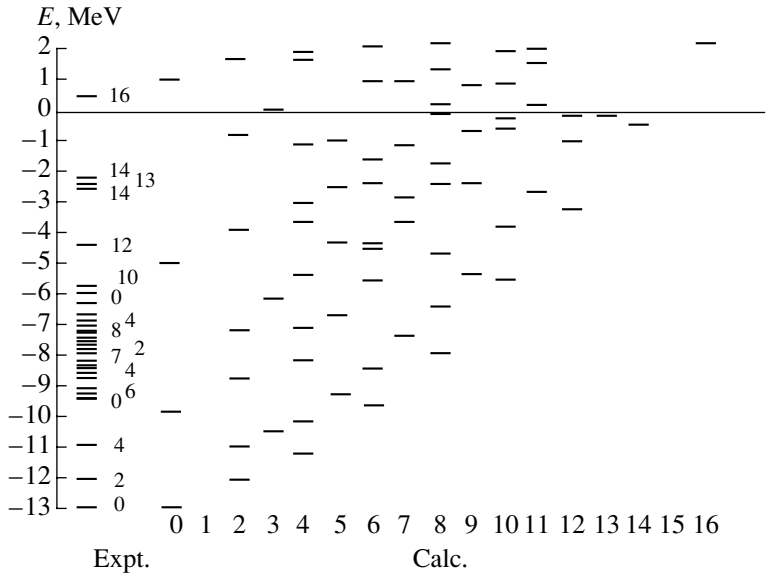

Fig. 3. Calculated and experimental positive-parity states of ^{48}Cr. The energy scale is measured from the $^{40}\mathrm{Ca}+\alpha+\alpha$ threshold ($E_{\mathrm{th}} = 12.82$ MeV).

$K = 0$ states. The second band built on the second 2^+ state is also predicted and is interpreted as the (16, 4) $K = 2$ band. As there is no experimental candidate for the 2^+ state at such low excitation, the calculated energy may be somewhat overbound. There is considerable mixing between these two bands at higher angular momenta ($J^\pi \geq 10^+$). The calculated wave functions of the yrast band are given in Table 2. The lowest $N = 24$ component of the ground 0^+ state is about 72%, which is larger than the lowest component (50%) of the ground state of ^{44}Ti. This means, however, that the ground state of ^{48}Cr still has 28% cluster components. The proportion of the $N = 24$ components increases from 72% for 0^+ to 87% for 16^+; that is, a higher spin state is a more shell-model state. It is also noteworthy that the (16, 4) $K = 0$ component decreases with spin, but, on the other hand, the (16, 4) $K = 2$ and 4 components increase with spin.

The γ-ray energies $E_\gamma(J) = E(J) - E(J-2)$ are plotted against angular momentum J in Fig. 4. The cluster model can describe the backbend at $J^\pi = 10^+$, but it unfortunately leads to a false backbend at $J^\pi = 14^+$. This may be due to a shortcoming of the model that the spin–orbit splittings of single-particle orbits are not included.

In Fig. 5, we present the calculated and experi-

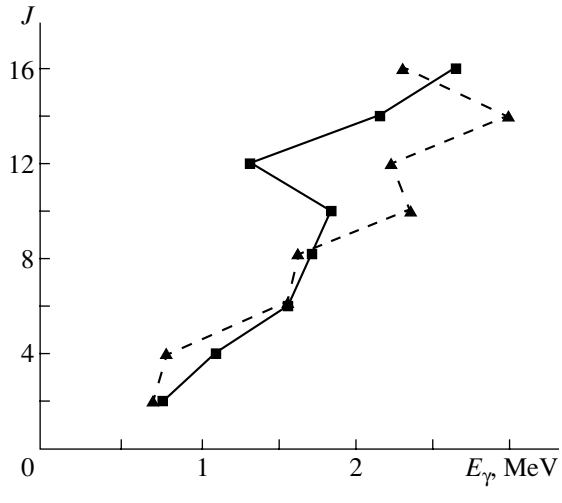

Fig. 4. The angular momentum J plotted against experimental (squares) and calculated (triangles) rotational energy $E_\gamma(J) = E(J) - E(J-2)$ for the yrast band of ^{48}Cr.

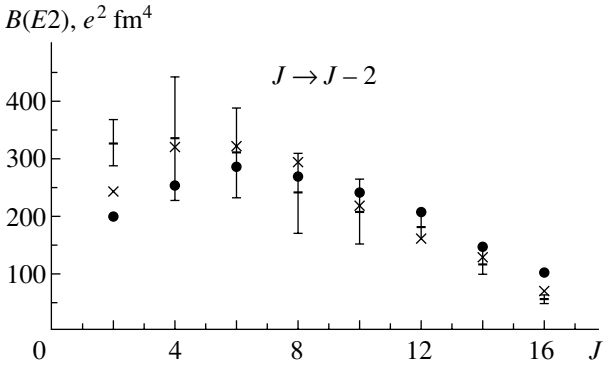

Fig. 5. Calculated (circles correspond to cluster model, crosses denote results for fp-shell model) and experimental $E2$-transitions for the yrast band of ^{48}Cr.

mental $B(E2)$ values. Both the cluster model and the full fp-shell model yield excellent agreement for the $E2$ transitions. In this calculation, additional effective charges $\delta e_p = \delta e_n = 0.22e$ are used, which are consistent with the values needed in the cluster model calculations for ^{40}Ca–^{44}Ti [1]. These values, however, are far smaller than the values $\delta e_p = \delta e_n = 0.5e$ required by the shell-model calculations [4]. There are important effects due to the α-clustering for enhancing the transitions. It is also noteworthy that the $B(E2)$ values decrease smoothly for higher spin states. This is because of a combined effect of smaller clustering and larger K mixing for higher spin states.

4. SUMMARY

We have applied the microscopic $^{40}\mathrm{Ca} + \alpha + \alpha$ cluster model to ^{48}Cr in order to attain a unified understanding of its structure. Within this model, the energy spectra and $E2$-transition probabilities are in very good agreement with the experimental data. The mechanism of backbending and smooth decrease of $B(E2)$ values of the yrast band is analyzed by the change of α-clustering and mixing of the (16, 4) $K = 0$, 2, and 4 configurations. It is concluded that the cluster model is very successful for the nucleus ^{48}Cr.

REFERENCES

1. T. Sakuda and S. Ohkubo, Phys. Rev. C **49**, 149 (1994); **51**, 586 (1995); **57**, 1184 (1998); Prog. Theor. Phys. Suppl., No. 132, 103 (1998).
2. J. A. Cameron *et al.*, Phys. Lett. B **387**, 266 (1996); **319**, 58 (1993); Phys. Rev. C **49**, 1347 (1994).
3. F. Brandolini *et al.*, Nucl. Phys. A **642**, 387 (1998).
4. E. Caurier *et al.*, Phys. Rev. C **50**, 225 (1994); Phys. Rev. Lett. **75**, 2466 (1995).
5. J. Terasaki, R. Wyss, and P.-H. Heenen, Phys. Lett. B **437**, 1 (1998).
6. T. Tanaka, K. Iwasaki, and F. Sakata, Phys. Rev. C **58**, 2765 (1998).
7. K. Hara, Y. Sun, and T. Mizusaki, Phys. Rev. Lett. **83**, 1922 (1999).

Physics of Atomic Nuclei, Vol. 65, No. 4, 2002, pp. 707–712. From Yadernaya Fizika, Vol. 65, No. 4, 2002, pp. 739–744.

Double-Folding Model Including the Pauli Exclusion Principle*

K. A. Gridnev, V. B. Soubbotin, W. von Oertzen[1),2)], H. G. Bohlen[1)], and X. Viñas[3)]**

Institute of Physics, St. Petersburg State University, Petrodvorets, Russia

Received August 31, 2001

Abstract—A new method for incorporating the Pauli exclusion principle into the double-folding approach to the heavy-ion potential is proposed. The description of the exchange terms at the level of the semiclassical one-body density matrix is used. It is shown that, in order to take into account Pauli blocking properly, the density matrices of free isolated nuclei must be redefined. A solution to the self-consistent incorporation of Pauli blocking effects in the mean-field nucleus–nucleus potential is obtained in the Thomas–Fermi approximation. © *2002 MAIK "Nauka/Interperiodica".*

1. INTRODUCTION

For a long time, microscopic calculations of the nucleus–nucleus potential to describe scattering phenomena have been a subject of interest in heavy-ion physics. A large variety of theoretical models have been proposed to this aim. Due to the extreme level of difficulty involved in this problem, many assumptions are needed to calculate the nucleus–nucleus potential at the numerical level. However, these simplified approaches must satisfy the fundamental quantum-mechanical principles, and the Pauli exclusion principle is one of the most important considered in the problem of nucleus–nucleus scattering. To incorporate the Pauli exclusion principle into the standard coupled-channel scattering theory, the resonating-group method (RGM) [1] was proposed. However, even for the simple elastic-scattering problem (one-channel approximation), microscopic calculation of the effective Hamiltonian that describes the relative motion of the nuclei in the RGM is very complicated.

Therefore, the double-folding model (DFM) [2], which is less fundamental than the RGM, but which starts from realistic nuclear densities, has become one of the most popular methods for calculating the real part of the optical potential. On the basis of the DFM, detailed fits to elastic-scattering data for many systems were obtained [3–10]. An analysis of nuclear-rainbow scattering provides arguments in favor of a deep DFM-like nucleus–nucleus potential. While, in early publications, one-particle exchange was described by a zero-range pseudopotential, more accurate methods were developed later to this aim [5–13]. When one uses a finite-range effective nucleon–nucleon force in the DFM calculation, the one-body density matrix (DM) for each isolated nucleus is needed. It can be obtained numerically from a solution to the Hartree–Fock (HF) equations. However, this is not suitable for a DFM calculation. Methods for expressing the DM by means of the local density are used according to the original DFM idea. One of the most popular approaches to the DM was given by Campi and Bouyssy (CB) [14]. Recently, another approach to the DM based on the extended Thomas–Fermi theory (ETF) was proposed [15].

There are still open questions concerning the theoretical foundations of the DFM. First of all, the DFM potential represents the interaction energy (energy surface) of two nuclei, depending on the distance between the centers of the mean fields rather than depending on the dynamical relative variable. Second, the Pauli exclusion principle should be treated correctly. It is known that the DFM is valid at large separation distances, where single-particle states of different nuclei are almost orthogonal. However, this is not true at intermediate distances. The nonorthogonality of single-particle states violates the Pauli exclusion principle. In the present article, we discuss the foundation of the DFM, starting from the generalized Born–Oppenheimer method [16] and using Slater determinants as wave functions for describing the interacting nuclei.

2. DOUBLE-FOLDING MODEL WITH PAULI EXCLUSION

The formal foundation of the DFM can be found in the generalized Born–Oppenheimer method [16],

*This article was submitted by the authors in English.

[1)]Hahn-Meitner-Institut-GmbH, Berlin, Germany; e-mail: oertzen@hmi.de

[2)]Fachbereich Physik, Free University of Berlin, Germany.

[3)]Departament d'Estructura i Consitituents de la Materia, Facultat de Fisica, Universitat de Barcelona, Spain; e-mail: xavier@ecm.ub.es

**e-mail: vbs@nuclpc1.phys.spbu.ru

where the potential between two nuclei (with N_1 and N_2 nucleons, $N = N_1 + N_2$) is defined as (see [17])

$$V(D) = E_0(\mathbf{D}) - E_0(D = \infty). \quad (1)$$

In this equation, $E_0(\mathbf{D})$ is the energy of the two nuclei separated by the distance $\mathbf{D}$ without their relative kinetic energy: $E_0(\mathbf{D}) = E(\mathbf{D}) - P^2(\mathbf{D})/2\mu m$, which is the expectation value of the energy operator $\hat{H} - \hat{T}_R$, where $\hat{H}$ and $\hat{T}_R$ are, respectively, the total microscopic Hamiltonian and the kinetic energy operator for relative motion.

We start from the normalized many-particle wave function (see also [16, 18])

$$\Phi = n(D)\hat{A}\left[\Phi_1(\mathbf{D}_1)\Phi_2(\mathbf{D}_2)e^{i(\mathbf{K}_1\cdot\mathbf{R}_1+\mathbf{K}_2\cdot\mathbf{R}_2)/\hbar}\right], \quad (2)$$

where $\mathbf{D}_I$ $(I = 1, 2)$ are the centers with respect to which the coordinates of the nucleons are defined (we set $N_1\mathbf{D}_1/N + N_2\mathbf{D}_2/N = 0$); $\hat{A} = \sum_P \delta_P P$ is the antisymmetrization operator; δ_P is the sign of the permutation P; $\Phi_I(\mathbf{D}_I)$ are the wave functions for the interacting nuclei; $\mathbf{K}_I$ and $\mathbf{R}_I (I = 1, 2)$ are, respectively, the center-of-mass momentum and the coordinate of the I nucleus; $\mathbf{D} = \mathbf{D}_1 - \mathbf{D}_2$; and $n(D)$ is the normalization constant. Let us assume that the center-of-mass momenta $\mathbf{K}_I$ depend on D and tend to their asymptotic values at an infinite separation distance.

Choosing, for intrinsic states, single-particle shell-model wave functions, one can write

$$\Phi_I = \frac{1}{\sqrt{N_I!}}\hat{A}_I \prod_{\alpha\in I} \phi'_\alpha(x'_\alpha) \quad (3)$$
$$= \frac{1}{\sqrt{N_I!}}\hat{A}_I \prod_{\alpha\in I} \phi_\alpha(x_\alpha),$$

where $I = 1, 2$; x contains the spatial $\mathbf{r}$ and the spin–isospin variables s, t $[x = (\mathbf{r}, s, t)]$; and $\phi'_\alpha(x')$ stands for the wave function of the shifted argument $x' = (\mathbf{r} - \mathbf{D}_I, s, t)$ $[\phi'_{\alpha\in I}(x') = \phi_\alpha(x)]$. The index of each state α contains orbital and spin–isospin quantum numbers.

Let us introduce momentum-dependent single-particle states in the following way:

$$\tilde{\phi}_{\alpha\in I}(x) \equiv \phi_{\alpha\in I}(x)\exp(i\mathbf{k}_I\cdot\mathbf{r}/\hbar), \quad (4)$$
$$\left(\mathbf{k}_I = \frac{\mathbf{K}_I}{N_I}\right).$$

The wave function (2) now can be written as a Slater determinant, that is,

$$\Phi(D) = \frac{1}{\sqrt{N!\Gamma}}\hat{A}\prod_{\alpha\in 1,2}\tilde{\phi}_\alpha(x_\alpha) = \frac{1}{\sqrt{N!\Gamma}}\det\Lambda_{\alpha,\beta}, \quad (5)$$

where $\Lambda_{\alpha,\beta} = \tilde{\phi}_\alpha(x_\beta)$, $G_{\alpha,\beta} = \{\langle\tilde{\phi}_\alpha|\tilde{\phi}_\beta\rangle\}$, and $\Gamma = \det G$ is the Gram determinant of the set $\{|\tilde{\phi}_\alpha\rangle\}$.

The functions $\{\tilde{\phi}_\alpha(x)\}$ are square-integrable and depend on the center positions $\mathbf{D}_{I=1,2}$ and the momenta $\mathbf{k}_{I=1,2}$. These functions are orthonormalized if they belong to the same nucleus $[G_{\alpha,\beta} \equiv \langle\tilde{\phi}_\alpha|\tilde{\phi}_\beta\rangle = \delta_{\alpha,\beta}(\alpha, \beta \in I)]$, but they are not if α and β are states of different nuclei $[G_{\alpha,\beta} \neq \delta_{\alpha,\beta}]$.

Since the functions $\{\phi_\alpha\}$ are finite with respect to $\mathbf{r}$, the functions $G_{\alpha,\beta}(D, K) \to 0$ if $D \to \infty$ and (or) $K \to \infty$. Thus, the matrix G is strictly diagonal at infinite separation distance and infinite K. It can also be approximately valid in the small-overlap region (where one-particle exchange dominates) or at sufficiently high energies.

If $D \neq 0$ or $K \neq 0$, the Gram determinant does not vanish, $\Gamma = \det\{\langle\tilde{\phi}_\alpha|\tilde{\phi}_\beta\rangle\} \neq 0$. The single-particle states of both nuclei are linearly independent, and the vectors $\{|\tilde{\phi}_\alpha\rangle\}$ form a basis in the N dimensional subspace of the Hilbert space. This is due to their separation in r space and in momentum space. In the case of a complete overlap, $\Gamma \to 0$ for $D \to 0$ and $K \to 0$, but Φ still remains well defined and tends to the ground-state shell-model configuration of the composite system [19]. However, we will not consider this case in this study because the value of the potential at zero separation is insignificant in the elastic-scattering problem. With the aid of the well-known technique from [19], one can calculate the potential (1) using the nonorthogonal basis $\{\tilde{\phi}_\alpha\}$, which coincides with the DFM potential at large separation distances, where the nonorthogonality vanishes.

We will use another option. If the set of states $\{\tilde{\phi}_\alpha\}$ is linearly independent ($\Gamma \neq 0$), one can orthogonalize it and consider the corresponding orthonormal set $\{\tilde{\psi}_\alpha\}$. Thus, one can write the wave function of Eq. (2) with the aid of this orthonormal basis. Using the expansion $\tilde{\phi}_\alpha = \sum_\beta C_{\alpha,\beta}\tilde{\psi}_\beta$, where $\det C \neq 0$, and the properties of the determinants, we obtain $\Phi = \exp[i\sigma]\det\{\tilde{\psi}_\alpha(x_\beta)\}$ [where $\sigma = \arg(\det C)$]. The set $\{\tilde{\psi}_\alpha\}$ is ordered in the sense that one can find the nucleus to which each state belongs by considering its asymptotic behavior: $\tilde{\psi}_\alpha \to \tilde{\phi}_\alpha$ when $D \to \infty$ (at finite k). The nucleus–nucleus potential (1) can easily be calculated by using the momentum-dependent orthonormal set $\{\tilde{\psi}_\alpha\}$. However, we define new wave functions $\psi_\alpha \equiv \tilde{\psi}_\alpha\exp[-i\mathbf{k}_I\cdot\mathbf{r}/\hbar]$ $(I = 1, 2, \alpha \in I)$ to obtain an expression close to the standard DFM one. In contrast to ϕ_α, these wave functions ψ_α depend on the relative momentum $\mathbf{k}$. Introducing $\psi'_\alpha(x') \equiv \psi_\alpha(x)$, one finally finds another

definition of the DFM potential, which will be referred to as the Pauli-distorted double-folding model (PDDFM). Assuming spin–isospin degeneracy (e.g., each orbital state is occupied by four nucleons [19]) and using the central nucleon–nucleon force, we can represent the nucleus–nucleus potential as

$$V(D) = X_d \int d\mathbf{r}_1 d\mathbf{r}_2 \rho_1(\mathbf{r}_1)\rho_2(\mathbf{r}_2) \quad (6)$$
$$\times\, v(|\mathbf{r}_1 - \mathbf{r}_2 + \mathbf{D}|) + X_e \int d\mathbf{r}_1 d\mathbf{r}_2 \rho_1(\mathbf{r}_1, \mathbf{r}_2)$$
$$\times\, \rho_2(\mathbf{r}_2 - \mathbf{D}, \mathbf{r}_1 - \mathbf{D}) v(s) e^{i\mathbf{k}\cdot\mathbf{s}/\hbar} + \varepsilon(D),$$

where $X_d = w + b/2 - h/2 - m/4$ and $X_e = m + h/2 - b/2 - w/4$ are the standard combinations of, respectively, the direct and the exchange parameter of the central nucleon–nucleon force; $\rho_I(\mathbf{r}_1, \mathbf{r}_2) = \sum_{st} \rho_I(x_1, x_2)$ ($x_1 = \mathbf{r}_1, s, t$; $x_2 = \mathbf{r}_2, s, t$) is the DM obtained from the wave functions $\{\psi_\alpha\}$, which is related to the DM associated with $\{\tilde{\psi}_\alpha\}$ by the equation $\tilde{\rho}(\mathbf{r}_1, \mathbf{r}_2) = \rho(\mathbf{r}_1, \mathbf{r}_2) e^{i\mathbf{k}_I\cdot\mathbf{s}/\hbar}$; and $\rho_I(\mathbf{r}) = \rho_I(\mathbf{r}, \mathbf{r})$. The last term on the right-hand side of Eq. (6) represents the excitation energy of the nuclei during the interaction, $\varepsilon(D) = \varepsilon_1(D) + \varepsilon_2(D)$; that is,

$$\varepsilon_I(D) = \frac{X_d}{2} \int d\mathbf{r}_1 d\mathbf{r}_2 \left[\rho_I(\mathbf{r}_1)\rho_I(\mathbf{r}_2) \right. \quad (7)$$
$$\left. - \rho_{I0}(\mathbf{r}_1)\rho_{I0}(\mathbf{r}_2)\right] v(|\mathbf{r}_1 - \mathbf{r}_2|)$$
$$+ \frac{X_e}{2} \int d\mathbf{R} d\mathbf{s} \left[\rho_I^2(\mathbf{R}, s) - \rho_{I0}^2(\mathbf{R}, s)\right] v(s)$$
$$+ \frac{\hbar^2}{2m} \int d\mathbf{r} \left[\tau_I(\mathbf{r}) - \tau_{I0}(\mathbf{r})\right],$$

where $I = 1$, 2 and τ_{I0} and τ_I are the kinetic energy densities of the ground and excited states, respectively. The potential $V(D)$ given by Eq. (6) differs from the DFM potential for two main reasons. First of all, the Pauli-distorted DM $\rho_I(x_1, x_2) = \sum_{\alpha\in I} \psi_\alpha^*(x_2)\psi_\alpha(x_1)$ enters into (6) instead of the ground-state DM for each isolated nucleus [$\rho_{I0}(x_1, x_2) = \sum_{\alpha\in I} \phi_\alpha^*(x_2)\phi_\alpha(x_1)$], the latter being used in the DFM. Second, the intrinsic-excitation-energy term appears in the PDDFM.

To calculate the DM ρ_I, one must also know the relative momentum $k(D)$ explicitly. In the DFM, it is assumed that $k^2(D) = 2mN(E_{\text{c.m.}} - V(D))/(N_1 N_2)$. Thus, the problem of determining the potential by considering the proper values of $k(D)$ must be solved self-consistently. Using Eq. (2) as an ansatz, one can calculate a model nucleus–nucleus potential by performing an orthogonalization of single-particle states at each separation D self-consistently.

Nothing is implied concerning the choice of these single-particle states. In fact, one can use the single-particle states of the isolated nuclei. However, the single-particle states of a given nucleus can change in the presence of a second one, which complicates the problem significantly. Another problem involved in applying the above procedure consists in the use of explicit single-particle states, while the main advantage of the DFM is that only local densities are employed. It will be shown in the next section that all these problems can be solved at a semiclassical level.

3. SEMICLASSICAL APPROXIMATION

It is possible to simplify the calculations of the potential (6) by using semiclassical approaches based on the Thomas–Fermi (TF) method and its extension. In fact, such approaches are applied in the majority of recent studies devoted to the DFM potential. For example, the CB approximation to the DM is used in many cases. In this approach, the DM is taken in the Slater form with an effective momentum that depends on the kinetic energy density τ and the Fermi momentum p_{F}. The CB DM corresponds to a truncation of the full quantal DM. However, τ and p_{F} are unknown at the quantum level, so that use is made of their semiclassical counterparts, which can be written in terms of the local density. In this case, the semiclassical CB DM corresponds to the truncation of the semiclassical DM in the ETF approximation [15]. Thus, a semiclassical approach is actually included in the DFM.

In coordinate space, the semiclassical density matrix is given by the inverse Wigner transformation of the distribution function $f(\mathbf{R}, \mathbf{p})$ (see, for example, [20]); for a moving nucleus, we have

$$\tilde{\rho}_I(\mathbf{r}, \mathbf{r}', \mathbf{k}_I) = \frac{g}{(2\pi\hbar)^3} \quad (8)$$
$$\times \int d\mathbf{p} f_I(\mathbf{R}, \mathbf{p}) e^{i(\mathbf{p}+\mathbf{k}_I)\cdot\mathbf{s}/\hbar},$$

where $\mathbf{R} = 1/2(\mathbf{r} + \mathbf{r}')$ and $\mathbf{s} = \mathbf{r} - \mathbf{r}'$, while g is the spin–isospin degeneracy factor. The ground-state distribution function for each nucleus at the Thomas–Fermi level (the $\hbar^0$-order term in the Wigner–Kirkwood expansion) is $f_I(\mathbf{R}, \mathbf{p}) = \Theta[p_{\text{F}_I}(\mathbf{R}) - p]$. One can define $\tilde{f}_I(\mathbf{R}, \mathbf{p}) = f_I(\mathbf{R}, \mathbf{p} - \mathbf{k}_I) = \Theta[p_{\text{F}_I}(\mathbf{R}) - |\mathbf{p} - \mathbf{k}_I|]$, where $\Theta(x)$ is the unit step function: $\Theta(x) = 1$ at $x \geq 0$ and $\Theta(x) = 0$ otherwise. Notice that this $\tilde{f}_I$ is precisely the distribution function related to the DM $\tilde{\rho}_I$ obtained with the orthogonal set $\tilde{\psi}_\alpha$ (see above).

We suggest that, during the interaction, these Fermi spheres can deform, so that, at each point in coordinate space, one can define, for each nucleus, an

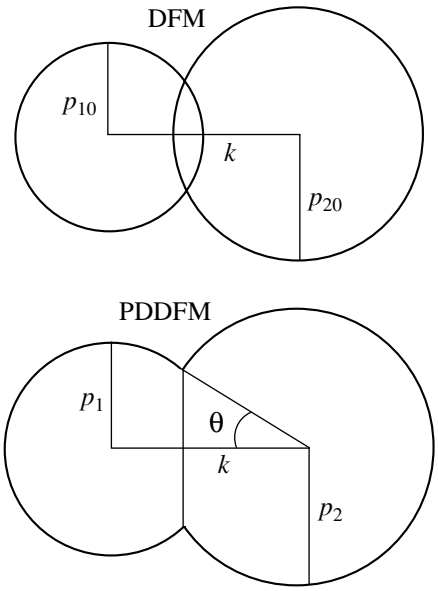

Fig. 1. Fermi spheres corresponding to different points in the coordinate space of interacting nuclei separated by the local momentum $k(D)$ in momentum space (D is the distance between the centers with respect to which the densities of nuclei are defined). The upper part corresponds to the DFM, where the two Fermi spheres with momenta p_{10} and p_{20} overlap and the Pauli exclusion principle is violated. In the lower part, the truncated Fermi spheres with momenta p_1 and p_2 according to the PDDFM are shown.

effective Fermi volume $\Omega_{\mathrm{F},I}$ and a distribution function $f_I(\mathbf{R},\mathbf{p}) = \Theta[p_{\mathrm{F}_I}(\omega_p,\mathbf{R}) - p]$. The Fermi momentum p_{F_I} is related to the local density of the nucleus I at this point of coordinate space and depends on its orientation ω_p in momentum space. At the semiclassical level, it is not possible to introduce single-particle states explicitly and the orthogonality condition should be formulated in terms of the semiclassical DM. For this purpose, we assume that the quantum orthogonality condition $\hat{\tilde{\rho}}_1\hat{\tilde{\rho}}_2 = 0$ has to be fulfilled at the semiclassical level as follows: $(\hat{\tilde{\rho}}_1\hat{\tilde{\rho}}_2)_{\mathrm{W}} = 0$, where the subindex W stands for the Wigner transformation of the quantal operator. At the TF level (considering only $\hbar^0$ terms in the Wigner–Kirkwood expansion), one will get

$$(\hat{\tilde{\rho}}_1\hat{\tilde{\rho}}_2)_{\mathrm{W}} = (\hat{\tilde{\rho}}_1)_{\mathrm{W}}(\hat{\tilde{\rho}}_2)_{\mathrm{W}} \qquad (9)$$
$$= f_1(\mathbf{R}-\mathbf{D}_1,\mathbf{p}-\mathbf{k}_1)f_2(\mathbf{R}-\mathbf{D}_2,\mathbf{p}-\mathbf{k}_2) = 0.$$

By using the translational invariance in the center-of-mass frame ($\mathbf{K}_1 + \mathbf{K}_2 = 0$), one obtains the relation

$$\Theta\left[p_{\mathrm{F}_1}(\omega_p,\mathbf{R}-\mathbf{D}_1) - p\right] \qquad (10)$$
$$\times\,\Theta\left[p_{\mathrm{F}_2}(\omega_p,\mathbf{R}-\mathbf{D}_2) - |\mathbf{p}+\mathbf{k}|\right] = 0.$$

This means that the Fermi volume of two interacting nuclei should not overlap in momentum space. Returning to the standard DFM potential, one can see that, at the semiclassical level, the nonorthogonality of the single-particle states of different nuclei at finite values of D and K means that their Fermi spheres overlap in momentum space as shown in Fig. 1 (upper part). The overlap region is forbidden by the Pauli exclusion principle. If $K \to \infty$, these Fermi spheres are separated and no overlap occurs. If $D \to \infty$, the Fermi momentum of one of the nuclei tends to zero ($p_{\mathrm{F}_I} \to 0$) and the Fermi spheres are also separated. At finite K and D, the overlap will appear, which means that the DFM is not applicable and that the orthogonalization procedure must be used.

There is a significant difference between the quantal and the semiclassical orthogonality conditions. In the first case, the orthogonalization procedure defines a distorted density matrix of interacting nuclei (up to a unitary transformation of the orthonormalized basis). In the semiclassical approximation, single-particle states are not defined; as a result, this orthogonalization procedure is not applicable. In order to solve this situation, we use the following geometric ansatz: If there is no overlap of the initial Fermi spheres, we have unperturbed states of the isolated nuclei and the Pauli exclusion principle will not affect the DFM potential. If there is an overlap, we assume that the distribution functions for the interacting nuclei are precisely the Fermi spheres truncated by the plane going through the curve along the connection line of the initial Fermi spheres. This ansatz is displayed in Fig. 1 (bottom). This is not a unique solution, but it is probably the simplest assumption used in [21] to calculate the adiabatic nucleus–nucleus potential in the nuclear-matter approach.

Actually, the Thomas–Fermi approximation corresponds to a local nuclear-matter approach. The truncated spheres are determined by two parameters: the radius p_{F_I} and the angle θ as defined in Fig. 1. The angle θ depends on the relative momenta k and the Fermi momenta p_{F_I}. Therefore, we have to calculate new values of p_{F_I}. To this aim, one can note that the local density is determined by the distribution function as

$$\rho_I(\mathbf{R}) = \frac{g}{(2\pi\hbar)^3}\int d\mathbf{p} f_I(\mathbf{R},\mathbf{p}) \qquad (11)$$
$$= \frac{g}{(2\pi\hbar)^3}V_{\mathrm{F}_I}(p_{\mathrm{F}_I},\mathbf{k}),$$

where we assume a sharp-border distribution function f_I and V_{F_I} is the volume in momentum space occupied by nucleons of a given nucleus after the distortion.

To determine the value of p_{F_I}, we must know the volume V_{F_I} or the value of the local density ρ_I. Following the frozen-density approximation used in

DFM, which means that the local densities of nuclei do not change during the interaction ($\rho_I(\mathbf{r}) = \rho_{I0}(\mathbf{r})$), one has to set $V_{\mathrm{F}_I} = V_{\mathrm{F}_{I0}}$.

The DM of the ground state at the TF level is given by a step function in momentum space. This case corresponds to a full Fermi sphere in momentum space. If there is overlap, we define truncated Fermi spheres (see Fig. 1). The truncated Fermi sphere corresponds to an excited state of the nucleus because we depopulate the states that correspond to the forbidden overlap region and occupy new states with a different Fermi momentum $p_{\mathrm{F}_I}(\omega, R)$. In this case, the distribution function is given by

$$f_I(\mathbf{R}, \mathbf{p}) = \Theta[p_{\mathrm{F}_I}(\omega_p, \mathbf{R}) - p], \qquad (12)$$

where the new Fermi momentum p_{F_I} depends on its orientation in p space. The DMs for the truncated Fermi spheres averaged over the direction $\mathbf{s}$ are obtained as

$$\rho_I(\mathbf{R}, s) = \frac{g p_{\mathrm{F}_I}^3}{12\pi^2\hbar^3}\Big[\hat{j}_1(p_{\mathrm{F}_I}s/\hbar)(1 - x_0) \qquad (13)$$
$$+ \frac{3\hbar^3}{(p_{\mathrm{F}_I}s)^3}(x_0 \sin(p_{\mathrm{F}_I}s/\hbar) - \sin(x_0 p_{\mathrm{F}_I}s/\hbar))\Big],$$

where $\hat{j}_1(x) = (3/x)j_1(x)$ is normalized to unity at $x = 0$, $j_1(x)$ is a first-order spherical Bessel function, and $x_0 = \cos(\theta)$ is the cosine of the angle determined by the point where the new Fermi spheres cross (see Fig. 1). At $s = 0$, one obtains the local density corresponding to the truncated Fermi sphere:

$$\rho_I(\mathbf{R}) = \frac{g p_{\mathrm{F}_I}^3}{24\pi^2\hbar^3}(2 - 3x_0 + x_0^3). \qquad (14)$$

One can see that, if there is no overlap ($x_0 = -1$), then Eqs. (13) and (14) give the usual formulas for the full Fermi spheres. For the ground state, the kinetic-energy density at the TF level has the form

$$\tau_{I0}(\mathbf{R}) = \frac{g p_{\mathrm{F}_I}^5}{10\pi^2\hbar^5}. \qquad (15)$$

To calculate the kinetic-energy density τ_I in an excited state, the integral of the TF distribution function (12) is taken over the truncated Fermi sphere of radius p_{F_I}. In this case, one obtains

$$\tau_I(\mathbf{R}) = \frac{g p_{\mathrm{F}_I}^5}{80\pi^2\hbar^5}(4 - 5x_0 + x_0^5). \qquad (16)$$

4. RESULTS AND SUMMARY

To estimate the importance of the Pauli distortion, we compare the potentials corresponding to elastic ^{16}O–^{16}O scattering that were obtained within the DFM and PDDFM approaches. Figure 2 displays the relative deviation of the PDDFM potential from the DFM one at various energies. Apart from the trivial result that the Pauli distortion decreases with increasing incident energy, it can be seen that the largest deviation of the two potentials appears at some distance that shifts to smaller radial distances with increasing energy. In order to understand this behavior, we look at the local definition of the relative momenta $k(D)$: if the potential is sufficiently deep, it will increase the momenta k and we will have, at small distances, a "repulsion" of the Fermi spheres, which induces a reduction of the Pauli distortion. Still, it is interesting to note that the maximum of the Pauli distortion appears in the range of distances between 3 and 5 fm, where a deep potential determines the occurrence of nuclear-rainbow scattering.

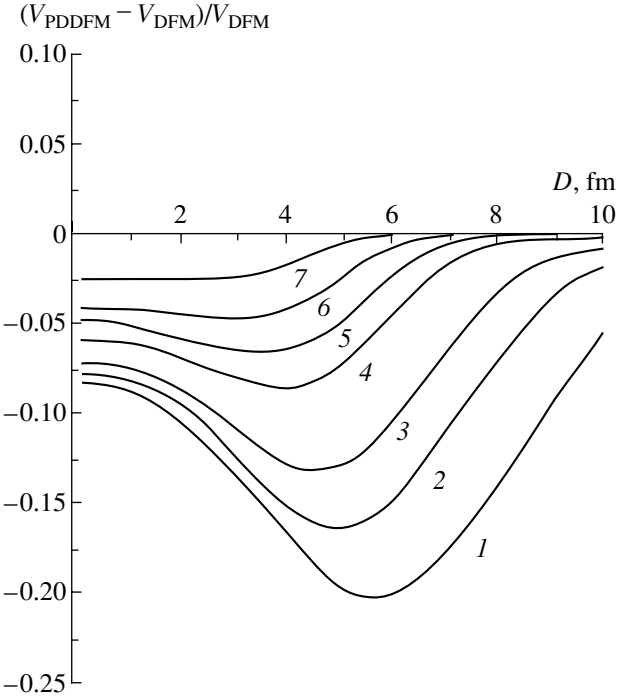

Fig. 2. Relative deviation of the PDDFM potential with respect to the DFM potential for the ^{16}O–^{16}O system with the BDM3Y1 force at different energies in the laboratory frame: (*1*) 40, (*2*) 75, (*3*) 124, (*4*) 250, (*5*) 350, (*6*) 480, (*7*) 750 MeV.

Thus, starting from the generalized Born–Oppenheimer approach, we have derived the PDDFM potential with a correct treatment of the Pauli exclusion principle at the semiclassical level. This PDDFM potential coincides with the DFM one at infinite energy and (or) infinite separation. The most surprising result is that, at finite energies, the Pauli exclusion principle does not affect the DFM potential dramatically in the interior. This is due to the fact that the local definition of the relative momentum increases

its value inside the potential. Thus, the PDDFM potentials remain deep over a large energy range (6–60 MeV/nucleon), which is important in explaining the systematics of nuclear-rainbow scattering.

ACKNOWLEDGMENTS

This work was supported in part by the German Ministry (BMFT) Verbundforschung under contract no. 06OB472D/4. X. Viñas is grateful for grant no. PB98-1247 from DGICYT (Spain) and Grant no. 1998SGR-00011 from DGR (Catalonia).

REFERENCES

1. J. A. Wheeler, Phys. Rev. **52**, 1083, 1107 (1937).
2. G. R. Satchler and W. G. Love, Phys. Rep. **55**, 183 (1979).
3. M. E. Brandan and G. R. Satchler, Phys. Rep. **285**, 143 (1997).
4. Dao T. Khoa, W. von Oertzen, and H. G. Bohlen, Phys. Rev. C **49**, 1652 (1994).
5. D. T. Khoa, G. R. Satchler, and W. von Oertzen, Phys. Rev. C **56**, 954 (1997).
6. M. P. Nicoli, F. Haas, R. M. Freeman, *et al.*, Phys. Rev. C **60**, 064608 (1999).
7. D. T. Khoa and W. von Oertzen, Phys. Lett. B **342**, 6 (1995).
8. U. Atzrott, P. Mohr, H. Abele, *et al.*, Phys. Rev. C **53**, 1336 (1996).
9. A. A. Ogloblin *et al.*, Phys. Rev. C **57**, 1797 (1998).
10. Dao T. Khoa, W. von Oertzen, H. G. Bohlen, *et al.*, Nucl. Phys. A **672**, 387 (2000).
11. B. C. Sinha, Phys. Rep. **20C**, 1 (1975); Phys. Rev. C **11**, 1546 (1975).
12. O. M. Knyaz'kov and A. A. Nekrasov, Yad. Fiz. **38**, 36 (1983) [Sov. J. Nucl. Phys. **38**, 20 (1983)].
13. Dao T. Khoa, Nucl. Phys. A **484**, 376 (1988); Dao Tien Khoa and O. M. Knyaz'kov, Yad. Fiz. **47**, 1246 (1988) [Sov. J. Nucl. Phys. **47**, 793 (1988)].
14. X. Campi and A. Bouyssy, Phys. Lett. B **73B**, 263 (1978); Nukleonika **24**, 1 (1979).
15. V. B. Soubbotin and X. Viñas, Nucl. Phys. A **665**, 291 (2000).
16. T. Fliessbach, Z. Phys. **247**, 117 (1971).
17. J. Fleckner and U. Mosel, Nucl. Phys. A **277**, 170 (1977).
18. D. M. Brink and Fl. Stancu, Nucl. Phys. A **243**, 175 (1975).
19. D. Brink, in *Proceedings of the International School in Physics "Enrico Fermi," Course XXXVI, 1966,* p. 247.
20. P. Ring and P. Schuck, *The Nuclear Many-Body Problem* (Springer-Verlag, New York, 1980).
21. T. Izumoto, S. Krewald, and A. Faessler, Nucl. Phys. A **341**, 319 (1980).

Physics of Atomic Nuclei, Vol. 65, No. 4, 2002, pp. 713–719. From Yadernaya Fizika, Vol. 65, No. 4, 2002, pp. 745–751.

Structure of Neutron-Rich s–d Shell Nuclei*

S. L. Tabor**, **M. W. Cooper, D. B. Campbell, C. Chandler, K. W. Kemper, A. Pipidis, M. A. Riley, M. Wiedeking, and I. Ragnarsson**[1)]

Department of Physics, Florida State University, Tallahassee, USA

Received July 20, 2001

Abstract—States in neutron-rich s–d shell nuclei were populated in the reaction of a ^{14}C beam at $E_{\rm lab} = 22$ MeV on a ^{14}C target. Coincidences between γ rays and either other γ rays or light charged particles were measured. γ rays in coincidence with protons established levels at 66.8, 1730, 1823, and 2219 keV in ^{27}Na. The states are compared with calculations based on the s–d shell model and the cranked Nilsson–Strutinsky model. A number of levels in ^{24}Ne were observed in both α–γ and α–γ–γ coincidences and are compared with shell-model calculations. © *2002 MAIK "Nauka/Interperiodica".*

1. INTRODUCTION

The positive-parity structure of nuclei near the valley of stability in the s–d shell has generally been reproduced rather well by shell-model calculations, although the effective interactions have been determined by fitting much of the same structure [1]. The exploration of nuclei farther from stability provides an excellent test of the calculations. Considerable interest has been focused on the properties of nuclei farther from stability, and the increasing availability of radioactive beams will allow further exploration beyond the valley of stability. However, experimental challenges provided by low-intensity, short-lived radioactive beams will limit what can be learned. It is therefore valuable to stretch the more conventional spectroscopic techniques as far as possible to form a bridge of nuclear-structure information reaching the nuclei that can only be studied with the future generation of radioactive beams.

In the past two decades, a vast amount has been learned about high-spin structures in heavier deformed nuclei, both experimentally and theoretically. The s–d shell provides an ideal arena where more collective calculations developed for heavier nuclei can be compared with both experiment and the more microscopic shell-model calculations, which become increasingly difficult for heavier mid-shell nuclei. A comparison of the descriptions of low-lying collective and noncollective states in ^{25}Mg provided new insights into both the microscopic and macroscopic models [2].

The long lifetime of ^{14}C provides the opportunity of exploring the structure of more neutron-rich nuclei at a level of detail usually seen only near the valley of stability by using it as both the target and the beam. A major goal of this project was the $T = 5/2$ nucleus ^{27}Na. Only a few levels had been seen previously with limited resolution by using the reaction ^{26}Mg (^{18}O,^{17}F) [3]. Without spin assignments, it was not possible to compare the results with model calculations.

2. EXPERIMENTAL PROCEDURE

The ^{14}C beam used was produced with a dedicated Cs sputter ion source. It was accelerated to 22 MeV by using the Florida State University FN tandem Van de Graaf accelerator. A highly enriched self-supporting ^{14}C foil of 280 μg/cm^2 was used as the target. However, subsequent analysis of the data has revealed that some ^{12}C contamination had built up on the target. Light charged particles from the reaction were detected by using a Si detector telescope placed at 0° relative to the beam. A stack of two 2000 μm Si diodes was used as the E detector, and a 150 μm Si diode served as the ΔE detector. A 33.8-mg/cm^2 Au foil was placed between the target and the telescope to stop the beam.

Two four-crystal "clover" detectors and seven Compton-suppressed HPGe detectors were used to detect γ rays at angles of 35°, 90°, and 145° relative to the beam. Both particle–γ and γ–γ coincidences (along with some higher multiplicity events) were written on a 8-mm tape for subsequent analysis. Because Compton scattering between elements of the clover detectors was common, the four crystals in a clover detector were treated as one detector. Events

*This article was submitted by the authors in English.

[1)]Department of Mathematical Physics, Lund Institute of Technology, Sweden.

**e-mail: tabor@nucott.physics.fsu.edu

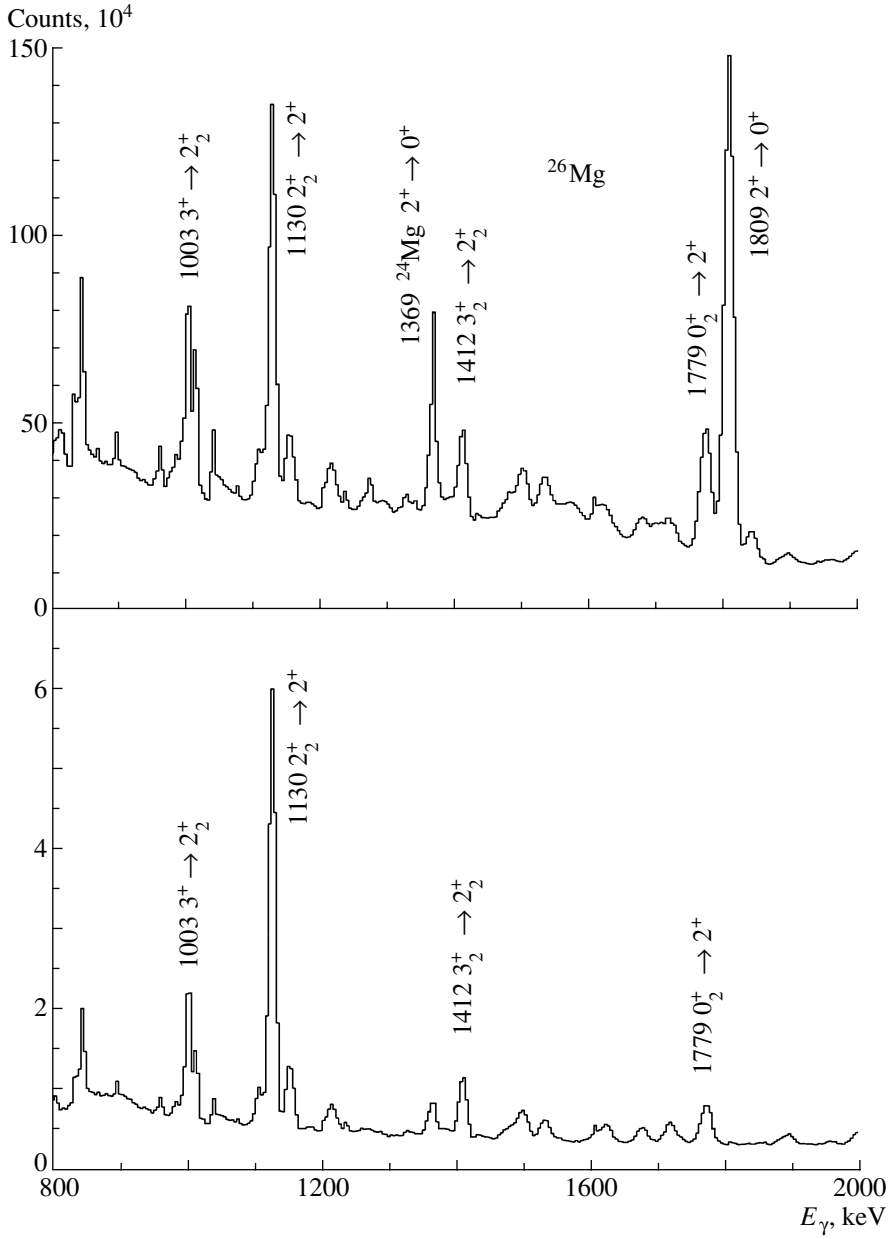

Fig. 1. Total projection of γ–γ coincidences (top) and γ spectrum in coincidence with the 1809-keV $2^+ \to 0^+$ transition in ^{26}Mg (bottom).

in which only elements of one clover detector was actuated were not recorded, and the energies detected by each crystal were added (add-back mode) to give a single γ energy.

After the experiment, the event data were stored on a computer disk to facilitate sorting in a variety of ways. Clear p, d, t, and α groups were seen in the E–ΔE matrix, although the d and t groups were significantly weaker.

3. γ–γ COINCIDENCES

All γ–γ coincidences were sorted into a $2D$ matrix. This was found to be completely dominated by transitions in ^{26}Mg. The emission of two neutrons was the major decay mode, by far, of the neutron-rich compound nucleus ^{28}Mg. This can be seen in Fig. 1. The region of the total projection is shown in the top panel, while a portion of the spectrum of γ rays in coincidence with the 1809-keV $2^+ \to 0^+$ transition is displayed in the bottom panel. The lower spectrum, consisting entirely of ^{26}Mg lines, is nearly identical

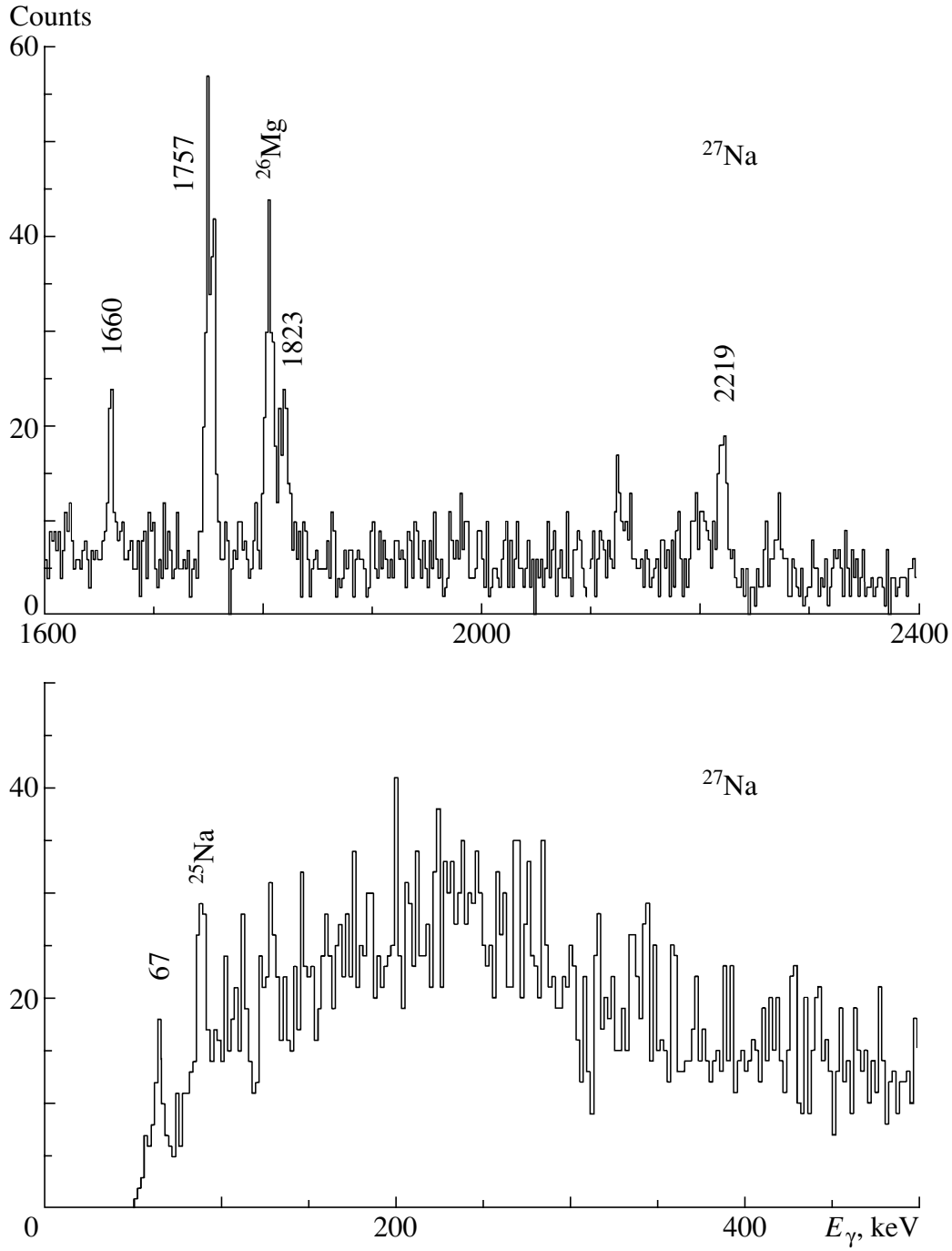

Fig. 2. Spectrum of γ rays in coincidence with higher energy protons. The ^{27}Na lines are labeled in keV.

to the total projection, except for the missing 1809-keV gating transition and a greatly reduced peak around 1369 keV. The latter peak arises mainly from the $2^+ \rightarrow 0^+$ transition in ^{24}Mg produced from the ^{12}C contamination in the target and multiple neutron emission.

4. ^{27}Na

A portion of the γ spectrum in coincidence with higher energy protons is shown in Fig. 2. The lines identified as those that are due to ^{27}Na are labeled with their energies in keV. The strongest ^{26}Mg line appears weakly from random coincidences, and the ^{25}Na line results from the small ^{12}C contamination in the target. The drastic reduction in the number of

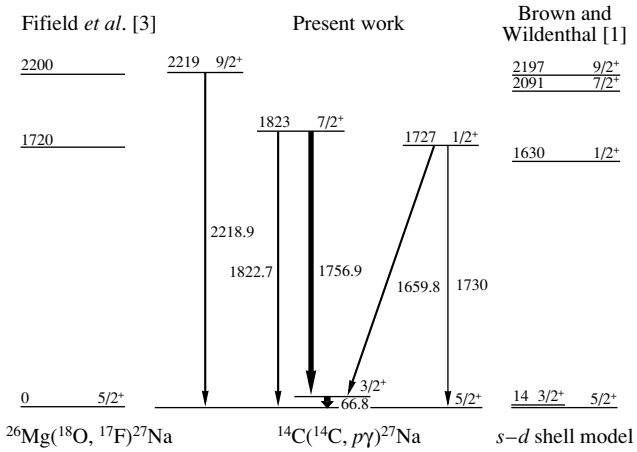

Fig. 3. Energy-level schemes for ^{27}Na observed in the present work and in an earlier reaction [3] and predicted by the shell model [1].

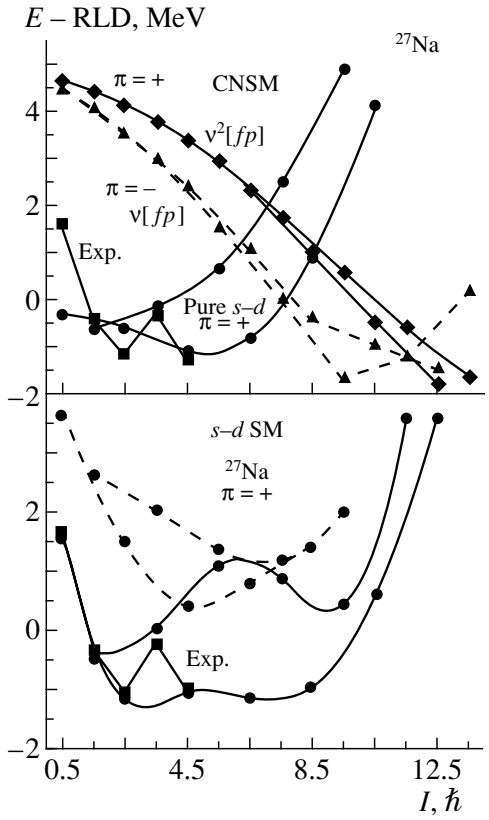

Fig. 4. Experimentally observed (squares) and theoretically predicted excitation energies minus those of a rotating liquid drop versus spin.

counts compared to Fig. 1 illustrates how weak the proton-emission channel is in relation to the emission of two neutrons.

The levels in ^{27}Na that were established by these p–γ coincidences are shown in the middle of Fig. 3. The energies of the two excited states at 1730 and 2219 keV are well within the stated uncertainties of the peaks seen in the reaction ^{26}Mg(^{18}O,^{17}F) [3], but two other excited states, at 67 and 1823 keV, were not seen in that reaction. The levels seen experimentally in ^{27}Na agree rather well in number and position with those predicted by the s–d shell model. (The next predicted shell-model state lies at 2671 keV.) The spin assignments are based on the observed decay

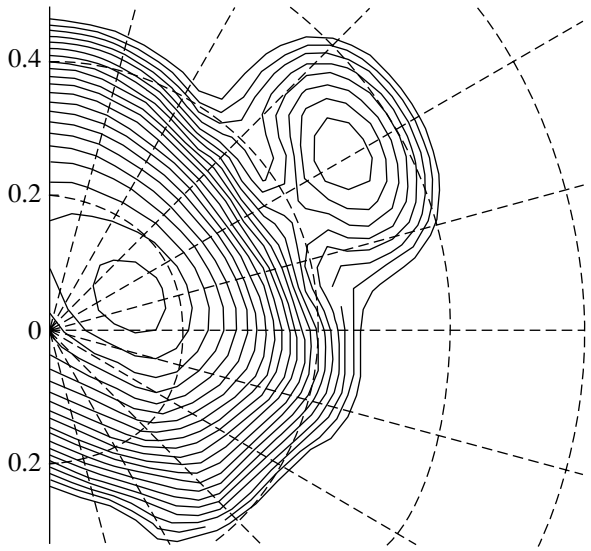

Fig. 5. Potential-energy surface calculated within the cranked Nilsson–Strutinsky for the $13/2^+$ states in ^{27}Na. The spacing between contour lines is 0.25 MeV. The labels on the ordinate refer to the magnitude of the quadrupole deformation ϵ_2 and apply to the semicircles. The dashed radial lines are drawn for various values of the triaxiality parameter γ at intervals of 15°. The line that passes just below the top right corner corresponds to the $\gamma = 0°$ prolate shape.

patterns and correspondence with shell-model calculations. By way of example, we indicate that, although the $7/2^+$ and $9/2^+$ levels lie close together in the shell model and could be inverted, the experimental 1823-keV state could not be the $9/2^+$ state because of its decay to the $3/2^+$ state.

The levels seen experimentally in ^{27}Na are compared with the band structures predicted in both the shell model (SM) and the cranked Nilsson–Strutinsky model (CNSM) [4] in Fig. 4. The energies of a rotating liquid drop with a constant moment of inertia of $\hbar^2/(2\Theta) = 0.133$ MeV have been subtracted from all energies on the ordinate. A rotational band with exactly this moment of inertia would lie on a horizontal line. The experimental results agree rather well with both the SM and the CNSM calculations, especially if we recall that the CNSM is optimized for high-spin states and neglects pairing. A major difference between the two models is the inclusion of higher orbitals in the CNSM. This may account for the reduced signature splitting in the CNSM at spins around 11/2. Observation of the $11/2^+$ level would help resolve this issue, and a further search for data is planned.

The lowest negative-parity bands have a dominant structure of $\nu[fp]$ in the CNSM. They are predicted to show small signature splitting, to fall rapidly with spin, and to become yrast at the spin value of 15/2. The $\nu^2[fp]$ structure is predicted to be superdeformed and to become yrast among the positive-parity states at the spin value of 17/2. The shape of this structure is driven by the nearby $Z = 10$ and $N = 16$ superdeformed gaps. The potential-energy surface for the $13/2^+$ states (Fig. 5) provides a comparison of the weakly deformed ($\epsilon_2 \approx 0.1$) pure s–d and the prolate superdeformed ($\epsilon_2 > 0.5$) $\nu^2[fp]$ configurations. Experimental observation of these structures remains a challenge, but the firm establishment of the lower level decay structure provides an important first step.

5. ^{24}Ne

The production of states of increasing excitation energy in ^{24}Ne with decreasing α energy can be seen in the α–γ coincidence spectra in Fig. 6. The top row of the spectra just shows random coincidences between α particles leaving ^{24}Ne in its ground state and the dominant γ rays from ^{26}Mg. The 1981-keV $2^+ \to 0^+$ transition in ^{24}Ne shows up clearly in the next row corresponding to somewhat lower α energies. More γ transitions in ^{24}Ne appear for lower α energies which leave the nucleus with increasing higher excitation energy. The 2082-keV $4^+ \to 2^+$ line in ^{22}Ne results from the ^{12}C contamination in the target.

The upper panel in Fig. 7 shows a portion of the γ spectrum in coincidence with α particles of all energies, while the lower panel shows α–γ–γ coincidences, namely, the spectrum of γ rays in coincidence with α particles and the 1981-keV γ line in ^{24}Ne. This clearly demonstrates that there are two γ rays near 1981 keV in coincidence with each other. They are the $2^+ \to 0^+$ and $4^+ \to 2^+$ transitions.

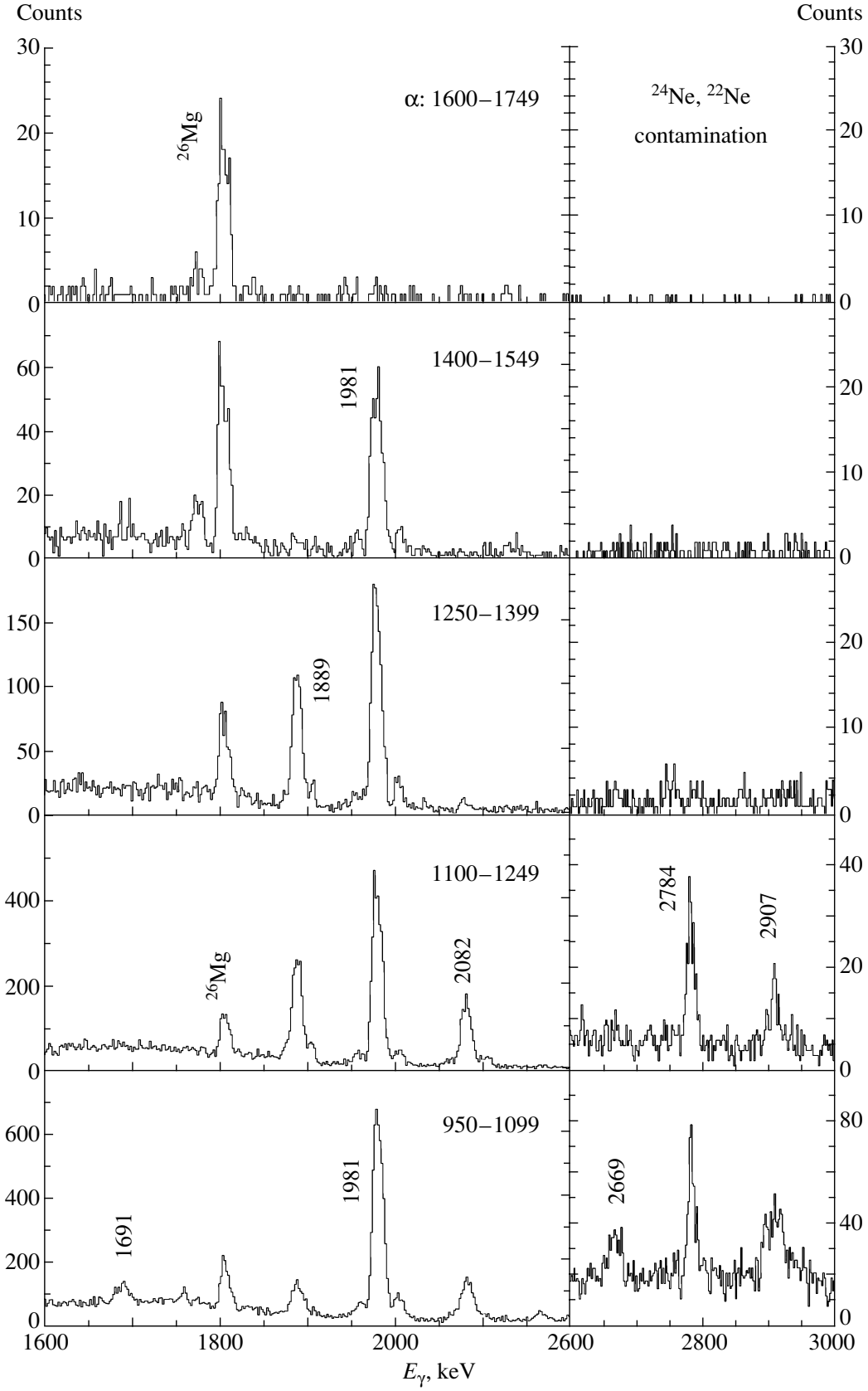

Fig. 6. γ spectra in coincidence with α particles. The range of α-channel numbers (and hence energies) is indicated for each row. The γ rays in ^{24}Ne are labeled with their energy in keV, except that the 2082 keV line comes from ^{22}Ne.

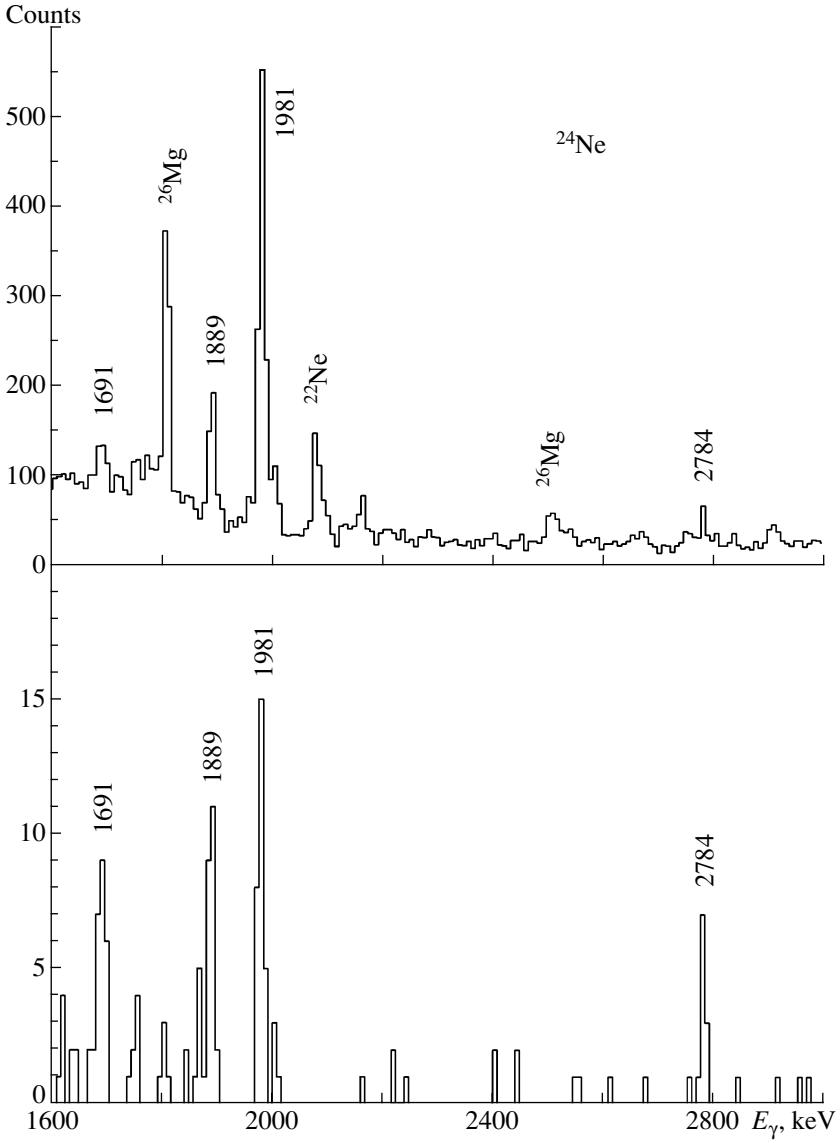

Fig. 7. A portion of the spectrum of γ rays in coincidence with α particles of any energy and with another γ ray of any energy (top) and the γ spectrum in coincidence with α particles of any energy and 1981-keV γ rays (bottom). Peaks in ^{24}Ne are labeled with their energies in keV.

ACKNOWLEDGMENTS

This work was supported in part by the U.S. National Science Foundation and in part by the Swedish Natural Science Council.

REFERENCES

1. B. H. Wildenthal, Prog. Part. Nucl. Phys. **11**, 5 (1984).
2. D. M. Headley, R. K. Sheline, S. L. Tabor, *et al.*, Phys. Lett. B **198**, 433 (1987).
3. L. K. Fifield, P. V. Drumm, M. A. C. Hotchis, *et al.*, Nucl. Phys. A **437**, 141 (1985).
4. T. Bengtsson and I. Ragnarsson, Nucl. Phys. A **436**, 14 (1985).

Physics of Atomic Nuclei, Vol. 65, No. 4, 2002, pp. 720–724. From Yadernaya Fizika, Vol. 65, No. 4, 2002, pp. 752–757.

Binding Energies and Radii of α-Cluster-Type Nuclei from Calculations Based on the Strictly Restricted Dynamics Model*

T. Krasta, J. Ruža, J. Tambergs[**], **O. Katkevičius**[1)], **and J. A. Castilho Alcarás**[2)]

Institute of Solid State Physics, University of Latvia, Riga

Received September 6, 2001

Abstract—The properties of α-cluster-type nuclei with $4 \leq A \leq 80$ are studied by employing the microscopic strictly restricted dynamics model (SRDM). The SRDM parameter set found via a fit to the experimental and theoretical values of nuclear binding and excited-level energies, classified according to the ground-state SU_3 configurations, includes a nuclear-radius parameter r_0 entering into the expression $R = r_0 A^{1/3}$ [fm], as well as the parameters of the effective central NN-interaction potential. The use of the microscopic SRDM allows one to obtain additional information about nuclei along the $Z = N$ line, including binding energies, radii, and spectra of low-lying levels. The calculated nuclear binding energies and nuclear root-mean-square radii $\langle r^2 \rangle^{1/2}$ are in reasonable agreement with their experimental counterparts. © *2002 MAIK "Nauka/Interperiodica".*

1. INTRODUCTION

The microscopic nuclear model proposed by Vanagas [1, 2] allows one to obtain a self-consistent description of nuclear radii, binding energies, and excited-level spectra via an approximate solution to the microscopic nuclear Schrödinger equation for a system of A nucleons. In the simplest case of low-lying states of α-cluster-type nuclei, when only central NN-interaction is taken into account, the nuclear microscopic Hamiltonian has the form

$$H^{\mathrm{micr}} = T^{\mathrm{micr}} + V^{\mathrm{micr}} = -\frac{\hbar^2}{2m}\frac{1}{A} \times \sum_{i<j=2}^{A} (\boldsymbol{\nabla}_i - \boldsymbol{\nabla}_j)^2 + \sum_{i<j=2}^{A} \Big(V_{\mathrm{W}}(r_{ij}) + P_{ij}^{(r_{ij})} \times V_{\mathrm{M}}(r_{ij}) + P_{ij}^{(\sigma_{ij})} \cdot V_{\mathrm{B}}(r_{ij}) + P_{ij}^{(\tau_{ij})} \cdot V_{\mathrm{H}}(r_{ij}) \Big). \quad (1)$$

Here, the subscripts W, M, B, and H refer to the Wigner, Majorana, Bartlett, and Heisenberg interactions, respectively; $P_{ij}^{(\ldots)}$ are the projection operators for the spatial, spin, and isospin states of nucleon pairs; and $r_{ij} = \mid \mathbf{r}_i - \mathbf{r}_j \mid$.

If one introduces Jacobi vectors and rewrites Eq. (1) in terms of Dzublik–Zickendraht variables, one can construct models either by restricting the Hilbert space where H^{micr} acts, by taking only some irreducible components of H^{micr} relative to some group of symmetry, by doing both the former and the latter. For the basis functions of H^{micr} Hilbert space, one can take those of the irreps of $U_{3(A-1)}$ labeled according to the following unitary chain of subgroups:

$$U_{3(A-1)} \supset (U_3 \supset SO_3) \times (U_{A-1} \supset O_{A-1} \supset S_A). \quad (2)$$

The strictly restricted dynamics model (SRDM) [1, 3] considers, in Eq. (1), only two terms: the U_{A-1}-scalar part of the collective term and the anticollective one (U_3-scalar); i.e., the general structure of the SRDM Hamiltonian is

$$H_{\mathrm{SRDM}} \equiv H^0 = H^{0\mathrm{coll}} + H^{0a}. \quad (3)$$

The best area for the application of SRDM are nuclei in the neighborhood of the $Z = N$ line.

A detailed description of the SRDM and of its application for α-cluster-type nuclei with $A \leq 40$, with an effective NN-interaction potential of the multipole–Gaussian–exponent type, can be found in [4]. In the present study, attention is given primarily to α-cluster-type nuclei with $A > 40$, which require further development of the SU_3-invariant density-matrix-evaluation technique [5], as well as a detailed study of the classification of SU_3 states [6].

The results presented here for α-cluster-type nuclei with $4 \leq A \leq 80$ include binding energies and

*This article was submitted by the authors in English.

[1)]Institute of Theoretical Physics and Astronomy, Vilnius, Lithuania.

[2)]Instituto de Fisica Teorica, Universidade Estadual Paulista, Sao Paulo, Brasil.

**e-mail: T.ijberzins@latnet.lv

root-mean-square radii $\langle r^2\rangle^{1/2}$. The values calculated within the SRDM are compared with their experimental counterparts and with the radii calculated by using other model approaches.

2. THE SRDM FOR α-CLUSTER-TYPE NUCLEI

The SRDM Hamiltonian for α-cluster-type nuclei has the form (see, e.g., [4, 7])

$$H_{\rm SRDM} = H_{\rm kin} + H_e^{\rm coll} + H_c^{\rm coll} + H_e^a + H_c^a, \quad (4)$$

where separate terms denote the kinetic energy (kin) and the collective (coll) and anticollective (a) terms of the Coulomb (e) and central (c) NN interaction. Combining all expressions for particular terms of the SRDM Hamiltonian (4) (for details, see [4]), one can obtain the following final expression for the SRDM matrix elements in terms of Wigner supermultiplet basis functions:

$$\begin{aligned}
&\frac{E_{\rm kin}}{2}\left(B^{(\lambda\mu)L}_{KK'}+1\right)+\frac{e^2}{8}\sqrt{\nu_A}A(A-2) \quad (5)\\
&\times E^{\rm coll}_{e\rm W}(KL,K'L)+C_1\left[\frac{3A(A+4)}{16}\right.\\
&\left.\times E^{\rm coll}_{c\rm W}(KL,K'L)+E_c^{+a}\right]\\
&+C_2\left[\frac{5A(A-4)}{16}E^{\rm coll}_{c\rm W}(KL,K'L)+E_c^{-a}\right]\\
&+\frac{e^2}{6}\left[E_e^{+a}+\frac{9}{5}E_e^{-a}\right]-EB^{(\lambda\mu)L}_{KK'}=0.
\end{aligned}$$

In Eq. (5),

$$E_{\rm kin} = 20.7357\nu_A\left(E_0+(3A-1)/2)\right)[\text{MeV}] \quad (6)$$

is the kinetic-energy term, in which ν_A is the oscillator frequency parameter

$$\nu_A = \frac{1}{r_\psi^2} = \frac{5(E_0+3(A-1)/2)}{3r_0^2A^{5/3}}, \quad (7)$$

where r_0 is the nuclear-radius parameter appearing in the well-known expression $R = r_0A^{1/3}$ for the nuclear radius.

The collective submatrix elements of the orbital operators for the Wigner interaction are given by

$$\begin{aligned}
&E^{\rm coll}_{c,e\rm W}(KL,K'L) \quad (8)\\
&=\sum_{\varepsilon=0}^{E_1} I^{r_\psi}_{\varepsilon\varepsilon}(V^c_{\rm W},V^e_{\rm W})Q^{[E_1,E_2,E_3],\rm coll}_{\varepsilon\varepsilon,\rm W}(KL,K'L),
\end{aligned}$$

where $Q^{[E_1,E_2,E_3]\rm coll}_{\varepsilon\varepsilon,\rm W}(KL,K'L)$ denotes the collective (U_{A-1}-invariant) density matrices in a compact form and $I^{r_\psi}_{\varepsilon\varepsilon}(V^c_{\rm W},V^e_{\rm W})$ are the Talmi integrals of the central ($V^c_{\rm W}$) or the Coulomb ($V^e_{\rm W}$) interaction. Some details concerning the collective density matrices are given in [4], and the technique for calculating them is described, e.g., in [8].

In Eq. (5), $E^{\pm a}_{c,e}$ denotes the anticollective (SU_3-invariant) orbital matrix elements of the central (c) and Coulomb (e) interactions:

$$E^{\pm a}_{c,e} = \left(\mathcal{E}^{[00]}_{\rm W} \pm \mathcal{E}^{[00]}_{\rm M}\right)/2. \quad (9)$$

The anticollective Wigner and Majorana energy submatrix elements $\mathcal{E}^{[00]}_{\rm W,M}$ are given by

$$\begin{aligned}
\mathcal{E}^{[00]}_{\rm W} &= \sum_\varepsilon I_{\varepsilon[00]}Q_{\varepsilon[00]}, \quad (10)\\
\mathcal{E}^{[00]}_{\rm M} &= \sum_\varepsilon (-1)^\varepsilon I_{\varepsilon[00]}Q_{\varepsilon[00]},
\end{aligned}$$

where $I_{\varepsilon[00]}$ are the SU_3-averaged interaction integrals

$$\begin{aligned}
I_{\varepsilon[00]} &= \frac{1}{d_\varepsilon}\sum_l (2l+1)I_{\varepsilon l}, \quad (11)\\
I_{\varepsilon l} &= \int_0^\infty r^2 dr R_{\varepsilon l}(r)V(r)R_{\varepsilon l}(r),
\end{aligned}$$

with $d_\varepsilon = (\varepsilon+1)(\varepsilon+2)/2$. The interaction integrals $I_{\varepsilon l}$ in turn can be reduced to the Talmi integrals $I_{\varepsilon\varepsilon}$ (see, e.g., [3, 7]).

The quantities $Q_{\varepsilon[00]}$ in Eq. (10) are the components of the SU_3-invariant density matrix. The exact expressions for the SU_3-invariant density matrix are known as yet only for $\varepsilon_0 = 0, 1, 2$ (see [9, 10]), which allows one to perform SRDM calculations for nuclei with $A \le 40$. In [11], approximate formulas were proposed for use in nuclei with $A > 40$. We reevaluated these approximate expressions in order to correct some mistakes and used them for SRDM calculations of some α-cluster-type nuclei with $44 \le A \le 60$ in [7]. Later, we revisited this problem in [5] and showed that new relationships between quantities forming Q'_εs can be evaluated, which allows one to obtain an improved approximation for the SU_3-invariant density matrices when $\varepsilon_0 > 2$.

The Talmi integrals appearing in the collective and anticollective energy terms are defined in terms of unknotted three-dimensional harmonic-oscillator radial wave functions as

$$\begin{aligned}
&I^{r_\psi}_{\varepsilon\varepsilon}(V_{\rm W,M,B,H}) \quad (12)\\
&= I^{r_\psi}_{\varepsilon\varepsilon,\varepsilon\varepsilon}\left(V_{\rm W,M,B,H}\left(\frac{r_\psi}{r_p}\sqrt{2}\rho_a\right)\right)
\end{aligned}$$

Table 1. SRDM ground-state configurations for α-cluster-type nuclei

Nuclei	ε_0	$[f]$	$[E_1, E_2, E_3]$	E_0	$(\lambda\mu)$	K
^{4}He	0	[4]	[0, 0, 0]	0	(0, 0)	0
^{8}Be	1	$[4^2]$	[4, 0, 0]	4	(4, 0)	0
^{12}C		$[4^3]$	[4, 4, 0]	8	(0, 4)	0
^{16}O		$[4^4]$	[4, 4, 4]	12	(0, 0)	0
^{20}Ne	2	$[4^5]$	[12, 4, 4]	20	(8, 0)	0
^{24}Mg		$[4^6]$	[16, 8, 4]	28	(8, 4)	0, 2, 4
^{28}Si		$[4^7]$	[16, 16, 4]	36	(0, 12)	0
^{32}S		$[4^8]$	[20, 16, 8]	44	(4, 8)	0, 2, 4
^{36}Ar		$[4^9]$	[20, 20, 12]	52	(0, 8)	0
^{40}Ca		$[4^{10}]$	[20, 20, 20]	60	(0, 0)	0
^{44}Ti	3	$[4^{11}]$	[32, 20, 20]	72	(12, 0)	0
^{48}Cr		$[4^{12}]$	[40, 24, 20]	84	(16, 4)	0, 2, 4
^{52}Fe		$[4^{13}]$	[48, 24, 24]	96	(24, 0)	0
^{56}Ni		$[4^{14}]$	[52, 32, 24]	108	(20, 8)	0, 2, 4, 6, 8
^{60}Zn		$[4^{15}]$	[52, 44, 24]	120	(8, 20)	0, 2, 4, 6, 8
^{64}Ge		$[4^{16}]$	[56, 48, 28]	132	(8, 20)	0, 2, 4, 6, 8
^{68}Se		$[4^{17}]$	[56, 56, 32]	144	(0, 24)	0
^{72}Kr		$[4^{18}]$	[60, 56, 40]	156	(4, 16)	0, 2, 4
^{76}Sr		$[4^{19}]$	[60, 60, 48]	168	(0, 12)	0
^{80}Zr		$[4^{20}]$	[60, 60, 60]	180	(0, 0)	0
^{84}Mo	4	$[4^{21}]$	[76, 60, 60]	196	(16, 0)	0
^{88}Ru		$[4^{22}]$	[88, 64, 60]	212	(24, 4)	0, 2, 4
^{92}Pd		$[4^{23}]$	[100, 64, 64]	228	(36, 0)	0
^{96}Cd		$[4^{24}]$	[108, 72, 64]	244	(36, 8)	0, 2, 4, 6, 8
^{100}Sn		$[4^{25}]$	[116, 76, 68]	260	(40, 8)	0, 2, 4, 6, 8

$$= \int_0^\infty \rho_a^2 d\rho_a R^{r_\psi}_{\varepsilon\varepsilon}(\rho_a) V_{\mathrm{W,M,B,H}}\left(\frac{r_\psi}{r_p}\sqrt{2}\rho_a\right) R^{r_\psi}_{\varepsilon'\varepsilon'}(\rho_a),$$

where $\rho_a = |\rho_a|$.

The choice of the effective NN-interaction potential is limited by the consideration that its expression should not be overly complicated, so that one could evaluate Talmi integrals. However, it must reproduce experimentally known features of NN interaction (e.g., it must be able to describe a hard core at small distances, and its tail must not extend outside the size of the nucleus). For this purpose, we will use NN potentials having a radial dependence of the multipole–Gaussian–exponential type (see [12]); that is,

$$V(\rho_a) = V_0\left(\frac{r_\psi}{r_p}\sqrt{2}\rho_a\right)^q \times \exp\left[-z_2\left(\frac{r_\psi}{r_p}\sqrt{2}\rho_a\right)^2 - z_1\left(\frac{r_\psi}{r_p}\sqrt{2}\rho_a\right)^\beta\right], \quad (13)$$

where r_p is the scale parameter of the potential and V_0 is the potential depth. Usually, $\beta = 1$; the potential shape parameters z_1 and z_2 can assume values of 0, ± 1; and $q = -2, -1, 0, 1, 2, \ldots$. This choice of potential shape allows one to model a vast class of NN potentials, as well as the Coulomb interaction potential when $V_0 = 1$, $r_p = 1$, $z_2 = z_1 = 0$, and $q = -1$. The evaluation of Talmi integrals for the effective NN potential employed in our calculations is described, e.g., in [4, 7].

The model parameters C_1 and C_2 are defined by

$$C_1 = V_{c0}\,(c_{\mathrm{W}} + c_{\mathrm{M}})\,, \quad (14)$$
$$C_2 = V_{c0}\left[(c_{\mathrm{W}} - c_{\mathrm{M}}) + \frac{4}{5}\,(c_{\mathrm{B}} + c_{\mathrm{H}})\right].$$

These parameters are two independent combinations of central NN-interaction exchange constants (subjected to the normalization condition $c_{\mathrm{W}} + c_{\mathrm{M}} + c_{\mathrm{B}} - c_{\mathrm{H}} = -1$) together with the common NN-interaction potential depth V_{c0} under the assumption that the effective central NN-interaction potential V^c_{NN} has the same shape for the Wigner, Majorana, Bartlett, and Heisenberg forces.

The SRDM Hamiltonian matrices are given in the Elliott basis $|(\lambda\mu)KL\rangle$, and the quantities $B^{(\lambda\mu)L}_{KK'}$ appearing in Eq. (5) can be expressed [4] in terms of the overlap integrals $\langle(\lambda\mu)KL|(\lambda\mu)K'L\rangle$ of SU_3-basis functions. Applying the orthogonalization and diagonalization procedures to Eq. (5), we obtain eigenvalues (energies E) and mixing amplitudes of the SRDM Hamiltonian [Eq. (4)].

3. BINDING ENERGIES AND RADII OF α-CLUSTER-TYPE NUCLEI WITH $4 \le A \le 80$ WITHIN THE SRDM

α-Cluster-type nuclei with $A = 4, 8, \ldots$ are characterized by the Young pattern $[f] = [4^{A/4}, 0, 0, 0]$ and the spin–isospin pair $(S, T) = (0, 0)$. The SRDM quantum numbers for α-cluster-type nuclei with $A = 4, 8, \ldots, 100$ (experimental data on $Z = N$ nuclei are available now up to $^{100}_{50}\mathrm{Sn}_{50}$) are presented in Table 1, where the ground-state SU_3 configurations $[E_1, E_2, E_3]$ are given with $E_0 = E_1 + E_2 + E_3$. In the same table, one can also find the Elliott quantum numbers $(\lambda, \mu) = (E_1 - E_2, E_2 - E_3)$ and K, which

Table 2. Binding energies and radius parameters of α-cluster-type nuclei with $4 \le A \le 80$

Nuclei	E_b^{SRDM}, MeV	E_b^{exp}, MeV	$\langle r^2\rangle^{1/2}_{\mathrm{SRDM}}$, fm	$\langle r^2\rangle^{1/2}$, fm[b)]	$\langle r^2\rangle^{1/2}$, fm[c)]	$\langle r^2\rangle^{1/2}$, fm[e)]
^{4}He[a)]	−28.329	−28.296	1.641	1.603	1.674[d)]	
^{8}Be	−56.987	−56.500	2.068	2.117		
^{12}C[a)]	−92.217	−92.162	2.397	2.414	2.468	
^{16}O	−127.620	−127.619	2.638	2.642	2.693	
^{20}Ne	−160.068	−160.645	3.005	2.833	3.006	
^{24}Mg	−196.791	−198.257	3.760	3.000	3.057	
^{28}Si	−236.201	−236.537	3.094	3.150	3.123	
^{32}S	−269.982	−271.781	3.335	3.285	3.263	
^{36}Ar[a)]	−306.516	−306.716	3.267	3.411	3.390	
^{40}Ca	−342.060	−342.052	3.384	3.527	3.478	3.415
^{44}Ti	−375.151	−375.475	3.643			3.493
^{48}Cr	−409.173	−411.462	3.755			3.620
^{52}Fe	−447.537	−447.697	3.831			3.705
^{56}Ni	−479.940	−483.988	3.978			3.778
^{60}Zn	−512.799	−514.992	4.039			3.860
^{64}Ge	−543.902	−545.954	4.139			3.950
^{68}Se[a)]	−577.520	−576.398	4.189			4.021
^{72}Kr	−605.794	−607.083	4.269			4.108
^{76}Sr	−637.171	−638.081	4.347			4.188
^{80}Zr	−670.843	−669.789	4.422			4.238

[a)] ^{4}He and ^{8}Be, ^{12}C and ^{16}O, and ^{36}Ar and ^{40}Ca were calculated together, because they have too few states in their respective ground-state SU_3 configurations; ^{68}Se, ^{72}Kr, ^{76}Sr, and ^{80}Zr were calculated together because experimental data available for these isotopes are insufficient;

[b)] value deduced by using the approximation $r_0^2 = a + b/A + c/A^2$ with $a = 1.717856$ fm^2, $b = 2.459589$ fm^2, and $c = -10.119970$ fm^2;

[c)] experimental values taken from [17];

[d)] from [18];

[e)] values from the DMM calculations [19].

is the multiplicity index of the SO_3 irrep (labeled with L) in the chain $U_3 \supset SO_3$.

The SRDM parameters r_0, r_p, C_1, and C_2 were found from a fit to the experimental and calculated binding and excited-level energies separately for each nucleus, except the pairs ^{4}He and ^{8}Be, ^{12}C and ^{16}O, and ^{36}Ar and ^{40}Ca, which were calculated together because they have too few states in their respective ground-state SU_3 configurations, and also the group of the nuclei ^{68}Se, ^{72}Kr, ^{76}Sr, ^{80}Zr, which were calculated together because experimental data available for these isotopes are insufficient. The experimental values of the binding energies were taken from [13], while experimental information about the spectra of excitations were borrowed from the compilations in [14, 16]. For the shape parameters of the effective NN-interaction potential, we used the same values as in our earlier calculations for α-cluster-type nuclei with $4 \le A \le 40$ [4], i.e., $q = -1$, $z_1 = 4$, and $z_2 = 0$. Table 2 presents the results of our calculations for the nuclear binding energies E_b and the root-mean-square radii $\langle r^2\rangle^{1/2}$.

For α-cluster-type nuclei, the nuclear binding energy within the SRDM is calculated by the formula

$$E_b = E_{\mathrm{kin}} + E_e^a + E_c^a; \qquad (15)$$

i.e., it depends only on the kinetic and anticollective terms of the Hamiltonian in (4). Therefore, it is essential to have a very good SU_3-invariant density-matrix

approximation in order to obtain good agreement for the binding energies. Such approximate expressions were obtained in [5].

Another factor that greatly affects the calculated SRDM binding energies is the nuclear-radius parameter r_0 appearing in Eq. (7). This means that r_0 values obtained via a fit to the binding and excited-level energies would provide valuable information about the sizes of nuclei along the $Z = N$ line. In Table 2, one can find nuclear root-mean-square radii $\langle r^2\rangle^{1/2}$, which can be obtained from r_0 by using the expression [20, 21]

$$\langle r^2\rangle^{1/2} = \left[\left\langle \left| \frac{1}{A}\sum_{i=1}^{A} \mathbf{r}_i^2 \right| \right\rangle\right]^{1/2} = \sqrt{\frac{3}{5}} r_0 A^{1/3}, \quad (16)$$

where $\mathbf{r}_i$ is the position vector of the ith nucleon with respect to the nuclear center of mass. One can see that the values obtained from our SRDM calculations are in good agreement with known experimental values for $A \leq 40$, except for ^{24}Mg.

Unfortunately, we had no access to experimental data on the radii for nuclei with $A > 40$, though, in this region, one can compare our results with the results of the calculations that use, e.g., the dynamical microscopic model (DMM) [19]. These calculations were made with the deformed single-particle Nilsson potential involving pairing forces; i.e., the DMM is based on a completely different understanding of the nuclear structure than the SRDM. Nevertheless, the results of the SRDM and DMM calculations reveal the same trend for $\langle r^2\rangle^{1/2}$ values, although the SRDM values are somewhat higher.

In our earlier calculations of α-cluster-type nuclei [4], the nuclear-radius parameter r_0 was not included in the set of fitted parameters. We used the approximation

$$r_0^2 = a + b/A + c/A^2 \quad (17)$$

with $a = 1.717856$ fm^2, $b = 2.459589$ fm^2, and $c = -10.119970$ fm^2, which were obtained for p- and sd-shell nuclei in [20, 21] by using the experimental radius values for ^{4}He, ^{12}C, ^{16}O, and ^{40}Ca from [22]. The $\langle r^2\rangle^{1/2}$ values calculated by using r_0 values from this approximation are also given in Table 2. One can see that the $\langle r^2\rangle^{1/2}_{\mathrm{SRDM}}$ values are close to those calculated by using the approximation specified in (17). However, the application of this r_0 approximation in the SRDM calculations of the $\varepsilon_0 = 3$ shell nuclei ($44 \leq A \leq 80$) leads to considerable deviations from the experimental binding-energy values, since the calculated SRDM energies are very sensitive to slight changes in the r_0 values. Thus, we conclude that, in order to obtain an approximation analogous to Eq. (17), one would need new experimental data on the radii for nuclei of the $44 \leq A \leq 80$ region.

REFERENCES

1. V. Vanagas, *The Microscopic Nuclear Theory within the Framework of the Restricted Dynamics. Lecture Notes* (University of Toronto, Department of Physics, Toronto, 1977).
2. V. Vanagas, *The Microscopic Theory of the Collective Motion in Nuclei,* in *Group Theory and Its Applications in Physics* (American Inst. of Physics, New York, 1980).
3. V. V. Vanagas, *Algebraic Foundations of Microscopic Theory of Nuclei* (Nauka, Moscow, 1988).
4. J. Tambergs *et al.,* Int. J. Mod. Phys. E **6**, 341 (1997).
5. J. A. Castilho Alcarás *et al.,* in *Topics in Theoretical Physics. Festschrift for A. H. Zimermann* (Instituto de Fisica Teorica, UNESP, Sao Paulo, 1998), Vol. II, p. 251.
6. O. Katkevičius *et al.,* J. Phys. G **25**, 925 (1999).
7. J. A. Castilho Alcarás *et al.,* Braz. J. Phys. **27**, 425 (1997).
8. V. Vanagas and J. A. Castilho Alcarás, J. Math. Phys. (N.Y.) **33**, 1550 (1992).
9. D. M. Brink, Nucl. Phys. **40**, 596 (1963).
10. R. Kalinauskas and V. Vanagas, Litov. Fiz. Sb. **9**, 655 (1969).
11. L. Sabaliauskas, Litov. Fiz. Sb. **22**, 3 (1982).
12. V. Vanagas, Litov. Fiz. Sb. **29**, 3 (1989).
13. G. Audi and A. H. Wapstra, Nucl. Phys. A **595**, 409 (1995).
14. F. Ajzenberg-Selove, Nucl. Phys. A **490**, 1 (1988); **506**, 1 (1990); **523**, 1 (1991); **460**, 1 (1986); **475**, 1 (1987).
15. P. M. Endt, Nucl. Phys. A **521**, 1 (1990).
16. *Table of Isotopes,* Ed. by R. B. Firestone and V. S. Shirley (Wiley, New York, 1996, 8th ed.), Vol. 1.
17. G. Fricke *et al.,* At. Data Nucl. Data Tables **60**, 177 (1995).
18. R. C. Barrett and D. F. Jackson, *Nuclear Sizes and Structure* (Clarendon, Oxford, 1977).
19. B. Nerlo-Pomorska and Beate Mach, At. Data Nucl. Data Tables **60**, 287 (1995).
20. L. Sabaliauskas *et al.,* Preprint LAFI-117, Latvian Academy of Sciences, Physics Institute (Salaspils, 1987).
21. L. Sabaliauskas *et al.,* Izv. Akad. Nauk SSSR, Ser. Fiz. **52**, 838 (1988).
22. L. R. B. Elton, *Nuclear Sizes* (Oxford Univ. Press, Oxford, 1961).

Physics of Atomic Nuclei, Vol. 65, No. 4, 2002, pp. 725–730. From Yadernaya Fizika, Vol. 65, No. 4, 2002, pp. 758–763.

Cluster Research in Jyväskylä*

W. H. Trzaska**

Department of Physics, University of Jyväskylä, Jyväskylä, Finland

Received July 20, 2001

Abstract—A short overview of the ongoing nuclear-reaction program at the Department of Physics, University of Jyväskylä, is presented. Special emphasis is put on cluster phenomena investigated with the $K = 130$ heavy-ion cyclotron, such as measurements of alpha-resonance states, rainbow scattering, and some special features in fusion–fission reactions. Relevant developments in detection techniques are mentioned, and the outlook for the possible continuation of the nuclear-reaction program in Jyväskylä is given. © *2002 MAIK "Nauka/Interperiodica".*

1. INTRODUCTION

The accelerator Laboratory of the Department of Physics at the University of Jyväskylä (JYFL) is one of the few low-energy nuclear laboratories that was able to defy the stagnation all too evident, both in Europe and in the USA, throughout the 1990s. At the same time, when the funding to the other laboratories was being drastically cut, Jyväskylä built a new laboratory and a new heavy-ion cyclotron with a K value of 130[1)]. Undoubtedly, one of the key factors that have since promoted steady growth of the laboratory is the outstanding operation of the new accelerator. As early as in 1994, the delivered beam time reached the expected capacity of 4000 h annually. Ever since, this value has been surpassed by a wide margin, reaching, in 1999, the absolute record of nearly 7500 h, of which only 275 h were spend for beam tuning and development. It should perhaps be recalled that a full calendar year has a total of about 8700 h. The quality of the accelerated beams has helped to attract new collaborators and start new research projects, often connected with the installation at JYFL of new experimental equipment generating further proposals. The position of Jyväskylä as one of the main European centers for nuclear physics was recognized back in 1995 by the award of the status of a Large Scale Facility under the Training and Mobility of the Researchers program of the European Commission. Recently, JYFL received an extension of this status (under a slightly different name) and was nominated by the Academy of Finland as a Center of Excellence in Nuclear and Material Physics.

About 15% of the beam time—that is, 1000 h annually—is devoted to nuclear-reaction (NR) studies. The NR program currently involves about 50 scientists from 14 institutes in eight countries. The two main experimental setups are the High Efficiency Neutron Detection System (HENDES) and a large scattering chamber (LSC). HENDES makes it possible to perform coincident measurements (with fission fragments) of neutrons and light charged particles (LCP). Fission fragments (FF) are detected in two (or more) arms of a position-sensitive time-of-flight (TOF) spectrometer that can be equipped with ancillary semiconductor detectors for measuring FF energies and for detecting LCP.

2. RESONANCE SCATTERING IN INVERSE KINEMATICS

Measurement of the resonance scattering of alpha particles is a well-known method for investigating alpha-cluster states. For many years, tandem accelerators have been widely used for this purpose. However, tandem beams have relatively low maximum energies because of a limited high voltage at the terminal, making them useless for studies of high-lying cluster states. Even at lower energies, many energy points are needed to cover, step-by-step, the full region of interest. Of course, high-energy alpha particles can easily be obtained from a cyclotron. However, the energy spread of a cyclotron beam is very broad in relation to a typical resonance width. Also, it is much more difficult and time-consuming to change the beam energy on a cyclotron in relation to a tandem. These two factors make cyclotrons a poor choice for resonance-scattering measurements. Fortunately, all these problems can be overcome by

*This article was submitted by the author in English.

**e-mail: trzaska@phys.jyu.fi

1)To estimate the maximum available beam energy (in MeV), one should multiply the K value by the square of the charge state of the injected ion and divide by its mass (in u). See also [www.phys.jyu.fi] for further references.

1063-7788/02/6504-0725$22.00

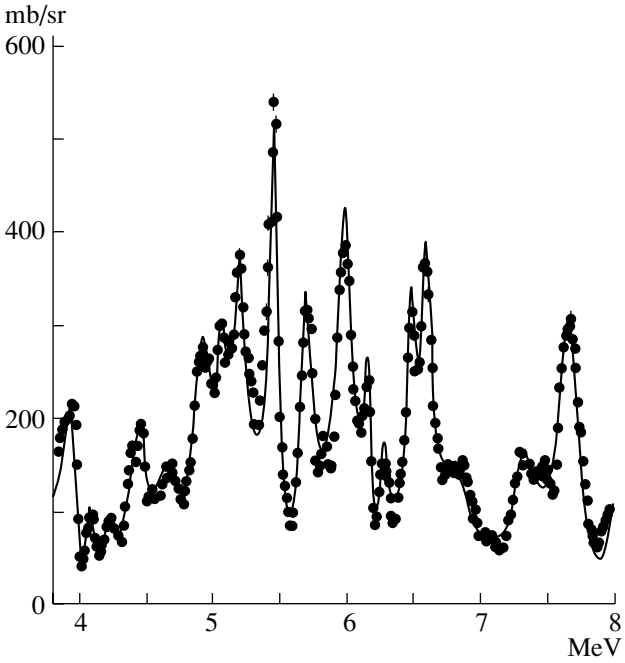

Fig. 1. Preliminary results of an R-matrix analysis of elastic scattering of ^{18}O on ^{4}He at 0° in the laboratory frame (180° in the c.m. frame) for the excitation-energy interval 13.5–17.7 MeV. The scale on the y axis indicates cross sections (in mb/sr). The x-axis scale shows alpha energy (in MeV) that differs from the excitation energy by the Q value of 9.67 MeV.

the new method of elastic resonance scattering on a thick target in inverse kinematics. This method [1, 2] was developed by a Moscow–Turku–Jyväskylä collaboration and was further refined to allow separation of elastic and inelastic scattering events by using the TOF technique. Recent experiments include scattering of 94-MeV ^{12}C, 135-MeV ^{16}O, 110-MeV ^{18}O, 150-MeV ^{20}Ne, and 160-MeV ^{32,34}S beams on ^{4}He. These beams entered the LSC, filled with a helium gas, via a thin Havar window. During the passage through the gas, heavy ions (HI), constantly loosing energy (mostly through interaction with atomic electrons), could, at any point of the trajectory, scatter on He nuclei. These recoil alpha particles were detected by silicon detectors placed inside the gas in the forward direction. Naturally, 0° in the laboratory frame corresponds to 180° in the c.m. frame. The gas pressure of helium was adjusted so that HI beams would stop completely before reaching the detectors. The energy of scattered alpha particles was recorded together with the arrival time measured with respect to a radio frequency (RF) pulse from the cyclotron. The energy of a recoil alpha particle at 0° (E_α) is $E_\alpha = 4m_\alpha M E_0/(m_\alpha + M)^2$, where m_α and M are the masses of alpha particles and of the incident HI and E_0 is the energy of HI at the time of scattering. Since the recoil velocity of the alpha particle is nearly twice as great as that of HI, inelastic events producing alpha particles of certain energy will arrive earlier than alpha particles having exactly the same energy but originating from an elastic process that obviously occurred somewhere closer to the detector. In the measurements, we could reach a time resolution of FWHM = 0.5 ns. This resolution was possible only after special tuning of the cyclotron.

Measurements of resonance scattering do not have to be restricted to 180° in the c.m. frame. On the contrary, only with angular distributions can one determine spin and parity values for alpha-cluster states in the "target + alpha" nuclei. Lately, such measurements were performed for the resonance scattering of ^{18}O ions on a thick helium target at bombarding energies of 80 and 120 MeV. These data are expected to yield new information about the spins and parities of alpha-cluster states in ^{22}Ne in the excitation energy region 10–25 MeV. Figure 1 illustrates the preliminary results of an R-matrix analysis of the elastic scattering of ^{18}O on ^{4}He at 0° in the laboratory frame (180° in the c.m. frame) for the excitation energy interval 13.5–17.7 MeV. The measurements were later repeated by using methane instead of He as a thick gas target and by recording scattered protons instead of alpha particles. These measurements should bring new evidence for the relationship between single-particle and cluster degrees of nuclear motion and pave the way for studying analogous states of very neutron-rich nuclei at radioactive-beam facilities.

3. RAINBOW SCATTERING

Elastic scattering, despite its apparent simplicity as the most fundamental nuclear reaction, continues to surprise us with the complexity of nuclear interactions it reveals. This is perhaps especially so in the region where the cross section drops well below the Rutherford value and where regular diffractive patterns diminish sufficiently to allow the refractive effects to show up. These refractive, or rainbow, phenomena provide important information about the HI interaction potential and deliver valuable data on the character of the optical potential, advancing us toward the goal of determining the equation of state of cold nuclear matter.

Since rainbow effects become visible at relatively large scattering angles, where cross sections are already two or three orders of magnitude below the Rutherford values, rainbow-scattering measurements present a major experimental challenge. They require not only the best possible equipment but also sufficient beam intensities and long irradiation times. The last point is perhaps the most restricting

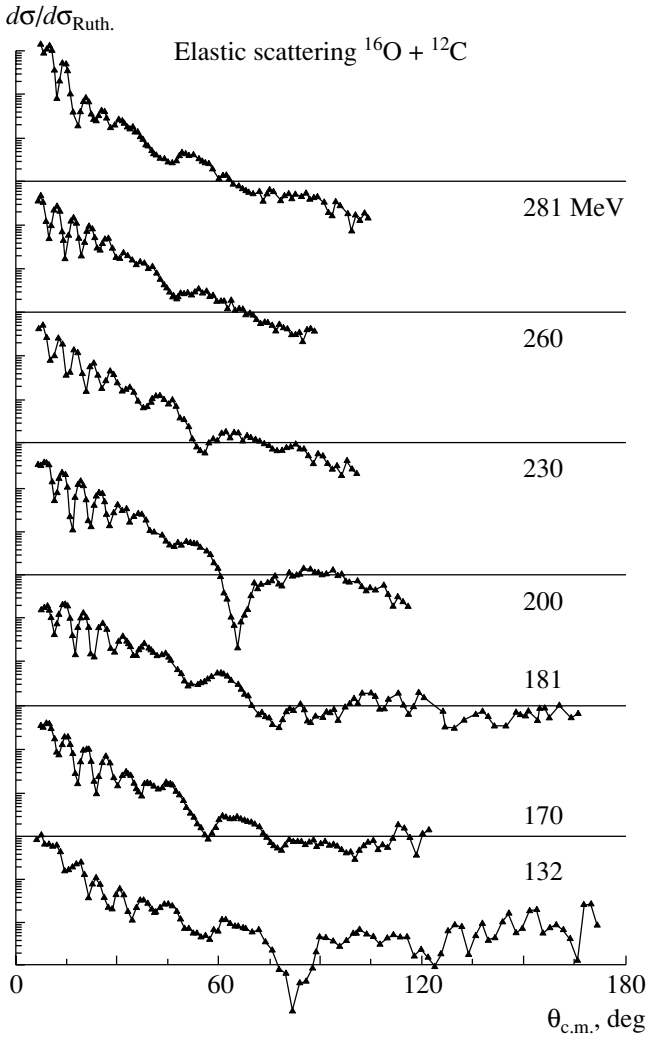

Fig. 2. Results of recent experimental work by the nuclear-rainbow collaboration. These curves and, especially, the large primary Airy minimum around 65° in 200-MeV data are among the most pronounced rainbow-scattering effects that have ever been observed.

requirement since, in Jyväskylä, this demand exceeds the available beam time by a factor of greater than 2. Therefore, it should be mentioned that the only way to collect impressive data, like those shown in Fig. 2, was to scarify several Christmas, New Year, and summer holidays.

Until recently, the most impressive manifestation of rainbow effects came from elastic scattering of symmetric systems, $^{12}C + ^{12}C$ and especially $^{16}O + ^{16}O$. Therefore, it was not at all obvious that one might expect more pronounced effects from the scattering of asymmetric systems such as $^{16}O + ^{12}C$. Figure 2 shows part of the recently published [3, 4] data from the Jyväskylä measurements. These curves and, especially, the impressive large primary Airy minimum around 65° in 200-MeV data are perhaps the most pronounced manifestation of rainbow-scattering effects that has ever been observed.

Equally interesting are precise measurements of elastic scattering on heavy targets, since they mimic the exit channel for the cluster radioactivity of superheavy nuclei. Unfortunately, the majority of the discovered clusters—for instance, ^{14}C—are radioactive themselves. This creates obvious experimental problems with the availability and maximum intensity of such beams. An important exception is ^{22}Ne. Recently, the first run of measurements of elastic $^{22}Ne + ^{208}Pb$ scattering was performed at JYFL. The preliminary angular distribution is shown in Fig. 3. As is obvious, the measured cross sections are three orders of magnitude smaller than the Rutherford values. Further analysis is needed to find whether (or not) this data would lead to determination of

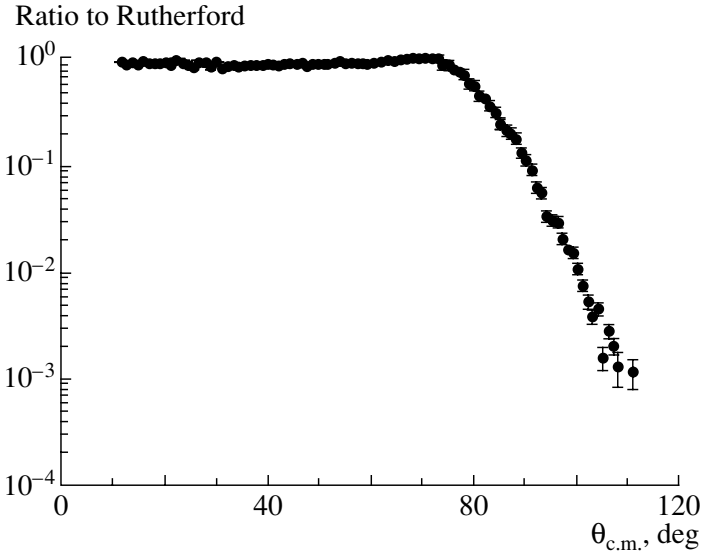

Fig. 3. Preliminary results from elastic ^{22}Ne $+^{208}$ Pb scattering at $E_{Ne} = 125$ MeV.

the shape and height of the barrier for ^{22}Ne cluster radioactivity.

4. FUSION–FISSION

Fusion-fission processes provide a good insight into a variety of fundamental questions of nuclear physics. They range from the fission dynamics of hot rotating nuclear matter to applied questions associated with the development of radioactive-beam facilities. Among the wide scope of problems studied at JYFL by the HENDES collaboration,[2)] the formation and decay of superheavy nuclear systems is perhaps the closest to the conference topic.

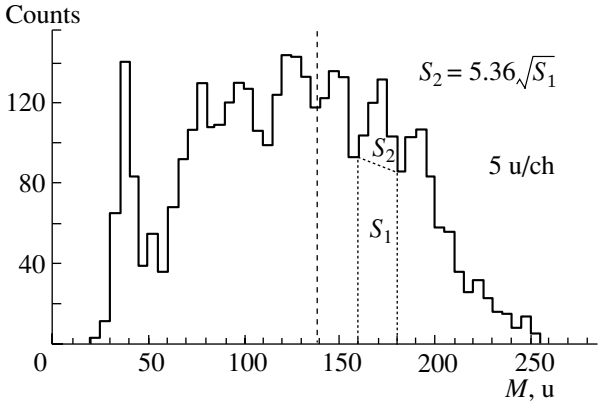

Fig. 4. Pronounced fine structure observed in the fragment-mass spectrum in the reaction ^{238}U $+^{40}$ Ar at $E_{Ar} = 243$ MeV.

Coulomb repulsion is the main obstacle in the formation of cold compound nuclei by means of fusion. To overcome the electrostatic barrier, one has to increase the bombarding energy. Unfortunately, this also leads to higher excitation energies, sharply reducing the survivability of the compound system. Finding the optimum between these opposite effects is the main challenge of superheavy research. There is, however, another approach that has been successfully applied in recent experiments at JYFL, yielding some very interesting results on shell effects in superheavy nuclei.

Fission is the main decay channel for a hot, heavy compound nucleus. Usually, fission is preceded by particle emission, mostly neutron emission, with a multiplicity dependent on the excitation energy. The relation works in the opposite direction as well: the greater the number of emitted prescission particles, the cooler the compound system. As the excitation energy decreases, shell effects come into play, affecting the decay probabilities and the FF mass distributions. Therefore, an experimental setup making it possible to detect prescission neutrons in coincidence with FFs should be a good tool for studying such effects. Figure 4 shows an interesting result obtained in this way in a recent HENDES experiment. The displayed FF mass spectrum for the ^{238}U + ^{40}Ar reaction at $E_{Ar} = 243$ MeV shows a pronounced fine structure (FS) instead of the smooth Gaussian-like shape expected from this reaction. The spectrum was constructed by requiring coincidence with neutrons emitted at backward angles. Such neutrons originate almost exclusively from prescission processes since the detection geometry strongly favors forward emission of postscission particles. The central dashed

[2)] A full list of the main publications by the HENDES collaboration is presented in [1].

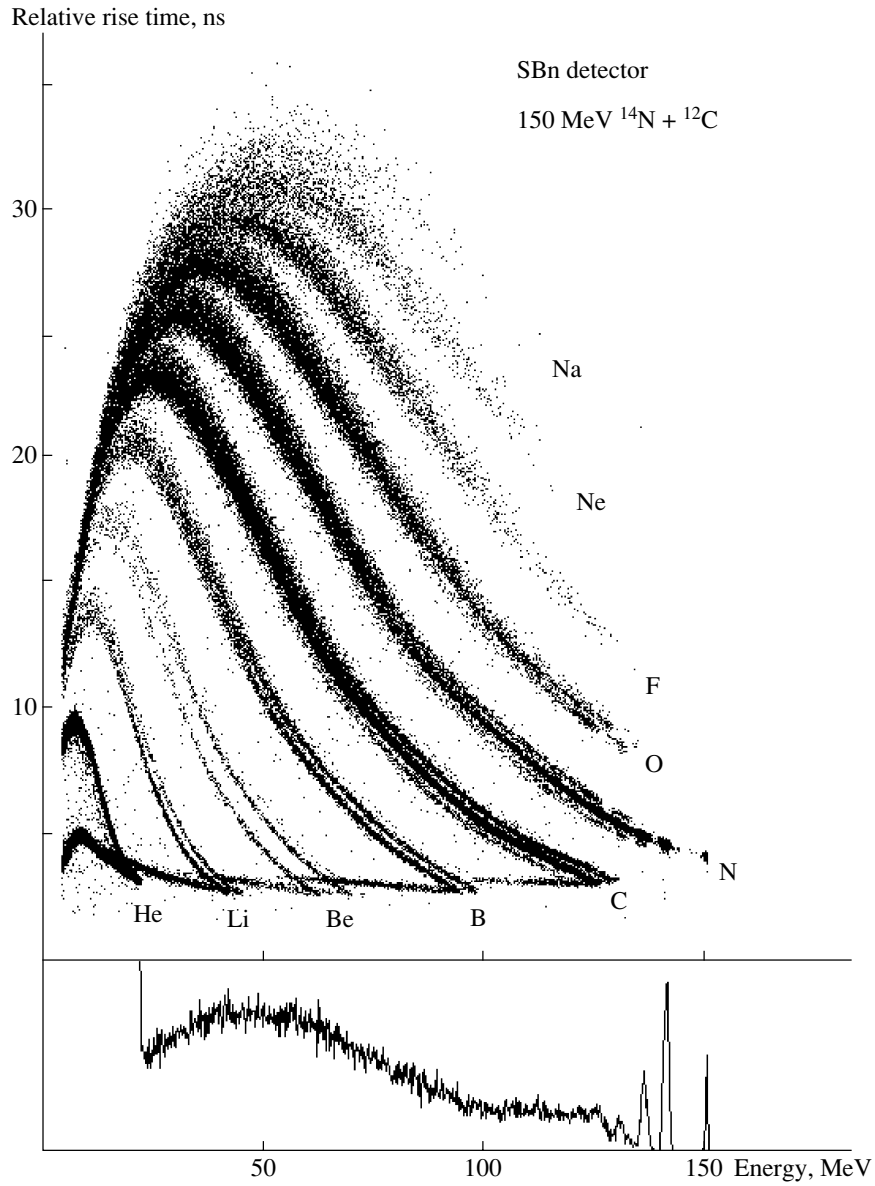

Fig. 5. Example of rise-time-based particle identification obtained with improved fast electronics and a surface-barrier detector made from 250-μm-thick NTD silicon. The energy projection of the $2D$ picture is shown below. A sharp peak at 150 MeV comes from trace amounts of heavy metals in the carbon target. Other peaks are broadened because of kinematics. The time scale of the 2D plot is only relative because zero value of the measured rise time was not precisely determined.

line indicates one-half of the mass of the compound system (^{238}U + ^{40} Ar). The positions of the FS peaks, each with a statistical significance of about 5σ, agree closely with the expected masses of spherical and deformed magic nuclei (clusters) of Ni, Ge, Zr, Sn, and Sr. The peaks have corresponding partners in the other half of the mass spectrum, even though the spectrum has not been forcefully symmetrized, as is the standard practice in the analysis. A highly suppressed reminiscence of beamlike particles at masses around 40 can still be visible.

The next run of experiments is scheduled for December 2000. They should finally determine whether the observed FS is indeed a manifestation of strong shell effects in a cooled compound nucleus. The present setup should allow an order of magnitude improvement in statistics in a one-week-long, dedicated experiment. Such a large margin should be well above any possible instrumental or statistical errors. A positive answer would open the doors for systematic studies at HENDES of these new fascinating phenomena, including supposed tripartition into a large, nearly stationary residue and two heavy, magic clusters.

5. DETECTOR RESEARCH

It is impossible to overstate the importance of proper experimental tools in basic research. One can even risk a general statement, well backed up by actual progress in modern nuclear physics, that it is new detection techniques and instrument development that push the cutting edge of science. Being well aware of that fact, the NR group devotes considerable effort to the refinement and development of its experimental arsenal: detectors, custom-designed electronics, data acquisition, etc. One of the most successful examples, which is, at the same time, relevant to a broader physics community, is our breakthrough in pulse-shape-based particle identification with a silicon detector [5].

The principle of using rise-time-based analysis in a single-detector particle identification is not new, but it has always been hampered by serious limitations, mostly by the degradation of timing properties and of the energy resolution to achieve a useful particle separation. We have managed to overcome these two major stumbling blocks of the method. The key elements of our success have been the following: (i) extracting rise-time information as early as at the preamplifier level; (ii) optimization of fast electronics; (iii) use of highly homogeneous detectors, polished on both sides, with thin front- and back-dead layers; and (iv) maintaining a high bias at the detectors.

As a result, our detectors did not exhibit any major resolution loss despite irradiation from the reverse side. The full dynamical range of a rise-time separation was below 35 ns. We have reached a discrimination threshold at a level equivalent to the 20-μm range in silicon. Neighboring elements ($\Delta Z = 1$) could be fully resolved down to energies corresponding to at least 30 μm of range in silicon, and individual isotopes ($\Delta A = 1$) could be fully resolved down to the effective range of about 100 μm (see Fig. 5). For any given isotope and energy value, the time resolution of the total drift time was very good. For instance, it was only 214 ps (FWHM) for ^{14}N at 120 MeV.

Further work is in progress, but, even now, our method is being successfully applied to ternary-fission studies at ILL Grenoble and in rainbow-scattering measurements at JYFL. Keen interest in our method has also been shown by the EURISOL community and by many individual researchers.

ACKNOWLEDGMENTS

This review is based on immense work contributed by about 50 scientists, students, and engineers from 14 institutes in eight countries. They all deserve full credit for the excellent results the collaboration was able to achieve. The resonance-scattering group was led by V. Goldberg and T. Lönnroth with considerable input by M. Brenner, K.-M. Källmann, G. Rogatchev, and R. Wolski. The rainbow-scattering project was pursued by A. Ogloblin with experiments lead by Y. Glukhov and A. Dem'yanova and with several theorists working on interpretation of the results. Most of the fusion–fission work is being carried out by the St. Petersburg–Dubna collaboration originally initiated by V. Rubchenya and Yu. Penionzhkevich with active support from A. Alexandrov, I. Alkhazov, S. Khlebnikov, A.V. Kuznetsov, and Yu.G. Sobolev. The quest for particularities in FF mass distributions has been championed by Yu. Pyatkov, who is also a member of the fusion–fission group. M. Mutterer contributes to all of the above mentioned projects not only thanks to his expertise in physics but also thanks to his valuable knowledge of specialized detectors and electronics. He is also a key person in work on pulse-shape-based particle identification. The success of our complex experiments rests, to a great extent, on the efforts of J. von Kalben, V. Lyapin, and G. Tiurin—electronic engineers of the collaboration. The lion share of all the experimental and data-analysis work was carried out by students as part of their Doctoral and Master thesis: A. Evsenin, V. Maslov, O. Osetrov, M. Rachev, Z. Radivijevic, M. Rojkov, B. Skorodumov, S. Torilov, and D. Vakhtin. Last but certainly not least, the strong support from J. Äystö and R. Julin—the directors of the Accelerator Laboratory—is gratefully acknowledged.

This work was supported by the University of Jyväskylä, Finnish Academy of Science, and the Access to Large-Scale Facility Program under the Training and Mobility of Researchers Program of the European Union. This work was supported in part by the Academy of Finland under the Finnish Center of Excellence Program 2000–2005 (project no. 44875, Nuclear and Condenced Matter Physics Program at JYFL).

REFERENCES

1. V. Z. Goldberg, V. I. Dukhanov, A. E. Pakhomov, *et al.*, Yad. Fiz. **60**, 1186 (1997) [Phys. At. Nucl. **60**, 1061 (1997)].
2. K. Markenroth, L. Axelsson, S. Baxter, *et al.*, Phys. Rev. C **62**, 034308 (2000).
3. A. A. Ogloblin, Yu. A. Glukhov, W. H. Trzaska, *et al.*, Phys. Rev. C **62**, 044601 (2000).
4. S. A. Goncharov, Yu. A. Glukhov, A. S. Dem'yanova, *et al.*, Preprint INP MSU 2000-26/630 (Inst. of Nuclear Physics, Moscow State Univ., Moscow, 2000).
5. M. Mutterer, W. H. Trzaska, G. P. Turin, *et al.*, IEEE Trans. Nucl. Sci. **47**, 756 (2000).

Physics of Atomic Nuclei, Vol. 65, No. 4, 2002, pp. 731–735. From Yadernaya Fizika, Vol. 65, No. 4, 2002, pp. 764–768.

Semiclassical and Statistical Description of the Nuclear Fermi Liquid Drop*

X. Viñas**, **P. Schuck**[1)], **M. Farine**[2)], **M. Durand**[1)], **and M. Centelles**

Departament d'Estructura i Constituents de la Matèria, Facultat de Física, Universitat de Barcelona, Spain

Received July 20, 2001

Abstract—Some basic concepts of the statistical description of the nuclear Fermi liquid drop are discussed. The key quantity, the Wigner distribution function corresponding to the one-body density matrix in phase space, is analyzed. Its asymptotic expansion in powers of $\hbar$, which leads to the Thomas–Fermi approach, is revisited. A survey of nuclear properties whose average value can be derived in Thomas–Fermi approximation is pointed out. © *2002 MAIK "Nauka/Interperiodica".*

1. INTRODUCTION

One of the basic problems of a finite quantum system composed of a set of interacting fermions (nuclei, atoms, helium, metallic clusters, etc.) is the determination of the ground-state energy and density. This is in general a complicated many-body problem. In the case of nuclei, an additional difficulty comes from the fact that the basic ingredient, the nuclear force, is still under debate. Even in the simplest mean field approximation, the calculation of the binding energy of finite nuclei can present serious technical difficulties. Therefore, very early statistical or semiclassical approaches have been worked out to describe the ground-state energy of the atomic nucleus. The simplest example of these approaches is the semiempirical mass formula [1], which contains a smooth part represented by the Bethe–Weizsäcker liquid drop formula and a shell correction (quantal effects) that is small ($\sim 1\%$) as compared to the smooth part.

The perturbative treatment of the shell correction energy in a Fermi system is justified, from the theoretical point of view, by the Strutinsky energy theorem [2], which states that the total quantal energy can be split in two parts. The largest part varies smoothly with the number of particles in the same way as the mass formula energy. The other part corresponds to the shell correction: it is small as compared to the smooth contribution and has a quantal origin and a nonsmooth behavior. In practice, computing the smooth part of the energy with the Strutinsky procedure can be as complicated as the full quantal calculation. To avoid this difficulty, semiclassical methods like the Thomas–Fermi (TF) approach, which is well known from its successful applications in atomic physics, have been developed. Like the droplet model or the Strutinsky calculations, these methods smooth out the quantal effects and estimate the average part of the Hartree–Fock energy. In this contribution, we want to outline some basic features of the statistical approach to the atomic nucleus.

2. BASIC THEORY

The Wigner transform of an operator [3] defines its representation in phase space, which is more suitable for semiclassical approximations. One key quantity in the TF theory is the Wigner transform of the one-body density matrix $\hat{\rho} = \Theta(\mu - \hat{H})$, where $\hat{H}$ is the single-particle Hamiltonian ($\hat{H}\varphi_\alpha = \varepsilon_\alpha \varphi_\alpha$) and μ is the chemical potential. It is defined by

$$f(\mathbf{r}, \mathbf{p}) = \int d\mathbf{s} e^{-i\mathbf{p}\cdot\mathbf{s}/\hbar} \langle \mathbf{r} + \mathbf{s}/2 | \hat{\rho} | \mathbf{r} - \mathbf{s}/2 \rangle, \quad (1)$$

where $\mathbf{r} = (\mathbf{r}_1 + \mathbf{r}_2)/2$ and $\mathbf{s} = \mathbf{r}_1 - \mathbf{r}_2$ are the center-of-mass and relative coordinates, respectively, and $\mathbf{p}$ is the momentum. The inverse operation to (1) is

$$\rho(\mathbf{r}_1, \mathbf{r}_2) = \frac{1}{(2\pi\hbar)^3} \int d\mathbf{p} e^{-i\mathbf{p}\cdot\mathbf{s}/\hbar} f(\mathbf{r}, \mathbf{p}). \quad (2)$$

The previous definitions can be generalized to any arbitrary single-particle hermitian operator $\hat{O}$. The expectation value of $\hat{O}$ is given by the trace

$$\langle \hat{O} \rangle = \mathrm{tr}[\hat{\rho}\hat{O}] \quad (3)$$

*This article was submitted by the authors in English.

[1)]Institut des Sciences Nucléaires, Université Joseph Fourier, Grenoble, France.

[2)]'Ecole Navale, Brest Naval, France.

**E-mail:xavier@ecm.ub.es

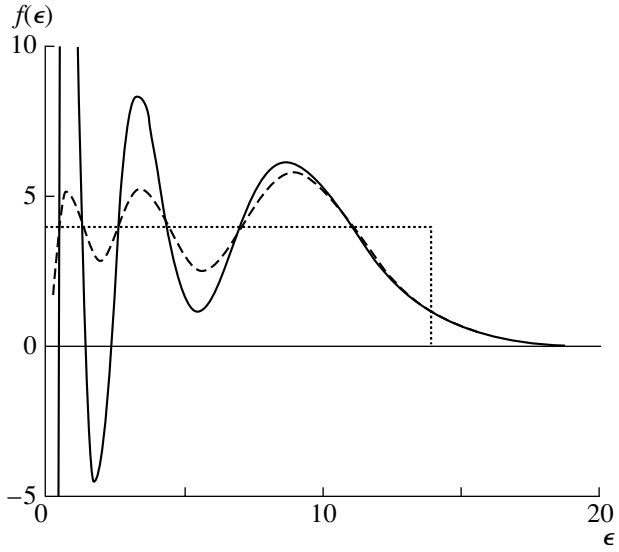

Fig. 1. Wigner function for a system of $A = 224$ nucleons bounded by a spherical harmonic oscillator well. Solid curve: the exact $f(\mathbf{r}, \mathbf{p})$, Eq. (5); dashed curve: the Strutinsky averaged result; dotted line: the lowest-order Thomas–Fermi approximation.

$$= \frac{1}{(2\pi\hbar)^3} \iint d\mathbf{r} d\mathbf{p} O_{\mathrm{W}}(\mathbf{r}, \mathbf{p}) f(\mathbf{r}, \mathbf{p}),$$

where $O_{\mathrm{W}}(\mathbf{r}, \mathbf{p})$ is the Wigner transform of $\hat{O}$ following Eq. (1). In particular, the number of particles A which fixes the chemical potential μ reads

$$A = \mathrm{tr}[\hat{\rho}] = \frac{4}{(2\pi\hbar)^3} \iint d\mathbf{r} d\mathbf{p} f(\mathbf{r}, \mathbf{p}), \qquad (4)$$

where a spin–isospin degeneracy of 4 has been assumed.

Let us now discuss some of the most salient features of the Wigner function $f(\mathbf{r}, \mathbf{p})$ for the simple but illustrative case of a spherical harmonic oscillator.

3. PROPERTIES OF THE WIGNER DISTRIBUTION FUNCTION

For closed-shell nuclei, the Wigner function corresponding to nucleons in a spherical harmonic oscillator potential is given by [4, 5]

$$f(\mathbf{r}, \mathbf{p}) = 8 \sum_{n=0}^{N} (-1)^n L_n^2 (4H_{\mathrm{W}}/\hbar\omega) e^{-2H_{\mathrm{W}}/\hbar\omega}. \quad (5)$$

The index n runs over the N occupied shells, the $L_n^{\alpha}(x)$ are associated Laguerre polynomials, and

$$H_{\mathrm{W}} = \frac{p^2}{2m} + \frac{1}{2} m\omega^2 r^2 \qquad (6)$$

is the classical Hamiltonian. For this special case, the dependence of $f(\mathbf{r}, \mathbf{p})$ on the six phase-space variables is lumped into one single variable, which is the classical energy. In the general case, $f(\mathbf{r}, \mathbf{p})$ will also depend on the direction of $\mathbf{r}$ and $\mathbf{p}$.

The Wigner function of the harmonic oscillator potential is represented in Fig. 1 as a function of the variable $\epsilon = 2H_{\mathrm{W}}/\hbar\omega$ for $A = 224$ nucleons, which means that six harmonic oscillator shells are filled. The solid curve represents Eq. (5): it displays six maxima and minima corresponding to the filled shells.

The dashed curve corresponds to the Strutinsky averaged Wigner function $\tilde{f}(\mathbf{r}, \mathbf{p})$. The Strutinsky averaging method [2] is a well-defined mathematical procedure to average out the shell effects, so that the dashed curve of the figure can be considered as the liquid drop part [1] of the phase-space distribution function. The figure shows that $\tilde{f}(\mathbf{r}, \mathbf{p})$ stays approximately constant and equal to 4 (due to the degeneracy) for $H_{\mathrm{W}} \leq \varepsilon_{\mathrm{F}}$, with ε_{F} being the Fermi energy. In the vicinity of ε_{F}, the averaged distribution function drops to zero within a characteristic domain of width δ. For nuclei at equilibrium, this width δ turns out to be much smaller than ε_{F}, in which case $\eta = \delta/\varepsilon_{\mathrm{F}}$ constitutes a small expansion parameter. Notice that due to (5), η depends on $\hbar$.

From Fig. 1 (and other examples with different potentials), one can see that the general shape of the distribution function is similar to that of Fermi function on top of which oscillations are built in the interior. This suggests derivation of the asymptotic $\hbar$ expansion of the Wigner function in analogy to what is done for the well-known low-temperature expansion in powers of T of the Fermi–Dirac function

$$F_T(\mu - \varepsilon) = \frac{1}{1 + \exp\left[(\varepsilon - \mu)/T\right]} \qquad (7)$$

(the Boltzmann constant has been put equal to 1). Under the condition $T/\varepsilon_{\mathrm{F}} \ll 1$, one derives the asymptotic formula [6]

$$F_T(\mu - \varepsilon) = \Theta(\mu - \varepsilon) + \frac{\pi^2}{6} T^2 \delta'(\mu - \varepsilon) \qquad (8)$$
$$+ \frac{7\pi^4}{360} T^4 \delta'''(\mu - \varepsilon) + \ldots,$$

known as Sommerfeld's low-temperature expansion.

The asymptotic expansion of $f(\mathbf{r}, \mathbf{p})$ in powers of $\hbar$ is derived from the so-called Wigner–Kirkwood expansion of the density matrix [3]. It can be obtained by formally expanding $f(\mathbf{r}, \mathbf{p}) = [\Theta(\mu - \hat{H})]_{\mathrm{W}}$ into a Taylor series about the classical Hamiltonian $H_{\mathrm{W}} = p^2/2m + V = [\hat{H}]_{\mathrm{W}}$, which reads

$$f(\mathbf{r}, \mathbf{p}) = \Theta(\mu - H_{\mathrm{W}}) - \frac{\hbar^2}{8m} \Delta V \delta'(\mu - H_{\mathrm{W}}) \qquad (9)$$

$$+\frac{\hbar^2}{24m}\left[(\boldsymbol{\nabla}V)^2+\frac{1}{m}(\mathbf{p}\cdot\boldsymbol{\nabla})^2V\right]\delta''(\mu-H_{\rm W})+\mathcal{O}(\hbar^4).$$

The lowest order or Thomas–Fermi approximation, i.e., the step function $\Theta(\mu-H_{\rm W})$, has been drawn in Fig. 1 for the harmonic oscillator. Usually, it is sufficient to stop the expansion at order $\hbar^2$, though extension to order $\hbar^4$ is possible. An important property of (9) is that it fulfils, order by order in $\hbar$, the idempotency property of the one-particle density matrix $\hat\rho^2=\hat\rho$ [7].

The analogy of the semiclassical expansion (9) with the low-temperature expansion (8) is manifest, even though the details are different. The Fermi–Dirac function (7) and the Wigner function [see example (5) for the latter] are nonanalytic in T and $\hbar$, respectively, thus, (8) and (9) are asymptotic expansions in powers of T and $\hbar$, respectively. In both cases, the derivatives of the step function Θ simulate the finite surface width. These derivatives of the step function in the expansion (9) of the Wigner function contain much information about the true quantal distribution.

To illustrate this point, we consider again the example of the harmonic oscillator. In this case, the semiclassical expansion (9) of the distribution function, as well as the exact distribution (5), depends on the classical $H_{\rm W}$ alone:

$$f(H_{\rm W})=\Theta(\mu-H_{\rm W})-\frac{3}{8}(\hbar\omega)^2\delta'(\mu-H_{\rm W}) \quad (10)$$
$$+\frac{1}{12}(\hbar\omega)^2H_{\rm W}\delta''(\mu-H_{\rm W})+\mathcal{O}(\hbar^4).$$

For this problem, $H_{\rm W}=p^2/2m+m\omega^2r^2/2=P^2+Q^2$ can be seen as the square of a radial component $\sqrt{P^2+Q^2}$ in polar coordinates with polar angle $\theta=\arctan(P/Q)$:

$$P=\frac{p}{\sqrt{2m}}=\sqrt{H_{\rm W}}\sin\theta, \quad (11)$$
$$Q=\sqrt{\frac{m\omega^2}{2}}r=\sqrt{H_{\rm W}}\cos\theta.$$

This allows switching from the variables $(\mathbf{r},\mathbf{p})$ to the new ones $(H_{\rm W},\theta)$ in the integrals over phase space. The number of particles then reads

$$A=\frac{2}{(\hbar\omega)^3}\int_0^\infty dH_{\rm W}H_{\rm W}^2f(H_{\rm W}), \quad (12)$$

which suggests considering $g(H_{\rm W})=H_{\rm W}^2f(H_{\rm W})$ as a kind of energy distribution function. Its width is

$$\delta=\frac{\langle H_{\rm W}^2\rangle}{A}-\frac{\langle H_{\rm W}\rangle^2}{A^2}, \quad (13)$$

Table 1. First moments and width of the energy distribution function

Method	$\langle H_{\rm W}\rangle/\hbar\omega$	$\langle H_{\rm W}^2\rangle/(\hbar\omega)^2$	$\delta/(\hbar\omega)^2$
WK–$\hbar^2$	1180.09	6779.19	2.509
Strutinsky	1180.12	6766.28	2.500
Quantal	1176.00	6720.00	2.438

where

$$\langle H_{\rm W}^n\rangle=\frac{2}{(\hbar\omega)^3}\int_0^\infty dH_{\rm W}H_{\rm W}^ng(H_{\rm W}). \quad (14)$$

For the harmonic oscillator potential, the moments $\langle H_{\rm W}^n\rangle$ can be calculated analytically, both semiclassically and quantally. Results for a nucleus with $A=224$ particles and $\hbar\omega=41A^{-1/3}$ are presented in Table 1. The Wigner–Kirkwood calculation of order $\hbar^2$ is compared with the result obtained with the Strutinsky averaged distribution function and with the quantal value. From the table, one can see that the Wigner–Kirkwood expansion reproduces very precisely the results provided by the averaged distribution function. The semiclassical expectation values correspond to the smoothly varying part of the quantal values. The difference between the semiclassical and quantal mean values is due to shell effects, and, as can be seen, they are small.

4. WIGNER FUNCTION ON THE ENERGY SHELL

Let us consider the density matrix of a bunch of states belonging to the same energy, as happens for a harmonic oscillator shell:

$$\hat\rho_E=\frac{1}{g(E)}\sum_i|i\rangle\langle i|\delta(E-\varepsilon_i), \quad (15)$$

with $g(E)=\mathrm{tr}[\delta(E-\hat H)]_{\rm W}$ being the level density. The interest of (15) lies in the fact that its Wigner–Kirkwood expansion is again very useful in computing matrix elements of one-body and two-body operators.

The TF approximation of (15) is given by

$$f_E^{\rm TF}(\mathbf{r},\mathbf{p})=\frac{1}{g^{\rm TF}(E)}\delta(E-H_{\rm W}). \quad (16)$$

Integrating over momentum yields the local density on the energy shell:

$$\rho_E^{\rm TF}(\mathbf{r})=\frac{4}{(2\pi\hbar)^3}\int d\mathbf{p}f_E^{\rm TF}(\mathbf{r},\mathbf{p}) \quad (17)$$
$$=\frac{1}{g^{\rm TF}(E)}\frac{2mk_E(\mathbf{r})}{\pi^2\hbar^2}$$

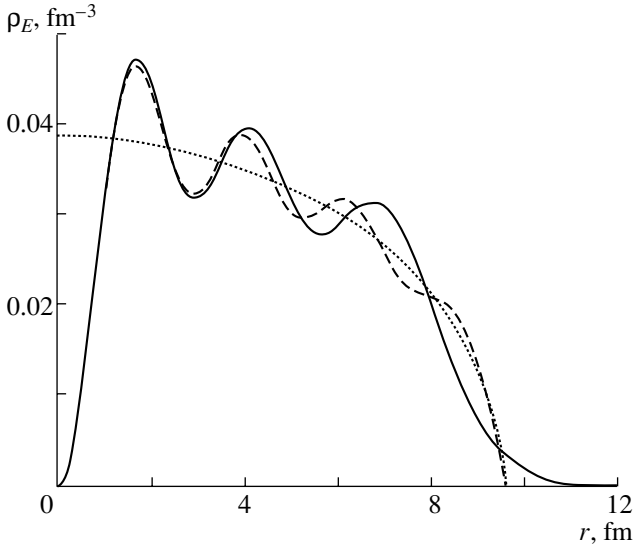

Fig. 2. The local density on the energy shell for a harmonic oscillator potential: comparison of the Thomas–Fermi approximations (17) (dotted curve) and (19) (dashed curve) with the quantal result (solid curve).

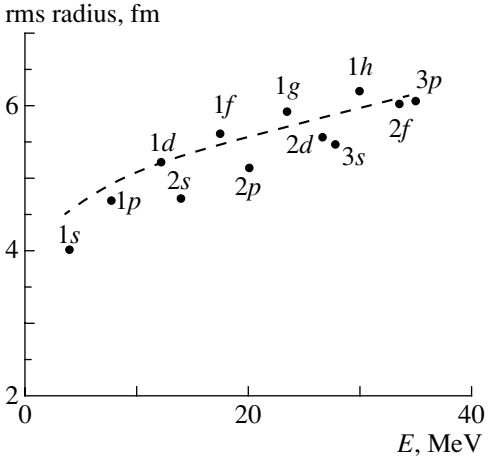

Fig. 3. TF (dashed curve) and QM results (•) for the rms radius as a function of energy E in a Woods–Saxon potential.

for a degeneracy of 4 and with $k_E(\mathbf{r}) = \{2m[E - V(\mathbf{r})]/\hbar^2\}^{1/2}$ being the local momentum at energy E. In Fig. 2, we display the quantal and TF densities of $A = 224$ particles in a harmonic oscillator potential for the $N = 5$ shell. The TF result passes quite well through the average.

From Fig. 2, it can be noted that quantally there exists a marked bump/hole structure at the origin for even/odd parity shells. One may suspect that this is due to the presence/absence of s waves. We can try to recover this feature from the TF approximation projecting it on good parity. To do this, we transform (16) into $(\mathbf{r}, \mathbf{r}')$ space,

$$\rho_E^{\mathrm{TF}}(\mathbf{r}, \mathbf{r}') = \frac{1}{g^{\mathrm{TF}}(E)} \frac{4}{(2\pi\hbar)^3} \times \int d\mathbf{p} e^{i\mathbf{p}\cdot\mathbf{s}/\hbar} \delta(E - H_{\mathrm{W}}) = \frac{1}{g^{\mathrm{TF}}(E)} \frac{2mk_E(\mathbf{R})}{\pi^2\hbar^2} \frac{\sin[sk_E(\mathbf{R})]}{sk_E(\mathbf{R})} = \rho_E^{\mathrm{TF}}(\mathbf{R}) j_0[sk_E(\mathbf{R})], \tag{18}$$

in terms of the center-of-mass $\mathbf{R} = (\mathbf{r} + \mathbf{r}')/2$ and relative $\mathbf{s} = \mathbf{r} - \mathbf{r}'$ coordinates and the spherical Bessel function j_0. Now, the even/odd parity density on the energy shell is obtained as

$$\rho_E^{\mathrm{even/odd}}(\mathbf{r}) = \frac{1}{2} \left\{ \rho_E^{\mathrm{TF}}(\mathbf{r}, \mathbf{r}') \pm \rho_E^{\mathrm{TF}}(\mathbf{r}, -\mathbf{r}') \right\}_{\mathbf{r}'=\mathbf{r}} = \frac{1}{2} \left\{ \rho_E^{\mathrm{TF}}(\mathbf{r}) \pm \rho_E^{\mathrm{TF}}(\mathbf{0}) j_0[2rk_E(\mathbf{0})] \right\}. \tag{19}$$

We have drawn this expression in Fig. 2. The bump/hole structure exhibited by the quantal density is well reproduced in the interior. The agreement only deteriorates near the classical turning point. It should be noted that the semiclassical expressions of Wigner–Kirkwood type for local densities should be regarded as distributions, in the sense that they are efficient when used in integrals to compute expectation values.

In Fig. 3, dashed curve represents the rms radius

Table 2. TF and QM calculations of the matrix elements $v(E, E')$ defined in Eq. (20) are compared for a harmonic oscillator

Method	N/N'	0	1	2	3	4	5
QM	0	0.99	1.48	1.85	2.16	2.43	2.68
TF		0.82	1.41	1.81	2.13	2.41	2.66
QM	1		3.71	5.00	6.02	6.89	7.66
TF			3.45	4.87	5.93	6.82	7.61
QM	2			8.66	11.0	12.9	14.5
TF				8.33	10.8	12.8	14.4
QM	3				16.3	19.9	22.8
TF					15.9	19.6	22.6
QM	4					26.9	31.9
TF						26.4	31.6
QM	5						40.8
TF							40.3

obtained using the TF on-shell density (17) as a function of the energy for a Woods–Saxon potential with $V_0 = -44$ MeV, $a = 0.67$ fm, and $R = 1.27A^{1/3}$ for $A = 224$ nucleons. The quantal values corresponding to the different energy levels are indicated by dots. The TF curve nicely averages the quantal results.

One can also consider two-body matrix elements of a force of δ type:

$$v(E, E') = v_0 \int d\mathbf{r} \rho_E(\mathbf{r}) \rho_{E'}(\mathbf{r}), \qquad (20)$$

where $\rho_E(\mathbf{r})$ is the on-shell density. As an example, we show in Table 2 the value of the matrix elements (20) calculated for a harmonic oscillator potential $[E = (N + 3/2)\hbar\omega]$ in the quantal and TF cases with $v_0 = 1$ in $100/\hbar\omega$ units.

5. VARIATIONAL CONTENT OF THE WIGNER–KIRKWOOD EXPANSION

The chemical potential μ in the expansion (9) for $f(\mathbf{r}, \mathbf{p})$ is to be determined from the particle number condition (4). Therefore, μ depends implicitly on $\hbar$, $\mu = \mu_0 + \hbar^2\mu_2 + \ldots$, and (9) does not yet constitute the proper sorting out of the $\hbar$ expansion. For a self-consistent mean field case, the potential V also depends implicitly on $\hbar$ and one thus has to write $V = V_0 + \hbar^2 V_2$. Therefore, the first term of (9) becomes

$$\Theta(\mu - H_{\mathrm{W}}) = \Theta\left(\mu_0 - \frac{p^2}{2m} - V_0\right) \qquad (21)$$
$$+ \hbar^2 \delta\left(\mu_0 - \frac{p^2}{2m} - V_0\right)(\mu_2 - V_2).$$

Inserting this expression into (9) and replacing μ and V by μ_0 and V_0 in the $\hbar^2$ part, one gets the proper $\hbar$ expansion of $f = f_0 + \hbar^2 f_2 + \mathcal{O}(\hbar^4)$. It can be used, for example, to compute the ground-state energy E in the mean field approximation by means of Eq. (3).

Functional minimization of E with respect to V_2 and V_0 yields variational equations for V_0 and V_2, the first one being the TF equation. The particle number condition determines μ_0 from $A = \int d\mathbf{r} d\mathbf{p} f_0/(2\pi\hbar)^3$, whereas μ_2 is obtained from the condition $\int d\mathbf{r} d\mathbf{p} f_2/(2\pi\hbar)^3 = 0$. This method has been called the variational Wigner–Kirkwood (VWK) approach [8]. In the VWK, the higher order corrections μ_2, V_2, etc., are all obtained in terms of the lowest order TF solution. In this sense, the VWK bears some similarity to the Schrödinger perturbation theory. The VWK approach differs from the usual extended Thomas–Fermi (ETF) formalism in the sense that the VWK properly sorts out the powers in $\hbar$ whereas ETF partially sums $\hbar$ to all orders [8].

6. SUMMARY

We have shown, with the help of the harmonic oscillator potential, that the Wigner–Kirkwood $\hbar$ expansion of the density matrix is very useful for the calculation of average nuclear properties. This is still valid for more realistic potentials. Many quantities can be calculated within the semiclassical method. We may mention optical potentials, nuclear pairing properties, giant resonance widths, etc. We think that the understanding of the average behavior of such quantities enlightens us and teaches us most of the salient features of nuclear physics.

ACKNOWLEDGMENTS

This work was supported in part by grant no. PB98-1247 from the DGICYT (Spain) and grant no. 2000 SGR-00024 from the DGR (Catalonia).

REFERENCES

1. W. D. Myers and W. J. Swiatecki, Ann. Phys. (N.Y.) **55**, 395 (1969); **84**, 186 (1974); W. D. Myers, *Droplet Model of Atomic Nuclei* (Plenum, New York, 1977).
2. V. M. Strutinsky, Nucl. Phys. A **122**, 1 (1968); **218**, 169 (1974); M. Brack, J. Damgård, A. S. Jensen, *et al.*, Rev. Mod. Phys. **44**, 320 (1972).
3. P. Ring and P. Schuck, *The Nuclear Many-Body Problem* (Springer-Verlag, New York, 1980).
4. M. Prakash, S. Shlomo, and V. M. Kolomietz, Nucl. Phys. A **370**, 30 (1981).
5. J. Martorell and E. Moya de Guerra, Ann. Phys. (N.Y.) **158**, 1 (1984).
6. R. K. Pathria, *Statistical Mechanics* (Pergamon, Oxford, 1985).
7. M. Centelles, X. Viñas, M. Barranco, *et al.*, Ann. Phys. (N.Y.) **221**, 165 (1993).
8. P. Schuck, Phys. Lett. B **302**, 1 (1993); M. Centelles, X. Viñas, M. Durand, *et al.*, Ann. Phys. (N.Y.) **266**, 207 (1998).

Physics of Atomic Nuclei, Vol. 65, No. 4, 2002, pp. 736–739. From Yadernaya Fizika, Vol. 65, No. 4, 2002, pp. 769–772.

Sensitivity Dependence of ^{8}He + p Elastic Scattering on the ^{8}He Density Distribution*

R. Wolski[1)], A. Pakou[2)], and N. Alamanos[3)]**

Joint Institute for Nuclear Research, Dubna, 141980 Russia

Received August 31, 2001

Abstract—Elastic proton scattering is investigated as a means for probing density the distribution of exotic neutron-rich nuclei. In this context, the calculations for elastic p + ^{8}He scattering within the JLM and eikonal-approximation models are performed by using the cluster-orbital-shell-model-approximation parameters for the density distribution. The results of the calculations are compared with existing experimental data. It is found that, at large scattering angles, both models are sensitive to the extension of valence neutrons. © *2002 MAIK "Nauka/Interperiodica".*

1. INTRODUCTION

Elastic proton scattering is a well-known tool for studying ground-state densities, since the interaction potential can be related to the ground-state nuclear densities. In recent years, radioactive beams became available, enabling one to use this inverse elastic proton scattering to probe features of the halo structure in exotic neutron-rich nuclei. There is a commonly shared conviction that one could extract, from proton scattering, at least the rms radius of nuclear matter [1, 2]. However, the ability of such studies to disclose the density distribution in more detail and, in particular, to discriminate halo (skin) nuclei from nonhalo (nonskin) states has not yet been clarified conclusively [1–3]. We investigate here the potential of elastic p + ^{8}He scattering at intermediate energies for differentiating between density distributions of the ^{8}He core and its four valence neutrons. The density distributions were simulated by the formulas of the cluster-orbital-shell-model approximation (COSMA) [4]. Each distribution was characterized by two parameters, being, this time, the rms core and valence-neutron radii. In this context, the terms "halo (skin)" or "nonhalo (nonskin)" used in this article mean a large or no difference between these radii. The low-density long tail of ^{8}He matter distribution and its manifestation at very forward angles in high-energy elastic scattering are beyond the scope of the present article. Two entirely different models, the microscopic JLM model [5] and the eikonal-approximation model [6], were used to calculate elastic scattering for a given density distribution. The calculations were performed for three energy values of 26, 45, and 72 MeV/nucleon accessible at the laboratories used. The results of the calculations for 26 and 72 MeV/nucleon were contrasted against two sets of experimental data, a preliminary one, obtained in a wide angular range at 26 MeV/nucleon in Dubna [7] and a set at 72 MeV/nucleon at RIKEN [8].

2. THE MODELS

Calculation on the basis of the JLM model. The elastic-scattering calculations were performed within the microscopic DWBA approach, where the optical potential (OP) for the entrance and exit channels, as well as transition form factors, are calculated consistently by using an energy- and density-dependent interaction. The starting point for computing the JLM potentials is the Brueckner–Hartree–Fock approximation and the Reid hard core nucleon–nucleon interaction, which provide, for energies up to 160 MeV, the energy and density dependence of the isoscalar, isovector, and Coulomb components of the complex OP in infinite matter. The OP for a finite nucleus is obtainable by replacing the nuclear matter density by the density distribution of the nucleus. The JLM central potential was extensively studied in [9, 10]. It has been particularly successful in describing elastic proton and neutron scattering by stable nuclei, provided that the imaginary part of the OP is slightly modified by a normalization factor on the order of 0.8. It should be emphasized that the isovector part

*This article was submitted by the authors in English.

1)Institute of Nuclear Physics, Cracow, Poland.

2)Department of Physics, The University of Ioannina, Greece; e-mail: apakou@cc.uoi.gr

3)CEA/DSM/DAPNIA/SED, Saclay, France; e-mail: nalamanos@Cea.fr

**e-mail: wolski@nrsun.jinr.ru

1063-7788/02/6504-0736$22.00

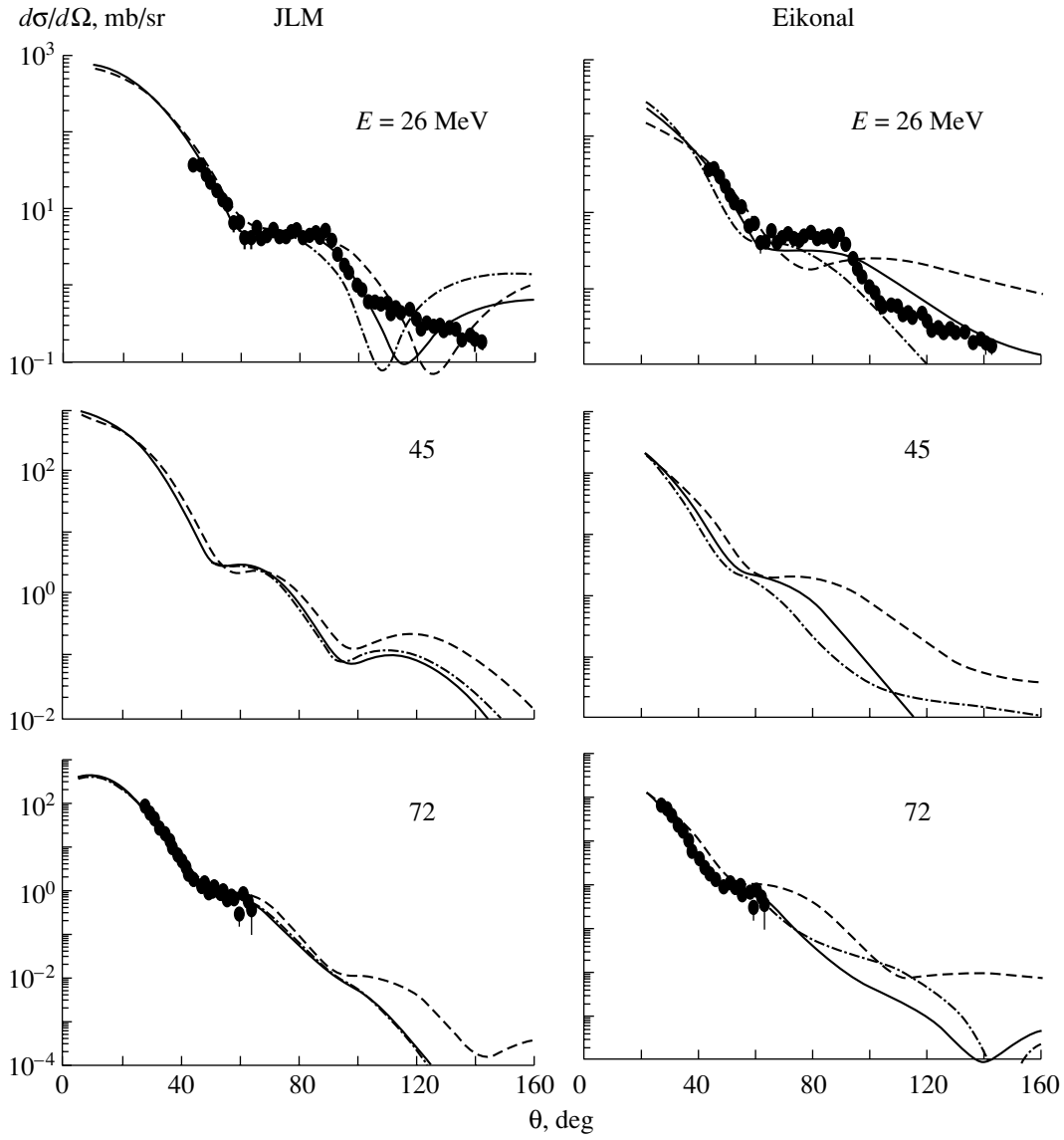

Fig. 1. Results of the (left) JLM and (right) eikonal-approximation calculations of the angular distributions for elastic ^{8}He + p scattering. The symbols are experimental points from [7, 8]. The curves correspond to various COSMA rms values of the radius of the total density distribution at a fixed rms core radius of 1.69 fm: (dashed curves) 2.14 fm, (dash-dotted curves) 2.84 fm, and (solid curves) 2.52 fm. The imaginary JLM potential was scaled down by a factor of 0.95 or 0.85 to fit the 26- or 72-MeV/nucleon data, respectively.

is included in the JLM model and that this is expected to produce a sensitivity dependence on the core and valence neutron distributions. In order to fit experimental data on elastic p+^{8}He scattering, the imaginary part of the JLM potential was normalized here by a factor of 0.95 for the 26-MeV/nucleon calculations and 0.85 for the 72-MeV/nucleon calculations. These values of the normalization factors are independent, within reasonable limits, of the density-distribution parameters.

Eikonal approximation. This approach belongs to a different class since the Schrödinger equation is not solved: the cross section is calculated directly from the scattering amplitude given by an integral of the Coulomb and nuclear phase shifts with respect to the impact parameter. The nuclear phase shift is expressed in terms of the nucleon–nucleus OP, which, in the optical-limit approximation, has the form [6]

$$U_0(r) = \langle t_{pn}\rangle \rho_n(r) + \langle t_{pp}\rangle \rho_p(r), \qquad (1)$$

where ρ_n(r) and ρ_p(r) are, respectively, the neutron and proton ground-state densities and $\langle t_{pn}\rangle$ and $\langle t_{pp}\rangle$ stand for, respectively, the proton–neutron and proton–proton transition matrix elements for proton–nucleon scattering, which are given by the nucleon–nucleon total cross sections corrected for

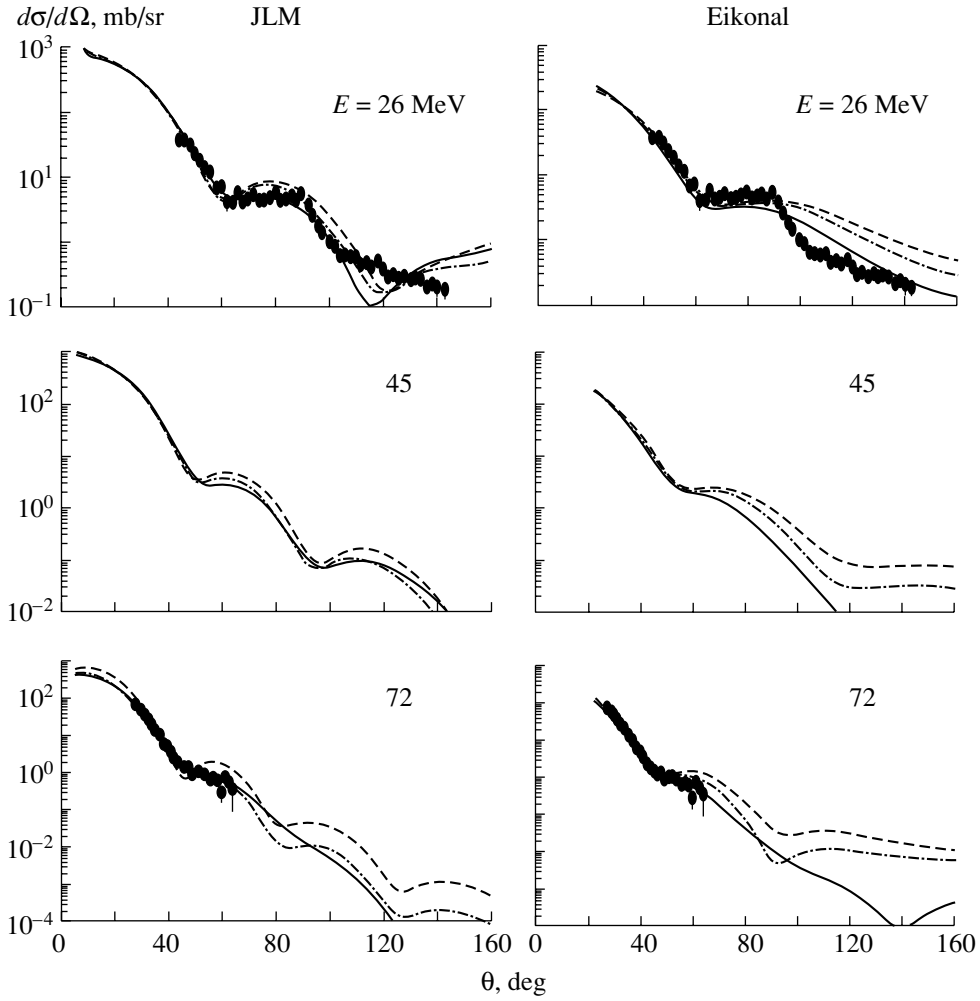

Fig. 2. Results of (left) JLM and (right) eikonal-approximation calculations of the angular distributions for elastic ^{8}He + p scattering. The symbols are experimental points from [7, 8]. The curves correspond to a fixed COSMA total rms radius of 2.52 fm and various values of the valence-neutron-skin thickness: (dashed curve) 0.0 fm (nonskin), (dash-dotted curve) 0.8 fm (thin skin), and (solid curve) 1.46 fm (thick skin). The imaginary JLM potential was scaled down by a factor of 0.95 or 0.85 to fit the 26- or 72-MeV/nucleon data, respectively.

Pauli blocking. In this model, the sensitivity of the calculated angular distribution for elastic proton scattering on the core and valence neutron densities originates from the difference between the densities $\rho_n(\mathrm{r})$ and $\rho_p(\mathrm{r})$, as well as between free proton–proton and proton–neutron total cross sections, the latter being larger at the energies in question. It should be noted that there are no free parameters in this approach.

COSMA density parameters. In order to perform the calculations, it is necessary to know the one-nucleon densities. For the core- and valence-neutron densities, we used here the simple formulas [4]

$$\rho_c(r) = \frac{1}{\pi}\sqrt{\frac{2}{\pi}}\frac{1}{a^3}\exp\frac{-r^2}{2a^2}, \quad a = \frac{\alpha}{\sqrt{3}}\ [\mathrm{fm}], \quad (2)$$

$$\rho_v(r) = \frac{8}{3\pi\sqrt{\pi}}\frac{r^2}{b^5}\exp\frac{-r^2}{b^2}, \quad b = \beta \quad [\mathrm{fm}]; \quad (3)$$

the total matter density is given by

$$\rho_t(r) = \rho_c(r) + \rho_v(r) \quad (4)$$

and is normalized to the total number of nucleons (eight). The parameter α is just the rms value of the core (proton) radius (the distance between a pointlike proton and the center of mass of ^{8}He), $\mathrm{r}_c = r_p = \alpha$, while the rms value of the valence neutron radius (the distance between the pointlike valence neutron and the center of mass of ^{8}He), r_v, is given by $\mathrm{r}_v = \sqrt{2.5} \times \beta^2$. Thus, by using these formulas, we have the flexibility of generating various density distributions and see their effect on the calculated angular distribution for elastic scattering. The authors of [4] proposed the values of $\mathrm{r}_c = 1.69$ fm and $\mathrm{r}_v = 3.15$ fm,

the resulting rms value of the total matter radius being $r_t = 2.52$ fm. These values were the starting point in our analysis. Figure 1 shows the angular distributions calculated by the two models with r_c kept fixed at 1.69 fm and with r_v varied, with the resulting r_t being 2.14, 2.52, or 2.84 fm. Since the effect of the core itself was found to be small, this, in fact, probes elastic scattering with various rms values of total radii.

Figure 2 presents the results of the calculations for three values of the valence-neutron-skin thickness defined as the difference $(r_v - r_c)$ but with r_t fixed at 2.52 fm. One can see that, at rather large scattering angles, the calculated elastic scattering is sensitive to the presence of a neutron halo (skin).

3. CONCLUSION

Elastic p + ^{8}He scattering has been analyzed by using two entirely different models of the interaction: the JLM model and the eikonal-approximation approach. Simple formulas of the COSMA have been taken for the ^{8}He density. The calculations have been performed for ^{8}He beam energies of 26, 45, and 72 MeV/nucleon. For the first and last cases, the results have been compared with the existing experimental data. The two models have produced similar results at forward scattering angles, in which case the imaginary part of the optical potential from the JLM calculations has been renormalized by a factor of 0.95 for 26-MeV/nucleon data and 0.85 for 72-MeV/nucleon data. For more backward scattering angles, the predictions of the two models are at variance. For extremely backward angles, a comparison between the models and the data could be misleading—in particular, for the lowest energy—because of the possible effects of nonpotential origin (e.g., exchange processes) and because of the inapplicability of the eikonal approximation in this angular region. The density-parameter values extracted from an analysis of the cross sections for the removal of two and four neutrons from ^{8}He at high energy [11] seem to be surprisingly well suited to describing elastic p + ^{8}He scattering. In terms of the density-parameters dependence, our simulation of elastic proton scattering suggests that the angular distribution depends on the rms value of the total matter radius at rather forward scattering angles; this is in accordance with the previous findings [1, 2]. At more backward angles, a distinction between the neutron skin and the nonskin structure can be revealed. It should be noted, however, that the differentiation is not striking and appears to be model-dependent. The difference between the two models needs further clarification. Precise measurements at large angles are required for the use of elastic proton scattering as a measure of the density distribution. However, this task could be hard to accomplish because the cross section at large angles is generally small.

ACKNOWLEDGMENTS

We are grateful to A.A. Korsheninnikov for placing his eikonal-approximation code at our disposal.

REFERENCES

1. L. V. Chulkov, C. A. Bertulani, and A. A. Korsheninnikov, Nucl. Phys. A **587**, 291 (1995).
2. A. A. Korsheninnikov *et al.*, Nucl. Phys. A **617**, 45 (1997).
3. S. P. Weppner, O. Garcia, and Ch. Elsner, Phys. Rev. C **61**, 044601 (2000).
4. M. V. Zhukov, A. A. Korsheninnikov, and M. H. Smelberg, Phys. Rev. C **50**, R1 (1994).
5. J.-P. Jeukenne, A. Lejeune, and C. Mahaux, Phys. Rev. C **10**, 1391 (1974).
6. C. A. Bertulani, L. F. Santo, and M. S. Hussein, Phys. Rep. **226**, 281 (1993).
7. R. Wolski *et al.*, *Contribution to the RNB 2000 Conference, Divonne, 2000.*
8. A. A. Korsheninnikov *et al.*, Phys. Lett. B **316**, 38 (1993).
9. S. Mellena *et al.*, Phys. Rev. C **28**, 2267 (1983).
10. J. S. Petler *et al.*, Phys. Rev. C **32**, 673 (1985).
11. I. Tanihata *et al.*, Phys. Lett. B **289**, 261 (1992).

Physics of Atomic Nuclei, Vol. 65, No. 4, 2002, pp. 740–745. From Yadernaya Fizika, Vol. 65, No. 4, 2002, pp. 773–776.

The Love–Hate Relationship between the Shell Model and Cluster Models*

L. Zamick** **and Sh. J. Q. Robinson**

Department of Physics and Astronomy, Rutgers University, Piscataway, New Jersey, USA

Received September 6, 2001

Abstract—We adopt a personal approach here reviewing several calculations over the years in which we have experienced confrontations between cluster models and the shell model. In previous cluster conferences, we have noted that cluster models go hand in hand with Skyrme–Hartree–Fock calculations in describing states which cannot easily, if at all, be handled by the shell model. These are the highly deformed (many particle–many hole) intruder states, linear chain states, etc. In the present work, we will consider several topics: the quadrupole moment of ^{6}Li; the nonexistence of low-lying intruders in ^{8}Be; and then jumping to the $f_{7/2}$ shell, we discuss the two-faceted nature of the nuclei, which sometimes display shell-model properties and other times cluster properties. © *2002 MAIK "Nauka/Interperiodica".*

1. THE QUADRUPOLE MOMENT OF THE $J = 1^+$ STATE IN ^{6}Li

Whereas the quadrupole moment of the deuteron is positive ($Q = +2.74$ mb), that of the $J = 1^+$ state of ^{6}Li is negative, $Q = -0.818(17)$ mb. The magnetic moment of the deuteron is $\mu = 0.85741$ nm, while that of ^{6}Li is 0.822 nm.

There appears to be a big discrepancy between cluster model calculations and the shell model calculations. In nearly all cluster model calculations, Q comes out positive. However, in many shell model calculations, Q comes out negative, sometimes too negative. This is an important problem that deserves further attention. See, for example, arguments in the literature between the cluster group [1] and the shell model group [2]. See also the recent compendium of $A = 6$ by Tilley *et al.* [3].

For example, a modern shell model approach by Forest *et al.* [4] gets about -8 mb for Q, a factor of 10 too large but of the correct sign. On the other hand, in a dynamical microscopic three cluster description of ^{6}Li where the clusters are α, n, and p, the result is $Q = 2.56$ mb [1].

In shell model calculations that we performed [5], we started with two valence particles in the $0p$ shell ($0\ \hbar\omega$). Then, we allowed up to $2\ \hbar\omega$ and then up to $4\ \hbar\omega$ excitations. In the $0\ \hbar\omega$, space if you do not have a tensor interaction, Q comes out positive. With a "realistic" tensor interaction Q comes out negative, but too negative $Q = -3.5$ mb. However, with a former student, Zheng, who, at Arizona, also developed the no-core approximation with Barrett *et al.* [6], we showed that when higher shell admixtures were admitted, Q became smaller in magnitude and closer to experiment [5].

Space, $\hbar\omega$	Q, mb	μ, nm
0	−3.60	0.866
2	−2.51	0.848
4	−0.085	0.846
Experiment	−0.82	0.822

Note that the shell model calculations cannot get the magnetic moment low enough. With up to $4\ \hbar\omega$ admixtures, we actually overshoot and get a quadrupole moment that is too small but still negative. Some cluster models appear to explain the low magnetic moment.

An excellent discussion of many shell model calcultion of Q and μ has been given by Karataglidis *et al.* [7]. The value of Q that they obtain with what they call the "Zheng" interaction [8] in the up to 0, 2, 4, and $6\ \hbar\omega$ spaces are -2.64, -2.08, -0.12, and 0.17 mb, respectively. Thus, they get Q to become positive at the $6\ \hbar\omega$ level. But then they quote Zheng *et al.* [8] as getting a value of -0.67 mb in the same $6\ \hbar\omega$ space. It is not clear why the two calculations give different answers. The changes in μ in [7] are more moderate, 0.869, 0.848, 0.845, and 0.840 nm, in the up to 0, 2, 4, and $6\ \hbar\omega$ spaces.

Looking at all the calculations by all groups (including our own), the situation is certainly confusing

*This article was submitted by the authors in English.

** e-mail: lzamick@physics.rutgers.edu

and the problem deserves further attention. This is certainly a basic problem, the deuteron embedded in the nuclear medium. This problem has wider implications: whether or not there is $T = 0$ pairing can depend on how higher order configurations affect the tensor interaction in the valence space.

2. ABSENCE OF LOW LYING INTRUDERS IN ^{8}Be AND THE α PARTICLE MODEL

The 0^+ bandhead for low lying intruders in ^{16}O, ^{12}C, and ^{10}Be are at 6.05, 7.65, and 6.18 MeV, respectively. In ^{16}O and ^{12}C, these are predominantly $4p$–$4h$ excitations. In ^{12}C, we identify the intrinsic state as a linear chain. In the 7th edition of the "Tables of Isotopes," possible intruders in ^{8}Be were indicated, a $J = 0^+$ state at 6 MeV and a $J = 2^+$ state at 9 MeV.

In shell model calculations allowing $2p$–$2h$ excitations, we were able, with a quadrupole–quadrupole force, to get a $J = 0^+$ state at 9.7 MeV in ^{10}Be, too high but in the right ballpark [7, 8]. However, we could not get low lying intruders in ^{8}Be below 30 MeV [7, 8]. We used a deformed oscillator model to show why one gets intruders in ^{12}C and ^{10}Be but not ^{8}Be.

But perhaps the simplest explanation, as suggested to us by Vogt [9], is given by the α particle model. In ^{12}C, we can rearrange the α particles from a triangle to a linear chain. In ^{8}Be, we have only two α particles. One can get a rotational band by having the two α rotate around each other, but that is all.

The mere existence of these intruder states is of astrophysical importance. In the beta decay $^8\mathrm{B} \to {}^8\mathrm{Be} + e^+ + \nu$, one goes from a $J = 2^+$ $T = 1$ to $J = 1$ or 2^+ states. This is the famous "Ray Davis" neutrino. If there were a 2^+ state at 9 MeV, then there would be more high energy alphas than there would be if the decay were to the 2^+_1 state at 3.04 MeV [10]. The α spectrum from the decay of ^{8}Be seems to show more high energy alphas, but we would say that they are not due to low lying intruders.

3. CLUSTERING AND SHELL MODEL IN THE $f_{7/2}$ REGION

In a previous cluster conference in Santorini (1993), a spectrum of ^{44}Ti was shown in an α cluster model [11]. The spectrum looked reasonable except that there was a wide gap between the 10^+ and 12^+ states. However, these states are sufficiently so close together that the 12^+ state is isomeric. In a single j shell basis ($j = f_{7/2}$), ^{52}Fe is the $4h$ system and it should have an identical spectrum to that of ^{44}Ti provided the same interaction is used. However, in ^{52}Fe, the 12^+ lies below the 10^+ state. It is extremely isomeric and has a lifetime of 12 min.

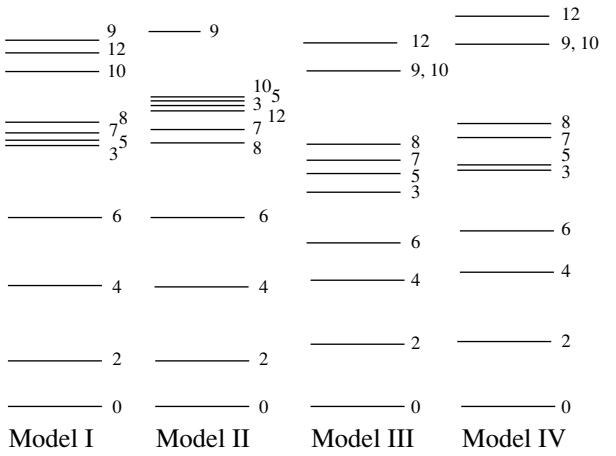

^{44}Ti spectra for Models I, II, III, IV.

We have studied this and other topics by calculating the spectrum of ^{44}Ti (^{52}Fe) with a variety of interactions designated as Model X (see Tables 1, 2 and the figure).

Model I. Use the spectrum of ^{42}Sc as input (particle–particle). Identify $\langle (j^2)^J V (j^2)^J \rangle = E(J)$ experimentally. For isospin $T = 0$, J can be 1, 3, 5, and 7, while, for $T = 1$, J is even 0, 2, 4, and 6.

Model II. Use the spectrum of ^{54}Co as input (hole–hole). If there were no configuration mixing, these two spectra would be identical. However, there are some differences, e.g., the 7^+ state is much lower in ^{54}Co than in ^{42}Sc.

Model III. Now, we play games. We want to find out how important the $T = 0$ matrix elements are for the structure of the nuclei (e.g., is $T = 0$ pairing important?). Noticing that, in ^{42}Sc, the $J = 2$, 3, and 5 states are nearly degenerate in this model, we set all the $T = 0$ matrix elements to be the same and all equal to $E(2^+) = 1.5863$ MeV.

In Model III, we then have $V^{T=1} = V(^{42}\mathrm{Sc})^{T=1}$ $J = 0$, 2, 4, 6 and $V^{T=0} = \mathrm{const} = E(2^+)$ $J = 1$, 3, 5, 7. We can then write $V^{T=0} = c(1/4 - t_1 \cdot t_2)$, where c is a constant. Hence $\sum_{i<j} V_{ij}^{T=0} = c/8(n(n-1)+6) - c/2T(T+1)$. This means that the spectrum of states of a given isospin, e.g., $T = 0$ in ^{44}Ti (^{52}Fe), is independent of what the constant is; it might as well be zero. Of course, the relative splitting of $T = 1$ and $T = 0$ states will be affected. Model III will be the standard from which we derive Model IV.

Model IV. Relative to the degenerate case above, we now move the $J = 1^+$ state down in energy to 0.5863 MeV. Our motivation is based on numerous

Table 1. Two particle matrix elements $\langle (j^2)^J V (j^2)^J \rangle$ (in MeV)

Model	Case							
	$J=0$ $T=1$	$J=2$ $T=1$	$J=4$ $T=1$	$J=6$ $T=1$	$J=1$ $T=0$	$J=3$ $T=0$	$J=5$ $T=0$	$J=7$ $T=0$
I[a)]	0.000	1.5863	2.8153	3.2420	0.6110	1.4904	1.5101	0.6163
II[b)]	0.000	1.4465	2.6450	2.9000	0.9372	1.8224	2.1490	0.1990
III[c)]	0.000	1.5863	2.8153	3.2420	1.5863	1.5863	1.5863	1.5863
IV[d)]	0.000	1.5863	2.8153	3.2420	0.5863	1.5863	1.5863	1.5863

[a)] Input is spectrum of ^{42}Sc (particle–particle).

[b)] Input is spectrum of ^{54}Co (hole–hole).

[c)] The $T=1$ matrix elements are from the spectrum of ^{42}Sc. The $T=0$ matrix elements are degenerate at 1.5863 MeV.

[d)] Same as Model III except that the $J=1^+$ $T=0$ energy is lowered to 0.5863 MeV.

Table 1. ^{44}Ti (^{52}Fe) spectra for Model I, II, III, and IV

Model I $(J^\pi\ E)$[a)]		Model II $(J^\pi\ E)$[b)]		Model III $(J^\pi\ E)$[c)]		Model IV $(J^\pi\ E)$[d)]	
0^+	0.000	0^+	0.000	0^+	0.000	0^+	0.000
2^+	1.163	2^+	1.015	2^+	1.303	2^+	1.253
4^+	2.790	4^+	2.628	4^+	2.741	4^+	2.800
6^+	4.062	6^+	4.079	6^+	3.500	6^+	3.738
3^+	5.786	8^+	5.772	3^+	4.716	3^+	5.031
5^+	5.871	7^+	6.018	5^+	4.998	5^+	5.082
7^+	6.043	12^+	6.514	7^+	5.356	7^+	5.687
8^+	6.084	3^+	6.540	8^+	5.656	8^+	6.045
10^+	7.384	5^+	6.602	9^+	7.200	9^+	7.731
12^+	7.702	10^+	6.722	10^+	7.200	10^+	7.731
9^+	7.984	9^+	8.048	12^+	7.840	12^+	8.371

Note: See Table 1.

discussions about the importance of $T=0$ $S=1$ "pairing" in nuclei. We hope to simulate the $T=0$ pairing by this lowering.

Model V. Relative to Model III, we bring the $J=1^+$ and $J=7^+$ states down to an energy of 0.5863 MeV but keep the $J=3^+$ and 5^+ at $E=E(2^+)=1.5863$ MeV. This spectrum is very close to that of ^{42}Sc.

4. DISCUSSION OF RESULTS

Let us first compare Model III (all $T=0$ matrix elements are degenerate) with Model I (spectra of ^{42}Sc). As already mentioned, making $T=0$ matrix elements degenerate is equivalent to making them zero as far as $T=0$ states are concerned.

The main difference is that the states with $J=6$, 4, 7, and 8 come down in energy as does $J=9^+$. Also, the 12–10 gap is a bit greater than for the ^{42}Sc spectra case, reminiscent of the α particle model. The $J=9^+$ state is below the 10^+ and 12^+ states in the degenerate case. Clearly, it is the high energy side of the spectrum which is most sensitive to the change from the experimental spectrum to the "$T=0$ degenerate" case.

Despite the changes, we can say that the $T=1$ two body matrix elements give the dominant structure

of the spectrum whilst the $T = 0$ matrix elements provide the fine tuning.

We now compare Model IV with Model III. The only difference is that we break the $T = 0$ degeneracy by lowering the $J = 1^+$ state from 1.5863 to 0.5863 MeV. We hope that this simulates, to some extent, $T = 0$ $S = 1$ neutron–proton pairing. The change from the degenerate case is not that large. There is a tendency to go toward the spectrum of ^{42}Sc. The $J = 3$, 5, 7, and 8 states are raised somewhat in energy. However, it is hard to find a clear signature of this $S = 1$ pairing.

Not shown is Model V, where we bring down both the $J = 1^+$ and 7^+ states to 0.5863 MeV keeping $J = 3$ and 5 at $E(2) = 1.5863$ MeV. This input spectrum is close to that of ^{42}Sc; therefore, it is not surprising that the ^{44}Ti spectrum is likewise close.

We lastly consider the results using the spectrum of ^{54}Co. This was done some time ago by Geesaman [12, 13]. Note that there are significant changes, all at the high-energy, high-angular-momentum part of the spectrum. Relative to the ^{42}Sc case, the 10^+ state, and 12^+ states are down in energy, with the 12^+ below the 10^+ state, thus leading to a long lifetime for the 12^+ state. Note that the 9^+ state is now at a much higher energy than the 10^+ or 12^+. Recently, the 10^+ state in ^{52}Fe, which lies above the 12^+, was found in ^{52}Fe by Ur *et al.* [14]. It would also be of interest to find the 9^+ state.

5. MANY PARTICLE, MANY HOLE STATES IN ^{40}Ca

This is a topic we discussed in previous cluster meetings [15]; therefore we will be brief. We just want to remind the reader that there are all sorts of many particle, many hole highly deformed states in ^{40}Ca. One cannot properly describe ^{40}Ca in a cluster model consisting of ^{36}Ar plus an alpha particle. At the very least, one has to start with ^{32}S plus two alpha particles.

In a Skyrme–Hartree–Fock calculation (*Sk* III), we obtain a near degeneracy of the $4p$–$4h$ and $8p$–$8h$ intrinsic state. The respective energies are 12.1 and 11.4 MeV. The $8p$–$8h$ intrinsic state energy is lower than the $4p$–$4h$. By the time projection and pairing are included, the $4p$–$4h$ comes lower than the $8p$–$8h$ (6.85 vs. 8.02 MeV), which is in agreement with the order of the $J = 0$ excitation energies of 3.0 and 5.1 MeV. Pairing will lower the states even more. We actually found many more deformed states of the form np–nh, $n = 2$, 3, 4, 5, 6, 7, and 8. The intrinsic states are nearly degenerate in energy—we called this a deformation condensate. We also found for these states that the deformation parameter was approximately proportional to n; i.e., the value of β for $8p$–$8h$ is approximately twice the value of β for $4p$–$4h$.

In ^{80}Zr, one of the np–nh states becomes the ground state. This is the $12p$–$12h$ state which has a calculated value of $\beta = 0.4$. A more superdeformed $16p$–$16h$ state with $\beta = 0.6$ is calculated to be at an excitation energy of about 8 MeV.

6. TWO DIFFERENT VIEWS OF THE $f_{7/2}$ REGION

In the March 2000 issue of Phys. Rev. C **61**, there are two side-by-side papers. One is by our group [16], and one is by Hasegawa and Koneko [17]. We both do calculations in the $f_{7/2}$ shell. We emphasize shell-model behavior; the other authors, the α cluster behaviors, even though their model space is limited to $f_{7/2}$.

The other authors point out that we can get an excellent approximation to the ground states of $n_p = n_n = 2m$ nuclei (n_p is the number of protons, etc):

$$|(f_{7/2})^{4m} I = T = 0\rangle = \frac{1}{\sqrt{N_0}}(\alpha_0^\dagger)^m |A_0\rangle, \quad (1)$$

where $(\alpha_0^\dagger)$ creates a four nucleon cluster:

$$\alpha_0^\dagger = \sum_{J,\tau}(J\tau, J\tau : I = T = 0) \times (A^\dagger_{J\tau} A^\dagger_{J\tau})_{I=0\ T=0}. \quad (2)$$

For ^{48}Cr, this approximation gives -32.04 MeV for the ground state energy, whereas the exact value is 32.70 MeV.

We, on the other hand, have emphasized the shell model aspects [16]. In the previously mentioned paper, we find an approximation for the excitation energies of single and double analog states in the $f_{7/2}$ region, and, in an earlier paper, "Fermionic Symmetries: Extension of the two-to-one relationship between spectra of even–even and neighboring odd mass nuclei," [18] we noted two things:

A. There is often a two-to-one relation between spectra of even–even and even–odd nuclei, and, in some cases, the single j shell model predicts this.

B. Excitation energies of the analog state are approximately the same if the neutron excess (or, equivalently, the ground-state isospin) is the same.

The above results can be parametrized by the following formulae.

Single analog excitation (SA)

$$E(\mathrm{SA}) = b(T + X). \quad (3)$$

Double analog excitation (DA)

$$E(\mathrm{DA}) = 2b(T + X + 1/2). \quad (4)$$

This formula will give a two-to-one ratio for $E(\mathrm{DA})/E(\mathrm{SA})$ for (^{44}Ti, ^{43}Ti), (^{51}Cr, ^{50}Cr), (^{47}Sc, ^{48}Ti), etc.

The experimental SA and DA are shown below:

T	Excitation energy
0	^{44}Ti (9.340), ^{48}Cr (8.75), ^{52}Fe (8.559)
1/2	^{43}Sc (4.274)[a)], ^{43}Ti (4.338)[a)], ^{45}Ti (4.176), ^{49}Cr(4.49), ^{51}Mn (4.451), ^{53}Co (4.390), ^{53}Fe (4.250)
1	^{46}Ti (14.153), ^{50}Cr (13.222)
3/2	^{45}Sc (6.752)[a)], ^{47}Ti (7.187), ^{51}Cr (6.611)
2	^{48}Ti (17.379)
5/2	^{47}Sc (8.487)[a)], ^{49}Ti (8.724)

[a)] Obtained from binding energy data.

In Table 2, we compare the theoretical single j shell calculations with the linear formula. We take $b = 2.32$ MeV, $X = 1.30$. Note that, in the $SU(4)$ limit, $X = 2.5$. The fact that $SU(3)$ gives the linear formula is not sufficient for it to be the correct theory. For a simple monopole–monopole interaction $a + bt(1)t(2)$, $X = 1$.

Some of the two-to-one ratios hold rigorously in the single j shell model. This holds for $3p$ and $4p$ systems or $3h$ and $4h$, e.g., (^{43}Ti,^{44}Ti), (^{43}Sc,^{44}Ti), (^{53}Fe,^{52}Fe). Here, not only a single or double analog but all the $J = j$ states in the odd spectrum are at half the energy of the $J = 0^+$ states in the even system.

Some of the relations hold approximately in the single j shell model; e.g., for (^{45}Sc,^{46}Ti) and for the cross conjugate pair (^{51}Cr,^{50}Cr), we would get a two-to-one ratio if the seniority four states could be neglected and one only had $v = 0$ and $v = 2$.

Miraculously, the two-to-one ratio holds remarkably well experimentally for (^{51}Cr,^{50}Cr)—the values are 6.511 and 13.022 MeV, respectively—despite the fact that, in the single j shell, it should only hold approximately. Ironically, the simplest system for which the two-to-one ratio should hold exactly does not work so well. That is to say, the values are 4.338 and 9.340 MeV for (^{43}Ti,^{44}Ti). When configuration mixing is included, agreement with the deviation is explained. This might be an example of a $4p$ clustering. For the hole system (^{53}Fe, ^{52}Fe), on the other hand, the two-to-one ratio works much better.

The fact that there is, in general, a close relation between even–even and even–odd nuclei puts to question whether there is any α-particle clustering in those numerous cases.

The single j shell calculation does not predict exact equality for the SA excitation energies in ^{43}Sc and ^{45}Ti. The relative values are very close, however, 4.142 and 4.112 MeV, respectively. This is fascinating. We take ^{43}Sc and jam a deuteron into it to form ^{45}Ti, and it seems hardly to make any difference for SA excitations [16].

7. TWO VIEWS OF CROSS CONJUGATE RELATIONS

In the single j shell model, the spectra of cross conjugate nuclei should be identical (for j^n states). A cross conjugate nucleus is one obtained by changing protons into neutron holes and neutrons into proton holes. The cross conjugate of ^{46}Ti is ^{50}Cr. Let us compare the spectra:

J	^{46}Ti	^{50}Cr	Ratio
0	0.000	0.000	
2	0.889	0.787	0.8853
4	2.010	1.884	0.9373
6	3.297	3.164	0.9597
8	4.896	4.740	0.9681

The fits are very good. The ^{50}Cr excitations are slightly smaller; it could be a universal A dependence. Where does the remarkable agreement leave room for α clustering?

However, we can look for other things besides the spectra. A recent experiment–theory collaboration where the leading experimentalists were Koller and Speidel [19], obtained good agreement for $g(2^+)$ in ^{50}Cr and bad agreement for ^{46}Ti. The shell model predicts a high value of $g(2^+)$ and $g(4^+)$ for ^{50}Cr but low values for ^{46}Ti (0.25 nm). The high values are confirmed for ^{50}Cr, but, for ^{46}Ti, the measured g factors are closer to 0.5, which suggests the rotational value $g_R = Z/A$. These results suggest that there must be considerable clustering in ^{46}Ti that is not present in ^{50}Cr. In general, the shell model appears to work better in the upper half of the "$f_{7/2}$ shell" than in the lower half. There appears to be much more going on in the lower half, and this is probably due to an intruder/cluster mixing with the basic shell model states.

8. CLOSING REMARKS

We have provided several examples where cluster models and the shell model confront each other usually to the mutual benefit of both models even though in the short term there might be some arguments. The two models give the opposite sign for the quadrupole moment of ^{6}Li, and this has to be resolved. The cluster model provides insight into some results of detailed shell model calculations, e.g., why there are no low lying intruders in ^{8}Be. The low-lying intruder states, e.g., $4p$–$4h$ and $8p$–$8h$ in ^{40}Ca, are essentially impossible to calculate in the shell model. However, here, cluster models and the Skyrme–Hartree–Fock model go together in describing such states. In the $f_{7/2}$ region, we raise the question (without fully answering it) of how to distinguish symmetry energy from clustering energy. Finally, we point out the issue of hidden clustering.

ACKNOWLEDGMENTS

This work was supported in part by the US Department of Energy (grant no. DE-FG02-95ER-40940).

REFERENCES

1. A. Csoto and R. G. Lovas, Phys. Rev. C **53**, 1444 (1996).
2. D. C. Zheng, J. P. Vory, and B. R. Barrett, Phys. Rev. C **53**, 1447 (1996).
3. D. R. Tilley *et al.*, *Energy Levels of Light Nuclei $A = 6$ (preliminary version 2)* (unpublished).
4. J. L. Forest *et al.*, Phys. Rev. C **54**, 646 (1996).
5. L. Zamick, D. C. Zheng, and M. Fayache, Phys. Rev. C **51**, 1253 (1995).
6. D. C. Zheng, B. R. Barrett, J. P. Vary, *et al.*, Phys. Rev. C **51**, 2471 (1995).
7. S. Karataglidis, B. A. Brown, K. Amos, *et al.*, Phys. Rev. C **55**, 2826 (1997).
8. D. C. Zheng, B. R. Barrett, J. P. Vary, *et al.*, Phys. Rev. C **52**, 2488 (1995).
9. E. Vogt, private communication.
10. M. S. Fayache, E. Moya de Guerra, P. Sarrugen, *et al.*, Phys. Rev. C **57**, 2351 (1998).
11. P. Hodgeson, in *Proceedings of the Second International Conference "Atomic and Nuclear Clusters," Santorini, Greece, 1993*, Z. Phys. A **349**, 197 (1994).
12. D. F. Geesaman, R. Malmin, R. L. McGrath, *et al.*, Phys. Rev. Lett. **34**, 326 (1975).
13. D. F. Geesaman, R. L. McGrath, J. W. Noe, *et al.*, Phys. Rev. C **19**, 1938 (1979).
14. C. A. Ur *et al.*, Phys. Rev. C **58**, 3163 (1998).
15. D. C. Zheng, D. Berdichovsky, and L. Zamick, Phys. Rev. C **38**, 437 (1988); J. Phys. Soc. Jpn. Suppl. **158**, 649 (1989); Phys. Rev. C **42**, 1408 (1990).
16. Y. Durga Devi, S. Robinson, and L. Zamick, Phys. Rev. C **61**, 037305 (2000).
17. M. Hasegawa and K. Kaneko, Phys. Rev. C **61**, 037306 (2000).
18. L. Zamick and Y. Durga Devi, Phys. Rev. C **60**, 054317 (1999).
19. N. Koller, private communication.

Physics of Atomic Nuclei, Vol. 65, No. 4, 2002, pp. 746–751. From Yadernaya Fizika, Vol. 65, No. 4, 2002, pp. 777–784.

Reaction Mechanisms for Light Halo Nuclei*

M. V. Zhukov**, **Yu. L. Parfenova**[1)], **and J. S. Vaagen**[2)]

Departments of Experimental Physics, Chalmers University of Technology and Göteborg University, S-41296 Göteborg, Sweden

Received July 20, 2001

Abstract—Current nuclear physics focuses on exploring nucleon matter under extreme conditions, such as those that can be created in modern accelerator laboratories. On the neutron-rich side of stability, radioactive beams have already led to the discovery of halos in nuclei with neutron distributions extending to large distances. Halo nuclei are composite systems with prominent features of few-body correlations, which reveal themselves in various reactions involving these systems. We will discuss experiments that probe a halo structure through studying various reactions involving halo nuclei, with special emphasis on how, from the theoretical point of view, such reactions contribute to our knowledge of the structure and dynamics of the nuclear halo. © *2002 MAIK "Nauka/Interperiodica".*

1. INTRODUCTION

Once exotic nuclei produced in radioactive-beam facilities have become accessible, the very limits of nuclear existence—that is, the edges of the nuclear landscape—can be explored. At these limits [the so-called neutron (proton) drip lines], additional neutrons (protons) can no longer be kept in a nucleus—they literally drip out. The exact location of the neutron drip line is far from clear, and it is known only for light nuclei. In the vicinity of the drip lines, the structural features of nuclei change in relation to nuclei closer to the beta-stability line. The disappearance of the normal nuclear-shell closures was found, and new magic numbers were introduced. Examples are recent observations of the breakdown of the $N = 8$ shell closure for ^{12}Be [1, 2] and the new magic number $N = 16$ [3].

On the neutron-rich side of stability, radioactive beams have already led to the discovery of nuclei with nucleon distributions extending to large distances. Light nuclei so far constitute the part of the nuclear landscape where the neutron drip line has been reached. Triggered by the discovery [4] of abnormally spatially extended nuclei (^{6}He, ^{11}Li, ^{11}Be) in the vicinity of the neutron drip line, the initial idea of (binary) halos was suggested in [5]. Subsequent developments have deepened and enriched the picture of halos as phenomena involving extreme clustering into an ordinary core nucleus and a veil of halo nucleons. The halo phenomenon is now a well-established structural feature of many light drip-line nuclei [6–8]. In this article, we will discuss various reactions featuring halo nuclei, with special emphasis on how, from the theoretical point of view, such reactions contribute to our knowledge of the structure and dynamics of the nuclear halo.

2. REACTIONS INVOLVING LIGHT HALO NUCLEI

2.1. Total Reaction (Interaction) Cross Sections

It is well known from traditional nuclear-physics courses that nuclei (many-particle systems bound by a strong and short-range interaction) are very condensed (saturated) systems with volumes proportional to the nucleon number A. As we have already mentioned in the Introduction, the first experiments with radioactive beams measured interaction cross sections (or reaction cross sections) for light neutron-drip-line nuclei and revealed abnormally large cross sections for some light neutron-rich nuclei. The measured cross sections (see also more recent measurements reported in [9, 10]) provide important information about the structure of exotic nuclei, namely, about their sizes. This means that, from the measured interaction cross sections, one can see an unexpected large increase in the radii of ^{6}He, ^{11}Li, ^{11}Be, ^{14}Be, and ^{17}B in relation to the corresponding lighter particle-stable isotopes; this is the first piece of evidence of an unusual structure of these nuclei.

Later theoretical studies [11, 12] indicate that the sizes of some of these systems can be larger than

*This article was submitted by the authors in English.

[1)]Institute of Nuclear Physics, Moscow State University, Russia; e-mail: parfenov@fu.chalmers.se

[2)]SENTEF, Institute of Physics, University of Bergen, Norway; e-mail: jans.vaagen@fi.uib.no

**e-mail: Mikhail.Zhukov@fy.chalmers.se

the sizes extracted from the cross sections at the first stage. For example, the ^{11}Li radius can be as large as 3.55 fm [11] (compare with the old estimate of 3.12 fm), making ^{11}Li comparable in size with stable nuclei having approximately four times more nucleons. Note that the root-mean-square (rms) radius of ^{11}Li is about 1 fm larger than the rms radius of ^{9}Li. This is very unusual for strongly interacting systems bound by short-range interactions. Thus, some distance within the ^{11}Li system must be very large. Combining this fact with the low two-neutron separation energy of ^{11}Li, one can conclude that, on average, the valence neutrons must be far from the ^{9}Li core.

There is another piece of important information about the structure of neutron-halo nuclei, which can be obtained if both the interaction cross section and the neutron-removal cross section on a light target at high energy are known. For example, the cross section for the interaction of high-energy ^{11}Li [$\sigma_I(^{11}\mathrm{Li})$] with light targets [4, 13] is approximately equal to the interaction cross section for ^{9}Li [$\sigma_I(^{9}\mathrm{Li})$] plus the two-neutron-removal cross section (σ_{-2n}): $\sigma_I(\mathrm{core}+n+n) \approx \sigma_I(\mathrm{core}) + \sigma_{-2n}$. This is strong evidence of rather well-defined clustering into the core and two neutrons.

This formula is valid not only for ^{11}Li but also for ^{6}He, but it is not valid if we assume the $^{6}\mathrm{He}+n+n$ structure for ^{8}He. Probably, systems like ^{8}He and ^{19}B can be classified as those that contain four-neutron halos. At least in the case of ^{8}He, we have strong evidence for such a classification. The cross section for the interaction of high-energy ^{8}He with light targets [13] is approximately equal to the interaction cross section for an α particle plus the sum of the two-neutron-removal and the four-neutron-removal cross section. Thus, this system may be considered a five-body system containing an α-particle core and four valence neutrons.

2.2. Elastic and Inelastic Scattering

The elastic scattering of ^{6}He, ^{8}He, and ^{11}Li halo nuclei on light targets was measured at low [14–16] and high [17] energies in inverse kinematics. In general, the measurements of elastic scattering were intended for providing information about density distributions in nuclear halos. However, detailed theoretical studies of elastic scattering at low energies (< 100 MeV/nucleon) clearly showed [16, 18] that this process (at least for the current level of accuracy and the currently measured angular range) does not set a stringent constraint to be used to determine features of the underlying structure, and it is not a very promising tool for obtaining information about the density distribution of the valence neutrons in the halo. The results also show that the size of the core in halo nuclei plays a more important role in determining the differential cross section for elastic scattering than the low density tail associated with the valence neutrons.

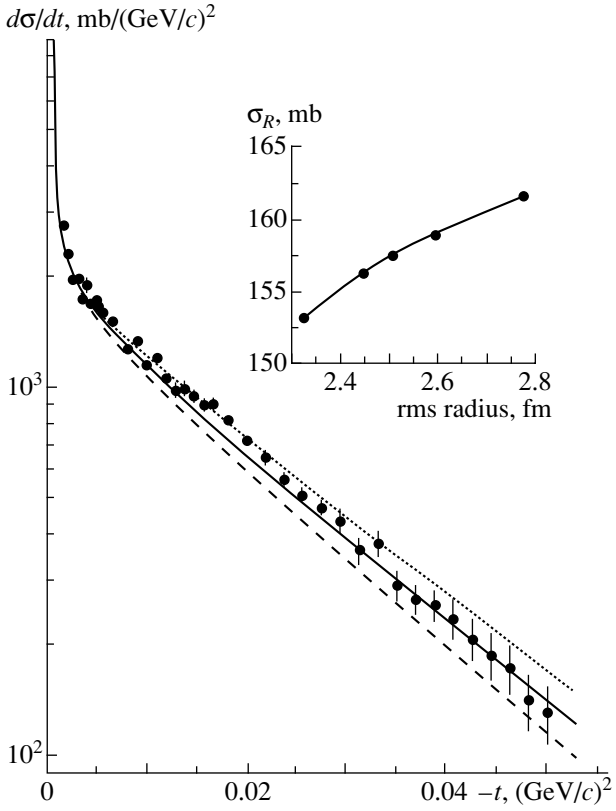

Fig. 1. Calculated [21] and experimental [17] angular distributions of the differential cross section for elastic p+^{6}He scattering versus the square of the 4-momentum transfer ($q^2 = -t$) at 717 MeV per nucleon. The calculations use various three-body ^{6}He wave functions with the indicated rms matter radii equal to (dotted line) 2.33, (solid line) 2.50, and (dashed line) 2.77 fm. The inset shows the predicted total reaction cross section versus the rms radius.

It should be noted, however, that elastic scattering on specific light targets at very low energies can still provide interesting information about the halo structure and correlations. As an example, we can refer to the elastic ^{6}He scattering on a ^{4}He target measured at 25 MeV per nucleon [19]. It is very important that these measurements covered a broad angular range, including backward angles. A theoretical treatment of the resulting differential cross section clearly indicates [20] that two-neutron transfer between two identical α particles plays a significant role in explaining the behavior of the cross section at backward angles. It is also found that the "dineutron" configuration of the ^{6}He nucleus (see [6]) makes a

dominant contribution to the two-neutron-transfer cross section.

Elastic scattering at high energies [17] is more sensitive to the halo tail of the density distribution than at low energies. A theoretical analysis performed within the Glauber models [21, 22] with microscopic ^{6}He wave functions led to the conclusion that the rms matter radius of ^{6}He is around 2.5 fm. In Fig. 1, taken from [21], the sensitivity of the results to the size of ^{6}He is demonstrated. The sensitivity of the reaction cross section to the ^{6}He rms matter radius is also shown.

The inelastic scattering of halo nuclei where all halo constituents are measured in coincidence furnishes information about the continuum structure of these nuclei. The positions and widths of the resonances, the momentum distributions, and momentum transfers can be extracted from the data. Note that, for the cases where the low-lying resonance is a dominant feature of the spectrum, the corresponding momentum distributions are not straightforwardly related to the distributions in the projectile [23]. The inelastic scattering of ^{6,8}He, ^{11}Li, and ^{14}Be were measured at low and high energies [14–16, 24–29] for light and heavy targets. For light targets, the experiments confirmed the existence of the known 2^+ state in ^{6}He [16, 24] and predicted new resonances in ^{8}He [14, 25] and a new three-body resonance at $E^* = 1.25$ MeV in ^{11}Li [15], which can be a candidate for a neutron halo excitation. The existence of such a state was confirmed later in a different experiment [30]. Note that, in the case of ^{6}He, theoretical calculations predict more three-body resonances at higher energies (see [31] and references therein), but the statistics of experimental data at high excitation energies limit the sensitivity of the data to these structures.

In general, there are many reaction mechanisms leading to the inelastic scattering of halo nuclei on light and heavy targets and a very complicated four-body problem must sometimes be solved in order to incorporate them properly in a theory. In [32], it was shown that, within some reasonable approximations, this problem can be solved and that the results for the high-energy inelastic scattering of ^{6}He are in good agreement with the experimental data reported in [24].

However, there is one special feature of halo systems that makes it possible to treat the inelastic scattering of these systems on heavy targets in a simpler way. Looking only at neutron-halo nuclei, one can expect a rather large difference between the positions of the charge and mass centers in the body-fixed frame. This will lead to large matrix elements for electromagnetic dissociation (in particular, for the $E1$ transition). All experiments employing heavy targets clearly showed [24–29] that the electromagnetic-dissociation (EMD) cross sections (mainly for an $E1$ transition) are much larger for neutron-halo nuclei (per unit charge) than for stable nuclei. Moreover, EMD (mainly through an $E1$ transition) is a dominant process for heavy targets that is characterized by large cross sections. The theory of Coulomb dissociation for high-energy projectiles on a heavy target is well known [33], and the differential cross section $d\sigma/dE$ is then obtained by multiplying the electromagnetic ($E1$) strength function $dB_{E1}(E)/dE$ by the virtual-photon spectrum $N_{E1}(E)$ [33]:

$$\frac{d\sigma}{dE} \sim N_{E1}(E)\frac{dB_{E1}(E)}{dE}, \qquad (1)$$

$$S_{\rm clus}^{\rm NEW} = \frac{3}{4\pi} Z_c^2 e^2 \langle r_c^2 \rangle,$$

where Z_c is the core charge. The function $dB_{E1}(E)/dE$ can be extracted from experimental data and can be obtained theoretically from the calculated ground state 0^+ and continuum 1^- wave functions. Another important characteristic is the $E1$ non-energy-weighted cluster sum rule $S_{\rm clus}^{\rm NEW}$ (1) [34, 35], which is the integral of the strength function with respect to energy.[3)] As can be seen from (1), $S_{\rm clus}^{\rm NEW}$ contains very important information about the geometry of the ground-state wave function—namely, the distance r_c between the center of mass of the core and the center of mass of the entire nucleus.

Very recently, the three-body breakup process (inelastic scattering) $^6\mathrm{He} \to {}^4\mathrm{He} + n + n$ was studied experimentally by using a ^{6}He beam of energy 240 MeV per nucleon incident on a lead target [24]. The $E1$-strength distribution deduced from electromagnetic cross sections is shown in Fig. 2 along with theoretical predictions. Despite rather large errors, the experimental strength function clearly demonstrates a large $E1$ strength at low energies, which leads to a very large electromagnetic cross section of about 500 mb. The three-body calculations performed in [31, 36] also predict a concentration of the strength at low energies. However, these calculations lead to $E1$-strength functions with maxima and more pronounced concentration at lower energies than that found experimentally. This fact should be comprehended, and improvements in these calculations are needed. In [24], the value of $S_{\rm clus}^{\rm NEW}$ was obtained by integrating the experimental $E1$ strength function (Fig. 2) up to the excitation energy of 10 MeV, whereby the experimental value of $r_c = 1.12 \pm 0.13$ fm (for ^{6}He) was deduced. This distance is in very good agreement with the theoretical results from few-body calculations [6].

[3)] Note that we discuss here only cluster strength functions.

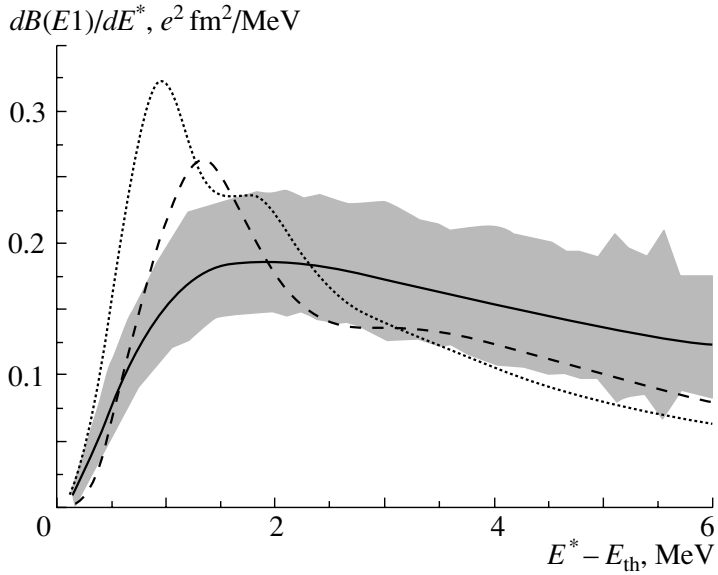

Fig. 2. Experimentally derived $E1$-strength distribution for ^{6}He [24] (solid curve) with the errors shown (shaded band). The theoretical distributions were borrowed from (dotted curve) [36] and (dashed curve) [31]. The excitation energy E^* minus the two-neutron-separation energy E_{th}, its experimental value being 0.975 MeV, is plotted along the abscissa.

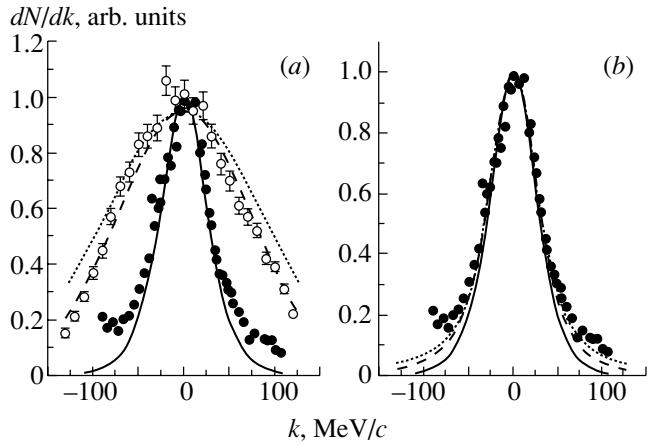

Fig. 3. Longitudinal-momentum distributions of ^{14}C fragments from one-neutron removal (experimental points and curves calculated theoretically). Closed circles represent experimental data from [39] without identification of a ^{14}C state, while open circles [46] correspond to excited fragment states. In both panels, the solid curve is the momentum distribution for $1s_{1/2}$-neutron removal accompanied by the production of ground-state fragments. The dashed (dotted) curve in Fig. 3*a* corresponds to the momentum distribution calculated for $0p_{1/2}$-neutron removal with the production of fragments in 1^- and 0^- states by using black-disk (realistic) profile functions, while the dashed and the dotted curve in Fig. 3*b* depict the distributions that are analogous to those in Fig. 3*a*, but which were obtained for neutron removal with the production of fragments in all final states.

2.3. One-Nucleon-Removal Reactions

One-nucleon-removal reactions usually have large cross sections and provide information on both the spatial structure and the features of the interaction process (see, for example, [37–39]). For few-neutron-halo nuclei, this process bears very important information about continuum states in the subsystems (see, for example, [25, 28, 40]).

To simplify the discussion, we will concentrate below only on one-neutron-halo nuclei. Generally, the momentum distribution of a heavy fragment from the neutron-removal reaction is determined by the Fourier transform of the function that describes the neutron–fragment relative-motion wave and which is corrected for fragment and nucleon interactions with the target nucleus. From the theoretical point of view, one expects that the longitudinal-momentum distribution is less perturbed by reaction mechanisms than

the transverse-momentum distribution. Thus, investigation of longitudinal-momentum distributions is a powerful tool for exploring both the spatial structure (in particular, for halo nuclei) and nuclear-reaction mechanisms.

Treatment of experimental data has usually been based on the assumption that the core of a halo nucleus (a heavy fragment) is an inert spectator of neutron removal. The corresponding theoretical approaches have achieved a good description of the shape and width of momentum distributions. However, there remain some open questions in describing the high-momentum part of the distributions and total cross sections. It appears that, apart from a process of valence-neutron removal, there are additional mechanisms capable of contributing to the yield of core fragments, such as (i) the removal of a neutron from states admixed to the s-wave component of the ground state of a halo nucleus [41, 42] and (ii) the removal of a neutron from the core nucleus with the production of excited core fragments and with the sequential deexcitation of core fragments through photon emission.

Recently, new experiments measuring longitudinal-momentum distributions of the heavy fragment from the one-neutron-removal channel were performed. Also, γ rays from the deexcitation of the heavy fragment were measured in [43, 44]. This made it possible to separate and to evaluate the contributions of core fragments in various excited states and to extract the momentum distributions that correspond to neutron removal from individual core states. These data also provide spectroscopic information about halo nuclei. The theoretical analysis [44, 45] of experimental data on the reaction ^{9}Be(^{11}Be, ^{10}Be $+ \gamma$) induced by a 60-MeV/nucleon ^{11}Be beam is consistent with the experimental finding [44] that about 22% of the one-neutron-removal cross section corresponds to the production of ^{10}Be in low-lying excited states.

There is another light nucleus (^{15}C) that is of particular interest in connection with the appearance of the halo phenomenon [39, 41]. In a preliminary experimental analysis of one-neutron removal from this nucleus, [^{9}Be(^{15}C, ^{14}C $+ \gamma$)] at an incident energy of 83 MeV/nucleon [46], it was found that, for ^{14}C formation in excited states, the cross section is about 25% of the total one-neutron-removal cross section. In [47], a theoretical analysis of this reaction was performed in the eikonal approximation. Both the momentum distributions and the cross sections for ^{14}C production in various excited states were calculated. Figure 3 shows some results of these studies. As can be seen from Fig. 3*a*, the longitudinal-momentum distributions of ^{14}C fragments are described correctly by the calculations. The inclusion of one-neutron removal from the core improves the agreement of the theoretical results with the experimental data in the high-momentum part (Fig. 3*b*) of the longitudinal-momentum distribution of ^{14}C fragments.

3. CONCLUSION

Instead of discussing all reactions that involve halo nuclei and which are used to extract the properties of these exotic systems, we have concentrated here on a few selected reactions that have large cross sections and which provide a bulk of information about the structure of halo nuclei. The quantities discussed in this report have been chosen as the best illustrations of dominant few-body features of the structure and reactions. However, a number of other observables related to two- and three-body halos have also been studied—e.g., in transfer reactions, fusion, charge exchange reactions, and beta decay, which all substantiate the overall picture discussed in the present article.

REFERENCES

1. A. Navin *et al.*, Phys. Rev. Lett. **85**, 266 (2000).
2. H. Iwasaki *et al.*, Phys. Lett. B **481**, 7 (2000).
3. A. Ozawa *et al.*, Phys. Rev. Lett. **84**, 5493 (2000).
4. I. Tanihata *et al.*, Phys. Rev. Lett. **55**, 2676 (1985).
5. P. G. Hansen and B. Jonson, Europhys. Lett. **4**, 409 (1987).
6. M. V. Zhukov *et al.*, Phys. Rep. **231**, 151 (1993).
7. P. G. Hansen, A. S. Jensen, and B. Jonson, Annu. Rev. Nucl. Part. Sci. **45**, 591 (1995).
8. I. Tanihata, J. Phys. G **22**, 157 (1996).
9. T. Suzuki *et al.*, Nucl. Phys. A **658**, 313 (1999).
10. A. Ozawa *et al.*, Nucl. Phys. A **673**, 411 (2000).
11. J. S. Al-Khalili and J. A. Tostevin, Phys. Rev. Lett. **76**, 3903 (1996).
12. L. V. Chulkov *et al.*, Europhys. Lett. **8**, 245 (1989).
13. I. Tanihata *et al.*, Phys. Lett. B **289**, 261 (1992).
14. A. A. Korsheninnikov *et al.*, Phys. Lett. B **316**, 38 (1993).
15. A. A. Korsheninnikov *et al.*, Phys. Rev. C **53**, R537 (1996).
16. A. A. Korsheninnikov *et al.*, Nucl. Phys. A **617**, 45 (1997).
17. G. D. Alkhazov *et al.*, Phys. Rev. Lett. **78**, 2313 (1997).
18. S. P. Weppner, Ofir Garcia, and Ch. Elster, Phys. Rev. C **61**, 044601 (2000).
19. G. M. Ter-Akopian *et al.*, Phys. Lett. B **426**, 251 (1998).
20. Yu. T. Oganessian, V. I. Zagrebaev, and J. S. Vaagen, Phys. Rev. Lett. **82**, 4996 (1999).
21. J. S. Al-Khalili and J. A. Tostevin, Phys. Rev. C **57**, 1846 (1998).
22. B. Abu-Ibrahim, K. Fujimura, and Y. Suzuki, Nucl. Phys. A **657**, 391 (1999).

23. M. V. Zhukov *et al.*, J. Phys. G **20**, 201 (1994).
24. T. Aumann *et al.*, Phys. Rev. C **59**, 1252 (1999).
25. K. Markenroth *et al.*, Nucl. Phys. A **679**, 462 (2001).
26. D. Sackett *et al.*, Phys. Rev. C **48**, 118 (1993).
27. S. Shimoura *et al.*, Phys. Lett. B **348**, 29 (1995).
28. M. Zinger *et al.*, Nucl. Phys. A **619**, 151 (1997).
29. M. Labiche *et al.*, Phys. Rev. Lett. **86**, 600 (2001).
30. M. G. Gornov *et al.*, Phys. Rev. Lett. **81**, 4325 (1998).
31. B. V. Danilin *et al.*, Nucl. Phys. A **632**, 383 (1998).
32. S. N. Ershov, B. V. Danilin, and J. S. Vaagen, Phys. Rev. C **62**, 041001(R) (2000).
33. C. A. Bertulani and G. Bauer, Phys. Rep. **163**, 299 (1988).
34. B. V. Danilin, Phys. Lett. B **302**, 129 (1993).
35. H. Esbensen and G. F. Bertsch, Nucl. Phys. A **542**, 310 (1992).
36. A. Cobis, D. V. Fedorov, and A. S. Jensen, Phys. Rev. C **58**, 1403 (1998).
37. H. Simon *et al.*, Phys. Rev. Lett. **83**, 496 (1999).
38. M. H. Smedberg *et al.*, Phys. Lett. B **452**, 1 (1999).
39. D. Bazin *et al.*, Phys. Rev. C **57**, 2156 (1998).
40. D. Aleksandrov *et al.*, Nucl. Phys. A **633**, 234 (1998).
41. D. Ridikas *et al.*, Nucl. Phys. A **628**, 363 (1998).
42. F. M. Nunes, I. J. Thompson, and R. C. Johnson, Nucl. Phys. A **596**, 171 (1996).
43. A. Navin *et al.*, Phys. Rev. Lett. **81**, 5089 (1998).
44. T. Aumann *et al.*, Phys. Rev. Lett. **84**, 35 (2000).
45. J. A. Tostevin, J. Phys. G **25**, 735 (1999).
46. A. Navin *et al.*, in *Proceedings of the "Experimental Nuclear Physics in Europe: Facing the New Millenium (ENPE 99)," Seville, 1999,* AIP Conf. Proc. **495**, 309 (1999).
47. Yu. L. Parfenova, M. V. Zhukov, and J. S. Vaagen, Phys. Rev. C **62**, 044602 (2000).